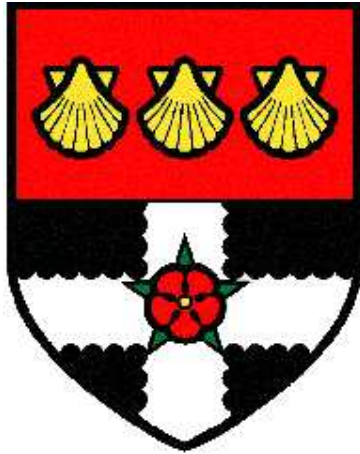


UNIVERSITY OF READING

Department of Meteorology



Boundary-layer ventilation by  
baroclinic life cycles

Victoria Anne Sinclair

*A thesis submitted for the degree of Doctor of Philosophy*

December 2008

Declaration

I confirm that this is my own work and the use of all material from other sources has been properly and fully acknowledged.

Victoria Anne Sinclair

---

# Abstract

---

The aim of this research is to understand how mid-latitude weather systems ventilate pollutants out of the boundary layer. Specifically, which regions of the boundary layer beneath mid-latitude weather systems can exchange air with the troposphere, which physical processes act to transport pollutants, and what controls the amount of ventilation. These questions are investigated by simulating dry baroclinic life cycles in the presence of a boundary-layer parameterisation scheme with a passive tracer included to represent pollutants.

Firstly, the boundary-layer structure and the exchange of mass between the boundary layer and free troposphere on synoptic scales is investigated. The boundary-layer structure is found to be strongly coupled to the large-scale dynamics and driven by thermal advection. Mass is cycled through the boundary layer on synoptic scales; the boundary layer gains mass in anticyclonic regions and loses mass in the warm sector.

Secondly, three interlinked processes are identified to transport tracer within the baroclinic life cycles. They are vertical turbulent mixing, horizontal divergence and convergence within the boundary layer (which is induced by the large-scale flow and by surface friction) and advection out of the boundary layer by the warm conveyor belt.

Finally, the relative importance of these processes is investigated. Sixteen life cycles are simulated with different large-scale dynamics or boundary-layer parameters. Advection by the warm conveyor belt is found to be the most critical transport process in determining the amount of ventilation. Transport of tracer within the boundary layer is shown to be of secondary importance. Quasi-geostrophic theory is used to determine how the ascent of the warm conveyor belt scales with environmental parameters. A strong correlation is found to exist between this and both the amount of mass and tracer ventilated out of the boundary-layer.

---

# Acknowledgements

---

Firstly, I am thoroughly grateful to my supervisors, Sue Gray and Stephen Belcher. I probably couldn't of found a better combination of supervisors; both have willingly shared their wealth of knowledge with me and have provided admirable role models for me as a researcher.

I would like to thank my old house mates of 20 Basingstoke Road for being great people to live with, and for giving me a real 'home' to go back to at the end of each day.

I would also like to thank the occupants of 1U07, and many other Ph.D students, who have made my time in Reading the great experience that is has been, have become good friends, and most importantly, provided many hours of necessary distractions.

I would not be writing this if my parents had not encouraged me throughout my life in all that I have done, for which I am very grateful. Finally, I would like to thank Ewan for so many things, but especially for proof reading all of this thesis, solving hundreds of computing problems that I would still be scratching my head at, and always believing in me regardless what.

---

# Contents

---

<b>Abstract</b>	<b>iii</b>
<b>Acknowledgements</b>	<b>iv</b>
<b>1 Introduction</b>	<b>1</b>
1.1 Overview . . . . .	1
1.2 Transport processes . . . . .	2
1.2.1 Coastal ventilation processes . . . . .	2
1.2.2 Orography . . . . .	2
1.2.3 Convection . . . . .	3
1.2.4 Turbulent mixing . . . . .	4
1.2.5 Synoptic scale advection . . . . .	5
1.3 Baroclinic Instability . . . . .	10
1.3.1 The Eady model of baroclinic instability . . . . .	12
1.3.2 Effects of friction on baroclinic life cycles . . . . .	14
1.4 Advantages of an idealised modelling approach . . . . .	17
1.5 Remaining unanswered questions . . . . .	18
1.6 Aims of this Thesis . . . . .	19
<b>2 Methods</b>	<b>21</b>
2.1 Introduction . . . . .	21
2.2 The Reading IGCM . . . . .	21
2.3 The IGCM boundary-layer parameterisation scheme . . . . .	22
2.3.1 Surface-layer fluxes . . . . .	24
2.3.2 Outer-layer fluxes . . . . .	29
2.4 Inclusion and treatment of tracers in the IGCM . . . . .	32
2.5 Setup of the Idealised Met Office Unified Model . . . . .	33
2.6 The Unified Model boundary-layer parameterisation scheme . . . . .	35
2.6.1 Surface-layer fluxes . . . . .	36

2.6.2	Outer-layer fluxes . . . . .	39
2.7	Treatment of tracers in the U.M. . . . .	43
2.8	Diagnostics . . . . .	44
2.8.1	Boundary-layer depth . . . . .	44
2.8.2	Boundary-layer bulk stability . . . . .	46
2.8.3	Conveyor belt location . . . . .	46
<b>3</b>	<b>Description of idealised life cycles</b>	<b>48</b>
3.1	Introduction . . . . .	48
3.2	Baroclinic life cycles in the IGCM . . . . .	48
3.3	Description of the U.M. control life cycle . . . . .	53
3.4	Differences between LC1 in the IGCM and the control U.M. cyclone . . . . .	58
3.5	Summary . . . . .	61
<b>4</b>	<b>Synoptic controls on boundary-layer structure</b>	<b>62</b>
4.1	Introduction . . . . .	62
4.2	Motivation . . . . .	62
4.3	Boundary-Layer Structure . . . . .	65
4.3.1	Surface Fluxes . . . . .	65
4.3.2	Boundary-layer depth and stability . . . . .	67
4.3.3	Comparison of boundary-layer structure in LC1 and LC2 . . . . .	71
4.4	Boundary layer mass budget . . . . .	73
4.4.1	Derivation of the mass budget equation . . . . .	75
4.4.2	Mass budget results . . . . .	78
4.5	Conclusions . . . . .	85
<b>5</b>	<b>Boundary-layer ventilation processes</b>	<b>89</b>
5.1	Introduction . . . . .	89
5.2	Vertical mixing by boundary-layer turbulence . . . . .	90
5.3	Advection in the boundary layer . . . . .	92
5.4	Ventilation by the warm conveyor belt . . . . .	94
5.4.1	Dependence on method of tracer initialisation . . . . .	100
5.5	Tracer budgets . . . . .	102
5.6	Transport in the free troposphere . . . . .	103
5.7	Discussion and conclusions . . . . .	107
5.8	Summary . . . . .	110
<b>6</b>	<b>Factors controlling ventilation</b>	<b>111</b>
6.1	Introduction . . . . .	111
6.2	Boundary-layer structure in the control U.M. cyclone . . . . .	113

---

6.3	Ventilation dependence on source strength . . . . .	116
6.4	Ventilation dependence on boundary layer transport processes . . . . .	117
6.4.1	Motivation for the selected experiments . . . . .	117
6.4.2	Effect of surface drag on life cycle dynamics and boundary-layer structure . . . . .	119
6.4.3	Effect of surface drag on the spatial distribution of mass and tracer fluxes . . . . .	123
6.4.4	Effect of surface drag on total amount of mass and tracer ventilation	128
6.4.5	Boundary-layer tracer budgets . . . . .	130
6.5	Dependence of ventilation on large-scale dynamics . . . . .	139
6.5.1	Theory . . . . .	139
6.5.2	Experiments conducted . . . . .	141
6.5.3	Effect of vertical shear, latitude and stability on life cycle evolution .	142
6.5.4	Quasi-Geostrophic mass and tracer fluxes . . . . .	142
6.5.5	Quantifying ventilation using QG theory . . . . .	146
6.6	Summary . . . . .	148
<b>7</b>	<b>Conclusions and Discussion</b>	<b>151</b>
7.1	Main Conclusions . . . . .	152
7.2	Future work . . . . .	158
	<b>References</b>	<b>160</b>

---

## CHAPTER ONE

# Introduction

---

### 1.1 Overview

An understanding of how pollutants are ventilated out of the boundary layer is required as pollutants can influence local air quality and alter chemical transformations near the source if they remain in the boundary layer. Alternatively, if pollutants are ventilated into the free troposphere they can be advected long distances, and have an impact on regional and global air quality. At higher altitudes pollutants can absorb long and short wave radiation, altering the radiative forcing of the Earth's climate. Pollutants are lost by dry deposition within the boundary layer but not the free troposphere. The rate at which pollution is ventilated into the free troposphere determines the residence time of pollutants in the boundary layer, and hence the amount of pollution that dry deposition can return to the surface. Therefore, the physical processes that control the rate of boundary-layer ventilation can also exert a control on the chemistry of the whole troposphere.

Cyclones are dominant features of the atmospheric circulation in the mid-latitudes. Mid-latitude weather systems are efficient at redistributing heat and moisture within the atmosphere, and many recent studies (e.g. Bey *et al.*, 2001; Hess and Vukicevic, 2003; Purvis *et al.*, 2003) suggest that they are also important for transporting pollutants out of the boundary layer and over long distances in the free troposphere. The overall aim of this research is to identify the physical processes that lead to boundary-layer ventilation, quantify the efficiency of cyclones to ventilate the boundary layer and determine what controls the amount of ventilation. These aims are addressed by taking an idealised modelling approach. Baroclinic life cycles, which are idealised mid-latitude weather systems,

are simulated using two different general circulation models. Passive tracers are included in all model simulations to represent pollutants. The transport and resulting distribution of these tracers is then analysed to answer the questions posed above.

## 1.2 Transport processes

A number of physical processes can act to transport pollution within mid-latitude cyclones. Donnell *et al.* (2001) and Agustí-Panareda *et al.* (2005) classified these processes into three categories: boundary-layer turbulent mixing, convection, and advection by synoptic-scale motions. Additionally, pollutants can be transported out of the boundary layer in the absence of synoptic weather systems by mesoscale features such as sea breezes and orographic flows.

### 1.2.1 Coastal ventilation processes

Transport of pollutants by sea-breezes is an important process as a large proportion of the Earth's population lives in coastal zones. During the day there is typically an on-shore flow near the surface, and a return off-shore flow at upper levels. Sea breezes can ventilate through two processes. The first process is by convergence and forced ascent where the low-level sea breeze collides with a prevailing wind. This lofts pollutants to the upper regions of the boundary layer and, in situations of strong ascent, can ventilate pollutants out of the boundary layer. Leon *et al.* (2001), in a mesoscale modelling study, showed that convergence between a sea breeze and prevailing winds caused air to rise up to 2.5 km. The second process is referred to as coastal outflow (Dacre *et al.*, 2007). Coastal outflow occurs when the prevailing wind is directed offshore. During the day the boundary layer is deeper over land than over sea. Pollutants are mixed to the top of the convective boundary layer over land, and then are advected horizontally offshore. As the pollutants in the land boundary layer are at a greater height than the marine boundary-layer inversion they are no longer within the boundary layer. Consequently, the pollutants are decoupled from the surface, no longer subject to dry deposition, and can be transported longer distances.

### 1.2.2 Orography

Orography in the form of hills or valleys can act to ventilate the boundary layer. As flow approaches a hill, or mountain, air is either forced around or over the obstacle depending

upon the Froude number,  $F_r = u/Nh_m$ , where  $u$  is the wind speed,  $N$  is the Brunt-Väisälä frequency and  $h_m$  is the height of the obstacle. If  $F_r$  is greater than unity then the flow will rise and travel over, not round, the hill. This induces vertical motion, which can act to transport pollutants out of the boundary layer. Valley flows have also been identified to ventilate pollutants out of the boundary layer. Henne *et al.* (2004) investigated the mechanisms involved in topographic venting in two separate alpine valleys and quantified the export of boundary-layer air to the free troposphere by means of air mass budgets. They found that during the day differential heating resulted in up-valley winds, parallel to the valley floor, and that at the valley side-walls up-slope winds were significant and could penetrate across the boundary-layer inversion. Henne *et al.* (2004) calculated that, on average, three times the valley air mass is exported to the troposphere per day, and hence is an important process for boundary-layer ventilation in mountainous regions.

### 1.2.3 Convection

Convection can develop as discrete upright cells forced by surface heating, convergence lines, or as slantwise cells embedded within frontal cloud-bands. All forms of convective activity cause rapid vertical transport and hence can ventilate pollutants out of the boundary layer into the free troposphere on timescales ranging from tens of minutes to a few hours. Transport of pollution by deep convection has received considerable attention. Dickerson *et al.* (1987) measured concentrations of carbon monoxide and non-methane hydrocarbons in the anvil of a thunderstorm and found concentrations far in excess of the concentrations observed outside of the anvil. They concluded that the deep convection was responsible for transporting pollutants vertically out of the boundary layer to the upper regions of the thunderstorm. As well as individual storms, studies have also investigated the climatological importance of deep convection in ventilating the boundary layer. Thompson *et al.* (1994) calculated terms in a carbon monoxide budget integrated over one month in early summer in the central U.S. and found the flux of carbon monoxide out of the boundary layer by deep convection to be the dominant term. Thompson *et al.* (1994) also showed that boundary-layer tracers can be transported as high as 15 - 16 km during a convective event and that the majority of tracers transported out of the boundary layer by convection reach an altitude between 8 and 10 km.

Deep convection has also been shown to be capable of transporting boundary-layer air to the lower stratosphere. Danielsen (1993) studied deep convection near Darwin,

Australia, and observed that the convective clouds could penetrate into the lower stratosphere. This potential for pollution transport into the lower stratosphere has been confirmed by Fischer *et al.* (2003) who measured concentrations of tropospheric trace gases in the stratosphere above the anvil of a Mediterranean thunderstorm. They found elevated concentrations of tropospheric gases far in excess of background values, confirming the direct transport of polluted boundary-layer air to the lower stratosphere.

Shallow convection has received less attention, however a number of studies have been conducted. Gimson (1997) used a mesoscale numerical model to investigate transport of an idealised tracer by shallow convection behind a cold front. The tracer is found to be transported from its initialisation height of 500 m up to the cloud-top level (4 - 5 km), demonstrating that shallow convection can ventilate the boundary-layer. Dacre *et al.* (2007) investigated the processes that led to boundary-layer ventilation during a non-frontal day over the U.K. again by using a mesoscale model, and also showed that, in the absence of fronts, shallow cumulus convection is a significant boundary-layer ventilation process. Convection embedded within frontal cloud bands has also been identified as an important transport process. In a case study of a frontal cyclone in North-West Europe Agustí-Panareda *et al.* (2005) found that including convection considerably enhanced the amount of boundary-layer ventilation compared to when large-scale advection was the only process acting to transport the tracer. Additionally, Purvis *et al.* (2003) found that embedded convection along a cold front, rather than large-scale advection, was the dominant process in ventilating the boundary layer.

#### 1.2.4 Turbulent mixing

Turbulent mixing acts to redistribute pollutants within the atmospheric boundary layer on timescales of a few hours. Mixing by turbulence within the boundary layer is critical for boundary-layer ventilation, despite the small vertical scale of most turbulent eddies, as it lofts pollutants away from surface based sources to the upper regions of the boundary layer where large-scale motions are present. The amount of mixing a pollutant experiences is dependent on the depth and stability of the boundary layer. For example, on microscales, Arya (1999) has shown boundary-layer stability and depth to strongly influence pollutant concentrations within the urban boundary layer. Additionally, Rigby and Toumi (2008) found using both a Gaussian plume model and a box model, both of which require an estimate of boundary-layer depth and stability class as input parameters, that pollutant

concentrations within London could be well modelled. On larger scales, previous work (e.g. Fleagle and Nuss, 1985; Bond and Fleagle, 1988) has shown there to be considerable horizontal variability in the boundary-layer depth and stability found beneath different parts (e.g. the warm sector, post-cold front zone, anticyclone) of mid-latitude weather systems. (This is described in more detail in Chapter 4).

Therefore, it is necessary to account for the different degrees of turbulent mixing within the boundary layer beneath different parts of a mid-latitude synoptic system, and it would be inappropriate to assume a well-mixed boundary layer with horizontally homogeneous pollutant concentrations across synoptic scales. This has been confirmed in previous studies (e.g. Donnell *et al.*, 2001; Agustí-Panareda *et al.*, 2005; Dacre *et al.*, 2007) which have attempted to quantify the importance of turbulent mixing in relation to other transport processes. Donnell *et al.* (2001) found that including transport by turbulent mixing in three case studies (two frontal situations and one anticyclonic) increased the amount of a passive tracer that was transported from the boundary layer to the free troposphere by between 9% and 13%. Similar findings were reported by Agustí-Panareda *et al.* (2005), who also state that the combination of different transport mechanisms (advection, convection, turbulent mixing) on the amount of ventilation is not additive, and often their interaction is more important than the role of individual process. The importance of including turbulent mixing was also emphasised by Dacre *et al.* (2007), who found in a coastal ventilation study that turbulent mixing considerably enhanced the amount of tracer transported from the boundary layer to the free troposphere. Clearly, the inclusion of turbulent mixing significantly alters the resulting distribution of pollutants. Therefore, to correctly model pollution transport, turbulent mixing not only should be included, but it is also vital to include the correct amount of turbulent mixing. This is highlighted by Roelofs and Lelieveld (1995) who hypothesised that the lack of sufficient turbulent mixing between the boundary layer and free troposphere in a chemistry general circulation model was responsible for the underestimation of tropospheric ozone concentrations in polluted continental regions.

### 1.2.5 Synoptic scale advection

Transport of pollution by advective processes occurs mainly due to synoptic systems on timescales of hours to days. To understand how pollutants may be transported within a mid-latitude cyclone it is useful to consider the typical structure of a mid-latitude cyclone.

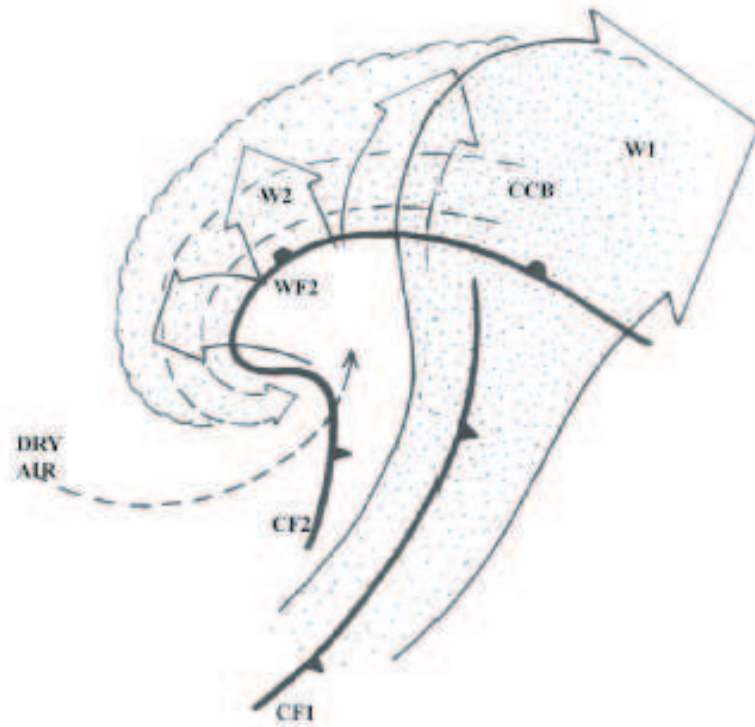


**Figure 1.1:** Schematic diagram of the principal flows within a typical mid-latitude cyclone adapted from Bader *et al.* (1995). W1 marks the main anticyclonic warm conveyor belt, W2, the cyclonic part of the warm conveyor belt and CCB, the cold conveyor belt. WF denotes the warm front and CF the cold front.

### *Conceptual models of cyclones*

Conceptual models of mid-latitude cyclones and the main airflows within them are discussed in numerous studies (e.g. Harrold, 1973; Carlson, 1980; Browning, 1985). A schematic of the main air flows observed within a typical mid-latitude cyclone is shown in Figure 1.1. Conceptual models refer to the main airflows within cyclones as conveyor belts. The first such conveyor belt is the warm conveyor belt (WCB), labelled W1 in Figure 1.1, which originates in the warm sector of the cyclone ahead of the cold front at low levels. This airstream experiences ascent as it moves polewards. At upper levels the WCB can follow a cyclonic path around the poleward side of the low centre, (W2 in Figure 1.1) or can overrun the surface warm front, hence experiencing additional ascent, and follow an anticyclonic path. The cyclonic branch of the WCB then descends as it forms the cloud head, a hook-shaped cloud feature on the poleward side of the main cloud band (Browning and Roberts, 1994), indicated by the scalloped shading in Figure 1.1. The WCB has a large potential to ventilate the boundary layer due to its ascent to the mid to upper troposphere from the boundary layer. The second conveyor belt is the cold conveyor belt (CCB)

which is also initially found at low levels but in the cool air ahead of the surface warm front. The CCB travels rearwards relative to the advancing system, around the poleward side of the low centre. In principle, ventilation by the CCB is possible, but this has not been identified in previous studies. The final airstream identified in conceptual models of mid-latitude cyclones is the dry intrusion (indicated by the dashed arrow labelled dry air in Figure 1.1). This airstream originates at upper levels and descends rapidly behind the cold front. Clearly the dry intrusion has no potential for boundary-layer ventilation, but does have important consequences for stratosphere - troposphere exchange.

### *Previous studies of ventilation and transport by large-scale advection*

Of all the physical processes that have been identified to ventilate the boundary layer large-scale advection has received the most attention in recent years, primarily due to the international consequences of long-range pollution transport.

Previous studies can be grouped into those that have considered individual case studies and those that have taken a more climatological approach. Taking a case study approach allows for smaller scale processes to be identified, and additional detail in the tracer transport to be realised, compared to what is achievable in a climatological type of study where such processes can be averaged out. However, the climatological approach has advantages; it produces more representative estimates of ventilation and transport as it does not depend on one individual weather system, which may have been an anomalous system.

Many case studies, which include observational (e.g. Bethan *et al.*, 1998; Cooper *et al.*, 2001; Stohl *et al.*, 2003b) modelling (e.g. Parker, 1999; Donnell *et al.*, 2001; Agustí-Panareda *et al.*, 2005), or combined studies (e.g. Li *et al.*, 2002; Fuelberg *et al.*, 2003; Cooper *et al.*, 2004; Mari *et al.*, 2004), of long range transport have been conducted and their results show that WCBs are capable of transporting pollution large distances. However, discrepancies exist between these studies, and by reviewing the literature (below) it becomes evident that the route pollutants follow as they are transported out of the boundary layer, and especially how efficient this transport is, is not yet fully understood.

Bethan *et al.* (1998) compared aircraft data taken in two WCBs, one associated with a developing low pressure and the other a mature system, in the Eastern Atlantic. Their observations confirmed that air can be transferred from the boundary layer to the free troposphere during the development of a baroclinic wave. However, Bethan *et al.* (1998)

also found that due to the different origins of the two WCBs the chemical signature of the two airstreams were considerably different. Huntrieser *et al.* (2005) presented experimental evidence which showed that baroclinic systems can not only ventilate the boundary layer but can also transport pollutants from North America to Europe; a pollution plume was tracked using airborne and surface measurements for one week from the Eastern U.S. (where pollutants were lifted from the boundary layer to the free troposphere by a WCB) to the European Alps (where one branch of the plume was observed to descend to ground level). Similar transport paths have also been shown to exist between Asia and North America. Hess and Vukicevic (2003) used an adjoint method (which unlike typical trajectory studies includes transport due to mixing and convection) to investigate transport paths between Asia and North America between 15 April 1992 and 15 May 1992 and found that pollutants are lofted out of the Asian boundary layer in a very narrow band above the surface cold front before being transported almost isentropically across the Pacific. The transport paths identified by Hess and Vukicevic (2003) are in good agreement with conceptual models of cyclones; one travels anticyclonically away from the surface low (W1 in Figure 1.1) and a second travels cyclonically around the low (W2 in Figure 1.1). Hannan *et al.* (2003) investigated transport from East Asia to North America by two different cyclones using in-situ and remotely sensed chemical data together with high-resolution meteorological modelling. The airstreams that were observed to ventilate the boundary layer differed considerably from those described in typical conceptual models, and were significantly more complex. This disagrees with the results of Hess and Vukicevic (2003) and highlights the amount of case-to-case variability between cyclones. The second main finding of Hannan *et al.* (2003) was that interactions between successive cyclones and anticyclones along a storm track are important for the resulting chemical composition of the airflows within cyclones. Hannan *et al.* (2003) showed evidence in agreement with Bethan *et al.* (1998); the origin of the airstream (e.g. continental boundary layer versus oceanic boundary layer) strongly affects the chemical composition of the airstream downstream. Esler *et al.* (2003) emphasised the degree of case to case variability in the amount of boundary-layer ventilation due to WCBs by examining two cold front systems over the U.K, using flight measurements, mesoscale model data and trajectory calculations. They found that the stronger of the two cyclones was eight times more efficient at ventilating the boundary layer than the weaker one.

Modelling studies (e.g. Kowol-Santen *et al.*, 2001; Donnell *et al.*, 2001) have con-

firmed that pollutants can be transported out of the boundary layer by mid-latitude weather systems. In a case study of a cyclone over Europe, Kowol-Santen *et al.* (2001) identified the WCB as the main advective process for boundary-layer ventilation and found that the WCB transported 70% of a tracer initialised in the boundary layer into the free troposphere within three days. Donnell *et al.* (2001) showed advection to be the dominant transport mechanism in three separate case studies where the role of turbulent mixing and convection was also considered. However, results of a case study presented by Agustí-Panareda *et al.* (2005) showed that embedded convection within the warm conveyor belt can be as, or more, important than advection for boundary-layer ventilation.

As well as the case-study approach to understanding transport by large-scale advection, some climatology-type studies, although considerably fewer in number than of the case study variety, have also been conducted. In an attempt to relate the numerous varied case studies to each other, Cooper *et al.* (2002) made the first attempt to develop a conceptual model of the chemical composition of a mid-latitude cyclone tracking across the Northern Atlantic. Their results showed that although synoptic-scale dynamics played a crucial role in determining the chemical characteristics of the main airflows, some characteristics of the conceptual model exerted the same influence on trace gases regardless of the cyclone's intensity or location (e.g. the CCB and WCB both experienced wet deposition but the WCB was found to be more photochemically active due to its more southerly location). Airstreams in the mid-troposphere were shown to be the most susceptible to mixing with other air masses. Hess (2005) used a global chemistry transport model to simulate the transport of two tracers during the summer (June, July, August) and winter (December, January, February) of 2001-2002. One tracer was transported by convective processes and the other advective processes. During the winter, in the mid-latitudes, transport by advection was found to be more important than transport by convection. A composite of the largest deviations in the advective tracer concentration at 500 mb with the corresponding surface pressure pattern was also shown. The highest tracer concentrations at 500 mb were found in the warm sectors of cyclones, which indicated, that averaged over a winter season, transport by the warm conveyor belt is the dominant transport process in mid-latitudes. Cotton *et al.* (1995) took a global climatological approach, combining numerical modelling experiments and observations, to quantify the efficiency of different cloud systems at ventilating the boundary layer. On average, extra-tropical cyclones were found to have the largest mass flux out of the boundary-layer of all cloud venting systems

(others analysed include ordinary cumuli, ordinary thunderstorms, mesoscale convective systems and tropical cyclones).

Finally, idealised modelling approaches are now considered. Currently there are few idealised modelling studies which investigate boundary-layer ventilation. Stone *et al.* (1999) analysed the transport of three passive tracers by idealised baroclinic life cycles in a general circulation model which excluded diabatic processes and turbulent mixing, but did not make an attempt to identify physical transport processes. The tracers were predominantly transported by the eddy flux associated with the life cycles and not the background flow, and the largest transport occurred during the nonlinear growth periods of the life cycle. Polvani and Esler (2007) investigated the exchange and mixing of different airmasses (boundary layer, free troposphere and stratospheric) during the evolution of two contrasting idealised baroclinic life cycles. They showed the warm conveyor belt to transport a similar amount of tracer out of the boundary layer in both cases. However, no boundary-layer parameterisation scheme was included and therefore the definition of the boundary-layer depth is arbitrary and is effectively assumed to be constant in time and space. Additionally, although Polvani and Esler (2007) identified transport processes, the absence of a boundary-layer scheme means that they did not investigate transport by boundary-layer processes. It is likely that, due to the proximity to the surface, transport processes within the boundary layer will differ considerably to those that have been observed in the free troposphere. It is thus hypothesised that a range of physical processes, within and above the boundary layer, interact with each other to transport pollution away from surface based sources and into the free troposphere.

### 1.3 Baroclinic Instability

As baroclinic life cycles are simulated throughout this thesis, an overview of baroclinic instability theory is now presented. Baroclinic instability is the well accepted theoretical explanation for cyclogenesis in the mid-latitudes (Charney, 1947; Eady, 1949). Baroclinic instability exists in the mid-latitudes due to the large meridional temperature gradients that develop between the equator and the poles (Holton, 1992). This background state exists as the equator receives considerably more solar radiation, and hence energy, than the polar regions do. To remove this imbalance, and decrease the North-South temperature gradient, pressure perturbations in the form of cyclones and anticyclones develop and act

to transport heat from the equator to the poles. The baroclinic systems that develop remove potential energy from the background state and convert it into kinetic energy through ascending poleward moving branches of warm air and descending equatorward moving branches of cold air (James, 1995).

The mechanism by which a small perturbation on a baroclinically unstable background state can grow into an intense weather systems can be explained by considering baroclinic instability in terms of potential vorticity (PV). Potential vorticity (Ertel's form (Ertel, 1942)) is given by

$$PV = \frac{1}{\rho} \zeta \cdot \nabla \theta, \quad (1.1)$$

where  $\rho$  is density,  $\zeta$  is absolute vorticity and  $\theta$  is potential temperature. The most significant property of potential vorticity is that it is conserved in the absence of diabatic and frictional effects (Rossby, 1940; Ertel, 1942), and therefore can be thought of as a tracer of air parcels in the atmosphere. In terms of understanding dynamical meteorology, the second useful quality of PV is that it is invertible. This means that, given a suitable balance condition (the simplest being geostrophic balance), if the full three-dimensional structure of the PV field is known, then the three-dimensional wind and temperature distributions can be obtained (Hoskins *et al.*, 1985). Therefore, temperature (or pressure) anomalies are closely related to anomalies in PV; a warm (cold) anomaly at the ground is associated with a positive (negative) PV anomaly and a warm (cold) anomaly at the tropopause is associated with a negative (positive) PV anomaly (Bretherton, 1966). By considering how PV anomalies at different height levels interact with each other, the growth of baroclinic systems can be understood. The schematic shown in Figure 1.2 shows how an upper level PV anomaly can act to alter the low-level circulation. If a positive (cold) PV anomaly at upper levels, such as a tropopause fold, is advected into a region with a strong surface temperature gradient, the cyclonic circulation associated with the upper PV anomaly extends downwards and induces a cyclonic PV anomaly at the surface, as indicated by the faint dashed lines in Figure 1.2. The low-level induced winds act to distort the initial North-South surface temperature gradient, moving warm air polewards and cold air equatorwards. The surface temperature wave that develops is out of phase with the upper level wave, and the two structures can become locked together. When this occurs, a positive feedback process occurs; the lower level PV anomaly will act

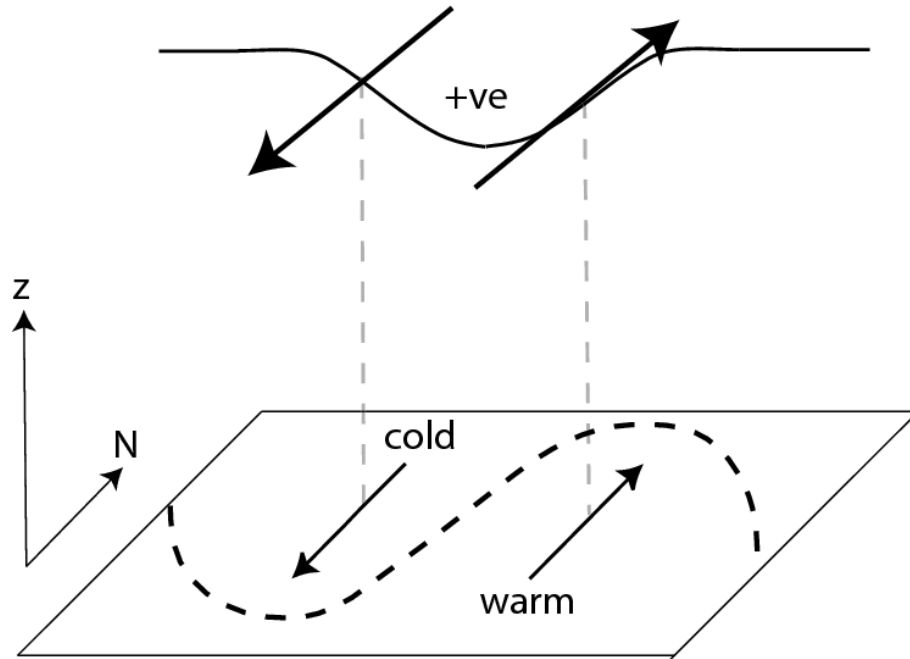


**Figure 1.2:** Schematic showing the interaction between an upper level positive (cold) PV anomaly in the form of a tropopause fold and the low level circulation. Solid arrows indicate wind direction, solid black line indicates the tropopause and dashed line indicates an isotherm with warm air to south and cold air to the north.

to enhance the upper level anomaly and vice-versa.

### 1.3.1 The Eady model of baroclinic instability

Eady (1949) developed an analytical model of linear baroclinic instability, which represents the growth of small amplitude wave like perturbations on a baroclinically unstable background state. The perturbations are constrained to be small to allow the governing equations to be linearised. The background state of the Eady model is a simple approximation to a typical wintertime storm track. It consists of a purely zonal flow (the meridional wind component is zero) with a constant vertical shear but no horizontal shear. Since there is constant vertical shear, thermal wind balance implies that there is a constant North-South temperature gradient. The  $f$ -plane assumption,  $f = f_0$ , is made, the Brunt-Väisälä frequency,  $N$ , is taken to be constant and the perturbation is assumed to have no  $y$ -dependence. The flow is constrained between two rigid boundaries, the lower of which represents the surface, and the upper the tropopause. As the vertical shear is constant, the steering level of the flow (the level at which the phase speed of the cyclone equals the velocity of the basic flow) is located midway between the surface and the tropopause.

Within the interior no perturbations to the quasi-geostrophic PV,  $q'$ , are allowed to exist (quasi-geostrophic PV differs from PV in that it is conserved following geostrophic flow along constant pressure surfaces):

$$q' = \frac{1}{f_0} \nabla_h^2 \Phi' + \frac{f_0}{N^2} \frac{\partial^2 \Phi'}{\partial z^2} = 0. \quad (1.2)$$

This constraint on the perturbation in geopotential height,  $\Phi'$ , combined with the requirement that the perturbation must also satisfy the quasi-geostrophic thermodynamic equation, allows for an analytical expression for the perturbation to be obtained. Eady (1949) analysed the normal modes of this system and found both exponentially growing and decaying waves as well as neutral modes beyond a short-wave cut off point. The wavenumber,  $k$ , of the the fastest growing normal mode is found to be

$$k = \frac{1.6f}{NH}. \quad (1.3)$$

If typical mid-latitude values of the Coriolis parameter  $f \sim 10^{-4} \text{s}^{-1}$ , the tropospheric depth,  $H \sim 10 \text{km}$  and the Brunt-Väisälä frequency  $N \sim 10^{-2} \text{s}^{-1}$ , are substituted into equation 1.3, the resulting wavelength ( $\lambda = 2\pi/k$ ) is approximately 4000 km, which is similar to the scale of observed mid-latitude weather systems. The maximum growth rate of the perturbation,  $\sigma$ , can also be found analytically and is given by

$$\sigma = -0.31 \frac{1}{N} \frac{g}{\theta_{\text{ref}}} \frac{\partial \theta}{\partial y}, \quad (1.4)$$

where  $g$  is the acceleration due to gravity and  $\theta_{\text{ref}}$  is a reference potential temperature. It is evident that the rate at which a baroclinic system intensifies is strongly related to the stability and meridional temperature gradient of the background state. Unsurprisingly, from an energetics view point, where stronger meridional temperature gradients exist the growth rate is larger as the atmosphere responds quicker to re-balance the meridional energy distribution. This is in agreement with observations; the strongest cyclones tend to develop on the eastern edges of continents, where there are strong sea surface temperature gradients such as the Gulf Stream and the Kuroshio Current.

The Eady model also predicts the structure of the growing waves; the pressure field is found to tilt westward with height, with the surface and upper boundary pressure waves

found to be  $90^\circ$  out of phase with each other. The temperature field has an eastward tilt with height whereas the vertical motion field tilts west with height, but not as significantly as the pressure field. Again, these structures are in good agreement with what is observed in baroclinic systems in reality, and this emphasises the usefulness of the Eady model as a first order approximation to baroclinic instability.

### 1.3.2 Effects of friction on baroclinic life cycles

Numerous studies (e.g. Petterssen and Smebye, 1977; Hoskins *et al.*, 1985; Thorncroft *et al.*, 1993; Hoskins, 1997) have focused on the growth and development of baroclinic waves in an idealised framework. However, all of these examples and the vast majority of studies consider the development of baroclinic life cycles in the absence of frictional effects. Clearly the inclusion of frictional processes and turbulent fluxes of momentum and heat will alter the development of baroclinic life cycles.

The traditional approach to this problem is to apply the theory that Ekman (1905) originally developed to explain an oceanographic observation: icebergs do not drift in the direction of the prevailing wind but at an angle of  $20^\circ$  -  $40^\circ$  to the right of the prevailing wind in the northern hemisphere. Ekman (1905) explained this observation in terms of the balance between the Coriolis force and frictional forces; the frictional drag of the ocean surface reduces the ocean currents, and therefore the Coriolis force exceeds the pressure gradient force, turning the ocean currents to the right. In an atmospheric boundary layer context this has the effect of turning the geostrophic wind towards low pressure and away from high pressure. This leads to convergence (divergence) in regions of low (high) pressure and induces ascent (descent) at the top of the boundary layer. This resulting vertical motion is referred to as Ekman pumping (ascent) or Ekman suction (descent). The effect of Ekman pumping on a cyclonic weather system is to squash the vortex tube associated with the large-scale cyclonic vorticity, which by conservation of momentum causes the vorticity to decrease and the weather system to weaken. This theory has been tested by a number of authors. Simmons and Hoskins (1978), in a study focusing on inviscid life cycles, briefly investigated the effect of a very simple surface friction parameterisation (which consists of a surface drag coefficient of 0.001 decreasing to zero at and above 2.5 km) on the evolution of a baroclinic life cycle. They found that the frictional drag acted to delay the life cycle's development by one day, and substantially reduced the mean meridional circulation at low levels. A more in depth investigation of the role of boundary-

layer parameterisation schemes on the evolution of baroclinic life cycles was presented by Valdes and Hoskins (1988) who compared life cycles with no frictional processes, an Ekman pumping parameterisation acting and with Rayleigh friction present. They concluded that both 'boundary-layer parameterisations' produce essentially the same results when incorporated into a baroclinic life cycle simulation; the growth rates of the fastest growing waves are reduced and the shorter wavelengths are stabilised. Many other studies (e.g. Williams and Robinson, 1974; Card and Barcilon, 1982; Farrell, 1985; Branscome *et al.*, 1989) have also shown that the inclusion of Ekman processes strongly inhibits the growth of normal mode life cycles. This is relevant for the study of boundary-layer ventilation; as surface friction can change the intensity of baroclinic life cycles, the inclusion of frictional processes can potentially change the efficiency of cyclones to ventilate the boundary layer.

The Ekman theory, which provides an explanation for why the growth rate of the life cycles is decreased, is based upon the assumption that the cyclonic vortex associated with the life cycle is barotropic. In reality, mid-latitude cyclones are baroclinic, and despite the numerous studies quoted above which explain their results using an Ekman dynamics framework, it is not clear whether the same mechanisms hold for baroclinic vortices that do for barotropic vortices. Adamson *et al.* (2006) investigated how the inclusion of momentum fluxes effected the dynamical evolution of idealised baroclinic life cycles by taking a different approach to previous studies. They studied the frictional generation of PV in the boundary layer and the transport of this PV into the free troposphere. The results found by Adamson *et al.* (2006) are in-line with previous studies; the inclusion of surface momentum fluxes decreased the strength of the cyclone and introduced a one day delay in the evolution. However, Adamson *et al.* (2006) suggested a different mechanism for this effect. Although the inclusion of drag was found to induce a negative PV anomaly through the Ekman pumping process, it remained confined to the low levels of the boundary layer, and hence could not have a significant effect on the large-scale dynamics. However, the surface drag was found to induce a significant positive PV anomaly in the boundary layer to the east of the low pressure centre, which was then advected into the free troposphere by the cyclonic part of the warm conveyor belt to above the low pressure centre. Once in the free troposphere the PV anomaly was found to be very shallow, but had considerable horizontal extent, and hence acted as a thin layer of high static stability, and reduced the coupling between the upper and lower level PV anomalies.

Identifying that the flow alterations induced by Ekman pumping are mainly confined

to the lower part of the boundary layer is important for the work presented in this thesis; if vertical motion caused by Ekman pumping does not extend to the top of the boundary layer it is unlikely to play a role in transporting pollutants out of the boundary, although it may still be important for redistributing pollutants within the boundary layer. Plant and Belcher (2007) built upon the work of Adamson *et al.* (2006), by simulating an additional contrasting life cycle, and repeating the life cycle experiment of Adamson *et al.* (2006), but with the inclusion of turbulent heat fluxes (as well as momentum fluxes) in both life cycles. Plant and Belcher (2007) found that the inclusion of turbulent heat fluxes had little effect on phase of the life cycle but did reduce the energy content of the life cycle. Also shown was that the frictionally generated positive PV anomaly develops regardless of the life cycle's frontal structure (the two life cycles studied by Plant and Belcher (2007) differ considerably in their frontal structures), and that the direct effect of the Ekman pumping spinning down the low-level vorticity is less significant than the frictional baroclinic process in which the positive PV anomaly acts to inhibit development.

Boundary-layer processes have been shown to alter the structure of the frontal features that develop during a baroclinic life cycle. Keyser and Anthes (1982) used a primitive equation horizontal-shear model to simulate frontogenesis with no friction, with a simple one layer bulk aerodynamic boundary-layer parameterisation, and with a more complex Blackadar (1962) type parameterisation scheme. They found that including the more complex parameterisation led to more realistic simulations which resolved a narrow updraught at the top of the boundary layer on the warm side of the cold front. This updraught was found to develop due to frictionally-driven, ageostrophic inflow (convergence) in the warm sector. The frictionally-induced convergence acted to maintain the cross-front potential temperature gradient, and counteracted the destruction of the frontal vorticity by turbulent mixing. These results are potentially highly significant for the experiments conducted in this thesis. Friction can induce convergence (and therefore divergence) within the boundary-layer, which indicates that pollutants are also likely to be transported horizontally within the boundary layer when frictional effects are included in experiments.

Hines and Mechoso (1993) investigated how the surface drag coefficient (surface roughness) affects the structure and evolution of fronts, and showed that surface drag acts to inhibit the formation of the warm fronts, whereas cold frontogenesis is not as sensitive to surface drag. In cases of no drag, very strong shallow, bent-back warm fronts were found to develop. Similar results are also presented by Rotunno *et al.* (1998) who in

addition used Ekman pumping to explain the different effects of surface drag on warm and cold fronts. Ekman-induced vertical motion, and hence cooling, was found to be large in the warm frontal region (near the surface low centre) which prevented the warm sector air moving northwards and forming a strong temperature gradient. In contrast, the Ekman pumping velocity was much weaker in the cold frontal region and hence there was limited effect on the intensity of the cold front. Although the physical mechanisms and explanations as to why drag has a much greater impact on warm fronts than cold are not fundamental to this thesis, the result is. It suggests that over rougher surfaces warm fronts will be significantly weakened which indicates that they would have less potential for boundary-layer ventilation. In contrast, as cold fronts are mainly unaffected by surface roughness, the type of surface a cold front is located over should have little effect on the amount of boundary-layer ventilation achieved.

## 1.4 Advantages of an idealised modelling approach

Before the details of the experiments conducted in this thesis are discussed, it is necessary to justify the idealised modelling approach that has been taken. Firstly, it should be noted that a wealth of knowledge in terms of the structure and development of mid-latitude weather systems has been obtained by modelling idealised baroclinic life cycles; all of the information presented in section 1.3 originates from such studies. This indicates that realistic systems can be modelled in an idealised framework and that this has been proven to be a useful experimental technique. The second reason for selecting an idealised modelling approach was that despite the large number of studies that have analysed boundary-layer ventilation using a case-study approach (see section 1.2.5 for extensive examples), there remains uncertainties as to which physical processes are important for ventilation, and what dynamical variables control the amount of ventilation. Case studies, while clearly more realistic than the idealised approach used here, are significantly more complicated and are not reproducible. This means that interpreting results and relating results from one case study to another is extremely challenging. Therefore, using an idealised approach allows for highly controlled, generic and clean experiments.

The baroclinic life cycles that are simulated in this thesis all exclude moisture and, except for the boundary-layer parameterisation, contain no physics. Dry life cycles have been simulated by numerous authors (e.g. Simmons and Hoskins, 1978; Rotunno *et al.*,

1998; Plant and Belcher, 2007) and have been shown to resemble mid-latitude weather systems. The absence of moisture in the model means that tracer transport by moist convection is not modelled. This has two consequences. Firstly, the amount of ventilation estimated in these simulations can be thought of either as the amount of ventilation due to dry processes alone or as a lower bound on the total amount of ventilation by all processes. Secondly, the results of these dry simulations are simpler to interpret: there are no small-scale features which would develop in moist simulations and hence transport by advective processes can be clearly identified. Therefore, this approach of dry idealised life cycle thus has significant advantages over both the case study and climate model approaches previously used.

## 1.5 Remaining unanswered questions

From the large number of studies quoted in section 1.2.5 it is clear that mid-latitude cyclones are capable of transporting pollutants large distance in the free troposphere. However, it remains unclear as to which of the physical processes, namely, turbulent mixing, convection or advection, is the dominant processes in ventilating pollutants out of the boundary layer and into the free troposphere. This uncertainty stems from our current inability to accurately quantify the efficiency of conveyor belt flows and convective activity to transport pollution out of the boundary layer. A second reason why questions remain unanswered in this field is that the majority of studies concentrate on modelling pollution transport paths once in the free troposphere, rather than in both the boundary layer and free troposphere. Those studies which have focused on pollution transport in the free troposphere have generally used a Lagrangian approach and have calculated back trajectories. This method provides a good understanding of transport paths in the adiabatic free troposphere but cannot be applied in the boundary layer (Stohl *et al.*, 2002). For this reason transport paths on synoptic spatial and temporal scales have rarely been studied within the boundary layer, for example Bethan *et al.* (1998) only calculated back trajectories down to 850 mb. Also evident from the reviewed literature is that it is difficult to predict the efficiency of a given cyclone at ventilating the boundary layer as it is not known what the main constraints and controls on this are.

## 1.6 Aims of this Thesis

From the introduction to the topic of boundary-layer ventilation provided here it is evident that to understand how pollutants are ventilated, and reliably quantify the amount of boundary-layer ventilation by all processes documented in section 1.2 is a task of daunting proportions. Therefore, this thesis will concentrate on two processes: turbulent mixing and large-scale advection by synoptic-scale weather systems. These two processes will be examined in unison so that the interaction between the large-scale dynamics and the turbulent structure of the boundary layer is captured. Although large-scale dynamics and boundary-layer mixing are to be considered together, they were selected for different reasons. Transport and ventilation by turbulent mixing has received limited attention, at least in the context of large-scale weather systems, and hence it is not well understood how turbulent mixing acts on large scales or interacts with large-scale processes. On the other hand, advection by synoptic systems has received significant attention. However, little progress has been made on drawing results from the numerous case studies together to provide a unified picture. Additional motivation for selecting this combination of transport processes is that there are few studies that investigate boundary-layer ventilation by considering the transport within the boundary layer prior to ventilation. Therefore, the experiments conducted here are designed to allow pollutant transport paths to be investigated from the surface source to the free troposphere. The first aim of this thesis is to develop a conceptual model of boundary-layer structures generated by mid-latitude weather systems. Within this aim a number of fundamental questions are addressed. Firstly, what is a typical pattern of surface fluxes, boundary-layer depth and stability in relation to mid-latitude weather features? Secondly, how do these properties evolve during the development of mid-latitude weather systems? Thirdly, how does the boundary-layer structure vary between different mid-latitude weather systems? Fourthly, which physical processes lead to the exchange of mass between the boundary layer and free troposphere, and finally, how does the exchange of mass vary spatially and as the weather systems intensify?

The second aim of this thesis is to identify physical mechanisms associated with synoptic-scale weather systems that redistribute pollutants within the boundary layer and free troposphere. Additionally, the interactions between these different transport processes are investigated. Again within this aim a number of specific questions will be addressed. Firstly, which physical processes can act to transport pollutants within the boundary

---

layer and free troposphere? Secondly, which regions of the boundary layer can pollutants be ventilated out of, and how do these areas change during the evolution of the cyclone? Thirdly, once pollutants are removed from the boundary layer, where are they transported to, and what is the timescale for this transport? Finally, how do these results vary between different cyclones?

The final aim of this thesis is to quantify the relative importance of different transport processes and to determine what aspects of the atmosphere control the amount of boundary-layer ventilation. Within this aim, a method for predicting the amount of ventilation given meteorological variables that are commonly found in large re-analysis datasets, is developed.

The overall approach of this thesis is that of an idealised modelling study, in which a variety of baroclinic life cycles are simulated using two global circulation models with differing degrees of complexity. Details of both models are presented in Chapter 2 and descriptions of the control life cycles are presented in Chapter 3. Chapter 4 shows how the large-scale dynamics affect the boundary-layer structure during the simulation of idealised baroclinic life cycles, and how air is exchanged between the boundary layer and free troposphere. The processes that lead to the transport and ventilation of tracers are then described in Chapter 5 and the controls on the efficiency of ventilation by different life cycles is investigated in Chapter 6. Finally, in Chapter 7 a summary of the results in this thesis is presented and are discussed in relation to previous studies and future applications.

---

## CHAPTER TWO

# Methods

---

### 2.1 Introduction

Baroclinic wave life cycle experiments, without moisture present, are used throughout this thesis to investigate the role of mid-latitude cyclones on boundary-layer ventilation. Idealised experiments have been conducted using two different numerical models: the Reading Intermediate Global Circulation Model (IGCM) and the Met Office Unified Model in idealised mode. The purpose of this Chapter is to describe both of these numerical models. The IGCM is a hemispheric spectral model and is described in detail in section 2.2. A boundary-layer parameterisation scheme is included in the IGCM, and this is described in section 2.3. In contrast to the intermediate nature of the IGCM, the Unified Model is a complex operational NWP model, which can be run at much higher resolution than the IGCM, and contains more sophisticated parameterisation schemes. The idealised Unified Model is described in section 2.5 and the boundary-layer parameterisation scheme applied in the Unified Model is described in section 2.6. In both numerical models a passive tracer is included to represent pollutants emitted at, or very near, the surface. The treatment of tracers by the IGCM is discussed in section 2.4 and by the Unified Model in section 2.7. Finally, diagnostics which are used throughout this thesis are introduced in section 2.8.

### 2.2 The Reading IGCM

Idealised baroclinic life cycles have been simulated with the Reading Intermediate Global Circulation Model (IGCM). This is a simplified global circulation model based on the

model of Hoskins and Simmons (1975) that solves the dry primitive equations on a sphere. The IGCM has a pedigree for simulating life cycles, and has been used successfully in a number of studies, (for example, Simmons and Hoskins, 1978; Thorncroft *et al.*, 1993). Variables in the horizontal are represented by a series of truncated spherical harmonics, and in the vertical a sigma coordinate is used. Horizontal internal diffusion is applied by the  $\nabla^6$  operator with a decay rate of  $4 \text{ h}^{-1}$  for the shortest retained wavelength. Initial simulations were conducted at a resolution of T42 L39, which corresponds to a horizontal grid spacing of approximately 180 km in the mid-latitudes ( $50^\circ\text{N}$ ). However, higher resolution experiments have also been conducted to quantify the sensitivity of the results to the numerical resolution. These higher resolution experiments were conducted at T85 L39 (approximate grid spacing of 90 km in mid-latitudes) and all figures in this thesis, except where explicitly noted, are from the T85 simulations. The vertical resolution was selected to provide a well resolved boundary layer. This is required to capture key boundary-layer features, such as the capping temperature inversion. Therefore, additional vertical levels have been added to the 15 vertical levels used by Thorncroft *et al.* (1993) and Simmons and Hoskins (1978). The new vertical resolution includes a stretched grid beneath sigma level 0.568 (approximately 4.3 km), which improves the boundary-layer level spacing to between 60 and 150 m for the 10 model levels below 1 km. Above this sigma level, the vertical resolution is double that used by Thorncroft *et al.* (1993). The heights of all of the new model levels are shown in Figure 2.1a, and the heights of the lowest 14 model levels (those within the 'boundary layer') are shown in Figure 2.1b.

### 2.3 The IGCM boundary-layer parameterisation scheme

A boundary-layer scheme is the only physical parameterisation scheme included in the simulations performed using the IGCM and is vital for the re-distribution of tracers in this study. The scheme is realistic for dry boundary layers and is based upon the parameterisation scheme used in the ECMWF forecast model (ECMWF Research Department, 1991). The parameterisation of the turbulent fluxes of momentum and heat was originally added to the IGCM by Adamson (2001). However, for the purpose of this thesis a few minor changes have been made to the original scheme. These changes were primarily made to account for the significantly increased vertical resolution in the boundary-layer, (in total Adamson (2001) had 19 model levels compared to the 39 used here) and to ensure that numerical stability is retained. The major difference between the boundary-layer

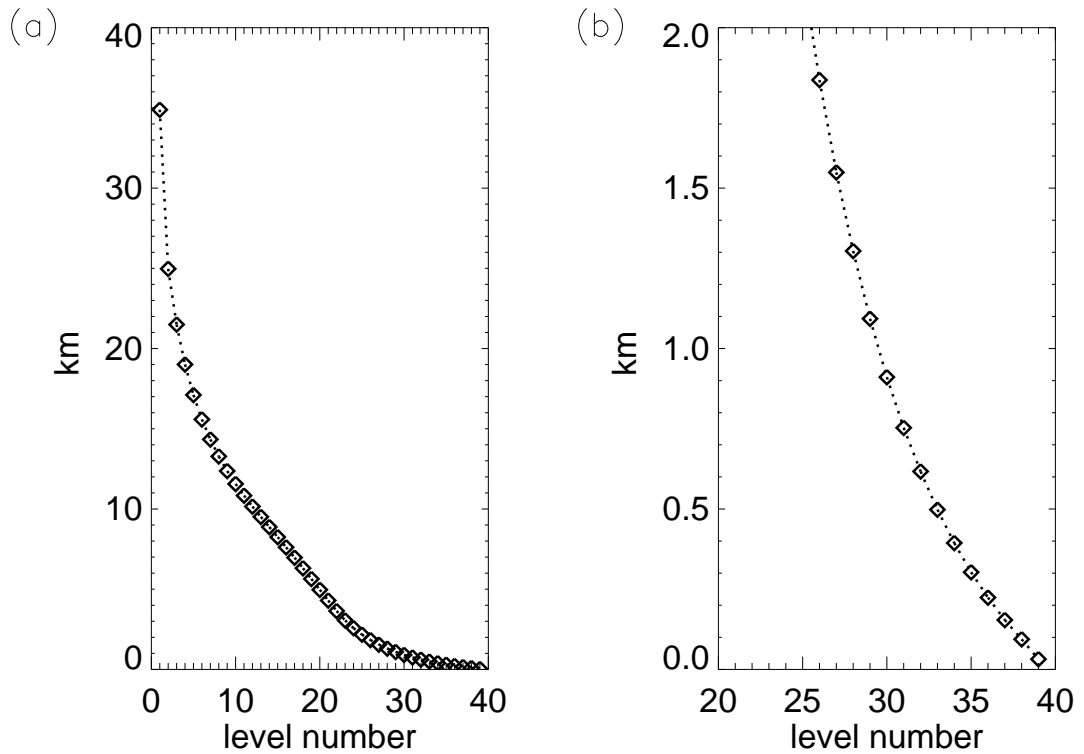


**Figure 2.1:** Height of model levels (km). (a) All 39 model levels (b) Model levels within the nominal boundary layer.

parameterisation used here and that of Adamson (2001) is that here turbulent fluxes of passive tracers are also included, the implementation of which is discussed in more detail in section 2.4.

The boundary-layer scheme uses bulk aerodynamic formulae to calculate fluxes of momentum, heat and tracers at the lowest model level, which is assumed to lie within the surface layer. Monin-Obukhov similarity theory is applied to include the effects of stratification on these fluxes. The surface roughness is calculated using the Charnock relation (Charnock, 1955). Above the surface layer turbulent fluxes are calculated using a mixing length approach, where the eddy diffusivities of heat and momentum include a stability dependence. Hence the boundary-layer scheme parameterises turbulence driven by both shear and buoyancy (dry convection). The parameterisation of surface fluxes is described first, followed by that of fluxes above the boundary layer.

### 2.3.1 Surface-layer fluxes

At the lowest model level the turbulent fluxes of momentum,  $\boldsymbol{\tau}$ , and heat,  $H$ , are calculated using bulk aerodynamic formulae;

$$\boldsymbol{\tau} = \rho C_d |\mathbf{V}| \mathbf{V}, \quad (2.1)$$

$$H = \rho c_p C_h |\mathbf{V}| (\theta_s - \theta_1), \quad (2.2)$$

where  $C_d$  and  $C_h$  are the non-dimensional drag coefficients for momentum and heat respectively.  $\rho$  is the density of air,  $c_p$  is the specific heat at constant pressure,  $\mathbf{V}$ , is the horizontal wind,  $\theta_1$  is the potential temperature at the lowest model level and  $\theta_s$  is surface temperature. In a neutrally stratified surface layer the drag coefficients for momentum and heat are calculated using

$$C_d = \left[ \frac{\kappa}{\log\left(\frac{z}{z_{0m}}\right)} \right]^2 \quad (2.3)$$

and

$$C_h = \left[ \frac{\kappa}{\ln\left(\frac{z}{z_{0m}}\right) \ln\left(\frac{z}{z_{0h}}\right)} \right]^2, \quad (2.4)$$

respectively, where  $\kappa$  is von Karman's constant (taken to be 0.4),  $z$  is the height above the surface,  $z_{0m}$  is the surface roughness length for momentum and  $z_{0h}$  is the roughness length for heat. The surface roughness length is obtained by using the Charnock relation,

$$z_{0m} = \alpha_c \frac{u_*^2}{g}, \quad (2.5)$$

where  $\alpha_c$  is the Charnock coefficient taken to be 0.018,  $u_*$  is the friction velocity and  $g$  is the acceleration due to gravity. The maximum value allowed for the surface roughness length is  $1.15 \times 10^{-5}$ m and the surface roughness length for heat is assumed to equal that of momentum ( $z_{0h} = z_{0m}$ ). Limiting the maximum value of the surface roughness length effectively allows the model user to define the type of surface that the baroclinic life

cycle will develop over. The small limiting value used here means that an ocean surface is effectively specified.

However, the surface layer is very rarely neutrally stratified; turbulent mixing by wind shear is inhibited during stable conditions and convectively driven turbulence is enhanced during unstable conditions. Therefore, the strength of the turbulent fluxes of heat and momentum are strongly determined by the stability of the surface layer. This effect is incorporated into the calculated turbulent fluxes by applying Monin-Obukhov similarity theory to the surface layer fluxes. Monin and Obukhov (1954) used dimensional analysis to develop a theory to account for the effects of different stratification. They assumed that the mean flow and turbulence depended only upon four variables: the height above the surface,  $z$ , the friction velocity,  $u_*$ , the surface heat flux,  $H$ , and a buoyancy parameter,  $g/\theta_1$ . The only possible way to combine these variables to obtain a dimensionless parameter is as  $z/L$ , where  $L$  is known as the Obukhov length and is given by

$$L = -\frac{u_*^3}{\kappa \frac{g}{\theta_1} \frac{H}{\rho c_p}}. \quad (2.6)$$

Within the surface layer the effect of stratification on the dimensionless wind shear and potential temperature gradients can be expressed by universal similarity functions of  $z/L$ :

$$\frac{\kappa z}{u_*} \frac{\partial \bar{U}}{\partial z} = \mathcal{F} \left( \frac{z}{L} \right) = \phi_m \left( \frac{z}{L} \right) \quad (2.7)$$

and

$$\frac{\kappa z}{\theta_*} \frac{\partial \bar{\theta}}{\partial z} = \mathcal{F} \left( \frac{z}{L} \right) = \phi_h \left( \frac{z}{L} \right), \quad (2.8)$$

respectively.  $\bar{U}$  and  $\bar{\theta}$  are the mean wind speed and potential temperature and  $\theta_*$  is a temperature scale obtained in Monin-Obukhov stability analysis. The form of the stability functions,  $\phi_h$  and  $\phi_m$ , which have been used here are those recommended by Arya (2001) for 'most practical applications'. In stable conditions, defined as when  $(z/L) \geq 0$ ,

$$\phi_h = \phi_m = \left( 1 + 5 \frac{z}{L} \right), \quad (2.9)$$

and in unstable conditions, defined as when  $(z/L) < 0$ ,

$$\phi_h = \phi_m^2 = \left(1 - 15\frac{z}{L}\right)^{-\frac{1}{2}}. \quad (2.10)$$

Integrating equations 2.7 and 2.8 with respect to height between  $z_0/L$  and  $z/L$  gives the following velocity and temperature profiles;

$$\frac{U}{u_*} = \frac{1}{\kappa} \left[ \ln \left( \frac{z}{z_{0m}} \right) - \Psi_m \left( \frac{z}{L} \right) \right] \quad (2.11)$$

and

$$\frac{\theta - \theta_0}{\theta_*} = \frac{1}{\kappa} \left[ \ln \left( \frac{z}{z_{0h}} \right) - \Psi_h \left( \frac{z}{L} \right) \right]. \quad (2.12)$$

$\Psi_m$  and  $\Psi_h$  are the integrated similarity functions for momentum and heat and are given by

$$\Psi_h = \Psi_m = -5\frac{z}{L} \quad (2.13)$$

in stable conditions and by

$$\Psi_h = 2 \ln \left[ \frac{1}{2} (1 + x^2) \right] \quad (2.14)$$

and

$$\Psi_m = \ln \left[ \frac{1}{8} (1 + x^2) (1 + x)^2 \right] - 2 \tan^{-1} x + \frac{\pi}{2} \quad (2.15)$$

in unstable conditions, where

$$x = \left(1 - 15\frac{z}{L}\right)^{0.25}. \quad (2.16)$$

By equating equation 2.1 with  $\tau = \rho U_*^2$ , it is evident that  $C_d = u_*^2/U^2$ . Substitution of this expression into equation 2.11 shows that the drag coefficient for momentum is a function of the integrated universal stability functions and is given by

$$C_d = \left[ \frac{\kappa}{\left( \ln \left( \frac{z}{z_{0m}} \right) - \Psi_m \left( \frac{z}{L} \right) \right)} \right]^2. \quad (2.17)$$

A similar argument exists for heat, which results in the drag coefficient for heat being described by

$$C_h = \left[ \frac{\kappa^2}{\left( \ln \left( \frac{z}{z_{0m}} \right) - \Psi_m \left( \frac{z}{L} \right) \right) \left( \ln \left( \frac{z}{z_{0h}} \right) - \Psi_h \left( \frac{z}{L} \right) \right)} \right]. \quad (2.18)$$

Typical magnitudes of the drag coefficient for momentum are of the order  $6 \times 10^{-4}$ , however maximum values can be as high as  $1 \times 10^{-2}$  in regions of strong winds and weak stratification. The drag coefficient for heat has a smaller magnitude, with typical values of  $2 \times 10^{-6}$ , and maximum values of  $3 \times 10^{-5}$ .

So far only the theoretical basis for the boundary layer scheme surface fluxes have been presented. A description of how this is conducted numerically in the IGCM is now presented.

### Numerical recipe to calculate surface fluxes

1. Calculate the surface roughness length using the Charnock relation (equation 2.5) assuming that the roughness length for heat and momentum are the same. Use the value of the friction velocity obtained at the end of the previous timestep.
2. Estimate the drag coefficients,  $C_d$  and  $C_h$ , for heat and momentum assuming neutral stratification (equations 2.3 and 2.4).
3. Perform an iteration to find the value of  $z/L$ .
  - (a) Specify first guesses for the likely maximum and minimum value of  $z/L$  which are chosen based upon the sign of  $z/L$ . For unstable conditions  $(z/L)_{min} = -50$  and  $(z/L)_{max} = -1 \times 10^{-3}$ . For stable conditions  $(z/L)_{min} = 1 \times 10^{-3}$  and  $(z/L)_{max} = 50$ .
  - (b) Using both the maximum and minimum values of  $z/L$  calculate a new maximum and minimum value of the drag coefficient for heat and momentum using equations 2.17 and 2.18.
  - (c) Using the 'new' maximum and minimum values for the drag coefficients calculate new maximum and minimum values of  $z/L$  values using

$$\frac{z}{L} = \frac{R \log(\sigma_1) \kappa C_h (\theta_s - \theta_1)}{C_d^{1.5} U_1^3} \quad (2.19)$$

where  $R$  is the gas constant for dry air,  $\sigma_1$  is the non-dimensional pressure at the first model level, and  $U_1$  is the wind speed at the lowest model level. This

expression for  $z/L$  is obtained by substituting equation 2.2 and  $\tau = \rho u_*^2$  into equation 2.6 to obtain

$$L = \frac{-C_d^{1.5} U^3}{\kappa \frac{g}{\theta_0} C_h (\theta_s - \theta_1)}. \quad (2.20)$$

This can then be substituted into  $z/L$ , and hydrostatic balance

$$\ln \left( \frac{p}{p_s} \right) = \frac{gz}{R\theta}, \quad (2.21)$$

can be used to finally obtain equation 2.19. (Note that  $\sigma = p/p_s$ ).

- (d) Test the new values of  $z/L$ . If the maximum value exceeds 1000 then the drag coefficients are assumed to be very small and are both set to  $1 \times 10^{-8}$ . If

$$|(z/L)_{max}^{new} - (z/L)_{max}^{old}| < |(z/L)_{min}^{new} - (z/L)_{min}^{old}|$$

then the value of  $(z/L)_{max}^{new}$  is retained to be used again in the iterative processes while the value of  $(z/L)_{min}^{new}$  is replaced by  $0.5 \times ((z/L)_{min}^{old} + (z/L)_{max}^{old})$ .

However if

$$|(z/L)_{max}^{new} - (z/L)_{max}^{old}| > |(z/L)_{min}^{new} - (z/L)_{min}^{old}|$$

then the value of  $(z/L)_{min}^{new}$  is retained to be used again in the iterative processes and the value of  $(z/L)_{max}^{new}$  is replaced by  $0.5 \times ((z/L)_{min}^{old} + (z/L)_{max}^{old})$ .

The relative error in the iteration is then calculated by dividing the difference between the current and previous estimate of  $z/L$  by the difference between the maximum and minimum values of  $z/L$ . If this is greater than the specified threshold, set to be 5%, then the values of  $z/L$  are passed back through the iteration until they do converge to within 5%.

4. With the final values of  $z/L$  calculate the Monin-Obukhov stability functions (equations 2.9 to 2.15)
5. Calculate stability dependent drag coefficients,  $C_d$  and  $C_h$ , using equations 2.17 and 2.18.
6. Calculate the surface fluxes of heat and momentum using bulk aerodynamic formulae (equations 2.1 and 2.2).

7. Calculate the value of the friction velocity using

$$u_* = \sqrt{C_d \bar{\mathbf{U}}^2} \quad (2.22)$$

to be used at the beginning of the next timestep to calculate the surface roughness length.

### 2.3.2 Outer-layer fluxes

Above the surface layer the scheme is based on the mixing length approach described by Louis (1979). Fluxes of momentum and heat are calculated using

$$\boldsymbol{\tau} = \rho K_m \frac{\partial \mathbf{U}}{\partial z} \quad (2.23)$$

and

$$H = -\rho c_p K_h \frac{\partial \theta}{\partial z}, \quad (2.24)$$

where

$$K_m = l_m^2 \left| \frac{\partial \mathbf{V}}{\partial z} \right| f_m(R_i) \quad (2.25)$$

and

$$K_h = l_m l_h \left| \frac{\partial \mathbf{V}}{\partial z} \right| f_h(R_i). \quad (2.26)$$

$R_i$  is the gradient Richardson number given by

$$R_i = \frac{\frac{g}{\theta_s} \frac{\partial \theta}{\partial z}}{\left( \frac{\partial u}{\partial z} \right)^2 + \left( \frac{\partial v}{\partial z} \right)^2}. \quad (2.27)$$

The mixing length for heat,  $l_h$ , is assumed equal to the mixing length for momentum,  $l_m$ , which is calculated using the method described by Blackadar (1962),

$$\frac{1}{l_m} = \frac{1}{\kappa z} + \frac{1}{l_0 \beta}, \quad (2.28)$$

where  $l_0 = 150\text{m}$ . The factor  $\beta$  is introduced to ensure that large mixing lengths do not occur at large heights (for example in the regions surrounding the mid-latitude zonal jet)

and hence including the  $\beta$ -term also removes the need to define the top of the boundary layer. With the  $\beta$  factor included the boundary-layer scheme can safely be applied over the whole depth of the atmosphere and negligible fluxes will be calculated above the boundary layer.  $\beta$  is calculated using the method used in the ECMWF forecast model (ECMWF Research Department (1991));

$$\beta = \beta_0 + \frac{1 - \beta_0}{1 + (z/D)^2}, \quad (2.29)$$

where  $\beta_0 = 0.2$  and  $D = 4000$  m. The variation of  $\beta$ , and the mixing length,  $l_m$ , with height is shown in Figure 2.2. It is evident that in the boundary layer  $\beta$  is large, and therefore the second term on the right hand side of equation 2.28 is small. This implies that in the boundary layer the mixing length mainly depends upon the distance from the ground. Physically, this is because the size of turbulent eddies that mix heat and momentum is limited by the distance from the surface. Above the boundary layer,  $\beta$  asymptotes to 0.2, and since the height,  $z$  is large, the first term on the right hand side of equation 2.28 becomes small. This means that far from the surface the amount of mixing is no longer determined by the height above the surface, but is limited by the beta term, and the mixing length tends towards a value of 30 m.

The function of the Richardson number in equations 2.25 and 2.26 represents the dependence of the eddy diffusivities on the atmospheric stability and hence strongly determines the amount of turbulent mixing within the boundary layer. The functions used are based upon those described by Louis (1979). For stable conditions ( $R_i \geq 0$ ) they are given by;

$$f_m(R_i) = \frac{1}{1 + 10R_i(1 + R_i)^{-0.5}} \quad (2.30)$$

and

$$f_h(R_i) = \frac{1}{1 + 10R_i(1 + R_i)^{0.5}}, \quad (2.31)$$

and for unstable conditions ( $R_i < 0$ ) by

$$f_m(R_i) = 1 - \frac{10R_i}{1 + 75\sqrt{-R_i} (l_m/z)^2 3^{-1.5}} \quad (2.32)$$

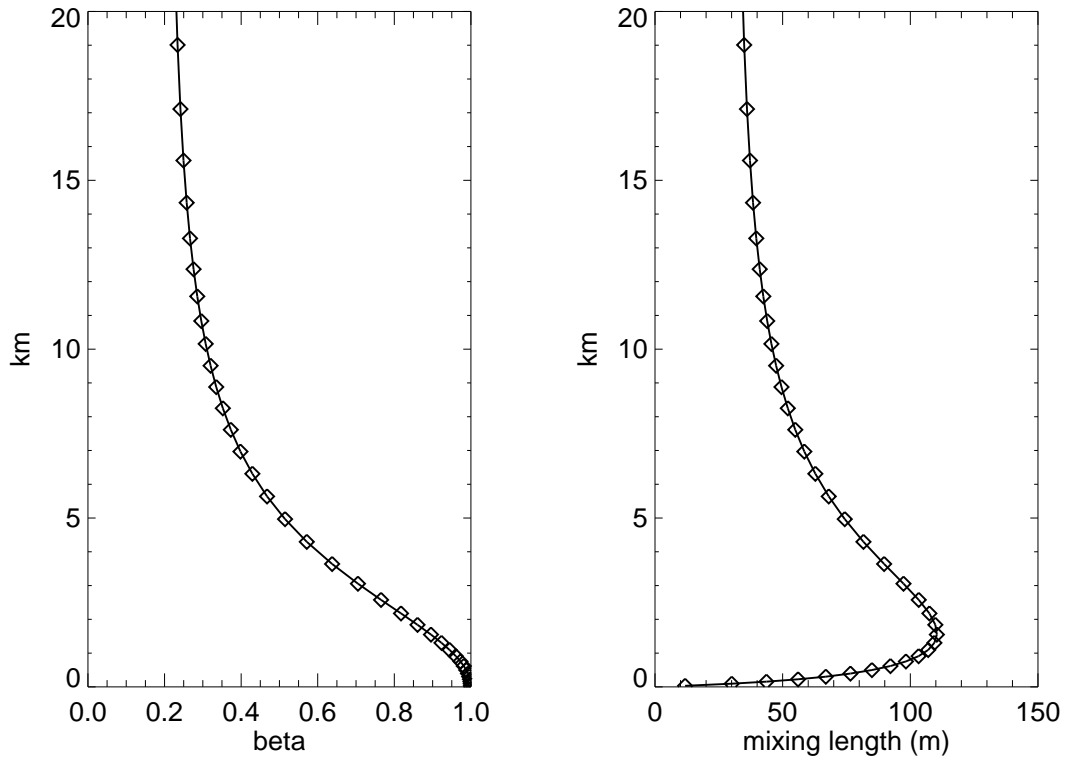


**Figure 2.2:** (a) beta and (b) mixing length both as functions of height (km)

and

$$f_h(R_i) = 1 - \frac{15R_i}{1 + 75\sqrt{-R_i} (l_m/z)^2 3^{-1.5}}. \quad (2.33)$$

The numerical treatment of the outer layer fluxes is much simpler, and also significantly computationally cheaper, than the surface layer fluxes as no iterative scheme is required. However for completeness a 'numerical recipe' for the treatment of the outer layer fluxes is also presented.

### Numerical recipe for outer layer fluxes

1. Calculate vertical gradients of the horizontal wind speed components and potential temperature using first order finite differences.
2. Define a value for the asymptotic length scale,  $l_0$  (150 m) and include a factor  $\beta$  to prevent capping the boundary layer
3. Calculate the gradient Richardson number using equation 2.27

4. Calculate the stability dependence using the calculated value of the gradient Richardson number substituted into equations 2.30 to 2.33.
5. Calculate eddy diffusivities for heat and momentum,  $K_h$  and  $K_m$ , using equations 2.25 and 2.26.
6. Calculate the turbulent fluxes of momentum and heat using equations 2.23 and 2.24.

## 2.4 Inclusion and treatment of tracers in the IGCM

A tracer has been added to the IGCM simulations to represent pollution emitted within the atmospheric surface layer. The passive tracer is initialised at the start of the simulation with an arbitrary horizontally uniform concentration ( $1 \text{ kg kg}^{-1}$ ) at the lowest model level,  $\sigma = 0.996$ , which corresponds to an approximate height of 32 m. No sources or sinks of tracer are present, and the tracer is acted upon by the model resolved wind components ( $u$ ,  $v$  and  $w$ ) as well as the turbulent motion diagnosed by the boundary-layer scheme. The horizontal advection of tracer occurs in wavenumber space so the derivatives that are evaluated are much more accurate than they would have been in a grid-point model. The vertical advection of tracer is by a total variation diminishing (TVD) scheme which uses a van Leer limiter. This scheme is based on that presented by Thuburn (1993). Using a TVD scheme eliminates any spurious oscillations in advected fields that would develop near strong gradients (which are likely to develop across the boundary layer inversion) if a second order centred finite difference approach was used. The tracer advection scheme is not positive definite. However, the domain integrated mass of tracer is conserved to within 1% of the total mass, and local concentrations only deviate outside of the initial range by 5%. (As this is an initial value problem with respect to the tracer distribution, tracer concentrations are expected to remain within the range of concentrations specified in the initial conditions:  $0 - 1 \text{ kg kg}^{-1}$ .) These errors only occur when the boundary-layer scheme acts upon the tracer which demonstrates that the large-scale tracer advection conserves tracer well.

The turbulent fluxes of the tracer are calculated in a similar way to those of heat; the drag coefficient ( $C_h$ ) and eddy diffusivity ( $K_h$ ) for heat are used. Therefore, within the surface layer the tracer flux is calculated using

$$F_{\text{tra}} = \rho C_h |\mathbf{U}| C_1, \quad (2.34)$$

where  $C_1$  is the tracer concentration at the lowest model level. If there was a surface based source included  $C_1$  would be replaced with  $C_1 - C_{\text{sfc}}$  where  $C_{\text{sfc}}$  is the surface concentration. However, in all experiments, except when explicitly noted,  $C_{\text{sfc}} = 0$ . Above the surface layer the turbulent fluxes of the tracer are calculated by

$$F_{\text{tra}} = \rho K_h \frac{\partial C}{\partial z}, \quad (2.35)$$

where the vertical gradient of the tracer concentration,  $C$ , is estimated using a first order finite difference method. It is hypothesised, though not explicitly proven, that the deviations in the local tracer concentrations out with the initial range occur due to this numerical approximation.

Using a passive tracer as a proxy for pollutants in these experiments has clear advantages and disadvantages over the obvious alternative: the use of a full chemical transport model combined with emissions data. The passive tracer is computationally cheaper than the chemistry transport model. Additionally, as there are no chemical sources or sinks of the passive tracer the resulting tracer distribution after the passage of the life cycle is only due to dynamical transport processes. Therefore, the passive tracer method provides clearer results to identify transport processes and estimate the efficiency of mid-latitude weather systems to ventilate the boundary layer. The disadvantage is that the uniform source at the surface is un-realistic; in practice there would be significant horizontal variations in the low-level pollution concentrations. This would effect the amount of pollutants removed from the boundary-layer. If the warm conveyor belt passed over a region with little pollution the amount of ventilation would be much smaller than if the warm conveyor belt passed over a region with high pollution concentrations.

## 2.5 Setup of the Idealised Met Office Unified Model

The Met Office Unified Model (U.M.) v6.1 is also used in an idealised configuration to simulate numerous baroclinic life cycles, and is now described. The U.M. solves the full primitive equations, is non-hydrostatic and is used operationally. The full dynamics and

parameterisation schemes from the global operational model, as described by Davies *et al.* (2005), are used in the idealised configuration. Previous studies which have used the U.M. in an idealised configuration include Dacre and Gray (2006), who investigated the development of shallow frontal waves, and Beare (2007) who considered boundary-layer mechanisms in extratropical cyclones. Here, a channel model is set up, which is achieved by specifying a rectangular domain with periodic east-west boundary conditions and fixed north-south boundaries. To allow the domain to wrap round in this manner it is necessary to use a cartesian coordinate system, instead of the standard spherical polar coordinates that are used operationally (the only possible way to apply the spherical polar coordinates in this idealised study would be to run the model over the whole globe, which is twelve times more computationally expensive than the simulations performed here). The only other difference in the numerical configuration of the idealised channel model compared to the operational version of the U.M. is that a f-plane approximation is used rather than  $f = 2\Omega \sin \phi$  which is used operationally. In the idealised configuration,  $f = 1.03 \times 10^{-4} \text{s}^{-1}$ , which corresponds to a latitude of  $45^\circ\text{N}$ , upon which the life cycles are centred. The idealised model is run here without the radiation parameterisation scheme acting, with no diurnal cycle, with no orography, and with no moisture present. The absence of moisture is achieved by setting the initial moisture fields in the whole domain to zero and forcing the surface latent heat fluxes to zero throughout the integration. The only physical parameterisation that is applied is the standard U.M. boundary-layer scheme (Lock *et al.*, 2000) which is used in all simulations and is described in detail in section 2.6. This model formulation (dynamics plus the boundary-layer parameterisation scheme) is the same that was used in the IGCM simulations.

The simulations are performed using a 10 minute timestep and a horizontal resolution of 0.4 degrees (approximately 44.5 km). The domain consists of  $150 \times 200 \times 38$  grid points in the x, y and z directions respectively, which results in a domain that is 60 degrees in longitude and 80 degrees in latitude. The domain size was chosen so that when wavenumber six baroclinic life cycles are simulated any downstream development will effectively develop on top of itself. Additionally, the longitudinal extent of the domain is the same that was used in the IGCM, and hence allows for easier comparisons to be made. The 38 vertical levels are non-uniformly spaced, with the highest resolution in the boundary layer ( $\sim 100$  m) decreasing to  $\sim 800$  m in the upper troposphere. The distribution of the model levels is shown in Figure 2.3; there are 10 levels below 2 km,

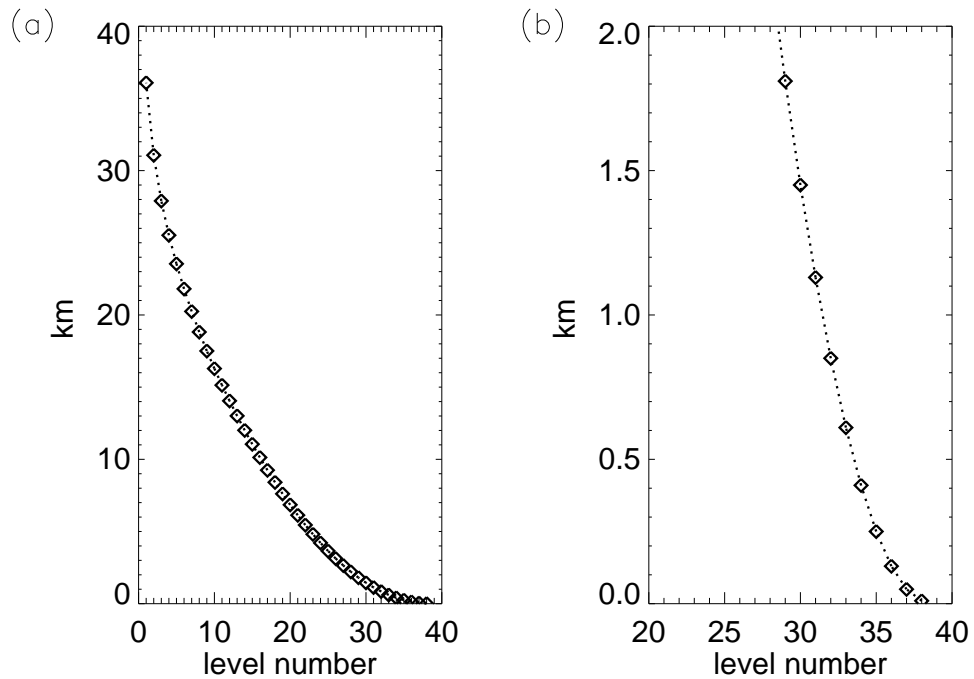


**Figure 2.3:** Height of model levels in U.M. (km) (a) All 38 model levels. (b) Model levels within the nominal boundary layer.

compared to 14 in the IGCM (Figure 2.1), however, the U.M. domain extends further into the stratosphere and is better resolved in the upper troposphere.

## 2.6 The Unified Model boundary-layer parameterisation scheme

The details of the boundary-layer parameterisation which is used in the U.M. are now presented. Firstly, the parameterisation of the surface fluxes is considered and then the turbulent fluxes above the surface layer are presented. The surface fluxes are represented in a very similar manner to those in the IGCM. However, there are two significant differences in the parameterisation of the outer layer fluxes. Firstly, the U.M. scheme includes non-local mixing in well-mixed boundary layers, and secondly, the U.M. has explicit entrainment. Both of these features are not included in the IGCM scheme. Additionally, the U.M. scheme distinguishes between different mixing regimes which exist in different types of boundary layers and therefore applies different turbulent mixing parameterisations to different types of boundary-layers. The U.M. has seven possible boundary layer types: stable boundary layer, boundary layer with stratocumulus over a stable near surface layer,

well mixed boundary layer, unstable boundary layer with a layer of decoupled stratocumulus, boundary layer with a decoupled stratocumulus layer over cumulus, cumulus capped boundary layer and lastly a shear dominated unstable boundary layer. As the model is run with no moisture here only three types of boundary layer can be diagnosed; stable, well mixed and shear dominated unstable boundary layers.

### 2.6.1 Surface-layer fluxes

The general form of the surface layer fluxes of momentum and heat is the same as in the IGCM, which is given by equations 2.1 and 2.2. However, the method that is applied to calculate the bulk drag coefficients in the U.M. scheme differs slightly to that used in the IGCM. The stability corrections to the neutral drag coefficients (equations 2.3 and 2.4) are calculated using Monin-Obukhov similarity theory but the form of these stability corrections differs, especially in the case of stable boundary layers.

The first step in the U.M. scheme is to calculate the surface roughness length for momentum,  $z_{0m}$ , which is done using the Charnock relation, (equation 2.5), as was the case in the IGCM. However, the Charnock coefficient,  $\alpha_c$ , is taken to be 0.011 in the U.M. scheme compared to 0.018 in the IGCM. The next step is to specify a first guess for the reciprocal of the Obukhov length,  $1/L$ , which is required to estimate the Monin-Obukhov stability functions. The first guess is different depending on whether the iteration begins from the convective limit (taken when the surface temperature exceeds the lowest model level temperature and when there is a wind shear of less than  $2 \text{ m s}^{-1}$  between the surface and first model level) or from neutral values (all other conditions). The first guesses of  $1/L$  in the convective limit is given by

$$\frac{1}{L} = \frac{-\kappa}{\mu^3 z_h}, \quad (2.36)$$

where  $\mu$  is a 'tunable' parameter which is taken to equal 0.08 and  $z_h$  is the boundary-layer depth. If the iteration begins from the neutral limit then  $1/L = 0$  is taken as the first approximation to the Obukhov length. Using these values of the Obukhov length, the first guess at the stability functions,  $\phi_m$  and  $\phi_h$  are calculated. In stable and neutral conditions  $\phi_m$  is estimated using

$$\begin{aligned} \phi_m &= \phi_{m(n)} + \left[ \zeta_m - \left( \frac{z_{0m}}{L} \right) \right] \\ &+ b \left\{ \left[ \zeta_m - \frac{c}{d} \right] \exp(-d\zeta_m) - \left[ \left( \frac{z_{0m}}{L} \right) - \frac{c}{d} \right] \exp \left( -d \left( \frac{z_{0m}}{L} \right) \right) \right\}, \end{aligned} \quad (2.37)$$

where  $b$ ,  $c$ , and  $d$  are constants derived by Beljaars and Holtslag (1991) which have the following values;  $b=2/3$ ,  $c=5$ ,  $d=0.35$ .

$$\phi_{m(n)} = \log \left( \frac{z + z_{0m}}{z_{0m}} \right) \quad (2.38)$$

and

$$\zeta_m = \frac{z + z_{0m}}{z_{0m}}. \quad (2.39)$$

In a similar manner  $\phi_h$  is estimated for stable and neutral conditions using

$$\begin{aligned} \phi_h &= \phi_{h(n)} + \left[ 1 + b\zeta_m \right]^{\frac{3}{2}} - \left[ 1 + b \left( \frac{z_{0h}}{L} \right) \right]^{\frac{3}{2}} \\ &+ b \left\{ \left[ \zeta_m - \frac{c}{d} \right] \exp(-d\zeta_m) - \left[ \left( \frac{z_{0h}}{L} \right) - \frac{c}{d} \right] \exp \left( -d \left( \frac{z_{0h}}{L} \right) \right) \right\}, \end{aligned} \quad (2.40)$$

where

$$\phi_{h(n)} = \log \left( \frac{z + z_{0h}}{z_{0h}} \right). \quad (2.41)$$

In unstable conditions the stability functions, are more similar to those used in the IGCM and are given by

$$\phi_m = \phi_{m(n)} - 2 \log \left( \frac{1 + X}{1 + X_0} \right) - \log \left( \frac{1 + X^2}{1 + X_0^2} \right) + 2 (\tan^{-1} X - \tan^{-1} X_0) \quad (2.42)$$

where

$$X = (1 - 16\zeta_m)^{0.25} \quad (2.43)$$

and

$$X_0 = \left(1 - 16 \left(\frac{z_{0m}}{L}\right)\right)^{0.25}. \quad (2.44)$$

The similar expression for heat is given by

$$\phi_h = \phi_{h(n)} - 2 \log \left(\frac{1 + Y}{1 + Y_0}\right) \quad (2.45)$$

where

$$Y = (1 - 16\zeta_h)^{0.5} \quad (2.46)$$

and

$$Y_0 = \left(1 - 16 \left(\frac{z_{0h}}{L}\right)\right)^{0.5}. \quad (2.47)$$

$\zeta_h$  is given by

$$\zeta_h = \frac{z + z_{0m}}{z_{0h}}. \quad (2.48)$$

Once the stability functions are evaluated the drag coefficients are estimated using

$$C_h = \frac{\kappa}{\phi_h} V_s \quad (2.49)$$

and

$$C_d = \frac{\kappa}{\phi_m} V_s, \quad (2.50)$$

where  $V_s$  is a surface scaling velocity. In the case of the convective limit this is given by

$$V_s = \mu \left[ \mu \frac{\kappa}{\phi_h} z_h (-\Delta b) \right]^{0.5}, \quad (2.51)$$

and by

$$V_s = \frac{\kappa}{\phi_m} (V_0 - V_1) \quad (2.52)$$

in the neutral case.  $\Delta b$  is the buoyancy difference (units of  $\text{ms}^{-2}$ ) between the surface and the lowest model level,  $V_1$  is the wind speed at the lowest model level and  $V_0$  is the wind speed at the surface.

After these first estimates of  $C_d$  and  $C_h$  have been obtained, an iteration is conducted to obtain progressively better approximations. The number of iterations is limited to five. The iterative procedure starts with the values of  $C_d$  and  $C_h$  obtained previously and calculates more representative scaling velocities based upon these. In unstable cases the new surface layer scaling velocity is calculated using

$$V_s = (u_*^2 + \mu^2 w_s^2)^{0.5}, \quad (2.53)$$

where the surface turbulent convective scaling velocity,  $w_s$  and the friction velocity,  $u_*$  are calculated using

$$w_s = (z_h C_h \Delta b)^{1/3} \quad (2.54)$$

and

$$u_* = (C_d (V_0 - V_1))^{0.5}. \quad (2.55)$$

In stable and neutral cases the new surface layer scaling velocity is taken to equal the friction velocity,  $V_s = u_*$ . These estimates of the scaling velocity are then used to calculate new estimates of the Obukhov length,

$$\frac{1}{L} = \frac{\kappa C_h \Delta b}{V_s^3}, \quad (2.56)$$

which are then used to calculate new estimates of  $\phi_m$  and  $\phi_h$  (equations 2.38 and 2.41). The new estimates of the stability functions are then applied to estimate the new drag coefficients using equations 2.49 and 2.50. After the iteration is completed the values of  $C_d$  and  $C_h$  are divided by  $(V_0 - V_1)$  to obtain the correct units (dimensionless).

### 2.6.2 Outer-layer fluxes

Above the surface layer the turbulent fluxes of momentum and heat are given by

$$\tau = \overline{\rho u'w'} + \overline{\rho v'w'} \quad (2.57)$$

and

$$H = -\rho C_p \overline{w'\theta'} \quad (2.58)$$

where the covariance terms are all estimated using the same general form:

$$\overline{w'\chi'} = -K_\chi \frac{\partial \chi}{\partial z} + K_\chi^{\text{surf}} \gamma_\chi. \quad (2.59)$$

$w'$  is the vertical velocity perturbation and  $K_\chi$  is the eddy diffusivity relevant for the variable  $\chi$  (either  $u$ ,  $v$  or  $\theta$ ). The second term on the right hand side of equation 2.59 is the non-local turbulent flux, which allows for mixing against the mean gradient of the field.  $K_\chi^{\text{surf}}$  is the non-local eddy diffusivity profile due to surface driven turbulence. This term is only calculated for non-local mixing arising from surface driven turbulence and only for potential temperature, not momentum.  $\gamma_\chi$  is the gradient adjustment term as described by Holtslag and Boville (1993) and is only calculated in unstable cases.  $\gamma_\chi$  is given by

$$\gamma_\theta = \min \left[ A_{ga} \frac{\sigma_{T1}}{z_h}, G_{\text{max}} \right], \quad (2.60)$$

where  $A_{ga} = 3.26$ ,  $\sigma_{T1} = 1.93 \overline{w'\theta'}/w_m$  and  $G_{\text{max}} = 10^{-3} \text{ K m}^{-1}$ , where the mixed layer value is used for  $w_m$  (see equation 2.69).

Therefore, to estimate the fluxes, estimates of  $K_h$ ,  $K_m$  and  $K_\chi^{\text{surf}}$  are required. The methods used to calculate these variables differ depending on what type of boundary layer has been diagnosed.

### ***Stable boundary layers***

In stable boundary layers the eddy diffusivities are calculated using a local Richardson number scheme. By definition,  $K_\chi^{\text{surf}} = 0$ , and therefore equation 2.59 simplifies to

$$\overline{w'\chi'} = -K_\chi(R_i) \frac{\partial \chi}{\partial z}. \quad (2.61)$$

The Richardson number scheme includes a first order mixing length approximation, as was the case in the IGCM boundary layer scheme. The eddy diffusivities for momentum,  $K_m(R_i)$ , and heat,  $K_h(R_i)$ , are given by equations 2.25 and 2.26. It should be noted

that whereas  $l_m = l_h$  in the IGCM boundary-layer scheme, this is not the case in the U.M. parameterisation. The method of calculating the mixing lengths is similar in both boundary-layer parameterisation schemes. In the U.M.

$$l_m = \frac{\kappa(z + z_{0m})}{1 + \kappa(z + z_{0m})/\lambda_m} \quad (2.62)$$

and

$$l_h = \frac{\kappa(z + z_{0m})}{1 + \kappa(z + z_{0m})/\lambda_h} \quad (2.63)$$

compared to equation 2.28 in the IGCM. The only difference is in the second term of the denominator; in the U.M. the asymptotic mixing lengths,  $\lambda_m$  and  $\lambda_h$ , are given by

$$\lambda_m = \max(40, 15z_h, 2h_b) \quad (2.64)$$

$$\lambda_h = \max(40, 15z_h), \quad (2.65)$$

where  $h_b$  is the orographic blending height and  $z_h$  is the boundary-layer height. The Richardson number,  $R_i$ , is defined to include a contribution to buoyancy from moisture as well as temperature, however as all experiments conducted here are dry, the Richardson number is effectively the same as was used in the IGCM boundary-layer scheme (equation 2.27). The stability functions,  $f_m(R_i)$  and  $f_h(R_i)$  in stable conditions ( $R_i \geq 0$ ) have different forms to those used in the IGCM boundary-layer parameterisation and are given by:

$$f_m(R_i) = f_h(R_i) = \frac{1}{1 + 10R_i}. \quad (2.66)$$

The stability functions for stable conditions are plotted in Figure 2.4 along with the corresponding functions used in the IGCM (equations 2.30 and 2.31). The functions, and therefore the amount of turbulent mixing, have very similar shapes, both with long tails at high values of the Richardson number. The similarity in these functions suggests that the tracer transport by turbulence above the surface layer in stable regions will be very similar in the U.M. and the IGCM.

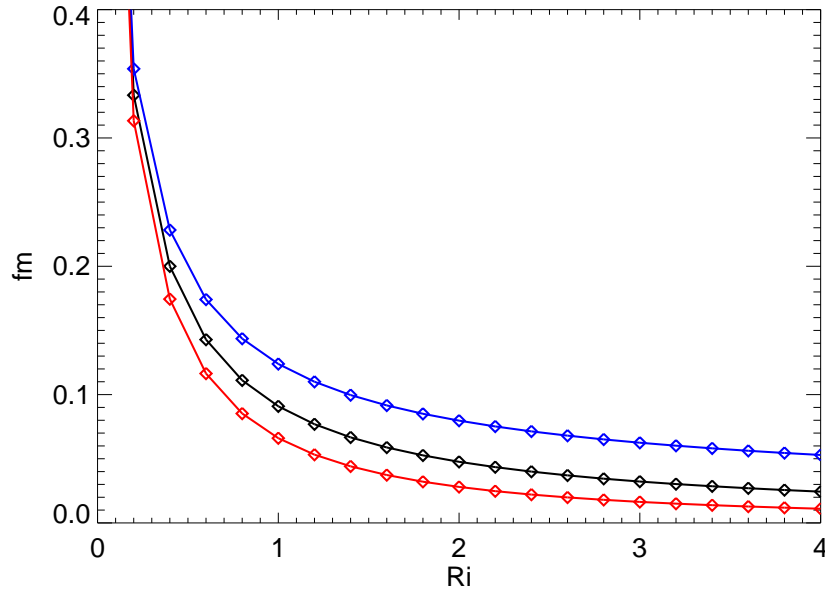


**Figure 2.4:** Stability functions applied above the surface layer in stable conditions. Black: U.M. function for heat and momentum, Red: IGCM function for heat, Blue: IGCM function for momentum.

### *Well-mixed boundary layers*

In well mixed boundary layers the eddy diffusivities are calculated using a non-local method. Hence the diffusivities do not depend on any local properties of the mean profile at the given height, but on the magnitude of the turbulent forcing applied to the layer, and the height within that layer. The non-local diffusivity due to surface based turbulence is given by

$$K_{\chi}^{\text{surf}} = kz_h w_m \frac{z}{z_h} \left( 1 - \epsilon_m^{\text{surf}} \frac{z}{z_h} \right)^2 \quad (2.67)$$

where  $k$  is von Karmens constant,  $w_m^3 = u_*^3 + w_s^3$ ,  $z$  is the height of the model level,  $\epsilon_m^{\text{surf}}$  is a factor to ensure that  $K_{\chi}^{\text{surf}}$  will tend to the entrainment eddy diffusivity when  $z$  tends to  $z_h$ .  $u_*$  is the friction velocity and  $w_s$ , which varies between the surface layer and the mixed layer, is related to the convective scaling velocity,  $w_*$  ( $w_*^3 = z_h \overline{w'b'_s}$ ). In the surface layer ( $z < 0.1z_h$ )

$$w_s^3 = 2.5 \frac{z}{z_h} w_*^3, \quad (2.68)$$

whereas in the well mixed outer layer

$$w_s^3 = 0.25w_*^3. \quad (2.69)$$

### *Shear-dominated unstable boundary layers*

In all locations where well-mixed boundary layers have been identified  $K_\chi^{surf}$  and  $K_\chi(R_i)$  are both calculated.  $K_\chi(R_i)$  is calculated using equations 2.25 and 2.26, where the stability functions for unstable boundary layers  $R_i < 0$  are given by

$$f_m(R_i) = 1 - \frac{10R_i}{1 + 2.5 \left(\frac{\tilde{l}_m}{l_h}\right) |R_i|^{0.5}} \quad (2.70)$$

and

$$f_h(R_i) = 1 - \frac{10R_i}{1 + 0.4 \left(\frac{\tilde{l}_m}{l_h}\right) |R_i|^{0.5}}, \quad (2.71)$$

where  $\tilde{l}_m$  and  $\tilde{l}_h$  are the mixing lengths at the lowest model level with a log profile correction applied. The covariance terms in well mixed layers are then calculated using

$$\overline{w'\chi'} = -\max \left[ (K_\chi^{surf} + K_\chi^{Sc}), K_\chi(R_i) \right] \frac{\partial \chi}{\partial z} + K_\chi^{surf} \gamma_\chi. \quad (2.72)$$

where  $K_\chi^{Sc}$  is the non-local driven mixing from cloud top downwards (which in these dry simulations will always be zero). If the eddy diffusivity calculated by local Richardson number scheme,  $K_\chi(R_i)$ , is greater than the non-local eddy diffusivity,  $K_\chi^{surf}$ , then the value calculated from the local scheme will be used. This will only occur in situations of strong wind shear where it is possible that turbulent mixing in unstable layers may be deeper than predicted from thermodynamic profiles alone. If this is the case the boundary layer is determined to be a shear dominated well mixed layer.

## 2.7 Treatment of tracers in the U.M.

A passive tracer is included in the U.M. simulations and is acted upon by the large-scale winds and turbulent motions as diagnosed by the boundary-layer scheme. A constant source of tracer is included in all simulations and is located at the lowest model level. In

the initial conditions the tracer concentration is set to zero throughout the whole domain. Tracer is emitted uniformly across the domain at a rate of  $1 \times 10^{-4} \text{ kg m}^{-2} \text{ s}^{-1}$ . The tracer is advected by the standard semi-Lagrangian advection scheme that is used to advect dynamical variables in the operational U.M.. Tracer mass is found to be conserved during the integrations. This is partly due to the positive definite scheme that is applied to prevent negative tracer concentrations from appearing. If negative values are calculated a correction is applied to the tracer field (in the same way that a correction is applied to the moisture field if negative values occur). This correction uses a weighted interpolation method to remove tracer mass from grid points around the negative value and 'move' this tracer mass to the grid point where the negative concentration was calculated, thus removing the negative value.

## 2.8 Diagnostics

This section describes important diagnostics that are used throughout this thesis. Firstly, a method for quantitatively diagnosing the boundary-layer depth from numerical model output is described. Secondly, the approach used to quantify the stability of the boundary layer is presented, and finally, a diagnostic which identifies the locations where conveyor belt flows (either warm or cold) leave the boundary layer is presented.

### 2.8.1 Boundary-layer depth

To investigate boundary-layer ventilation it is important to have a clear definition of boundary-layer depth, primarily to identify whether pollutants are within the boundary layer or free troposphere. Additionally, the boundary-layer depth determines the height to which pollutants can be lofted by turbulence alone. A qualitative description of the boundary layer is that it is the part of the atmosphere that is influenced by the surface, and hence characterised by turbulent flow. However, for the numerical experiments conducted here it is necessary to objectively diagnose boundary-layer depth.

Previous studies have used a large range of definitions for boundary-layer depth. The simplest option is to define the boundary-layer depth to be a constant value fixed in time and space. This was the approach used by Polvani and Esler (2007), who in a study which investigated the amount of mixing between different airmasses defined the boundary-layer depth to be 1.5 km. This approach has clear disadvantages; the depth of the boundary

layer is unrelated to both the turbulent structure of the boundary-layer and the large-scale flow. Adamson (2001) used a slightly more complex method; the boundary-layer top was defined to be the level where the momentum flux had decayed to 5% of its surface value. The disadvantage of this method is that it does not account for the thermal structure of the boundary layer. The next level of complexity is to use a parcel ascent method, where the boundary-layer top is defined as where a parcel ascending from the surface reaches its level of neutral buoyancy. This method is also often referred to as a critical Richardson method, and is applied in the Met Office Unified Model (Lock *et al.*, 2000) and in the Lagrangian particle dispersion model, FLEXPART (Stohl *et al.*, 2005), which is used in numerous pollution transport studies (e.g. Trickl *et al.*, 2003; Eckhardt *et al.*, 2003; Stohl *et al.*, 2003a).

In this thesis a critical Richardson number / parcel ascent method is used in all experiments to define the boundary-layer depth. This is done off-line and is based on the method described by Troen and Mahrt (1986). The bulk Richardson number,  $Ri_b$ , is calculated between the surface and subsequent higher levels in the model using

$$Ri_b(z) = \frac{g(\theta(z) - \theta_{s'})z}{u(z)^2 + v(z)^2}, \quad (2.73)$$

where  $z$  denotes the model level at which the Richardson number is evaluated,  $\theta$  is potential temperature and  $u$  and  $v$  are the horizontal velocity components.  $\theta_{s'}$  is an appropriate temperature of air near the surface.  $\theta_{s'}$  is estimated using the method described by Troen and Mahrt (1986);

$$\theta_{s'} = \theta_1 + b \frac{\overline{(w'\theta')_0}}{\frac{u_*}{\phi_m}}, \quad (2.74)$$

where  $\overline{(w'\theta')_0}$  is the virtual surface heat flux and  $\phi_m$  is the dimensionless vertical wind gradient for unstable conditions given by equation 2.10.  $b$  is a dimensionless constant taken to be 8.5 as in Holtslag and Boville (1993). The second term on the right hand side of equation 2.74 represents a temperature excess which is a measure of the strength of dry convective thermals in the boundary layer, and is only applied in unstable regions (defined as where the surface heat flux is positive). This additional term allows the boundary-layer depth to be diagnosed to be the level where surface based convective thermals reach their level of neutral buoyancy. In stable conditions (negative heat flux)  $\theta_{s'} = \theta_1$ .

**Table 2.1:** Summary of stability conditions

Heat Flux	L	$h/L$	Stability
large +ve	small -ve	large -ve	very unstable
large -ve	small +ve	large +ve	very stable
0	infinity	0	neutral

Once bulk Richardson numbers are evaluated the boundary-layer depth is diagnosed to be at the level where the bulk Richardson number exceeds a critical value taken to be 0.25. If this level lies between model levels a linear interpolation is performed between the level where the Richardson number exceeds the critical value and the level below.

### 2.8.2 Boundary-layer bulk stability

As well as diagnosing boundary-layer depth it is necessary to develop a quantitative method for measuring the stability of the boundary layer, as the stratification of the boundary layer exerts a strong control on the degree of turbulent mixing. Therefore, the bulk stability of the boundary layer is quantified by the ratio,  $h/L$ , where  $h$  is the boundary-layer depth and  $L$  is the Obukhov length (calculated using equation 2.6). Negative values of  $h/L$  correspond to unstable boundary layers and positive values stably stratified boundary layers. For neutral boundary layers, where the heat flux is close to zero,  $L$  tends to either positive or negative infinity. For strongly stratified or well-mixed boundary layers, the magnitude of  $L$  is small as the magnitude of the heat flux is large. The boundary-layer stability implied by the sign and magnitude of the parameter  $h/L$  is summarised in Table 2.1.

### 2.8.3 Conveyor belt location

A review of recent literature, as presented in Chapter 1, highlights the importance of conveyor belt flows for boundary-layer ventilation. Therefore, to understand how pollutants are transported out of the boundary layer and through the free troposphere it is important to be able to objectively identify conveyor belt flows. Recently there have been attempts to objectively identify airflows within cyclones, primarily by using numerical model output. Wernli and Davies (1997) used a Lagrangian approach to identify coherent ensembles of trajectories defined as groups of air parcel trajectories that all met specific geometrical and

physical criteria. Certain coherent ensembles of trajectories were shown to be reminiscent of WCBs by Wernli (1997). A similar method was used by Eckhardt *et al.* (2004) in their 15 year climatology of WCBs. They identified a WCB if, during a period of two days, a trajectory ascended at least 60% of the zonally and climatologically averaged tropopause height and travelled north-eastwards. In a one year airstream climatology Stohl (2001) set the criterion for a WCB to be ascent of 8000 m in 48 hours (independent of latitude) whereas Kiley and Fuelberg (2006) chose an ascent criterion of 5000 m in 48 hours, combined with increases in potential temperature and decreases in specific humidity. The variation in the criteria used to identify WCBs shows the subjective nature of such classification schemes. These previous studies focused on the path WCBs take once in the free troposphere, whereas in this thesis the emphasis is on identifying where the boundary layer can be ventilated and hence, where the WCB leaves the boundary layer. Therefore, rather than applying one of these pre-existing methods, a new objective diagnostic has been developed to identify where any type of conveyor belt (warm or cold) leaves the boundary layer.

The new diagnostic has been developed to locate where the majority, rather than just the core of, the conveyor belt flow leaves the boundary layer. The diagnostic was also developed to be as simple as possible using variables that are readily available in climatological data sets such as ERA-40. To identify the region where the conveyor belts leave the boundary layer, and hence the region of the boundary layer that is likely to be ventilated, first it is necessary to define the boundary-layer depth. The vertical velocity is then interpolated onto the surface identified as the boundary layer top. The footprint area of a conveyor belt is defined to be the area inside the vertical velocity contour on the boundary layer top that corresponds to the 95th percentile in the boundary layer top vertical velocity dataset. This was found to be the  $0.5 \text{ cm s}^{-1}$  vertical velocity contour in both IGCM life cycle experiments at T42 resolution, and the  $0.65 \text{ cm s}^{-1}$  vertical velocity contour in both IGCM life cycle experiments at T85 resolution. This value is greater at higher resolution as frontal ascent is better resolved, resulting in narrower but stronger bands of ascent. This method can be applied in a variety of situations, e.g. different model configurations or observations, but will result in a different vertical velocity contour being selected. However, it should be noted that this new Eulerian method, as is the case with the Lagrangian methods discussed above, contains a subjective element; the selection of the percentile.

---

## CHAPTER THREE

# Description of idealised life cycles

---

### 3.1 Introduction

This Chapter describes the dynamical development of the idealised life cycles simulated in both the Reading IGCM and the idealised U.M. The IGCM life cycles are discussed first in section 3.2, and then the control life cycle in the U.M. is presented in section 3.3. A comparison of the life cycles in the two different models is presented in section 3.4. The dynamical description of the life cycles presented in this chapter, and the results in the following chapters, focus on the growth and mature stages of the life cycles, not the decay stage. This is for two reasons. Firstly, the majority of ventilation out of the boundary layer is believed to occur when the system is developing, and secondly, the decay phase of the baroclinic systems modelled here are not thought to be as realistic as the growth stages.

### 3.2 Baroclinic life cycles in the IGCM

Two life cycles were examined by Thorncroft *et al.* (1993) in the IGCM, life cycle 1 (LC1) and life cycle 2 (LC2), and are re-simulated here. The life cycles are initialised by adding the fastest growing normal mode (normalised to have a pressure perturbation of 1 mb with wavenumber 6) to a baroclinically unstable background state. The basic state differs between LC1 and LC2. The basic state of LC1 is shown in Figure 3.1a and consists of a zonally uniform mid-latitude jet, with a maximum wind speed of  $47 \text{ m s}^{-1}$  centred on the tropopause at  $43^\circ\text{N}$ . In the background state of LC2 (Figure 3.1b) there is an additional

barotropic component added to the zonal wind; a  $10 \text{ m s}^{-1}$  westerly wind is applied at  $20^\circ\text{N}$ , and a  $10 \text{ m s}^{-1}$  easterly is applied at  $50^\circ\text{N}$ . This contributes a cyclonic shear to the basic state. In both life cycles the initial conditions are in thermal wind balance, therefore a meridional temperature gradient is present. The surface temperature is a prescribed function of latitude. It is fixed throughout the integrations and is equal to the temperature of the first model level at the initialisation time.

The characteristics of both baroclinic life cycles are now summarised. Figure 3.2 shows the domain averaged eddy kinetic energy for both LC1 and LC2 as a function of time. LC1 is found to peak after eight days and then decay rapidly. In contrast LC2 peaks later, after 11 days, but does not decay nearly as quickly as LC1. During the first three days (early stages) of the integration both life cycles undergo a period of linear baroclinic growth. Alternating high and low pressure dipoles develop along the  $50^\circ\text{N}$  latitude circle. During days four to eight the systems experience nonlinear baroclinic growth (as is evident by the increase in eddy kinetic energy in Figure 3.2) and the pressure anomalies intensify. By day six (approaching the mature stage) the cyclones present in both life cycle experiments resemble mature mid-latitude cyclones with warm and cold frontal structures evident in the temperature and pressure patterns (Figure 3.3 - note that this figure and all subsequent figures that show horizontal cross sections of variables in the x-y plane show twice the modelled domain:  $120^\circ$  of longitude, rather than the east-west extent of the domain which is only  $60^\circ$ ). By day nine LC1 has undergone barotropic decay, the baroclinicity has been destroyed in mid-latitudes, and the remaining pressure pattern resembles a decaying wave. In contrast, LC2 is continuing to wrap up cyclonically, and strong pressure gradients remain in mid-latitudes.

The synoptic and frontal evolution differs between LC1 and LC2. Figure 3.3a shows that in LC1 the anticyclones move equatorward while the cyclones migrate polewards and become zonally confined. By day six of LC1 (Figure 3.4a) there are strong temperature gradients present to the north of the low centre, ahead of the warm sector, which form a strong bent back warm front. There is also a cold front of similar intensity to the south. The cold front is extensive, starting from  $55^\circ\text{N}$  and then extending south-westward, resembling a typical trailing cold front. Additionally, there is a pronounced pressure trough associated with the cold front and a much weaker one associated with the warm front (Figure 3.3a). By day eight (Figure 3.4c) the meridional extent of the cold front has increased further, and the temperature gradient associated with the cold front has

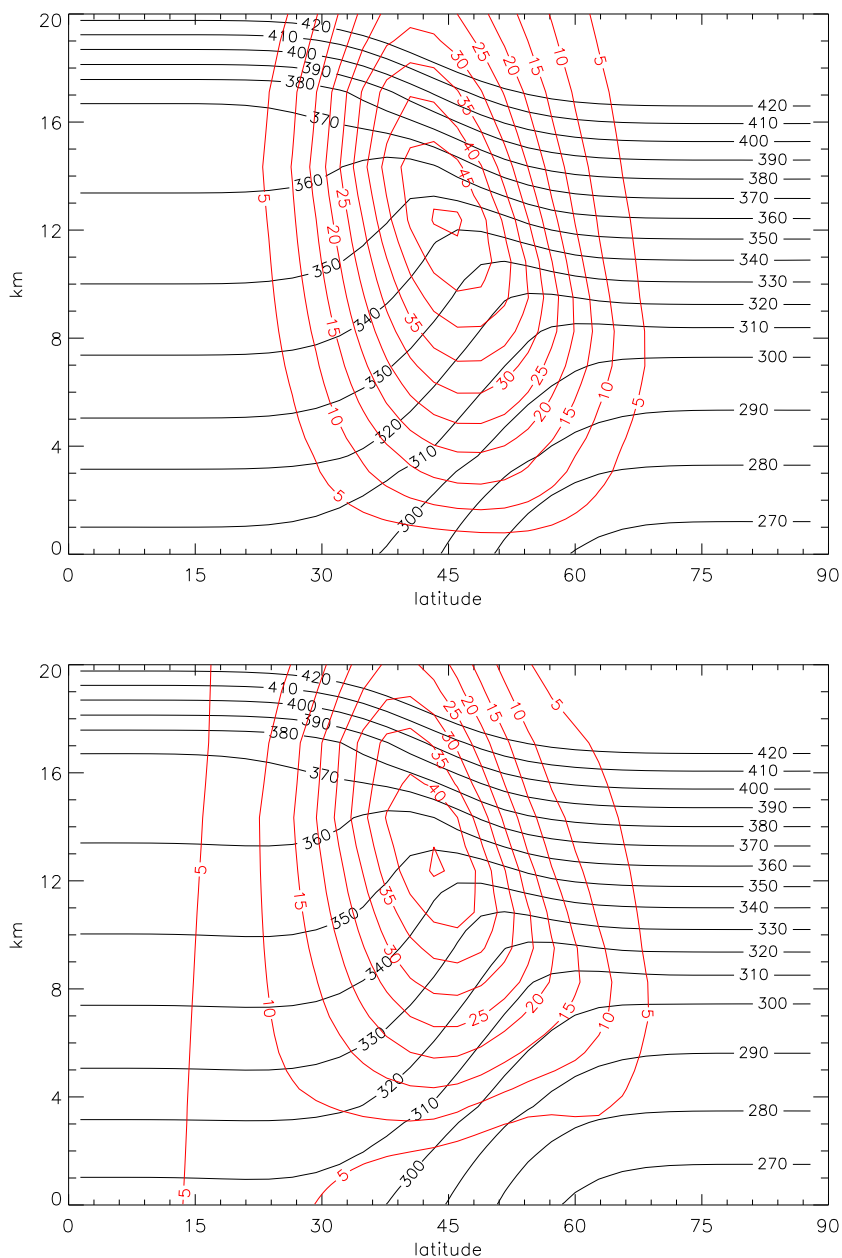


**Figure 3.1:** Initial background state for (a) LC1 and (b) LC2. Black contours show potential temperature (K) and red contours the zonal component of the wind speed ( $\text{ms}^{-1}$ ).

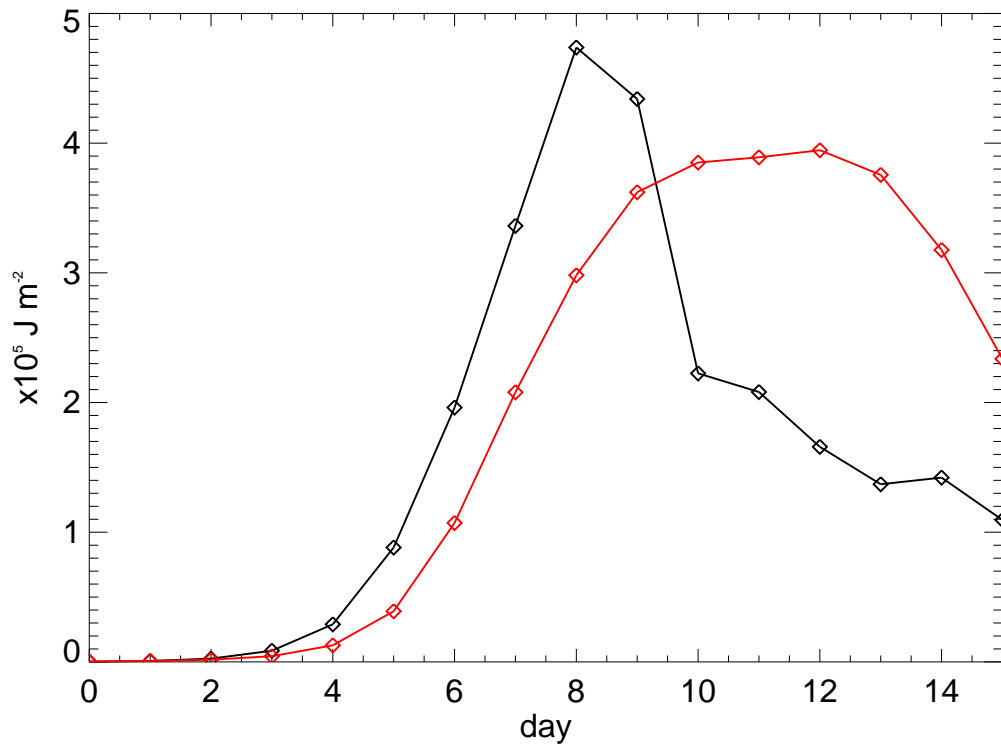


**Figure 3.2:** Domain averaged eddy kinetic energy for LC1 (Black) and LC2 (Red).

intensified. However, the warm front has shortened and changed little in intensity allowing the cold front to dominate the later stages of LC1.

In contrast, Figure 3.3b shows that the synoptic systems in LC2 show little meridional displacement, but the resulting cyclone is broader and is more prominent than the anticyclone. The surface temperature and pressure waves tilt more north-west south-east than in LC1, due to the additional cyclonic shear. Figure 3.4b shows that after six days of LC2 there are very strong temperature gradients to the north-east of the low pressure centre which forms a strong warm front. There is little evidence of a cold front in LC2 at this stage. By day eight (Figure 3.4d) it is apparent that the warm front in LC2 remains significantly stronger than the cold front. The fronts, unlike in LC1, continue to exist for the next 2 days as the cyclone continues to expand.

Figure 1 of Thorncroft *et al.* (1993), which is reproduced here as Figure 3.5, shows a generalised overview of motion on an isentropic surface in a typical mid-latitude cyclone. Four airstreams, two descending (A and B) and two ascending (C and D), are identified. The airstreams either have anticyclonic (A and D) or cyclonic (B and C) curvature associated with them. Cyclones can be classified by the partitioning of flow between the

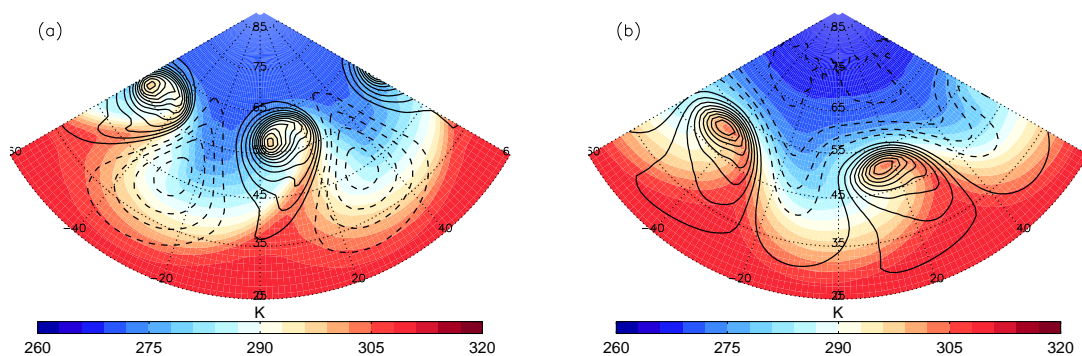


**Figure 3.3:** Surface pressure (black contours, contour interval 4 mb) and potential temperature (colours) at 1 km after six days of (a) LC1 and (b) LC2. Solid black contours show pressure less than 1000 mb and dashed contours pressure greater than 1000 mb. The 1000 mb contour is omitted for clarity.

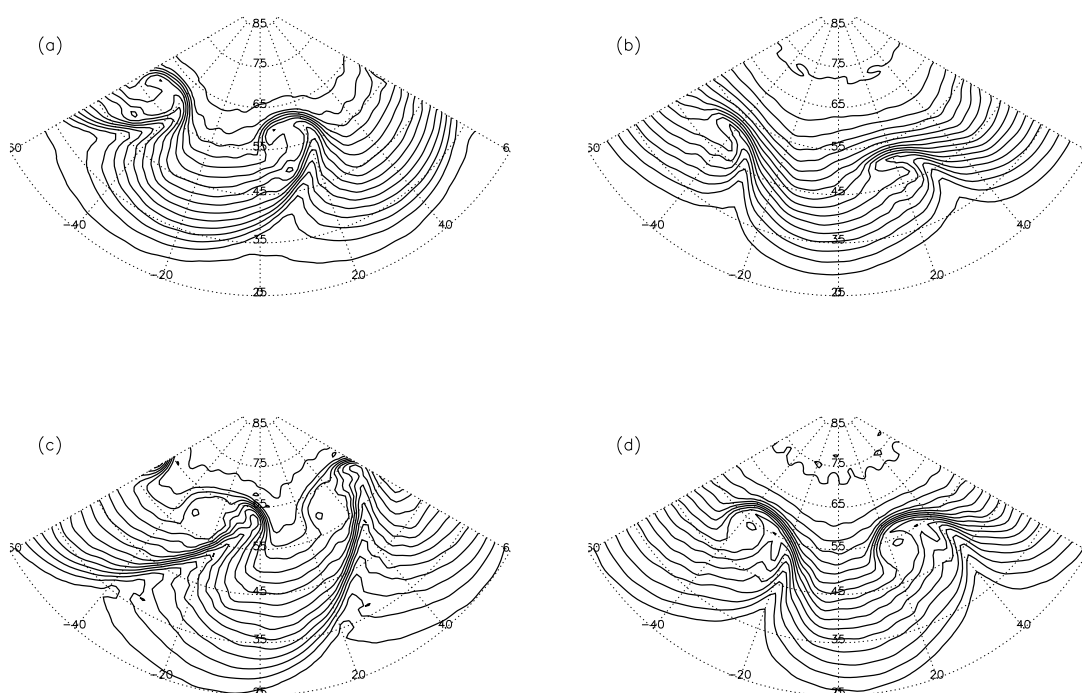


**Figure 3.4:** Potential temperature at 32 m after (a) day six of LC1 (b) day six of LC2 (c) day eight of LC1 and (d) day eight of LC2. Contours are drawn every 2.5 K.

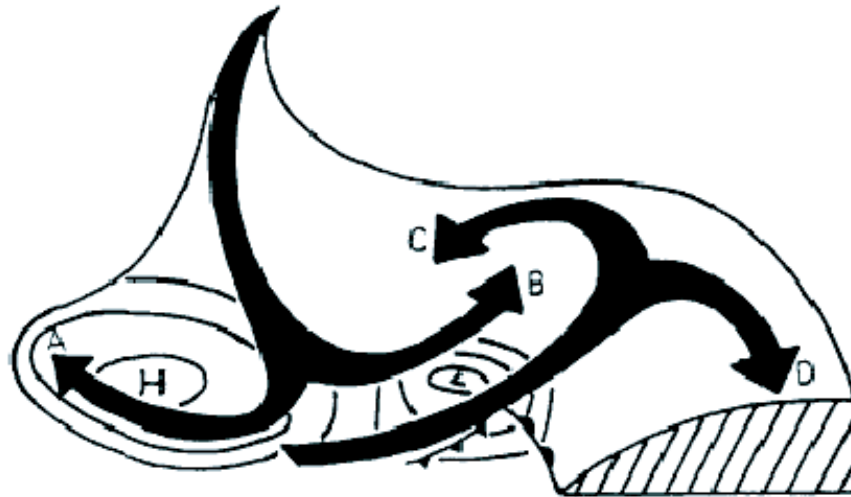


**Figure 3.5:** Figure 1 of Thorncroft et. al. (1993) : A schematic of isentropic relative flow within a baroclinic wave. Solid arrows represent flow along a sloping isentropic surface. Branches A and B represent the descending dry intrusion, whereas branches C and D represent the ascending warm conveyor belt. The surface pressure pattern is also indicated.

cyclonic and anticyclonic branches. This can be visualised by considering the potential temperature contours on the dynamical tropopause, defined as the surface where potential vorticity,  $PV$ , equals  $2PVU$  ( $1PVU = 1 \times 10^{-6} \text{ m}^2 \text{ s}^{-1} \text{ K kg}^{-1}$ ). Figure 3.6a shows that after six days LC1 has a slight cyclonic nature but by days eight and ten (Figures 3.6c and 3.6e) anticyclonic wave breaking dominates LC1. In contrast, LC2 is dominated by cyclonic wave breaking throughout the life cycle (Figures 3.6b, 3.6d and 3.6f).

### 3.3 Description of the U.M. control life cycle

The control baroclinic life cycle that is simulated using the U.M. is now discussed. This life cycle was designed to be as close as possible to LC1 in the IGCM in terms of the large-scale dynamics and evolution. The control U.M. life cycle is initialised using a different method to that used in the IGCM; the method that Polvani and Esler (2007) used to simulate a replica of LC1 in a spectral model is adopted. The basic state for the control U.M. life cycle consists of a zonal wind profile that is a function of latitude ( $\phi$ ) and height ( $z$ );

$$u(\phi, z) = U_0 F(\phi) \left[ \frac{z}{z_t} \exp \left( -\frac{((z/z_t)^2 - 1)}{2} \right) \right]. \quad (3.1)$$

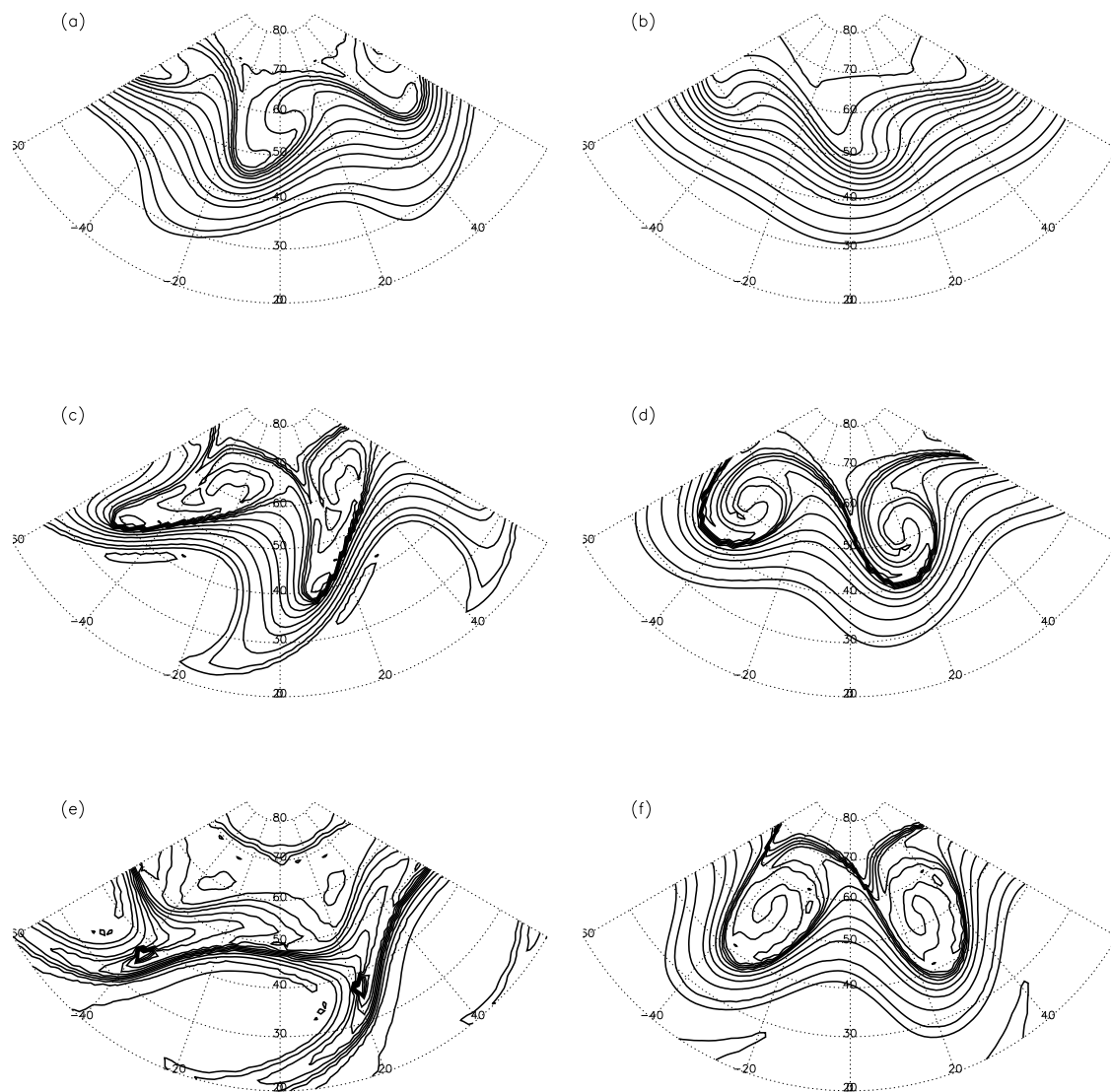


**Figure 3.6:** Potential temperature on the  $PV=2$  PVU surface (a) day six of LC1 (b) day six of LC2, (c) day eight of LC1 (d) day eight of LC2, (e) day ten of LC1 and (f) day ten of LC2. Contours are drawn every 5 K. Lowest contour is the 300 K isentrope.

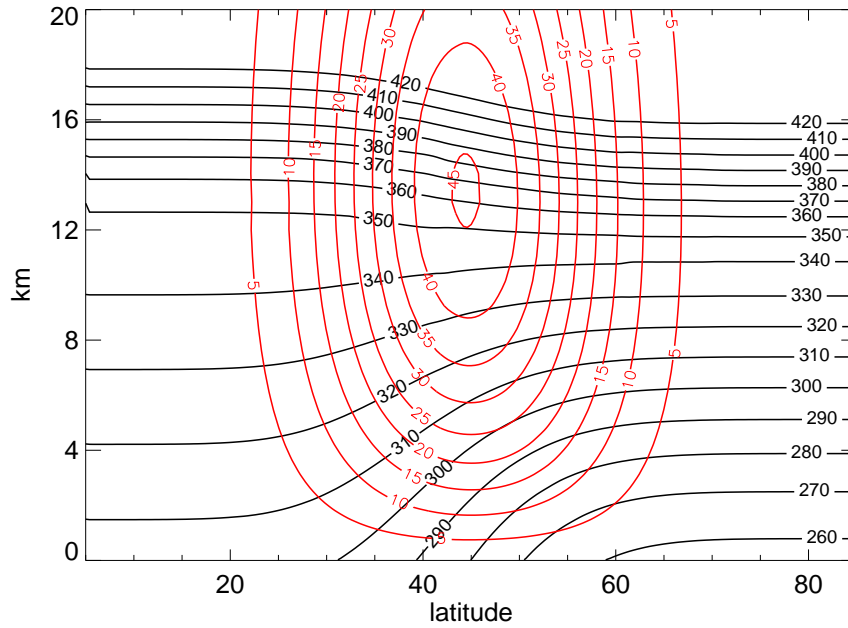


**Figure 3.7:** Initial background state for the control baroclinic life cycle simulated in the U.M. Black lines show potential temperature and red lines the zonal component of the wind speed.

$U_o$  is the maximum strength of the upper level jet, taken to be  $45\text{ms}^{-1}$ , and  $z_t$  is the tropopause height, taken to be 13 km.  $F(\phi)$  is a latitudinal dependence given by

$$F(\phi) = [\sin(\pi(\sin \phi)^2)]^3. \quad (3.2)$$

The resulting zonal jet is shown in Figure 3.7. Many similarities can be seen with the initial zonal jet used to simulate LC1 in the IGCM. When Figure 3.7 is compared with Figure 3.1a it can be seen that the height of the jet is similar in both experiments (13 km), and the surface temperature gradient is a similar strength (40 K between  $30^\circ\text{N}$  and  $60^\circ\text{N}$ ). The only noticeable difference that can be seen is that the jet in the IGCM experiments tilts slightly equatorward with height, whereas the jet in the U.M. experiments is vertically orientated.

During the initialisation of the U.M. life cycle the meridional wind component is set to zero and a reference potential temperature profile, shown in Figure 3.8, is defined. Within this reference profile a number of layers can be specified with different vertical temperature gradients (stratifications). In all experiments two layers are specified, one which is representative of the troposphere, and the other, the stratosphere. In the control experiment the lowest layer has a constant lapse rate of  $0.004\text{ K m}^{-1}$  that extends from

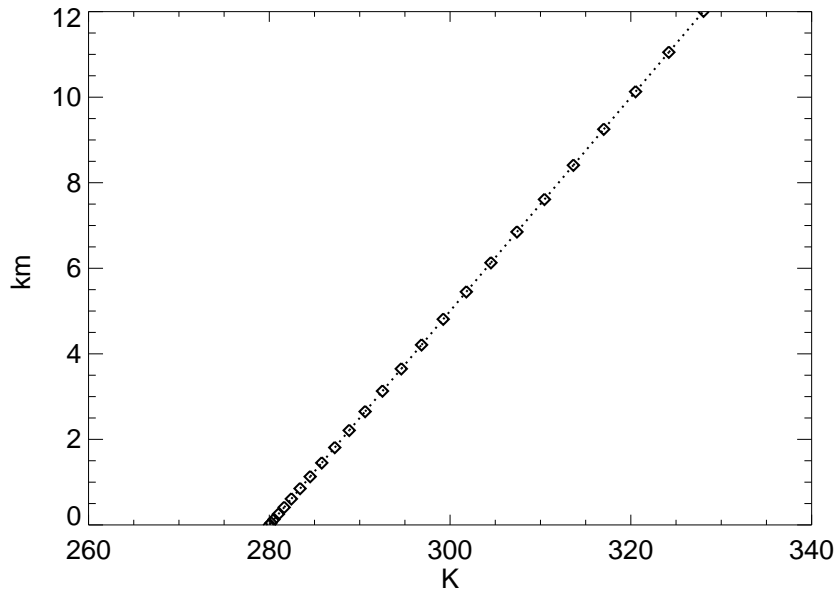


**Figure 3.8:** Reference tropospheric potential temperature profile used in U.M. simulations.

the surface to 13 km. The second layer, above 13 km, has a stronger stratification; the lapse rate is  $0.016 \text{ K m}^{-1}$ . The initial three-dimensional potential temperature field is calculated using thermal wind balance and the prescribed wind fields. To ensure that the boundary-layer stability is perfectly neutral in the centre of the domain ( $x=75, y=100$ ) at the beginning of the simulation a correction ( $corr$ ) is applied over the whole domain to force the potential temperature at the lowest model level to equal the reference potential temperature at the lowest model level ( $\theta_{ref}(1)$ );

$$corr = \theta_{ref}(1) - \theta(75, 100, 1) \quad (3.3)$$

$$\theta_{corr}(i, j, k) = \theta(i, j, k) + corr \quad (3.4)$$

where  $\theta_{corr}(i, j, k)$  is the corrected potential temperature. The surface temperatures are set equal to the corrected lowest model level temperatures,  $\theta_{corr}(i, j, 0)$ , and are then held constant throughout the simulations, as was the case in the IGC. A balanced pressure field is found by integrating hydrostatic balance given the corrected potential temperature distribution.

To generate the development of baroclinic life cycles on this baroclinically unstable jet an initial perturbation is required. A small temperature perturbation  $T'$ , which is independent of height, is added to the temperature field and is given by

$$T'(\lambda, \phi) = \hat{T} \cos(m\lambda) [\operatorname{sech}(m(\phi - \hat{\phi}))], \quad (3.5)$$

where  $m$  is the zonal wavenumber, taken to be 6 in all experiments,  $\lambda$  is longitude and  $\hat{\phi}$  is the latitude that the jet is centred upon (45°N in the control experiment).  $\hat{T}$  is the maximum temperature perturbation, which equals 1 K in all experiments.

A description of the large-scale dynamics of the resulting life cycle is now presented. Figures 3.9a and 3.9b show the surface pressure pattern after eight and twelve days respectively. By day eight features resembling typical cyclones and anticyclones are evident; the minimum pressure in the centre of the cyclone is 970 mb and the maximum pressure in the anticyclone is 1014 mb. However, at this stage there is little meridional displacement of the cyclones and anticyclones and from the pressure contours alone no fronts can be identified. When the near surface potential temperature distribution after eight days is considered (Figure 3.9c), a warm front to the north of the low centre and a weak cold front to the south-west of the low centre can be identified. The intensity of these fronts is confirmed when the vorticity at 1 km (Figure 3.9e) is considered. Cyclonic vorticity is observed in the region of the warm front; however at this stage (day eight), there is no evidence of a cold front in the vorticity field. After a further four days of development the system has reached its mature stage; the minimum pressure is now 966 mb. The surface pressure is shown in Figure 3.9b and shows that the low centre has moved poleward; it is now located at 55°N compared to 50°N four days previously. Additionally, there is now a pressure trough evident on the western edge of the warm sector which marks the location of the cold front. Figures 3.9d and 3.9f show that by day twelve the cold front has intensified considerably and now has a large meridional extent, reaching from 30°N to 55°N. Also evident is that the vorticity associated with the warm front to the east of the low centre is small implying that there is limited ascent associated with the warm front. However, there are high values of vorticity located to the west of the low centre which is related to the portion of the warm front that has been bent backwards around the low centre by the strong easterly winds. This part of the front is referred to as a bent-back warm front (Shapiro and Keyser, 1990).

Figures 3.9g and 3.9h show the potential temperature on the dynamical tropopause, the  $PV = 2$  PVU surface. The lower values of potential temperature indicate where the tropopause is lower, and hence where there are large-scale descending motions. Consider-

ing the potential temperature on the tropopause allows for the type of wave-breaking to be identified. The mature stages of LC1 in the IGCM was dominated by anticyclonic wave breaking whereas LC2 was dominated by cyclonic wave breaking (Figure 3.6). The control simulation in the U.M. is found to wrap up in a cyclonic manner; there is no evidence of anticyclonic wave breaking at either day eight (Figure 3.9g) or day twelve (Figure 3.9h), but neither do strong cyclonic vortices develop as was found in LC2 in the IGCM. This discrepancy between LC1 in the IGCM and the control U.M. life cycle will be discussed further in section 3.4

### 3.4 Differences between LC1 in the IGCM and the control U.M. cyclone

Three main differences are found to exist between LC1 in the IGCM and the control life cycle in the U.M.. The first is that the U.M. control cyclone develops at a slower rate than LC1, and is less intense than LC1, secondly the U.M. control cyclone exhibits much more cyclonic behaviour than LC1 does, and thirdly the U.M. control cyclone experiences less meridional displacement than LC1.

The difference in the intensity between LC1 and the U.M. control cyclone can be seen by comparing Figures 3.2 and 3.10. LC1 is more intense which is due to the smoother surface, and hence weaker frictional damping, in the IGCM compared to U.M. However, the difference in intensity between the two life cycles is not as large as suggested by these plots; the domain is larger in the U.M. experiments than in the IGCM experiments (a consequence of the different geometry), and hence the domain averaged eddy kinetic energy will always be less in the U.M. experiments even if identical life cycles are simulated.

To account for the remaining differences between LC1 and the U.M. control cyclone it is necessary to consider the geometrical differences between the IGCM and the idealised U.M.. Two main differences exist, firstly the IGCM uses full spherical geometry while cartesian geometry is used in the U.M. and secondly, whereas the IGCM assumes a  $\beta$ -plane, an f-plane approximation is used in the U.M.. Previous studies (e.g Nakamura, 1993; Balasubramanian and Garner, 1997) have shown that these two factors can cause differences in the dynamical development of baroclinic life cycles. Balasubramanian and Garner (1997) investigated the effects of geometry on life cycle simulations and found that a life cycle simulated using spherical geometry reached its maximum intensity two

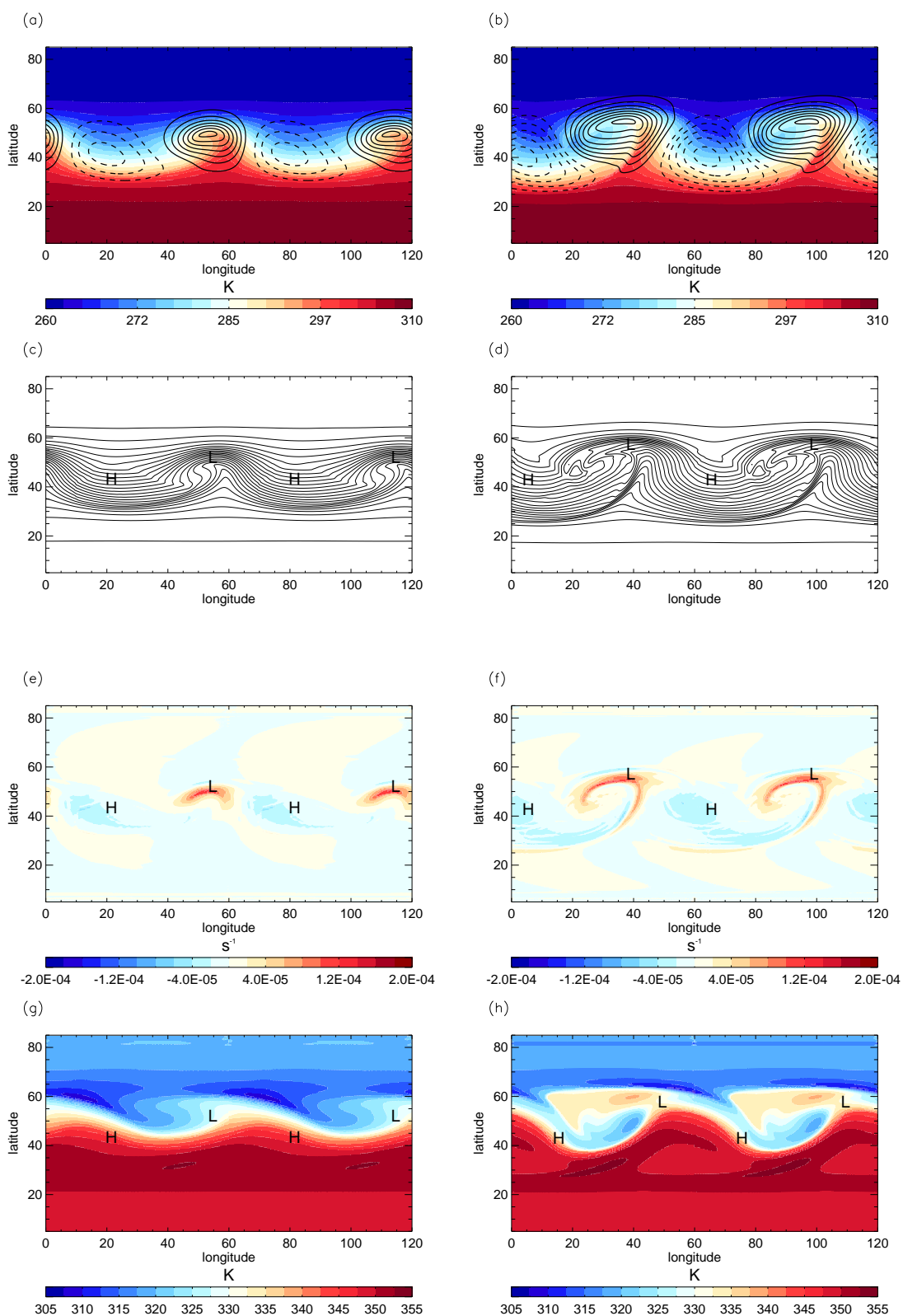


**Figure 3.9:** Surface pressure (contours) and potential temperature at 1 km (colours shaded) after (a) 8 days, (b) 12 days. Pressure contours are drawn every 4 mb with the 1000 mb contour omitted. Solid black contours show values less than 1000 mb and dashed contours values greater than 1000 mb. (c) Potential temperature (contour interval 2 K) at 980 m after 8 days and (d) 12 days. (e) Vorticity at 1 km after 8 days and (f) 12 days. (g) Potential temperature on the PV=2 PVU surface after 8 days and (h) 12 days.

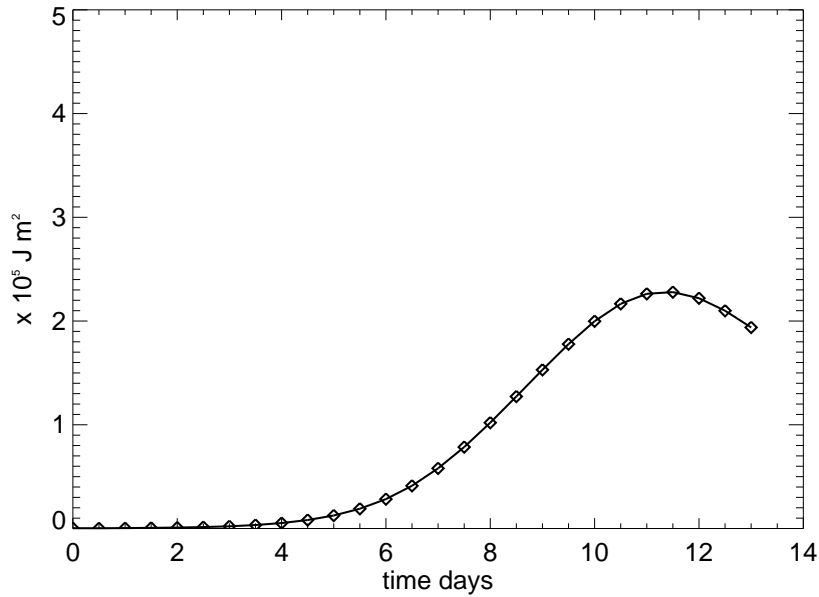


**Figure 3.10:** Domain averaged eddy kinetic energy for the control U.M. cyclone.

days before a life cycle simulated using cartesian geometry. The peak in the eddy kinetic energy of LC1 in the IGCM occurs after 8 days (Figure 3.2), whereas the peak in the U.M. control cyclone is after 11.5 days (Figure 3.10). This lag of three and a half days is greater than found by Balasubramanian and Garner (1997). It is thought that this is because the initial perturbation to the basic state differs between the IGCM and U.M. experiments; in the IGCM the fastest growing normal mode was carefully calculated, whereas it is likely that the perturbation used in the U.M. (equation 3.5) is not the fastest growing mode and hence initially develops more slowly. The more cyclonic nature of the cyclone in the U.M. control cyclone can also be explained by the differences in geometry; Snyder *et al.* (1991) found baroclinic waves in cartesian models to have a bias towards developing North-West to South-East tilts and cyclonic wave breaking. Similar results are also presented by Rotunno *et al.* (1994) and Nakamura (1993), while Hollingsworth *et al.* (1976) showed that with spherical geometry anticyclonic wave breaking is more likely to occur than cyclonic wave breaking. However, when Figures 3.9g and 3.9h are compared with Figures 3.6b, 3.6d, and 3.6e it is clear that although the control U.M. cyclone is dominated by cyclonic behaviour and the frontal structures are resemblant of LC2, LC2 wraps up much more cyclonically, forming cut off vortices, than the U.M. control cyclone does. This is a consequence of the f-plane approximation used in the idealised U.M.; there is no reservoir of high potential vorticity air near the pole for the cyclone to feed off as there is in the IGCM  $\beta$ -plane

simulations. The difference in the degree of meridional displacement observed between LC1 in the IGCM and the control U.M. cyclone again is a consequence of the differing geometries; in the case of cartesian geometry Balasubramanian and Garner (1997) have shown the eddy momentum fluxes to be shifted equatorward compared to the spherical geometry case. This means that while the zonal jet, and hence the perturbation, was displaced polewards in the spherical geometry case, the zonal jet in the cartesian case did not experience the same degree of meridional displacement.

Finally, it is noted that instead of replicating LC1 in the U.M. as intended, a life cycle which has more in common the baroclinic waves simulated by Wernli *et al.* (1998) has been modelled using the U.M.. Wernli *et al.* (1998) also used a model with cartesian geometry and an f-plane approximation and found three archetypal life cycles to exist which did not exactly match with the LC1/LC2 life cycles simulated in spherical models. This demonstrates that although the control U.M. life cycle does not directly resemble LC1 or LC2, it is a realistic and dynamically understood baroclinic system.

### 3.5 Summary

The dynamical characteristics of the baroclinic life cycles simulated in the IGCM and the U.M. have been presented. LC1 and LC2 were shown to differ considerably from each other, despite the small difference in the initial conditions, but both were found to resemble typical mid-latitude weather systems. Although this has been demonstrated previously for LC1 and LC2, (Simmons and Hoskins, 1978; Thorncroft *et al.*, 1993), these studies did not include a complex boundary-layer parameterisation.

The control life cycle in the U.M. is unique to this study and therefore it has been shown that realistic life cycles can be simulated in the idealised U.M. The U.M. life cycle was designed to replicate LC1, but some notable differences were found to exist between LC1 and the control U.M. cyclone. However, the differences have largely been explained by the differing geometrical aspects of the two models. While it would have been ideal to simulate life cycles in the U.M. with a  $\beta$ -plane, rather than an f-plane approximation, technical difficulties prevented this from occurring.

---

## CHAPTER FOUR

# Synoptic controls on boundary-layer structure

---

### 4.1 Introduction

This Chapter describes in detail the boundary-layer structures that develop beneath the LC1 and LC2 baroclinic waves in the IGCM simulations, and identifies regions of the boundary-layer that can either lose or gain air from the free troposphere. The motivation for this is described in section 4.2 before the boundary-layer structures are described in section 4.3. Section 4.4 examines terms of a mass budget equation, which is derived in section 4.4.1, to develop an understanding of the physical processes responsible for transporting air between the boundary layer and free troposphere and vice-versa.

### 4.2 Motivation

The atmospheric boundary layer is an important part of the atmosphere. It controls how the surface modifies air masses, moderates how much energy is available to the troposphere, and is where the vast majority of pollutants are emitted. The characteristics of the boundary layer vary considerably in time and in space and the structure of the boundary layer plays an important role in determining how pollutants are transported at low levels. Previous work on boundary-layer structure has often concentrated on the evolution of the boundary layer on small temporal and spatial scales. As a result, conceptual models of boundary-layer structure driven by the diurnal cycle and changes in surface type (ru-

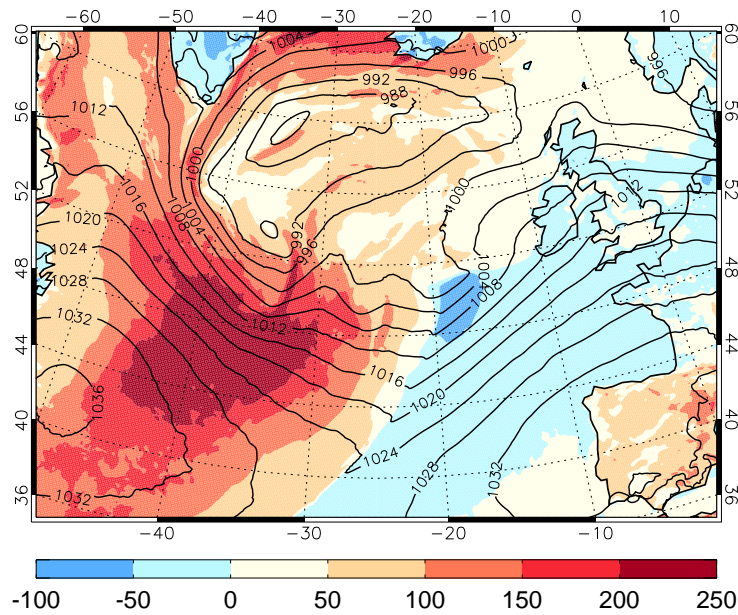


**Figure 4.1:** Surface heat flux (colours,  $\text{W m}^{-2}$ ) and surface pressure (black contours, m b) from the UK Met Office Unified Model analysis (North-Atlantic European domain, 12 km horizontal resolution) at 12:00 UTC 19th January 2007. Coastlines are marked for reference.

ral, urban, ocean, land) exist (e.g Lowry, 1967; Oke and East, 1971; Carson, 1973). Also known is that the boundary layer can be driven on much larger scales and that synoptic-scale weather systems can lead to spatial and temporal variations of the boundary-layer structure. This is evident in analysis charts from operational forecast models. Figure 4.1 shows the surface heat flux from the operational U.K. Met Office Unified Model at midday on the 19th January 2007. The surface pressure in Figure 4.1 shows a mature low pressure located to the north-west of the U.K with a cold front located between  $40^{\circ}\text{N}$  and  $50^{\circ}\text{N}$ . A region of high pressure is located in the mid-Atlantic. It is evident that the spatial distribution of the surface heat flux is correlated with these synoptic features; a clear change in sign in the heat flux is evident across the cold front. However, no conceptual model of boundary-layer structure at these synoptic scales currently exists.

Current observations of variations in boundary-layer structure due to the passage of synoptic systems are somewhat inadequate due to logistical and technical challenges. Observational campaigns such as the Storm Transfer and Response Experiment (STREX) (Fleagle and Nuss, 1985; Bond and Fleagle, 1988), Joint Air Sea Interaction Project (JASIN) (Pollard *et al.*, 1983; Businger and Charnock, 1983) and Genesis of Atlantic Lows Experiment (GALE) (Holt and Raman, 1990) have provided some in-situ observations of boundary-layer structure across synoptic scales. However, often these observations consist

of a relatively small number of point measurements that are almost always confined to within the atmospheric surface layer, and hence do not describe the vertical structure of the boundary layer. Additionally, the majority of synoptic-scale field campaigns in the mid-latitudes have a strong bias to studying cyclones; very limited investigations have been conducted into the spatial and temporal variations in boundary-layer structure beneath anticyclones in the mid-latitudes.

Remote sensing of boundary-layer properties on large horizontal scales has been attempted, but currently only the surface momentum flux, which can be inferred from scatterometer data over oceans (Chelton *et al.*, 1990), is well observed. Surface sensible heat fluxes, boundary-layer depths and boundary-layer stabilities are not easily obtained remotely across synoptic spatial scales. Climatologies of such variables have been constructed (e.g. Woodruff *et al.*, 1998; Chou *et al.*, 2003) from combinations of in-situ, re-analysis, and satellite data, but variations on synoptic temporal scales are then averaged out. Therefore, it is not yet clear from observations alone i) how the boundary-layer structure changes as the synoptic systems develop, ii) what is the vertical structure of the boundary layer at different locations within the synoptic systems, and iii) what are the ranges of the magnitudes and the spatial distribution of fluxes that are typical of mid-latitude weather systems. These three points are addressed in this thesis in Section 4.3.

In addition, there is limited knowledge as to how the boundary layer and free troposphere interact during the passage of synoptic systems. Previous studies have shown the effect that a boundary layer has on the development of fronts and cyclones (e.g Keyser and Anthes, 1982; Neiman *et al.*, 1990; Adamson *et al.*, 2006; Plant and Belcher, 2007), but it is not clear how air is exchanged between the boundary layer and free troposphere. The rate at which boundary-layer air is either lost to, or gained from, the free troposphere determines the mass of air within the boundary layer. This has important consequences for air pollution studies and for the modification of air masses. The rate at which boundary-layer air is lost to the free troposphere determines how rapidly pollutants can be removed from the boundary layer. Additionally, pollutants emitted within the boundary layer are known to become trapped within the boundary layer by capping temperature inversions. Therefore, as pollutants disperse within the boundary layer the concentration may change significantly due to changes in the depth of the boundary layer even when the mass of the pollutants remains constant. Therefore, the volume of air within the boundary layer

provides an important control of pollution concentrations. The volume of air within the boundary layer also dictates the proportion of the atmosphere that is in direct contact with the underlying surface and hence can be directly modified by surface fluxes and frictional effects. The boundary layer regulates the energy budget of the whole atmosphere; solar radiation, the atmosphere's main energy source, is absorbed at the surface and then transferred through the boundary layer to the free troposphere. Additionally, typically 50% of the atmosphere's kinetic energy is dissipated within the boundary layer (Stull, 1988). Therefore, the amount of mass within the boundary layer has a large impact on the energy budget of the whole atmosphere.

Given the importance to boundary-layer ventilation, the rate of change of boundary-layer mass in different regions of synoptic-scale systems is investigated in Section 4.4 by analysing terms of a mass budget equation.

## 4.3 Boundary-Layer Structure

The boundary-layer structure which evolves during LC1 is now described in detail. It is shown that the spatial variation of the boundary-layer structure is strongly coupled to the large-scale dynamical structure of the idealised baroclinic system which was described in Section 3.2.

### 4.3.1 Surface Fluxes

Throughout the life cycle the heat flux is determined primarily by low-level thermal advection. Figure 4.2a shows the sea surface temperature and the near surface wind vectors for LC1. To the west of the low centre and on the eastern edges of the high pressure region there are north-westerly winds bringing cooler air south over warmer surfaces. In the warm sector, ahead of the cold front, southerly winds are advecting warm air northwards over cooler surfaces. Figure 4.2c shows the surface heat flux after five days of synoptic development. The largest positive (upwards) heat fluxes are found to exceed  $30 \text{ W m}^{-2}$  and are located on the eastern edges of the anticyclone, where there is strong cold-air advection. Positive heat fluxes are also found to the south of the anticyclone centre. This spatial pattern occurs due to the clockwise circulation of air at low levels in the anticyclone. The wind vectors in Figure 4.2a show that typically an air parcel will travel southwards around the eastern edge of the anticyclone before travelling westwards along the southern part of

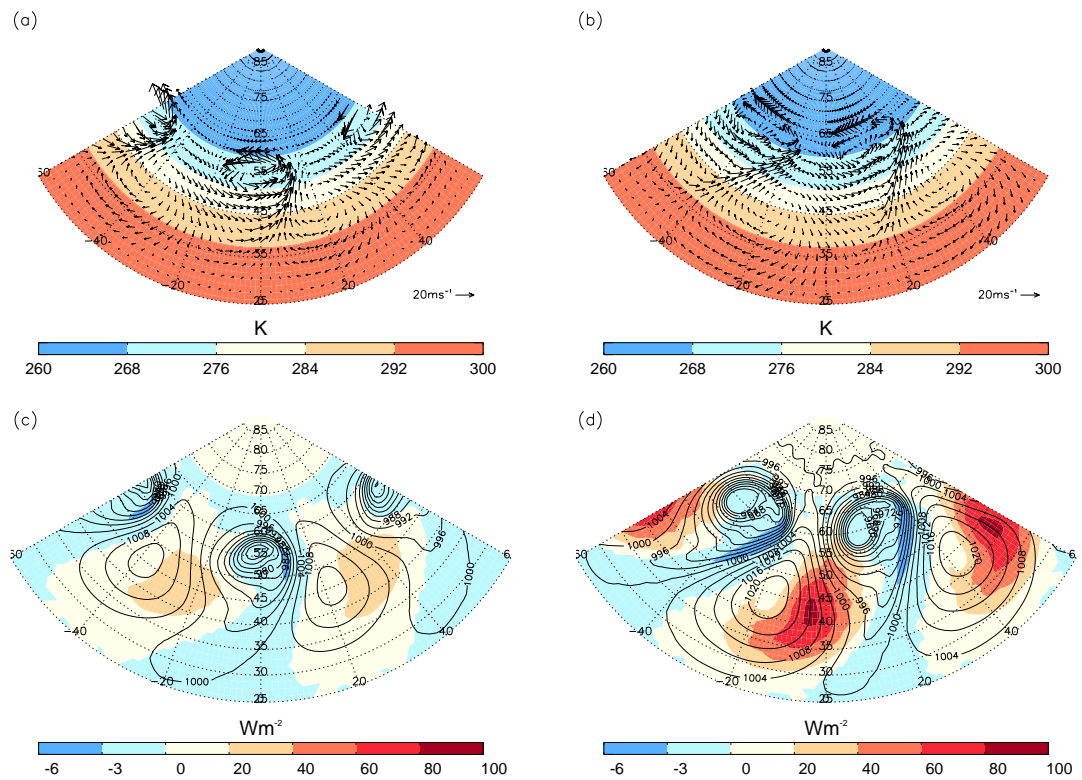


**Figure 4.2:** LC1: Panels (a) and (b) show the sea surface temperature (colours) and the wind vectors at 32 m after five and seven days respectively. Wind vector scale is representative of wind vectors at  $45^{\circ}$  N. Panels (c) and (d) show the surface heat flux (colours) and surface pressure (contours) after five and seven days.

the anticyclone. The magnitude of the heat flux decreases along this trajectory (to the western edge of the anticyclone) as air parcels slowly regain thermal equilibrium with the underlying surface. In cyclonic regions the surface heat flux is negative (downwards) but small in magnitude. The warm sector of the cyclone has the strongest negative heat fluxes as well as the strongest warm-air advection. After five days of the system's evolution, the minimum heat flux is found to be  $-4 \text{ W m}^{-2}$  and is located in the warm sector between  $50^{\circ}\text{N}$  and  $55^{\circ}\text{N}$ . The centre of the cyclone is found to have very small negative values of surface heat flux, with a magnitude less than  $1 \text{ W m}^{-2}$ . This is a response to air becoming trapped in the convergent low pressure centre, and the limited meridional displacement of the low pressure centre.

After a further two days of development (Figure 4.2d) the region of maximum positive heat flux remains on the eastern edge of the anticyclone but has moved southwards and the magnitude has more than doubled; the largest heat flux is now  $84 \text{ W m}^{-2}$ . In the warm sector the area of negative heat flux has increased to extend between  $45^{\circ}\text{N}$  and  $60^{\circ}\text{N}$

in the warm sector, and the minimum observed heat flux is  $-6 \text{ W m}^{-2}$ . This amplification in the magnitude of the surface heat flux is due to larger pressure gradients and stronger winds (Figure 4.2b), which lead to stronger cold and warm air advection. This maximises the temperature difference, and hence the heat flux, between the surface and the overlying air.

The momentum flux is calculated using equation 2.1 and is proportional to the wind speed squared. Hence, it is expected that the largest values of surface momentum flux will be found in regions of strongest wind speeds. After 7 days of development the largest values of the surface momentum flux, typically  $0.8 \text{ N m}^{-2}$ , are found to the west of the low pressure centre, and to the south of the bent-back warm front (Figure 4.3). In this region there are strong winds and also a well-mixed potential temperature profile. The values of the surface momentum flux are found to be larger in the southern and eastern regions of the anticyclone than in the warm sector of the cyclone. This is due to very stably-stratified air in the warm sector severely limiting the amount of vertical momentum transfer which is able to occur, despite the presence of moderate winds (typical speeds of  $12 \text{ m s}^{-1}$ ). In contrast, in the anticyclone there are light winds (typically  $4 \text{ m s}^{-1}$ ) but as the boundary layer is well-mixed the stratification does not inhibit vertical transport of momentum. Calm conditions in the centre of the anticyclone mean that surface momentum flux is at a minimum here. This is a similar spatial pattern to that observed 48 hours previously (not shown). As was found with the heat fluxes, the magnitudes of the surface momentum flux increase with time, again due to the stronger winds and the increased destabilisation of the anticyclonic region.

### 4.3.2 Boundary-layer depth and stability

The boundary-layer depth after 5 days of development of LC1 (not shown) is found to strongly resemble the spatial pattern of the surface heat flux (Figure 4.2c). The deepest boundary layers, of up to 2 km, are found behind the cold front and in the southern and eastern regions of the anticyclone. This pattern is still evident two days later (Figure 4.4); the depth of the boundary layer increases as the life cycle reaches its mature stages, in the same manner as the heat flux does. By day 7 the maximum boundary-layer depth exceeds 3 km. Since at both days 5 and 7 there is a strong correlation between the boundary-layer depth and surface heat flux in the anticyclonic region, it is clear that here the boundary layer is buoyancy driven. However, at all times the boundary layer in the warm sector

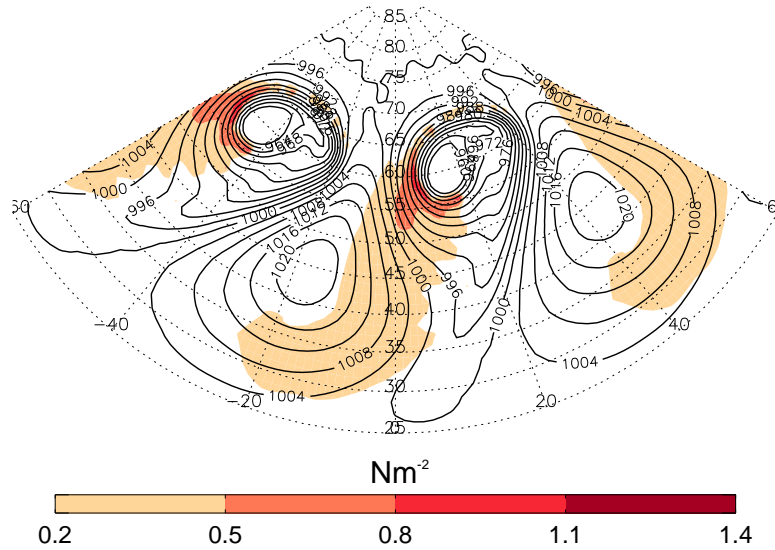
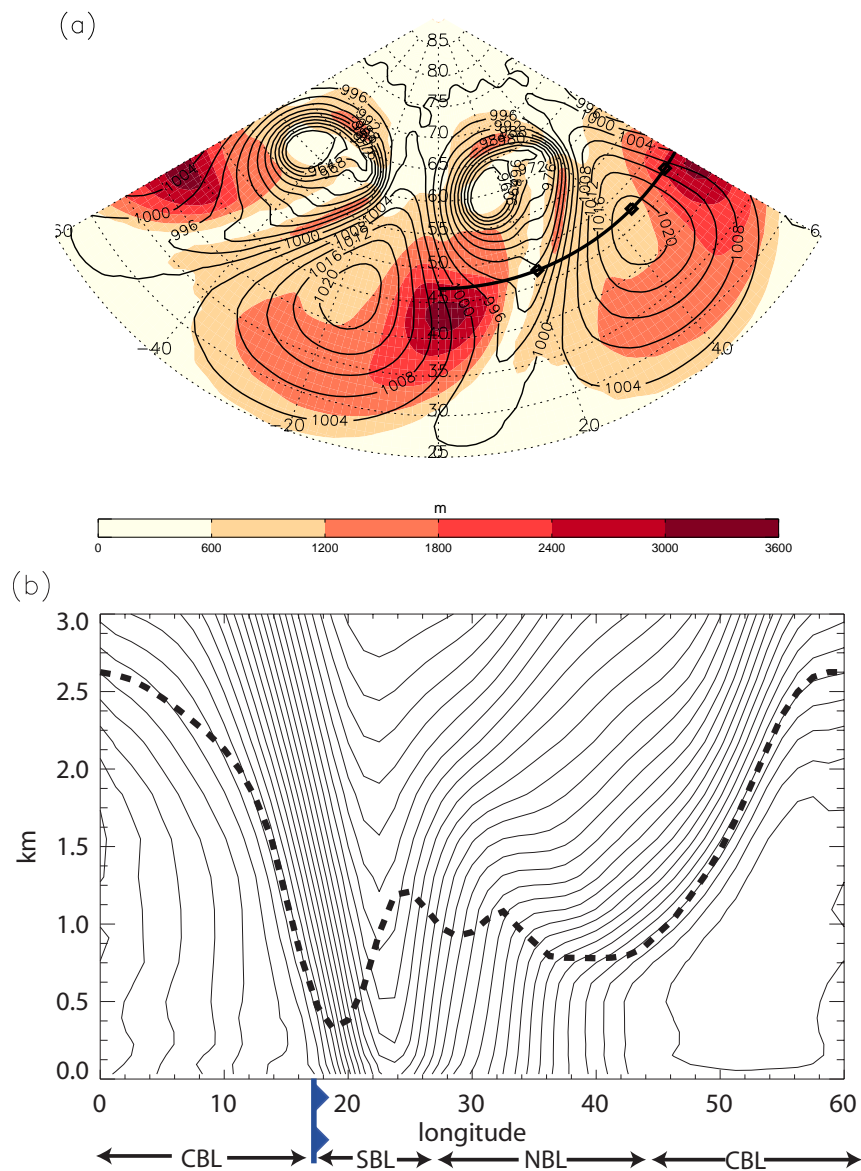


**Figure 4.3:** Surface momentum flux after seven days of the LC1 life cycle. Thin black lines indicate surface pressure (mb).

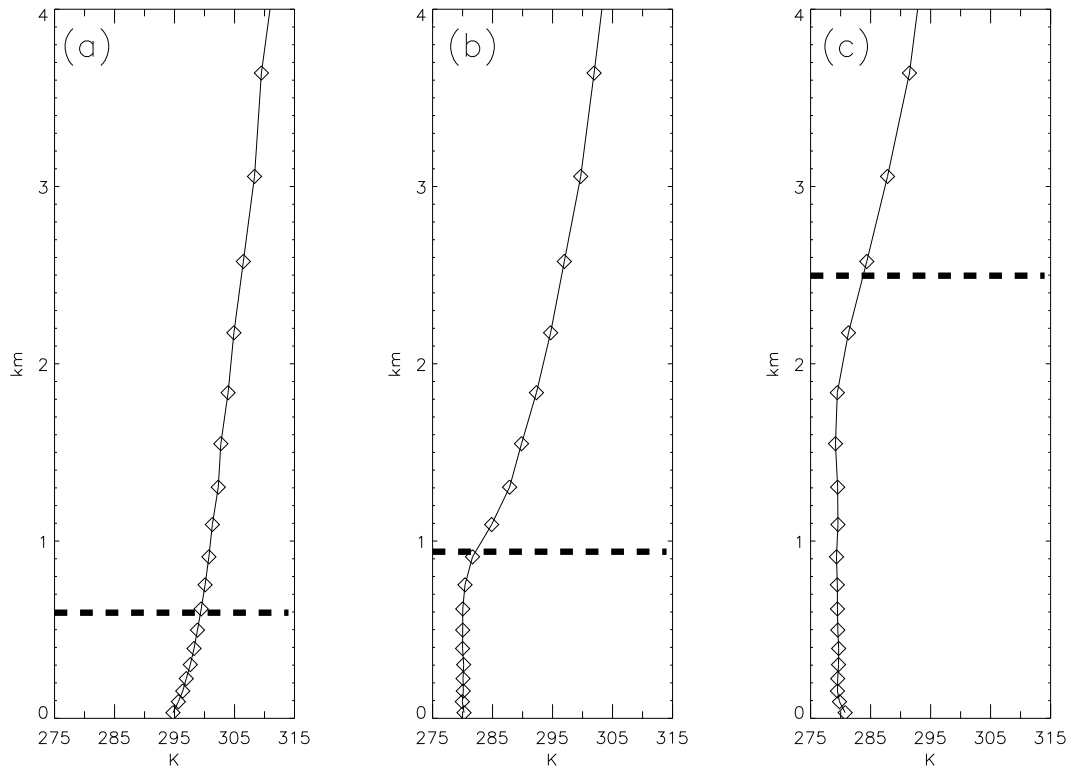
is observed to be shallower, at typically 800 m, than in the anticyclonic region. Outwith the anticyclonic regions two additional local maxima in boundary-layer depth are evident; one in the warm sector close behind the warm front, and a second on the poleward edge of the low centre. In these two regions strong low-level winds cause the boundary layer to be dominated by shear-driven turbulence.

Figure 4.4b shows that large horizontal gradients in boundary-layer depth are found to exist across the cold front. Behind the cold front the boundary layer has a depth of  $\sim 2.5$  km whereas immediately ahead of the cold front this is reduced to around 0.5 km. This illustrates the considerable localised horizontal variability in the depth of the boundary layer, directly related to the presence of synoptic weather systems. This, combined with the relatively constant spatial patterns of boundary-layer structure in time relative to the synoptic features, demonstrates that the boundary layer is strongly coupled to, and its structure is largely determined by the, large-scale dynamics.

The stability of the boundary layer can be qualitatively investigated by considering vertical profiles of potential temperature taken during the mature stage (7 days) of LC1. Three such profiles have been selected from different parts of the synoptic systems, which are marked by black diamonds on Figure 4.4a. Figure 4.5a shows the potential temperature profile in the warm sector of the LC1 cyclone. This shows a stable profile, with the strongest potential temperature gradients near the surface, and no temperature inversion.



**Figure 4.4:** (a) Boundary-layer depth (colours) after seven days of LC1. Black contours indicate surface pressure (mb). (b) Vertical cross section along 47°N (marked by the bold line in (a)) showing potential temperature (thin black contours) contour interval 2.5 K, and boundary-layer depth (heavy dashed line). The surface cold front (blue line with triangles) is located at 18°E. CBL identifies the location of convective boundary layers, NBL, neutral boundary layers, and SBL, stable boundary layers.



**Figure 4.5:** Vertical profiles of potential temperature after 7 days of LC1 taken along the cross section shown in Figure 4.4b. Specific locations are shown by diamonds in Figure 4.4a. (a) warm sector (21°E, 47°N) (b) anticyclonic region (45°E, 47°N) (c) eastern edge of anticyclone (57°E, 47°N). Heavy dashed line marks the diagnosed boundary-layer depth.

The depth of the boundary layer is not clear from Figure 4.5a but is diagnosed to be 596 m. The vertical profile of potential temperature found in the centre of the anticyclone is shown in Figure 4.5b. This shows a well-mixed layer up to 800 m, above which a subsidence inversion is present. At this point the boundary-layer depth was diagnosed to be 940 m. Figure 4.5c shows the vertical profile of potential temperature on the eastern edge of the anticyclone. This shows an unstable potential temperature profile, initially with a decrease in potential temperature with height near the surface and then a well mixed layer to 1.8 km. The diagnosed boundary-layer depth was found to be 2497 m, which appears to be higher than the temperature inversion. However, as the boundary-layer depth is defined to be where surface based thermals reach their level of neutral buoyancy (section 2.8.1) it is likely that the boundary-layer depth will be diagnosed slightly above the inversion in this case, because the surface is warmer than the mixed layer.

The bulk stability of the boundary layer is quantified by the ratio of the boundary-layer depth,  $h$ , to the Monin-Obukhov length,  $L$ . The sign of this ratio is determined by the

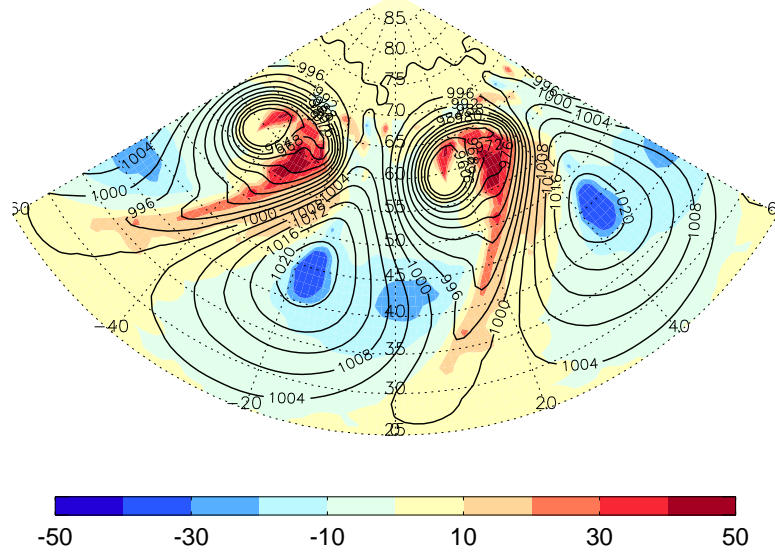


**Figure 4.6:** Bulk stability ( $h/L$ ) after seven days of LC1. Black contours show surface pressure (mb).

sign of the Obukhov length; negative values represent unstable regions and positive values stable regions. Figure 4.6 shows the pattern of  $h/L$  after 7 days. The largest negative values of -40 are found in the centre of the anticyclone. This location of the extreme values differs from the distributions of surface heat flux and boundary-layer depth, which is due to the very light winds in the centre of the anticyclone forcing the Obukhov length to be very small, and hence the bulk stability to be large. In the region of maximum heat flux, surface winds and hence the friction velocity are larger. This means negative values of -25 are found in this region. The largest positive values of 45 are found to identify the warm sector of the cyclone well.

Unlike the surface heat flux, surface momentum flux and boundary-layer depth the bulk stability was not found to increase in magnitude during the life cycle, but was found to be reasonably constant. This occurs as both  $h$  and  $L$  increase at similar rates. The spatial pattern of the bulk stability in relation to synoptic features was also found to be constant with time.

### 4.3.3 Comparison of boundary-layer structure in LC1 and LC2

Figure 4.7a shows the surface heat flux for the contrasting synoptic system, LC2, after 7 days of development. The spatial pattern of the heat fluxes, in relation to the surface fronts, is similar to that seen in LC1. The largest positive heat fluxes are found on

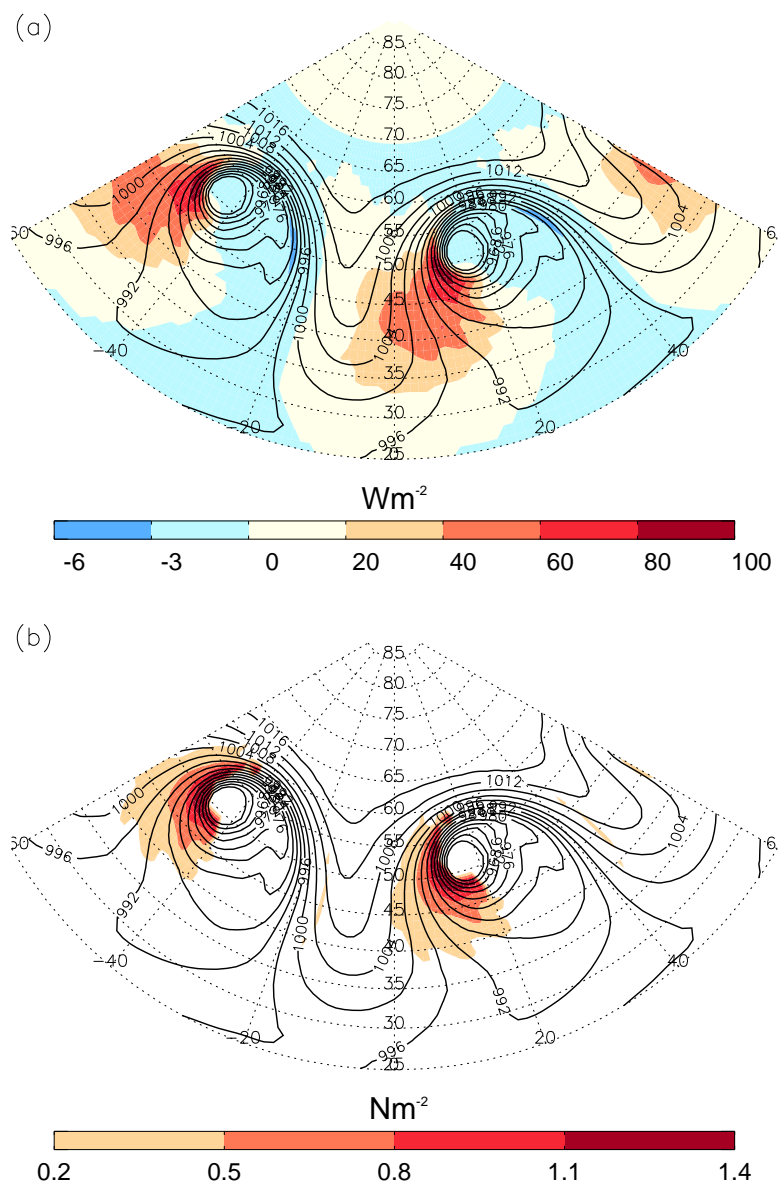


**Figure 4.7:** (a) Surface heat flux (b) and surface momentum flux after seven days of LC2. Black contours show surface pressure (mb).

the leading edge of the anticyclone. However, the magnitudes and areal extent of the positive heat fluxes are less in LC2 than those found in LC1. This arises as the meridional displacement of the cyclone and anticyclone, and hence the strength of thermal advection, is less in LC2 than in LC1. This results in smaller differences between the sea surface temperatures and the low level temperatures. Figure 4.7b shows the surface momentum fluxes for LC2. When this is compared to Figure 4.3 some similarities can be seen. The largest values still occur in the cold air on the rearward side of the low pressure centre. However, LC2 has slightly elevated values of momentum flux ahead of the warm front which were not observed in LC1. This is explained by considering the differences in the stability of the boundary layer between LC1 and LC2. It can be seen by comparing Figures 4.6 and 4.8b (which show the bulk stability for LC1 and LC2 respectively) that the warm sector in LC2 is considerably less stably stratified than in LC1. Additionally, unlike in LC1, there are very small values of momentum flux in the anticyclonic region of LC2. This is due to the combination of weaker winds in the anticyclonic region of LC2 and a less unstable stratification. Boundary-layer depth for LC2 is shown in Figure 4.8a and can be compared to the boundary-layer depths found in LC1 (Figure 4.4a). Similar spatial patterns in relation to the synoptic features are found in both life cycles, however the convective boundary-layer depth in the anticyclonic region is less in LC2 than in LC1. These differences in the structure of the boundary layer arise from the different degrees of meridional displacement that LC1 and LC2 experience, and hence different amounts of low-level thermal advection.

#### 4.4 Boundary layer mass budget

A description of the boundary-layer structure beneath intensifying cyclone and anticyclones has been presented. However, only a qualitative discussion has been presented on the physical mechanisms which act to induce the observed changes in boundary-layer structure with time. To quantify how the boundary-layer structure is altered by the passage of synoptic systems, and to identify locations within mid-latitude synoptic systems where air is exchanged between the boundary layer and free troposphere, changes in boundary-layer mass are now examined.

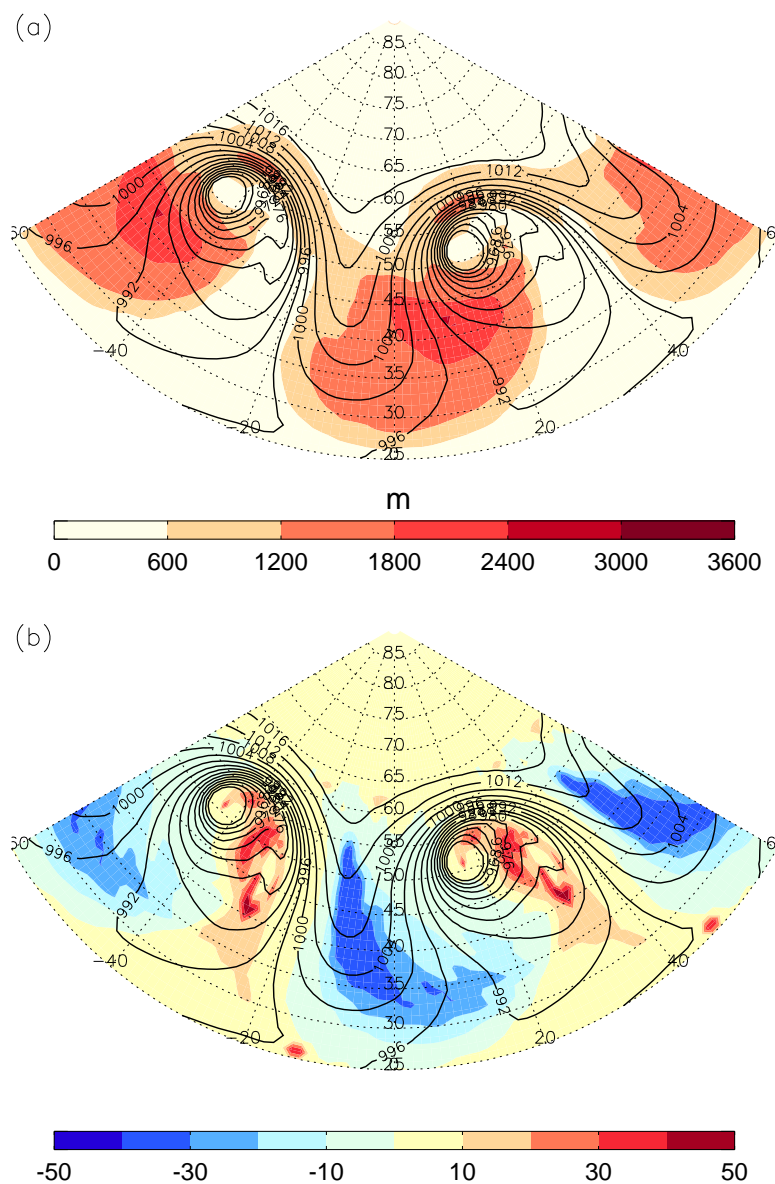


**Figure 4.8:** (a) Boundary-layer depth (b) and bulk stability ( $h/L$ ) after seven days of LC2. Black contours show surface pressure (mb).

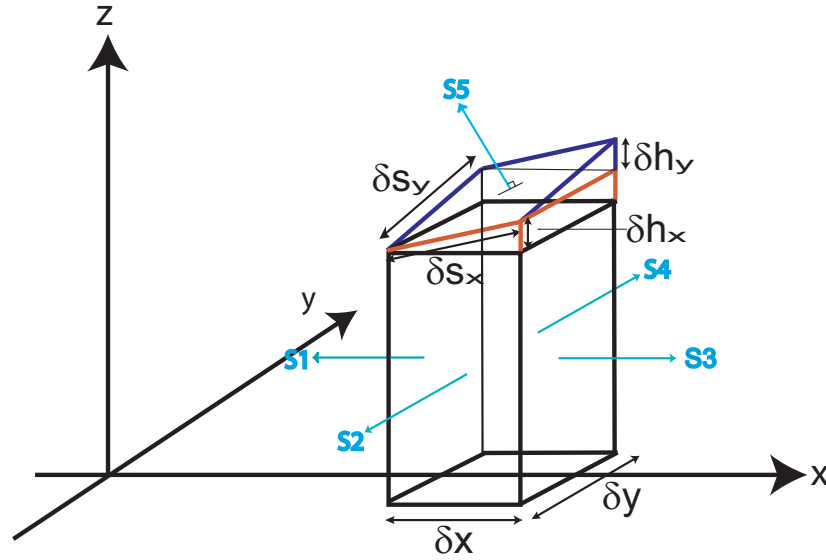


**Figure 4.9:** The volume over which the rate of change of mass is calculated. This represents a column of the boundary layer. Blue arrows represent the fluxes across the five surfaces (S1 to S5).

#### 4.4.1 Derivation of the mass budget equation

In this section an equation for the rate of change of boundary-layer mass, per unit area, will be developed. Total mass,  $M$ , within a specified volume,  $V$ , is given by

$$M = \int_V \rho dV. \quad (4.1)$$

The volume that is of interest here is a column of the boundary layer, given by  $V = \delta x \delta y h$ .  $\delta x$  and  $\delta y$ , are the horizontal dimensions of the model grid boxes and  $h$  is the depth of the boundary layer. This volume is schematically shown in Figure 4.9. The mass within this volume can change as the boundary-layer depth increases or decreases with time, or as the density,  $\rho$ , within the boundary-layer column changes.

The rate of change of mass within this volume is related to the flux of mass through the surfaces,  $\mathbf{S}$ , of the volume by

$$\frac{d}{dt} \int_V \rho dV = - \int_S \rho \mathbf{u} \cdot d\mathbf{S}, \quad (4.2)$$

and therefore the change of mass can be calculated by evaluating the right hand side of equation 4.2.  $d\mathbf{S}$  can be split into five surfaces, the four lateral edges and the top of the boundary layer, and therefore  $\mathbf{S} = \mathbf{S}_1 + \mathbf{S}_2 + \mathbf{S}_3 + \mathbf{S}_4 + \mathbf{S}_5$ . (Note that there a 6th surface

to this volume; the bottom. However, there are no fluxes of mass across this surface due to the boundary condition,  $w(z=0)=0$ ). The fluxes across these surfaces, as shown by the light blue arrows in Figure 4.9, can then be calculated separately. Starting with the lateral edges of this volume the fluxes over these surfaces are given by

$$\begin{aligned}
 \int_{S_1} \rho \mathbf{u} \cdot d\mathbf{S}_1 + \int_{S_3} \rho \mathbf{u} \cdot d\mathbf{S}_3 &= - \int_0^h \rho(x) u(x) dz \delta y + \int_0^{h+\delta h_x} \rho(x+\delta x) u(x+\delta x) dz \delta y \\
 &= \left[ \frac{d}{dx} \int_0^h \rho u dz \right] \delta x \delta y \\
 &= \frac{d}{dx} (\widehat{\rho u}) \delta x \delta y
 \end{aligned} \tag{4.3}$$

and

$$\begin{aligned}
 \int_{S_2} \rho \mathbf{u} \cdot d\mathbf{S}_2 + \int_{S_4} \rho \mathbf{u} \cdot d\mathbf{S}_4 &= - \int_0^h \rho(y) v(y) dz \delta x + \int_0^{h+\delta h_y} \rho(y+\delta y) v(y+\delta y) dz \delta x \\
 &= \left[ \frac{d}{dy} \int_0^h \rho v dz \right] \delta x \delta y \\
 &= \frac{d}{dy} (\widehat{\rho v}) \delta x \delta y,
 \end{aligned} \tag{4.4}$$

where a  $\widehat{\phantom{x}}$  represents a quantity integrated over the depth of the boundary layer. The fluxes over the edges of the volume (equations 4.3 and 4.4) can be combined to give

$$\int_{S_1} \rho \mathbf{u} \cdot d\mathbf{S}_1 + \int_{S_3} \rho \mathbf{u} \cdot d\mathbf{S}_3 + \int_{S_2} \rho \mathbf{u} \cdot d\mathbf{S}_2 + \int_{S_4} \rho \mathbf{u} \cdot d\mathbf{S}_4 = \widehat{D} \delta x \delta y, \tag{4.5}$$

where  $\widehat{D}$  is the boundary-layer integrated mass divergence given by

$$\widehat{D} = \frac{d}{dx} (\widehat{\rho u}) + \frac{d}{dy} (\widehat{\rho v}). \tag{4.6}$$

Next, the flux of mass across the boundary-layer top must be calculated. There are two caveats to this. The first is that, unlike the other surfaces, the boundary-layer top moves up and down with time, and therefore the wind components relative to this movement,  $\mathbf{u}_{\text{rel}} = (u, v, w - \frac{\partial h}{\partial t})$ , should be used rather than the total wind component. Secondly, the

top of the boundary layer slopes in both the  $x$  and  $y$  directions, as indicated in Figure 4.9, and hence the area of this surface,  $S_5$ , is given by

$$\begin{aligned} S_5 &= \delta S_x \delta S_y \\ &= \sqrt{1 + \left(\frac{\partial h}{\partial x}\right)^2} \delta x \sqrt{1 + \left(\frac{\partial h}{\partial y}\right)^2} \delta y. \end{aligned} \quad (4.7)$$

Therefore, the flux of mass across the top of the boundary layer is given by

$$\int_{S_5} \rho \mathbf{u} \cdot d\mathbf{S}_5 = \rho_h (\mathbf{u}_{\text{rel}} \cdot \mathbf{n})_h S_5 \quad (4.8)$$

where  $\rho_h$  is the density on the boundary-layer top and  $\mathbf{n}$  is the unit normal vector perpendicular to the top surface,  $S_5$ , given by

$$\mathbf{n} = \frac{1}{\sqrt{1 + (\partial h/\partial x)^2 + (\partial h/\partial y)^2}} \left[ -\frac{\partial h}{\partial x} \mathbf{i} - \frac{\partial h}{\partial y} \mathbf{j} + \mathbf{k} \right]. \quad (4.9)$$

The horizontal gradients of boundary-layer depth are known to be much less than unity, and therefore the square of these terms are very small and thus are neglected in both equation 4.7 and 4.9. Hence, the area of surface  $S_5$  is given by  $\delta x \delta y$  and the unit normal by

$$\mathbf{n} = \left[ -\frac{\partial h}{\partial x} \mathbf{i} - \frac{\partial h}{\partial y} \mathbf{j} + \mathbf{k} \right]. \quad (4.10)$$

Both of these expressions, and  $\mathbf{u}_{\text{rel}}$ , can be substituted into equation 4.8 to give

$$\int_{S_5} \rho \mathbf{u} \cdot d\mathbf{S}_5 = \rho_h \left[ (\mathbf{u} \cdot \mathbf{n})_h - \frac{\partial h}{\partial t} \right] \delta x \delta y. \quad (4.11)$$

Neglecting the  $(\partial h/\partial x)^2$  and  $(\partial h/\partial y)^2$  terms results in a fourth-order, and hence very good, approximation. (This can be shown by performing a Taylor expansion on these terms.) The approximation is fourth order as the horizontal gradient terms appear in two places; both in the numerator and the denominator of equation 4.8.

By definition the entrainment velocity,  $w_e$ , is given by

$$w_e = \frac{\partial h}{\partial t} - (\mathbf{u} \cdot \mathbf{n})_h, \quad (4.12)$$

which allows equation 4.8 to be re-written as

$$\int_{S_5} \rho \mathbf{u} \cdot d\mathbf{S}_5 = -[\rho_h w_e] \delta x \delta y. \quad (4.13)$$

Combining the fluxes across all five surface (equations 4.5 and 4.13) and substituting into the right hand side of equation 4.2 gives

$$-\int_S \rho \mathbf{u} \cdot d\mathbf{S} = -[\widehat{D} - \rho_h w_e] \delta x \delta y = [\rho_h w_e - \widehat{D}] \delta x \delta y. \quad (4.14)$$

The left hand side of equation 4.2 can also be re-written:

$$\frac{d}{dt} \int_V \rho dV = \frac{d}{dt} \int_0^h \rho dz \delta x \delta y = \frac{d}{dt} \widehat{\rho} \delta x \delta y \quad (4.15)$$

where  $\widehat{\rho}$  is the depth-integrated density given by

$$\widehat{\rho} = \int_0^h \rho dz. \quad (4.16)$$

Once equations 4.14 and 4.15 are equated, and all terms are divided by the grid box area,  $\delta x \delta y$ , the rate of change of boundary-layer mass, per unit area, can be concisely written as

$$\frac{d}{dt} (\widehat{\rho}) = \rho_h w_e - \widehat{D}. \quad (4.17)$$

This demonstrates that mass accumulates due to convergence within the boundary layer and entrainment of new mass across the boundary-layer top.

#### 4.4.2 Mass budget results

The spatial distributions of all components of the mass budget equation have been calculated and are now presented. In addition, the total rate of change of boundary-layer mass has been calculated from the sum of the individual terms on the right hand side of equation 4.17 and is shown in Figure 4.10a. The greatest increases in boundary-layer mass occur behind the cold front, whereas the largest decreases in boundary-layer mass are found on the eastern side of the anticyclone. The total rate of change of boundary-layer mass is

also estimated directly from the model output. To evaluate the left hand side of equation 4.17, a first order, forward-in-time approximation to the derivative was used with a 30 minute time step. The results from this direct estimation are shown in Figure 4.10b and agree well with the results shown in Figure 4.10a. The only location where the budget does not balance well is on the poleward edge of the low pressure system. In the direct model output there is little change in boundary-layer mass in this location, but when the sum of all terms are considered (Figure 4.10a) there is a dipole structure here. This dipole is artificial and arises from the Eulerian, instantaneous in time, calculation of the divergence term. Due to the easterly winds in this location, which are a maximum in between the dipole, the boundary-layer appears to lose mass to the north-east to the low pressure centre and gain mass to the north-west. In practice, these changes in boundary-layer mass are cancelled out by the eastward propagation of the life cycle.

To develop a clear physical understanding of how mass is transported through the boundary-layer it has been necessary to consider both components of the entrainment term in equation 4.17;

$$\rho_h w_e = \rho_h \frac{\partial h}{\partial t} - \rho_h (\mathbf{u} \cdot \mathbf{n})_h. \quad (4.18)$$

The first term on the right hand side will be referred to as the change in boundary-layer depth and the second as the advective term. The divergence,  $\widehat{D}$ , and the advective terms will now be considered. The change in boundary-layer mass due to convergence (negative divergence) is shown in Figure 4.11a. The greatest loss of mass occurs in the anticyclone, where the boundary-layer winds are divergent and hence transport mass horizontally within the boundary layer towards the convergent cyclonic system. There is a gain of mass in the warm sector as a result of this expulsion of mass from the anticyclonic region.

The advection term is shown in Figure 4.11b. The boundary layer gains mass from the free troposphere in the anticyclonic region. The maximum gain is not observed in the centre of the anticyclone, but is co-located with the deepest boundary layers. A second, smaller region where the boundary layer gains mass from the troposphere due to advection is observed to occur behind the cold front, directly to the south of the low pressure centre. This is due to strong descent associated with the dry intrusion. Figure 4.11b also shows that mass is lost from the boundary layer to the free troposphere ahead of the cold front in

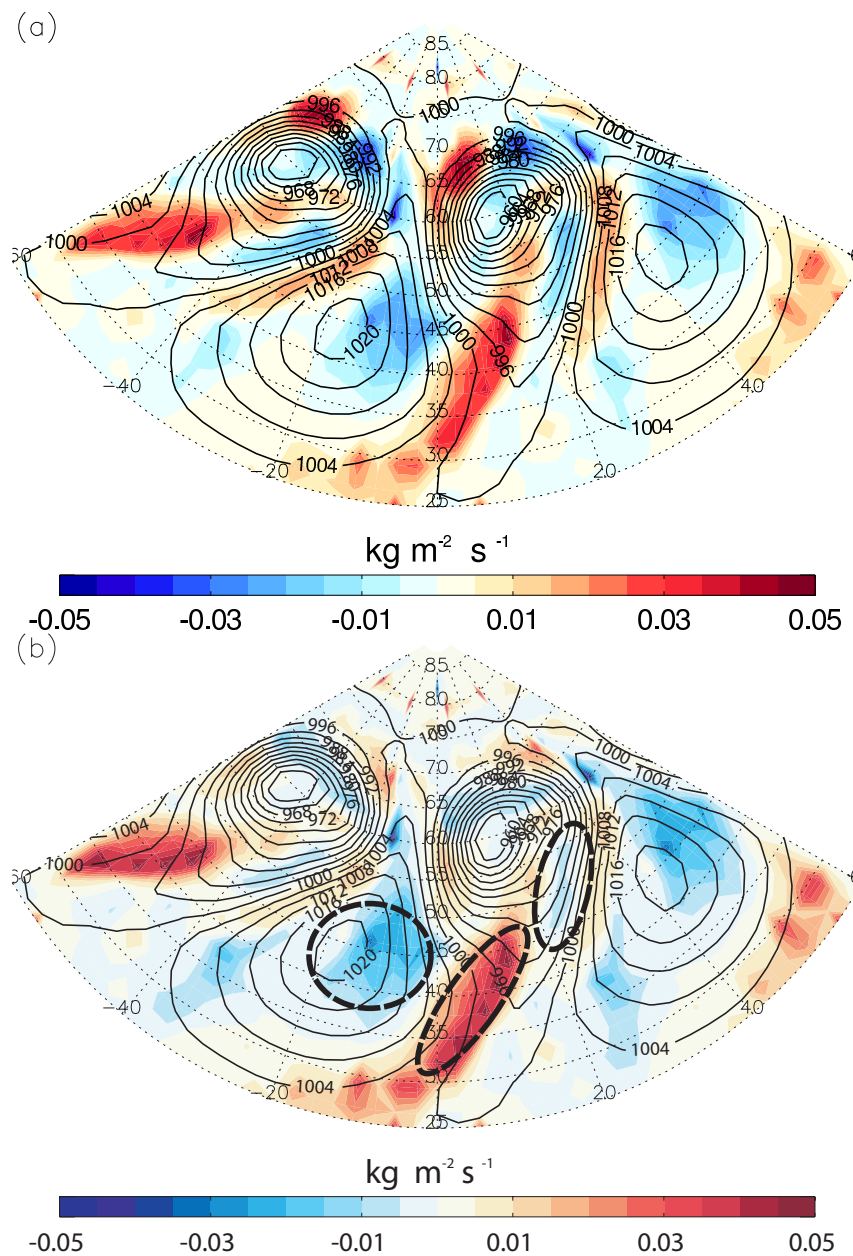


**Figure 4.10:** Total rate of change of boundary-layer mass for LC1 after 7 days calculated from (a) the sum of the individual terms on the right hand side of Equation 4.17 and (b) directly from model output. Black contours show surface pressure (mb).

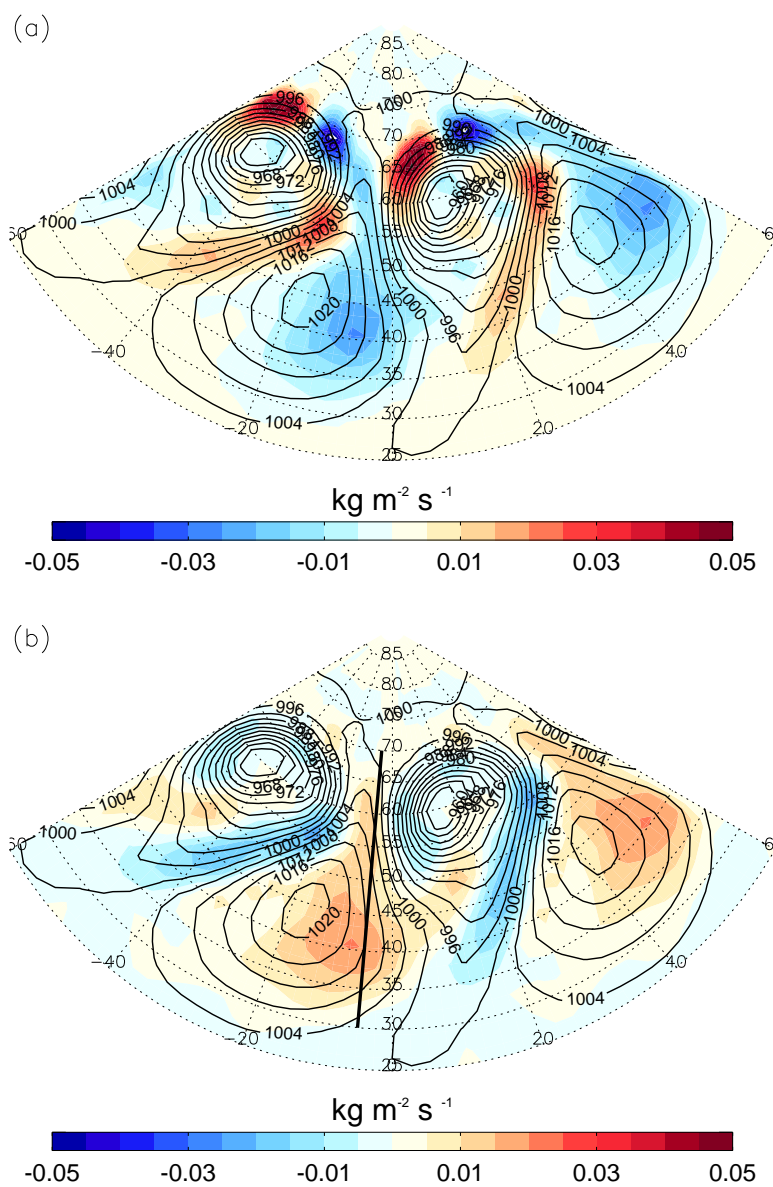


**Figure 4.11:** Rate of change of boundary-layer mass for LC1 after 7 days due to (a) convergence within the boundary layer and (b) large-scale advection. Black contours show surface pressure (mb). The thick black line in (b) shows the location of the vertical cross section shown in Figure 4.12.

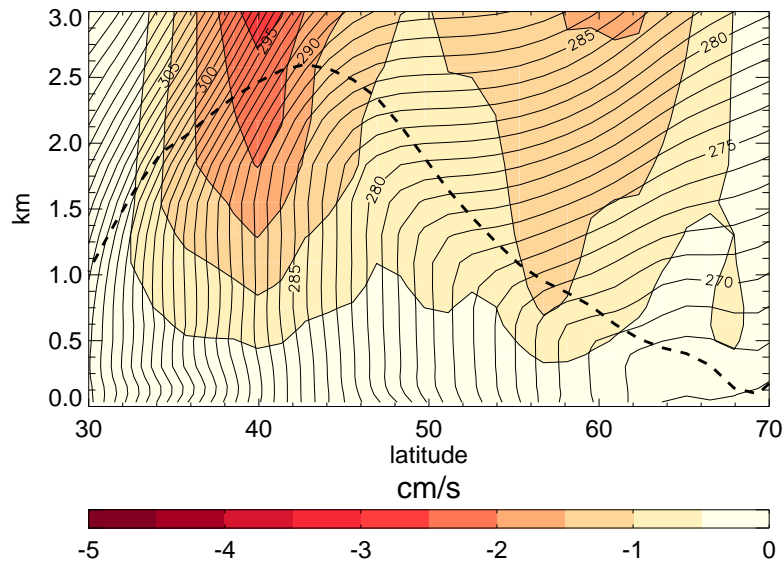


**Figure 4.12:** Vertical cross section of vertical velocity (colours), potential temperature (black contours, contour interval 1 K) and boundary-layer depth (thick dashed line) at  $55^{\circ}E$  - the thick black line in Figure 4.11b

the warm sector. This is where synoptically-driven ascent occurs and is where the warm conveyor belt originates (Browning, 1985). By comparing Figures 4.11a and 4.11b it is evident that the change in boundary-layer mass due to the large-scale advection strongly resembles, but is opposite in sign to, the change in boundary-layer mass due to convergence. This implies that these two terms describe a cycling of mass from the troposphere into the boundary layer beneath the anticyclones, horizontally through the boundary layer to the region beneath the warm sector and then back to the free troposphere by the warm conveyor belt.

Having described the large-scale transport of mass through the boundary layer and free troposphere the physical processes acting in three specific regions will now be discussed. The three areas of interest are the anticyclone, the warm sector and the cold frontal region.

### *Anticyclone*

To the east of the anticyclonic centre there are deep boundary layers and strong positive heat fluxes. There is also divergence within the boundary layer due to Ekman processes which causes a decrease in boundary-layer mass. Associated with this divergence is large-scale descent (Figure 4.12); near  $40^{\circ}N$ , where the boundary layer is deep, there is descent

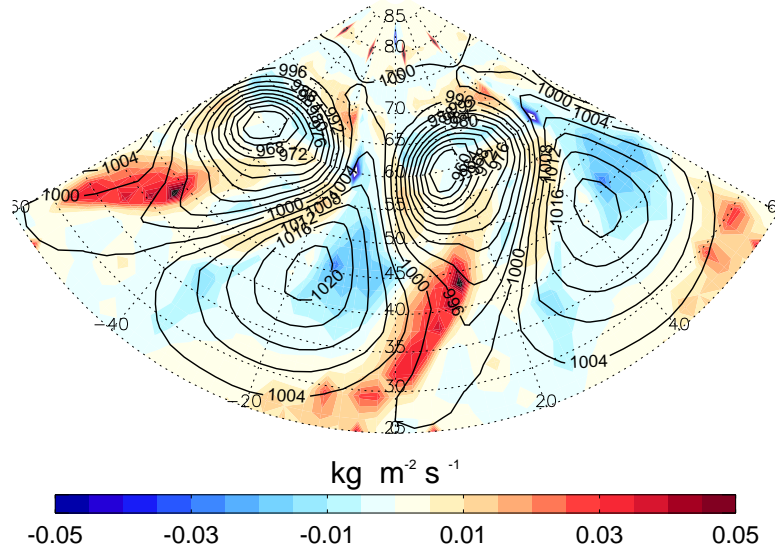


**Figure 4.13:** Rate of change of boundary-layer mass for LC1 after 7 days due to local changes in boundary-layer depth. Black contours show surface pressure (mb).

exceeding  $2 \text{ cm s}^{-1}$  on the top of the boundary layer. This demonstrates that there are two competing factors which are acting to determine the boundary-layer depth in the anticyclonic region. The subsidence acts to advect the potential temperature contours downwards, which consequently reduces the depth of the boundary layer. This is evident in Figure 4.13, which shows the change in mass due to local changes in boundary-layer depth. However, at the same time the large positive heat fluxes (Figure 4.2) are acting to increase the depth of the boundary layer by entrainment (Figure 4.14). Transport of mass from the troposphere to the boundary layer can occur in this region due to the absence of strong temperature inversions (which was shown in Figure 4.4c). Additionally, Figure 4.12 also shows that the descent penetrates over a kilometre into the boundary layer and that in this region of strong subsidence the isentropes are found to make a large angle with the diagnosed boundary-layer top. As above the boundary layer, and in the absence of diabatic processes, air parcels will travel along surfaces of constant potential temperature, this suggests that there will be considerable transport from the free troposphere into the boundary layer in this area.

Therefore the net result is a small absolute change in boundary-layer depth but a considerable flux of mass from the troposphere into the boundary layer occurs in this region, which is almost balanced by the divergent flux of mass out of the anticyclone.

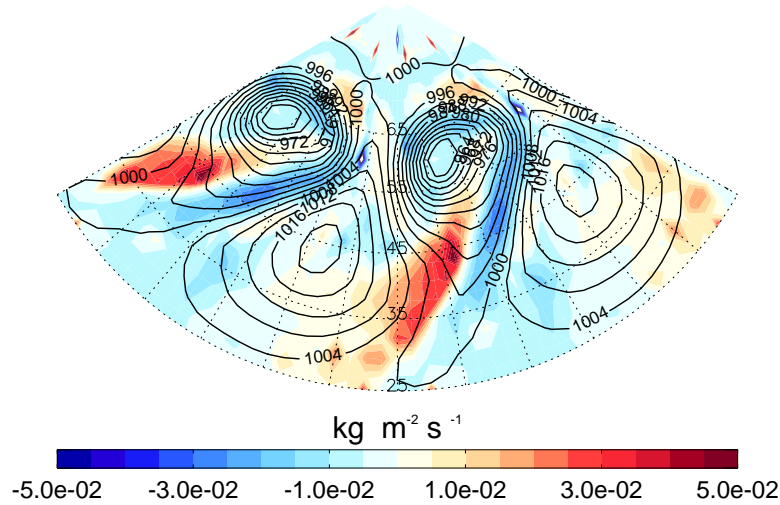


**Figure 4.14:** Rate of change of boundary-layer mass for LC1 after 7 days due to entrainment. Black contours show surface pressure (mb).

### *Warm sector*

The boundary layer in the warm sector of the cyclone gains mass due to convergence and therefore by large-scale mass conservation loses mass by large-scale advection, as was shown in Figure 4.11. The loss due to advection is greater than the gain due to convergence, especially in the southern part of the warm sector. The boundary layer in this region is stably stratified and does not change significantly in height, (i.e.  $\partial h/\partial t$  is small but slightly negative as shown in Figure 4.13). Therefore, the most important term in the budget equation is the advection term, which is one component of the entrainment term. When Figure 4.11b (advection) is compared to Figure 4.14 (entrainment) the values in the warm sector are similar, emphasising that the advective term, which causes a loss of boundary-layer mass, is the dominant term in the warm sector. The total rate of change of boundary-layer mass (Figure 4.10) confirms that the warm sector is a region where mass can be efficiently transported from the boundary layer to the free troposphere.

### *Cold front*

Behind the cold front the cold air mass moves south over much warmer surfaces which leads to very strong positive heat fluxes. These heat fluxes lead to a rapid increase in boundary-layer depth behind the cold front (Figure 4.13), which allows large amounts

of tropospheric mass to be transported into the boundary layer. Immediately behind the front there is little change of boundary-layer mass due to the advective component (Figure 4.11b). Therefore this differs significantly from the anticyclonic region in which  $\partial h/\partial t$  was small and the advective component was large. Therefore the passage of the cold front introduces significant amounts of tropospheric air into the boundary layer due to entrainment (Figure 4.14), which more accurately can be described as encroachment, since the warming due to the large surface heat fluxes is directly responsible for the growth of the boundary layer immediately behind the cold front.

## 4.5 Conclusions

The boundary layers that developed beneath two characteristic life cycles, LC1 and LC2, have been considered in detail. It has been shown that synoptic systems strongly influence the structure of the boundary layer that develops beneath them. However, the differences in the spatial patterns of boundary-layer parameters, in relation to the synoptic features, were found to be small between LC1 and LC2. The magnitudes of the surface fluxes, bulk stability and boundary-layer depths were found to vary slightly between LC1 and LC2, due to the different degrees of meridional displacement that the cyclones and anticyclones in the different life cycles experienced. The warm sectors of the cyclones in both life cycles were found to have shallow, shear-driven boundary layers. Here, heat fluxes were small and negative, which is consistent with the stable bulk stratification of the boundary layer observed in the warm sectors. In the eastern flanks of the anticyclone in both LC1 and LC2 deep convective boundary layers were present. Heat fluxes in these regions were large and positive. In the central and southern parts of the anticyclonic regions, the boundary layer was unstably stratified, but the magnitude of the surface heat fluxes was smaller than on the eastern edge of the anticyclone. As the synoptic systems intensify, the magnitude of the surface fluxes of both momentum and heat increase. This causes the boundary layer to be deeper in unstable regions in the later stages of the simulations. Additionally, the boundary-layer depth increases in stable regions as the cyclone reaches maturity, due to increased wind speeds causing greater shear-driven turbulent mixing. It was found that the synoptically-driven boundary layers are controlled by thermal advection. The strength of the thermal advection is determined by the initial North-South temperature gradient (the strength of baroclinicity) and the meridional displacement of air parcels by the high and low pressure systems. The processes that determine the structure of the boundary

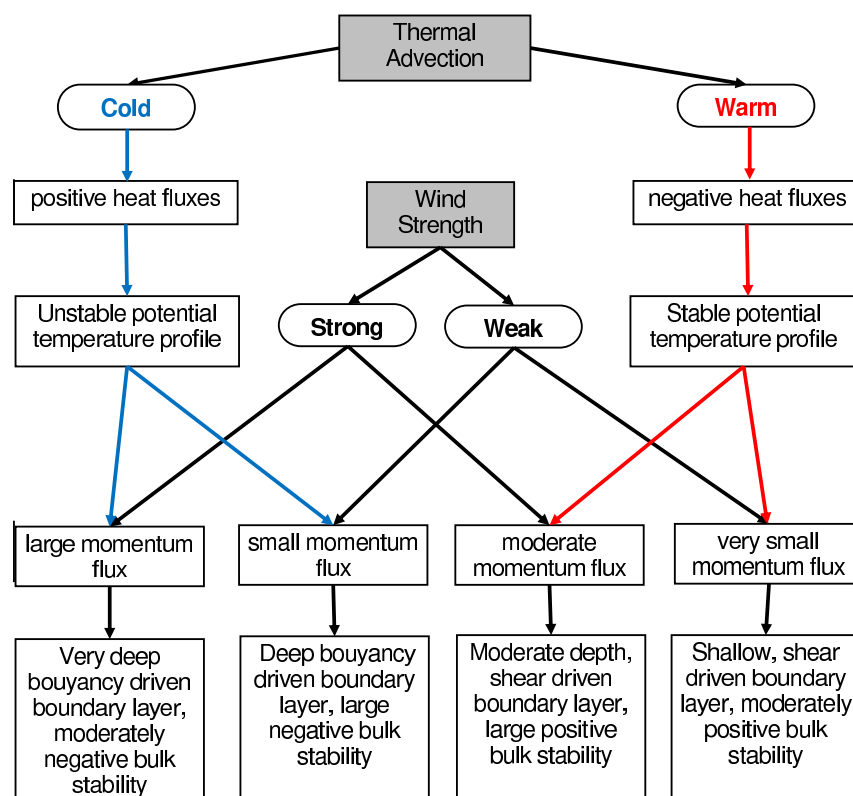


**Figure 4.15:** Decision tree that determines the type of boundary layer given different synoptic conditions

layer are represented in a flow diagram in Figure 4.15. This demonstrates that four types of conceptual boundary-layer structure occur due to synoptic forcing. To establish the general characteristics of a synoptically-forced boundary layer only knowledge about the low-level thermal advection and wind speeds is required.

It has also been shown that frontal features cause the greatest horizontal variations in the boundary-layer structure. The largest horizontal gradients in both the surface heat flux and boundary-layer depth were found to occur across the cold front. This occurs because the cold front represents a boundary between cold-air advection and warm-air advection. The results from evaluating the boundary-layer mass budget emphasise the importance of the cold front. The passage of the cold front leads to large amounts of tropospheric air being transported into the boundary layer by entrainment. This is shown schematically in Figure 4.16; the large heat fluxes cause the boundary layer to deepen by encroachment. The mass budget also demonstrated that air is cycled between the troposphere and boundary layer on large spatial scales, with limited net gain of mass in the boundary layer. It was shown that mass is transported into the boundary layer by large-scale subsidence in the anticyclonic region, especially the eastern edges. Once

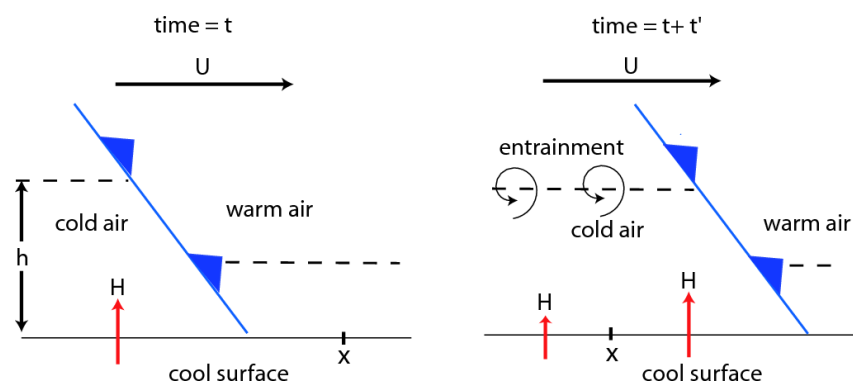


**Figure 4.16:** Schematic diagram showing the net gain of mass into the boundary layer by the passage of a cold front (blue lines). Dashed line represents the boundary layer top. Flow is from left to right. Red arrows represent the surface heat flux.

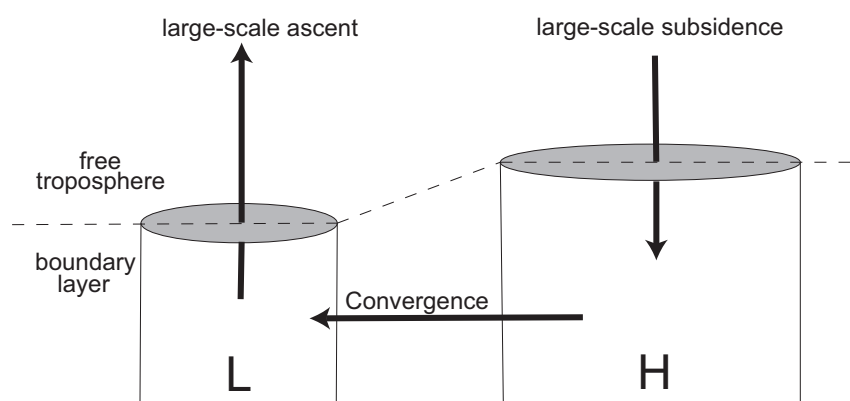


**Figure 4.17:** Schematic diagram showing the exchange of mass between the boundary layer and free troposphere.  $H$  indicates the location of the anticyclone and  $L$  the location of cyclone. Solid black arrows show the path air follows as it is cycled through the boundary layer. Dashed line represents the boundary layer top.

within the boundary layer beneath the anticyclone, mass is then transported through the boundary layer towards the convergent cyclonic regions. This low level transport, which involves no exchange with the troposphere, occurs due to divergent and convergent motions that are induced by a combination of the large-scale vertical motion and frictional turning of the winds near the surface (Ekman dynamics). Once mass is transported to the boundary layer beneath the cyclone's warm sector it can then be returned to the free troposphere by large-scale ascent in the warm conveyor belt. This is shown schematically in Figure 4.17.

This is an idealised study and hence, to isolate the effect synoptic-scale weather systems have on the boundary-layer structure, not all processes that can act to alter the

structure of the boundary layer were included. No diurnal cycle is included in these simulations, which over land is an important control on the boundary layer. As the majority of cyclones develop over oceans, where diurnal variations of the boundary layer are small, it is thought that the results obtained here are representative of reality. To ensure that this is the case, a brief comparison has been made between the magnitudes of the surface fluxes obtained here and observations. Good agreement on both the magnitudes and the spatial patterns is found. Persson *et al.* (2005) reported surface heat fluxes of  $\sim 100 \text{ W m}^{-2}$  behind a cold front and  $-10 \text{ W m}^{-2}$  in the warm sector of a cyclone while Bond and Fleagle (1988) reported a mean surface heat flux values of  $-4 \text{ W m}^{-2}$  in the warm sector and  $76 \text{ W m}^{-2}$  behind the cold front. Additionally, when the surface heat fluxes obtained in these idealised simulations (Figures 4.2 and 4.7a) are compared to heat fluxes from the operational Met Office Unified Model (Figure 4.1), a state of the art, complex general circulation model, good agreement is found, especially on the spatial variation that occurs. This implies that during winter over oceans the diurnal forcing of the boundary layer is of secondary importance compared to the synoptic forcing. This is further emphasised when the heat fluxes found on the eastern edge of the anticyclone in Figure 4.1, which have a typical magnitude of  $200 \text{ W m}^{-2}$ , are compared to the heat fluxes over Spain, which typically are less than  $100 \text{ W m}^{-2}$ .

---

## CHAPTER FIVE

# Boundary-layer ventilation processes

---

### 5.1 Introduction

The purpose of this chapter is threefold. The first aim of this chapter is to identify the physical processes that lead to the transport of tracers within the boundary layer and free troposphere during the idealised simulations of LC1 and LC2 in the IGCM. Transport confined to within the boundary layer will first be investigated. Previous studies (e.g. Agustí-Panareda *et al.*, 2005; Dacre *et al.*, 2007) have indicated that turbulent mixing increases the overall efficiency of boundary-layer ventilation, and therefore, it appears likely that turbulent mixing is an important transport process within the boundary layer. Secondly, as studies which have considered how surface friction affects frontal structures (e.g. Keyser and Anthes, 1982) have shown that surface friction can induce considerable horizontal convergence and divergence at low levels, horizontal transport within the boundary layer is investigated. The conveyor belt structures that develop in both life cycles are examined and the tracer transport within these airstreams is reported. The second question addressed in this chapter is how do different transport processes interact with each other? The third and final aim is to identify the regions of the boundary layer that tracer is efficiently ventilated out of during the passage of a frontal cyclone. These three aims are addressed by an in depth analysis of the tracer distributions that are found to develop during the evolution of LC1 and LC2. The reader is reminded that a passive tracer has been included in all experiments. The tracer has an uniform concentration at the lowest

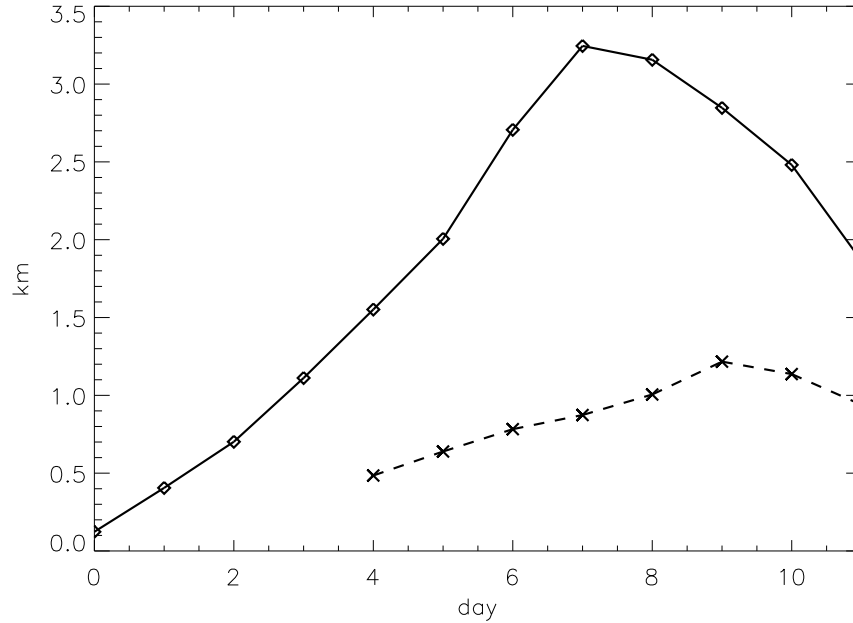


**Figure 5.1:** Maximum diagnosed boundary-layer depth (solid line) for LC1 and the mean boundary-layer depth in the region identified as the conveyor belt footprint (dashed line). Note that no conveyor belt is identified until day 4.

model level at the beginning of the life cycles and is then re-distributed throughout the domain by turbulent motions and the large-scale winds.

## 5.2 Vertical mixing by boundary-layer turbulence

The boundary-layer structure has been shown in Chapter 4 to be synoptically driven in these life cycles, as the surface heat flux, and hence boundary-layer depth and stability, are determined primarily by advective processes. Therefore, the boundary-layer forcing strengthens as the life cycles intensify. This is seen in Figure 5.1; the boundary-layer depth increases with time in the same manner as the intensity of the life cycle does.

The structure of the boundary layer was described in detail in Chapter 4. To the south-west of the low pressure centre, where there is strong cold air advection in the northerly winds behind the cold front over warmer surface temperatures, the boundary layer was found to be deep and well mixed with respect to potential temperature. Similar behaviour was found in the anticyclonic regions. The cyclonic regions were found to be stably stratified with much shallower boundary layers, due to warm air advection over colder surfaces. The boundary-layer structure is important as transport of tracer away from the surface source is initially dominated by boundary-layer turbulence. During

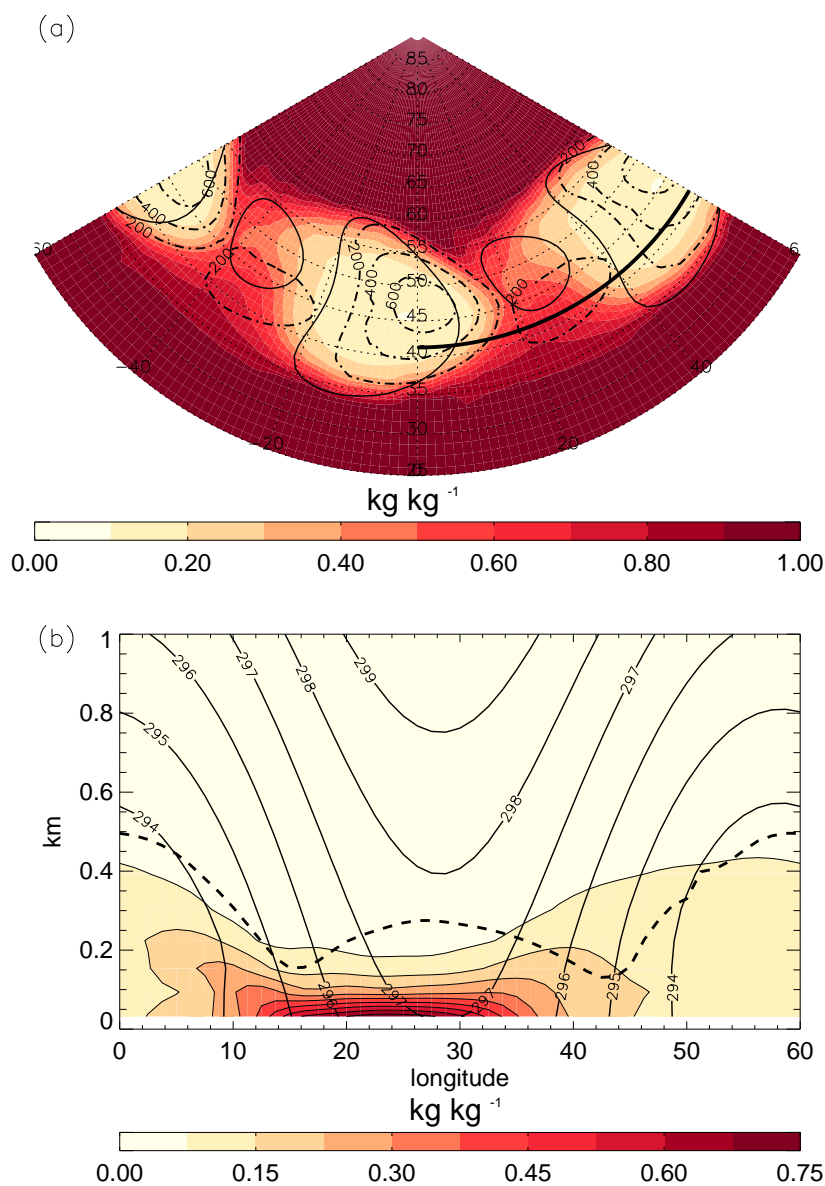


**Figure 5.2:** Tracer concentrations after 48 hours of LC1. (a) Horizontal cross section at 32 m. Dash-dot lines show boundary layer depth (contour interval of 200 m). Solid lines represent surface pressure (contour interval of 2 mb). (b) Vertical cross section taken along the heavy black line in panel (a). Heavy dashed line represents the diagnosed boundary-layer depth and the solid black contours are potential temperature (K). Note different colour scales for tracer concentrations in panels (a) and (b).

the early stages of the life cycles the synoptic scale motions are weak, and thus do not penetrate deep into the boundary layer and so do not directly transport tracer in the vertical. The redistribution of tracers within the boundary layer is highly non-uniform. Figure 5.2a shows the spatial correlation between boundary-layer depth, synoptic-scale features and tracer concentrations. Anticyclonic regions have deeper boundary layers than cyclonic regions, with the maximum boundary-layer depth located to the east of the anticyclonic centres. Near surface tracer concentrations are weak underneath anticyclonic regions as the tracer has been mixed almost to the top of the boundary layer (Figure 5.2b). This vertical transport occurs despite large-scale subsidence, illustrating the dominance of boundary-layer motions in redistributing tracer in the vertical when synoptic forcing is weak. In cyclonic regions the surface concentrations remain strong as a consequence of stable boundary layer profiles with respect to potential temperature, which inhibit vertical transport of tracer away from the surface. This early inhomogeneity in the tracer distribution is a response to the high spatial variability of the turbulent structure and depth of the boundary layer. Turbulent mixing of the tracer within the boundary layer is vital for boundary-layer ventilation and also for long range transport in the free troposphere. It allows the tracer to be lifted away from the surface to the mid to upper regions of the boundary layer. The large-scale driven ascent and horizontal winds extend down to these levels and can then transport the tracer out of the boundary layer and considerable distances in the free troposphere.

### 5.3 Advection in the boundary layer

Tracer can be effectively redistributed in the horizontal, as well as in the vertical, within the boundary layer. In the anticyclonic regions of both life cycles large-scale divergent winds, driven by descent and enhanced by surface friction, push the tracer out of the centre of the anticyclones, towards the convergent cyclonic regions. These Ekman motions have an important impact on the horizontal tracer distribution throughout the depth of the boundary layer. Figure 5.3a shows the near surface concentrations of the tracer in the divergent anticyclones to be weak, with stronger concentrations in the convergent regions. Also visible in Figure 5.3a is the horizontal advection of tracer from low latitudes north towards the cyclonic centres. The tracer concentration at 400 m (Figure 5.3b) shows a ring of high concentrations around the edge of the anticyclone, which exists as the tracer has been mixed up to this level by turbulence and then diverged out of the anticyclonic centre.

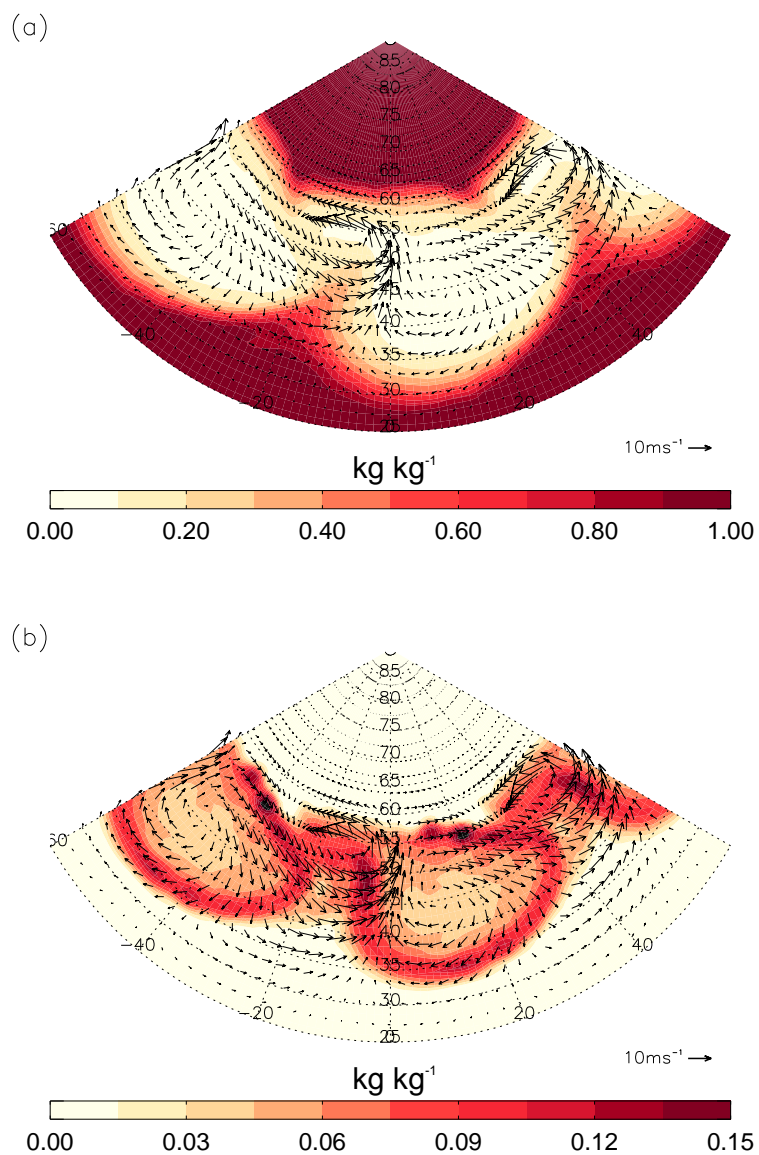


**Figure 5.3:** Tracer concentrations and wind vectors after 4 days of LC1. (a) Horizontal cross section at 32 m, (b) 400 m. Note different colour scales for tracer concentrations in panels (a) and (b).

This, along with the wind vectors displayed in Figure 5.3b, shows that the horizontal motions, and hence the potential for horizontal advection of the tracer, are greatest near the top of the boundary layer. This demonstrates the interaction between the turbulent mixing and the horizontal Ekman transport; without the turbulent mixing of tracer to the upper regions of the boundary layer, the full potential of the Ekman motions to advect tracer would not be realised. This horizontal redistribution of the tracer within the boundary layer causes the ridges of high pressure which develop between the cyclones to be depleted of tracer and the cyclonic regions to be fed with a supply of tracer. The tracer is not found to accumulate in the cyclonic regions but is acted upon by large-scale driven ascent. Therefore, the Ekman motions transport the tracer into regions where there is a greater potential for the tracer to be ventilated out of the boundary layer.

## 5.4 Ventilation by the warm conveyor belt

Using the conveyor belt diagnostic introduced in Section 2.8.3 a conveyor belt (warm or cold) is not present in LC1 until day 4 of the simulation. Once identified, the conveyor belt footprint is found to be in the warm sector ahead of the cold front, and is identified as a warm conveyor belt (WCB). The evolution of the conveyor belt footprint is shown in Figure 5.4 for LC1 and in Figure 5.5 for LC2. During the developing phase of the LC1 cyclone, Figure 5.4a, the WCB footprint is centred around  $50^{\circ}\text{N}$ , and extends approximately 1000 km in a meridional direction. As the cyclone reaches its mature phase (Figure 5.4c) the footprint of the WCB is found to extend northwards to  $60^{\circ}\text{N}$  and southwards to  $35^{\circ}\text{N}$ . The width of the footprint remains reasonably consistent covering  $5^{\circ}$  of longitude, and the location of the WCB source regions in relation to the frontal features does not change significantly during the life cycle. In LC1, where the cold front is dominant throughout the life cycle, the conveyor belt diagnostic does not identify a CCB at any point of the life cycle. The weak warm front inhibits the formation of a CCB.

In LC2 a conveyor belt footprint is not identified until day 5 (Figure 5.5a). At this point in the LC2 simulation the footprint is located in the cool air ahead of the warm front, around  $45^{\circ}\text{N}$ , and not directly ahead of the cold front. Therefore, after 5 days of LC2 the conveyor belt diagnostic has identified ascent which resembles a CCB. Semple (2003) and Schultz (2001) both note that the CCB can bifurcate once west of the low centre. One branch can continue to ascend and follow an anticyclonic branch, while the

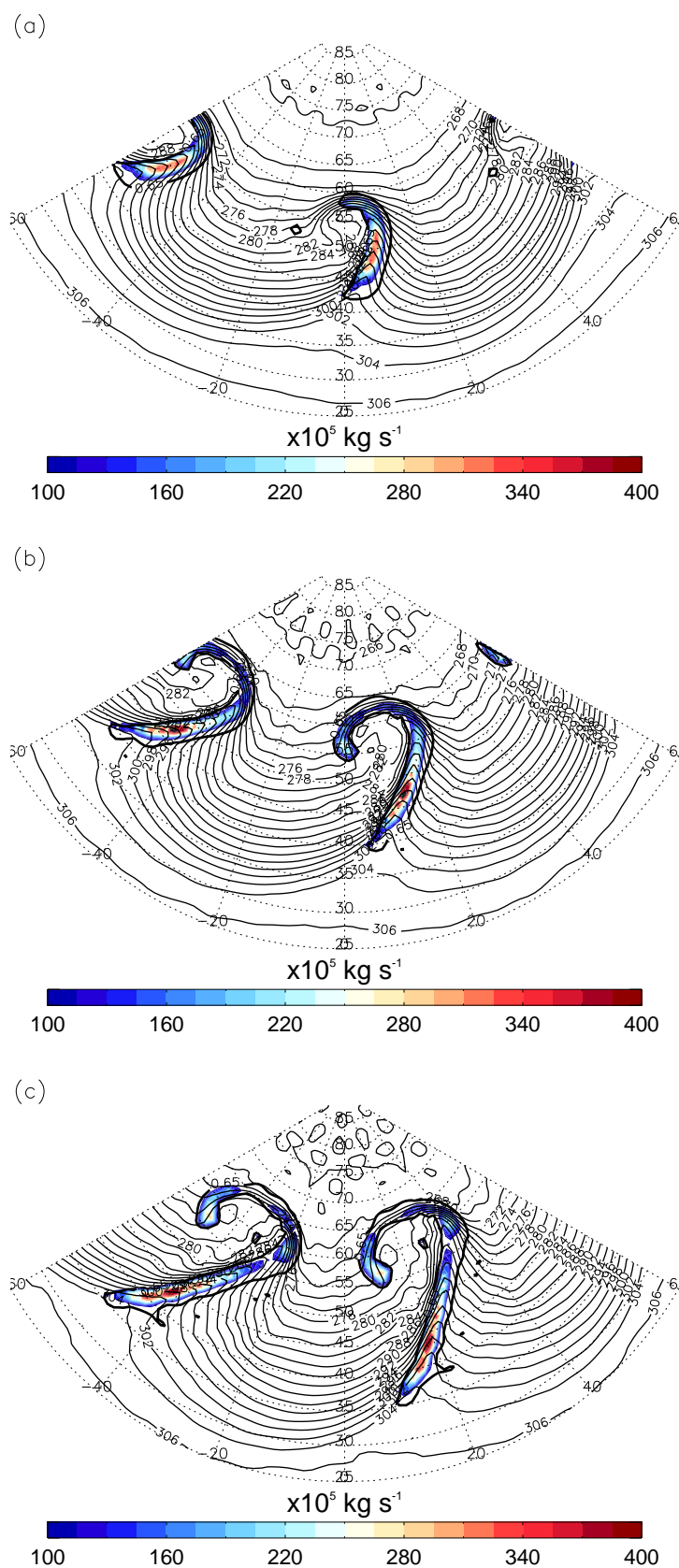


**Figure 5.4:** Tracer flux across boundary-layer top (shaded contours) for LC1 after (a) 5 days, (b) 6 days, (c) 7 days. Thick contours are the  $0.5 \text{ cm s}^{-1}$  vertical velocity contour on the boundary-layer top. Thin contours are surface potential temperature, contour interval 2 K.

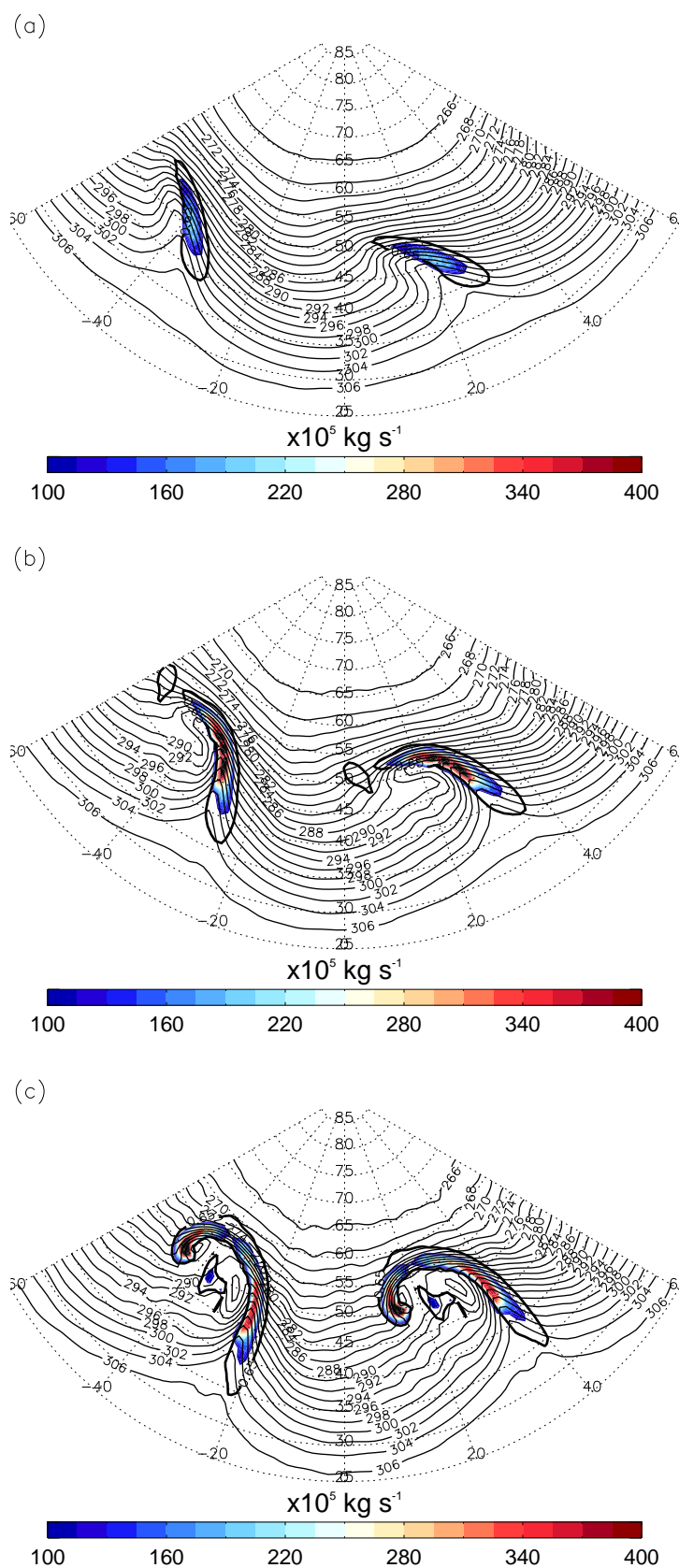


**Figure 5.5:** Tracer flux across boundary-layer top (shaded contours) for LC2 after (a) 5 days, (b) 6 days, (c) 7 days. Thick contours are the  $0.5 \text{ cm s}^{-1}$  vertical velocity contour on the boundary-layer top. Thin contours are surface potential temperature, contour interval 2 K.

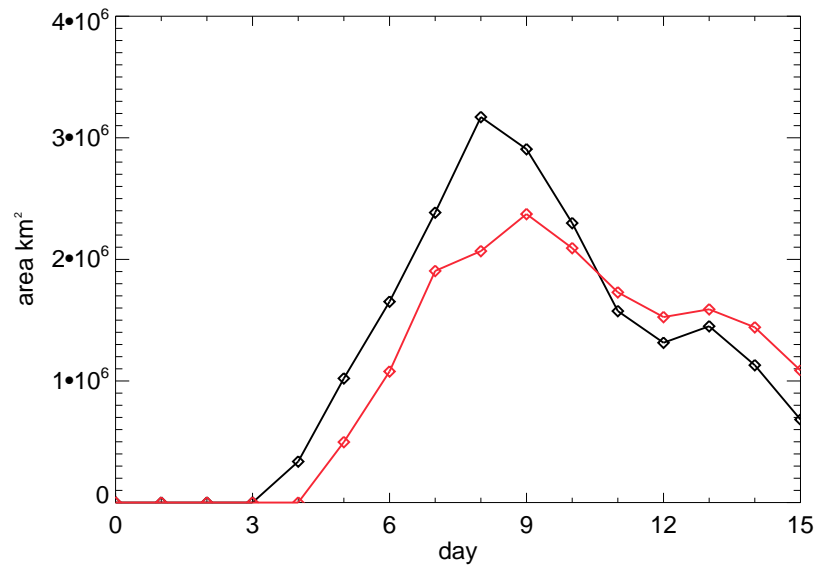


**Figure 5.6:** Time series of conveyor belt footprint area for LC1 (black line) and LC2 (red line).

other descends cyclonically around the low centre. No ascending anticyclonic branch of the CCB is present in the LC2 simulation, but a weak CCB is found to travel westward at low levels, cyclonically around the poleward side of the low and then descend. The vertical extent of the CCB is limited to less than 2 km, primarily due to the dry nature of the simulations. In reality, the CCB acquires moisture and buoyancy from the surface via a latent heat flux and also by evaporation of rain falling into it from the WCB, which it has undercut. In these dry simulations there is no source of buoyancy and therefore the CCB does not extend far in the vertical. At day 6, Figure 5.5b, the conveyor belt diagnostic shows a footprint in the warm air ahead of the cold front. This implies that the flux of tracer out of the boundary layer is now due to a WCB. The transition from a CCB to a WCB occurs due to the strengthening cold front and increased ascent in the warm sector compared to in the warm frontal region. At this stage a low level easterly jet, resembling of a CCB, is still evident but only within the boundary layer. Therefore after 6 days the CCB type flow has the ability to transport tracer within the boundary layer but not to ventilate tracer out of the boundary layer. By day 7, the mature stage of LC2, the conveyor belt diagnostic continues to identify a WCB (Figure 5.5c). This has a footprint in a similar position, in relation to the surface fronts, to that in LC1 (in the warm sector ahead of the cold front, between 40°N and 50°N). However, unlike LC1, the WCB footprint area in LC2 is orientated south-east to north-west.

Timeseries of the conveyor belts footprint area are shown in Figure 5.6. The growth

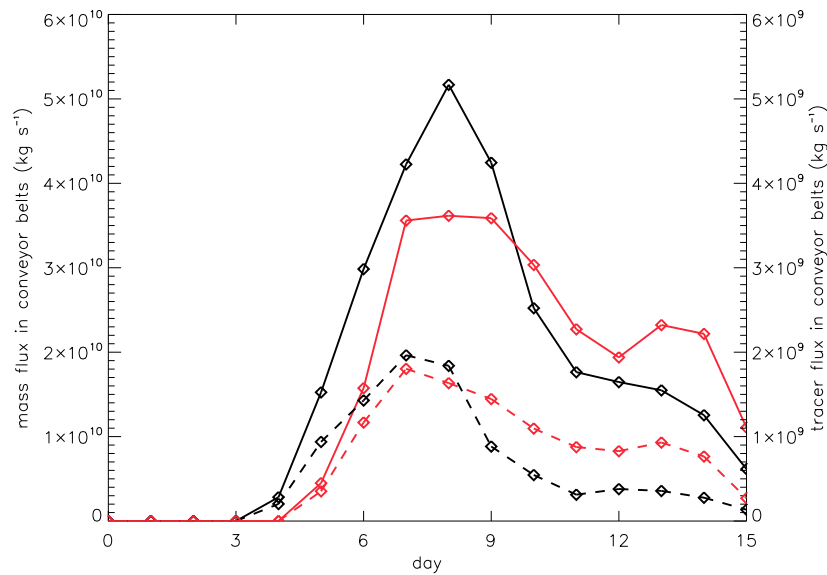


**Figure 5.7:** Time series of mass flux (solid) and tracer flux (dashed) due to the conveyor belts for LC1 (black lines) and LC2 (red lines).

rate of the footprint area is similar for both LC1 and LC2 and approximately constant between days 4 and 7. LC1 has a larger conveyor belt footprint area than LC2 during this developing period, and reaches a greater maximum, due to the stronger cold front, and hence the dominance and greater meridional extent of the WCB in LC1, compared to LC2 at this stage. The conveyor belt area is found to decay rapidly in LC1 after day 8, but not in LC2. This agrees well with the dynamical aspects of these systems reported in Chapter 3. The similarity between the evolution of the conveyor belt area (Figure 5.6) and the eddy kinetic energy (Figure 3.2) suggests that the extent of the conveyor belt is well constrained by dynamical parameters.

To quantify the intensity of the conveyor belts, the conveyor belt mass flux ( $CMF$ ) across the boundary layer top within the region defined as the conveyor belt is defined to be

$$CMF = - \int \frac{\omega}{g} dA, \quad (5.1)$$

where  $\omega$  is the vertical velocity in  $\text{Pa s}^{-1}$ ,  $A$  is the area identified as the conveyor belt footprint, and  $g$  is acceleration due to gravity. A timeseries of the mass flux for both life cycles is shown in Figure 5.7; this shows a similar pattern to the area of the conveyor belt (Figure 5.6). Both life cycles have a very similar mass flux for the first 7 days, which is surprising considering the very different synoptic evolutions. The total mass

flux in the conveyor belts is found to reach a maximum of  $5 \times 10^{10} \text{ kg s}^{-1}$  for LC1 and  $3.5 \times 10^{10} \text{ kg s}^{-1}$  for LC2. These values compare reasonably well with the annual mean value of the WCB mass flux in the North America / Atlantic region of  $5 \times 10^9 \text{ kg s}^{-1}$ , found by Eckhardt *et al.* (2004) in a WCB climatology study. The differences in the magnitude of the WCB mass fluxes are potentially due to the different methods applied to identify the WCBs (Section 2.8.3). To quantify the rate at which tracer is removed from the boundary layer, the total flux of tracer across the boundary-layer top within the conveyor belt region is also calculated and is shown in Figure 5.7. Both life cycles experience large tracer fluxes out of the boundary layer by the WCB between day 4 (in LC1) or 5 (in LC2) and day 7. The peak in the total WCB tracer flux is found to occur after 7 days in both life cycles. The effect of increased horizontal resolution (not shown) is to decrease the area identified as a conveyor belt, but increase the conveyor belt mass and tracer fluxes. This occurs because at T85 resolution mesoscale features, such as fronts, are better resolved. Therefore, the conveyor belt ascent is much stronger than at T42 but is confined to a smaller region.

The evolution of the spatial distribution of the tracer flux out of the boundary layer for LC1 and LC2 between day 5 and 7 is plotted in Figures 5.4 and 5.5. For LC1 after 5 days, (Figure 5.4a), the maximum tracer flux is concentrated between  $40^\circ$  and  $50^\circ\text{N}$  and is orientated in a south-west north-east direction. After 6 days (Figure 5.4b), the tracer flux is found to extend further north and south, a trend which continues to day 7 (Figure 5.4c), when the tracer flux is found to reach from  $30^\circ\text{N}$  to  $65^\circ\text{N}$ . It is apparent that at day 7 the maximum tracer flux (located between  $37^\circ\text{N}$  to  $47^\circ\text{N}$ ) is not directly co-located with the maximum ascent across the boundary layer top, whereas during the developing stages (day 5) of the life cycle these two regions were co-located. Additionally, Figure 5.7 shows that in LC1 the peak in the mass flux due to the conveyor belt occurs a day later than the peak in the tracer flux. Combined, this evidence shows that the LC1 cyclone has the dynamical capability to ventilate more tracer than it actually has; the source regions of the conveyor belts in the boundary layer have begun to run out of tracer to ventilate.

The area of maximum tracer flux in LC2 (Figure 5.5a) is initially within the same latitude band,  $40^\circ$  to  $50^\circ\text{N}$ , as found in LC1, but is orientated south-east to north-west. The area of maximum tracer flux extends in the meridional direction and becomes more North - South orientated by day 6 (Figure 5.5b). After 7 days (Figure 5.5c) the tracer flux out of the boundary layer in LC2 reaches from  $40^\circ\text{N}$  to  $60^\circ\text{N}$ , and has two localised

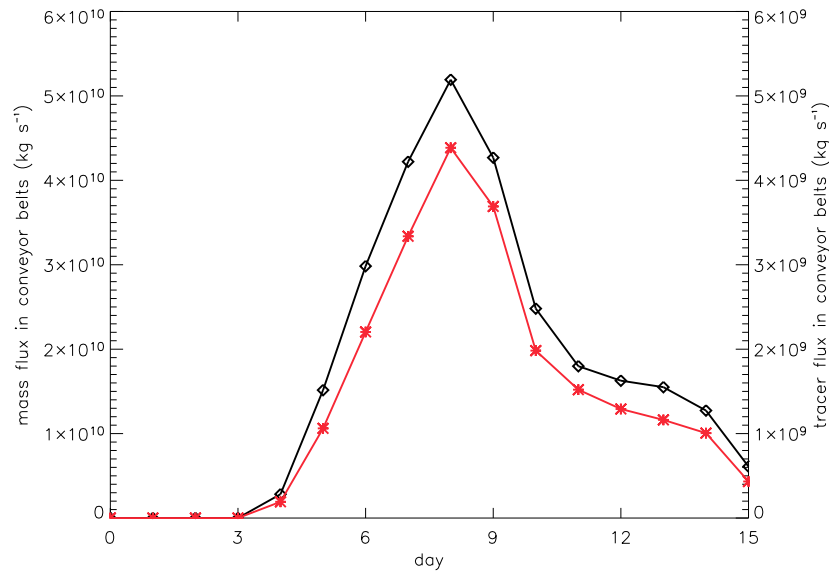


**Figure 5.8:** Time series of mass flux (black line) and tracer flux (red line) due to the conveyor belts for LC1 in the case of the constant tracer emission.

maxima; one in the warm sector and the other to the west of the low pressure centre which is due to the cyclonic branch of the WCB. Unlike in LC1 the regions of maximum tracer flux and vertical velocity in LC2 remain approximately co-located at this time. This indicates that in LC2 the boundary-layer motions are providing a supply of tracer into the ventilation region at a rate equal to or greater than the ventilation rate.

These tracer flux results demonstrate that boundary-layer ventilation depends on both synoptically-driven ascent and the availability of tracer in the source regions of the conveyor belts. Therefore, for maximum boundary layer ventilation it is necessary to transport tracer to the regions of the boundary layer that are passed over by a conveyor belt. This occurs via boundary-layer turbulent mixing and horizontal advection (Ekman motions) within the boundary layer.

#### 5.4.1 Dependence on method of tracer initialisation

It is apparent that the availability of tracer in the boundary layer affects the amount of boundary-layer ventilation. It is also possible that the extent of transport in the free troposphere will not be fully realised using an initial condition tracer as the model may run out of tracer within the boundary layer to vent into the free troposphere. Therefore, a second experiment with a constant emission of tracer has been conducted. To ensure clarity between the two experiments they will hereafter be referred to as the “initial condition

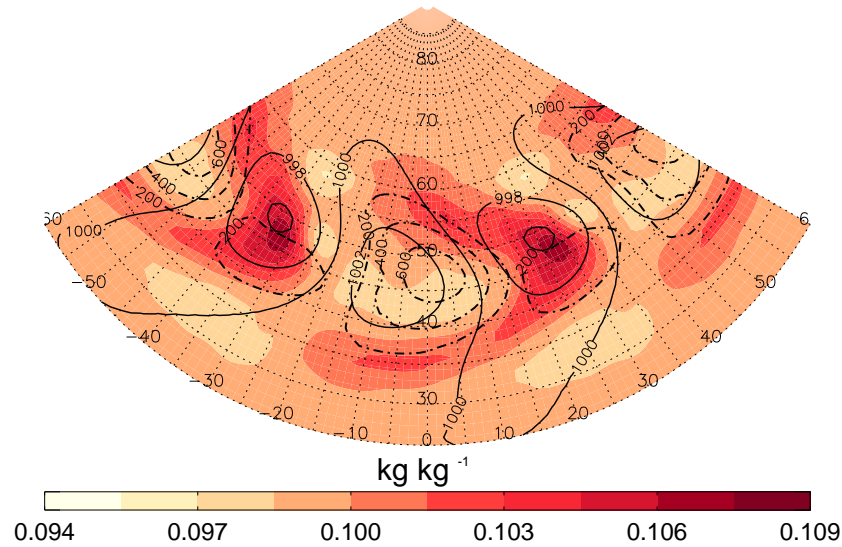


**Figure 5.9:** Horizontal cross section of concentration of the constant emission tracer in  $\text{kg kg}^{-1}$  at 32 m after 48 hours of the LC1 life cycle. Dash-dot lines show boundary layer depth (contour interval of 200 m). Solid lines represent surface pressure (contour interval of 2 mb).

case” and the “constant emission case”. The flux of tracer into the domain from the surface is chosen to have an arbitrary value ( $1 \times 10^{-4} \text{ kg m}^{-2} \text{ s}^{-1}$ ), and is constant across the whole domain and throughout the life cycle. A comparison of the results from the two different experiments allows for the sensitivity of boundary-layer ventilation to the type of tracer emission to be investigated.

The case of a constant tracer emission is now briefly considered. The regions where tracer is ventilated out of the boundary layer (not shown) remain unchanged, but the amount of ventilation to the free troposphere is moderated by the source strength. The total flux of the constant emission tracer out of the boundary layer by the conveyor belts is shown in Figure 5.8 for LC1. The tracer flux is now directly correlated with, and hence controlled by, the mass flux. This demonstrates that, in the constant emission case, the footprint area of the conveyor belt does not run out of tracer, and hence confirms the hypothesis that in the initial condition case the full extent of boundary-layer ventilation is not realised due to the lack of tracer. This lack of tracer resulted in the anticyclones becoming depleted of tracer. This is not observed in the constant emission case as, although tracer is still mixed away from the surface by turbulence, and is transported horizontally by Ekman motions towards the cyclonic regions, the tracer source rapidly replenishes the deficit in the anticyclonic regions. This can be seen in Figure 5.9, which is the same as

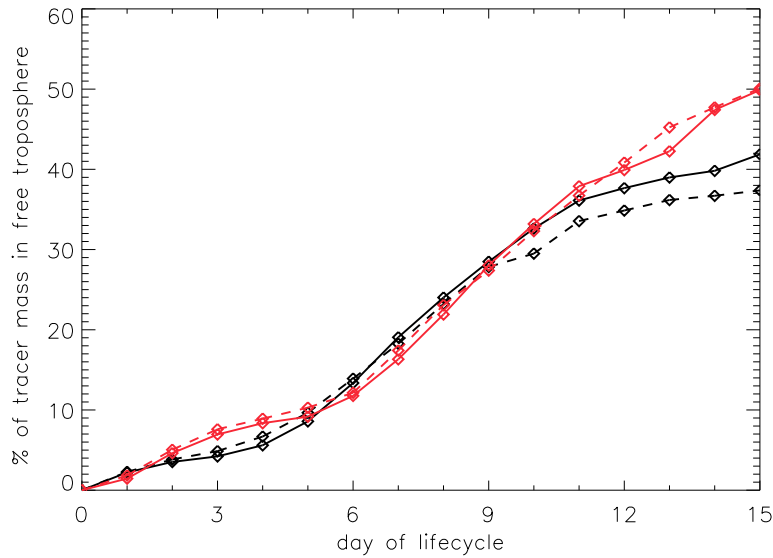


**Figure 5.10:** Percentage of domain total tracer mass that has been ventilated into the free troposphere as a function of life cycle day. Black lines shows LC1 and red lines LC2. Solid lines show T85 resolution and dashed lines T42 resolution.

Figure 5.2a, except for the constant tracer emission case. Additionally, Figure 5.9 shows that during the early stages of the life cycle when synoptic ascent is weak there is a slight accumulation of tracer near the surface in the cyclonic regions. This occurs as the boundary layer is shallow and there is very limited transport across the boundary-layer inversion at this stage in the cyclone. The results from the two different experiments do not differ significantly; in both experiments the same physical processes act and tracer is ventilated out of the boundary layer in the same locations.

## 5.5 Tracer budgets

Tracer budgets have been calculated to quantify the strength of boundary-layer ventilation. The mass of tracer in the free troposphere for the initial condition tracer case is plotted as a percentage of the total mass of tracer in the whole domain at both horizontal resolutions (T42 and T85) in Figure 5.10. The first 4 days sees very little ventilation into the free troposphere due to limited synoptic activity. By day 5 both life cycles have transported  $\sim 10\%$  of the tracer into the free troposphere, by day 9 this value is  $\sim 28\%$ , and by day 15 this is  $\sim 40\%$ . This illustrates that the amount of boundary-layer ventilation is very similar for cyclones which exhibit considerably different frontal features. However, it should be

noted that the actual percentage of tracer in the free troposphere is not a particularly meaningful number, as it depends on the experimental design through the domain size and method of tracer initialisation. For example, in these experiments very little tracer is ventilated in the north and south of the domain, away from the storm track region. More relevant is the boundary-layer ventilation rate which can be found by calculating either the rate of increase of tracer mass in the free troposphere or the rate of decrease of tracer mass in the boundary layer. The gradients of the lines plotted in Figure 5.10 are directly proportional, but not equal to, the rate of change of tracer mass in the free troposphere. The boundary-layer ventilation rate of LC2 is greater than that of LC1 between days one and three. The opposite is true between days three and six, when LC1 has a stronger cold front and WCB than LC2. However, between days six and ten the boundary-layer ventilation rate is similar for both life cycles. After 12 days of development the rate of ventilation by LC1 has decrease significantly, but this is not true for LC2. This is because LC1 has begun to decay by day 12, whereas LC2 continues to wrap up cyclonically and begins to resemble a barotropic vortex. Figure 5.10 also shows that the amount of tracer ventilated into the free troposphere is largely independent of horizontal resolution. However, by increasing the horizontal resolution the rate of ventilation by LC1 between days 5 and 9 is slightly increased.

## 5.6 Transport in the free troposphere

To visualise tracer transport by the WCB, tracer concentrations from the initial condition experiment have been plotted on a range of isentropic surfaces from 280 K to 310 K. As the experiments conducted here are dry, it is expected that above the boundary layer there will be little or no cross-isentropic motions.

For LC1 on the cooler and lower isentropic surfaces the tracer is advected cyclonically around the poleward side of the low centre. On warmer and higher surfaces the tracer is advected anticyclonically, over-running the warm front and travelling eastward over the downstream anticyclone (not shown). On intermediate surfaces, e.g. 295 K as shown in Figure 5.11a, both transport paths are observed. The resulting tracer distribution resembles the hammerhead shape of the ascending airstreams shown in Figure 3.5. In LC2 different behaviour is observed (Figure 5.11b). On all considered isentropic surfaces the tracer was found to follow a cyclonic path, with no tracer travelling anticyclonically

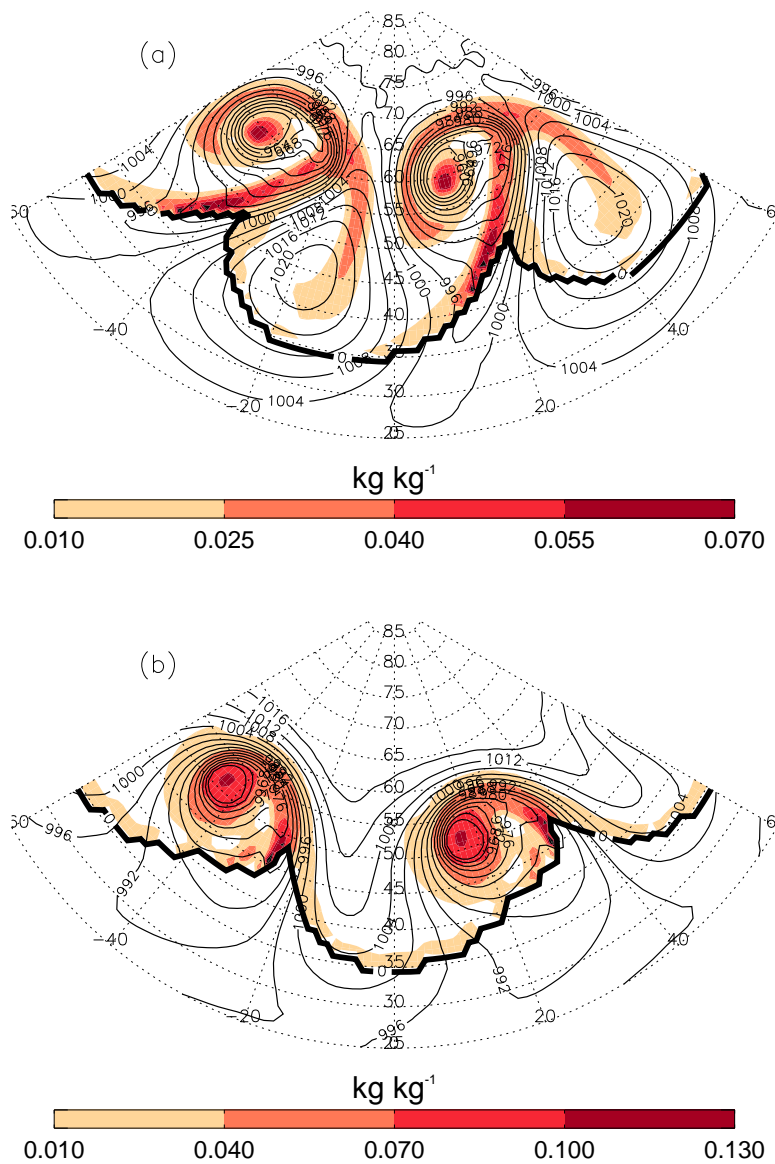


**Figure 5.11:** Initial condition tracer concentration after 7 days on the 295 K isentropic surface for (a) LC1 and (b) LC2. Thin contours are surface pressure (4 mb interval) and the thick contour shows where the isentropic surface intersects the surface. Note different colour scales.

ahead of the surface warm front. This is due to the well documented cyclonic nature of LC2 (Thorncroft and Hoskins, 1990; Thorncroft *et al.*, 1993) and the stronger warm frontogenesis in LC2 compared to LC1. On cooler isentropic surfaces (not shown) no tracer transport due to a CCB existed, and it is concluded that the CCB has very limited potential for boundary-layer ventilation or transporting tracer long distances in the free troposphere.

Figure 5.12 shows the tracer distribution for the initial condition tracer in three dimensions in the well developed stage of both life cycles. In LC1 tracer has been transported vertically in two peaks. The easterly peak reaches 5.5 km and is due to the main branch of the WCB which ascends and travels anticyclonically. This anticyclonic branch then descends once the WCB has travelled eastward over the anticyclonic region. The large-scale descent causes tracer, which was initially lofted away from the surface by the WCB, to descend. This demonstrates that pollution removed from the boundary layer can be returned to low levels large distances away from where it was originally ventilated into the free troposphere. The second branch of the WCB does not extend as high, ascending only to 4.5 km, and is due to the cyclonic WCB branch. The two peaks are connected to each other, the WCB is initially one airstream at southern latitudes, but the cyclonic branch peels off the lower edge and travels rearwards once the WCB ascends and moves polewards. In LC2 tracer has only been transported in one airstream; there are not two distinct peaks as was observed in LC1. LC2 transports the tracer to 6 km, around the poleward and rearward edges of the low pressure centre. This is due to the strong cyclonic nature of LC2 and shows the WCB is predominately following a cyclonic path. Tracer is transported almost 1 km higher in LC2 than in LC1, but the mechanism, the WCB which is responsible for the vertical transport, is the same. This shows that tracer can be lofted considerable distances (4 - 6 km) vertically into the troposphere in two separate longitude bands, which at upper levels can be separated by up to 25° longitude. Thus in different cyclones the WCB will deliver ventilated tracer to different regions of the free troposphere. However, these regions are to some degree predictable, and the structure of the WCB is strongly related to the dynamical aspects of the extra-tropical cyclone, and the background conditions in which it develops.

Polvani and Esler (2007) in their paper on transport and mixing in idealised life cycles have also produced three dimensional plots of their boundary layer tracer distributions (their Figure 13). When Figure 5.12 here is compared to their figures 13 and 14 it can be

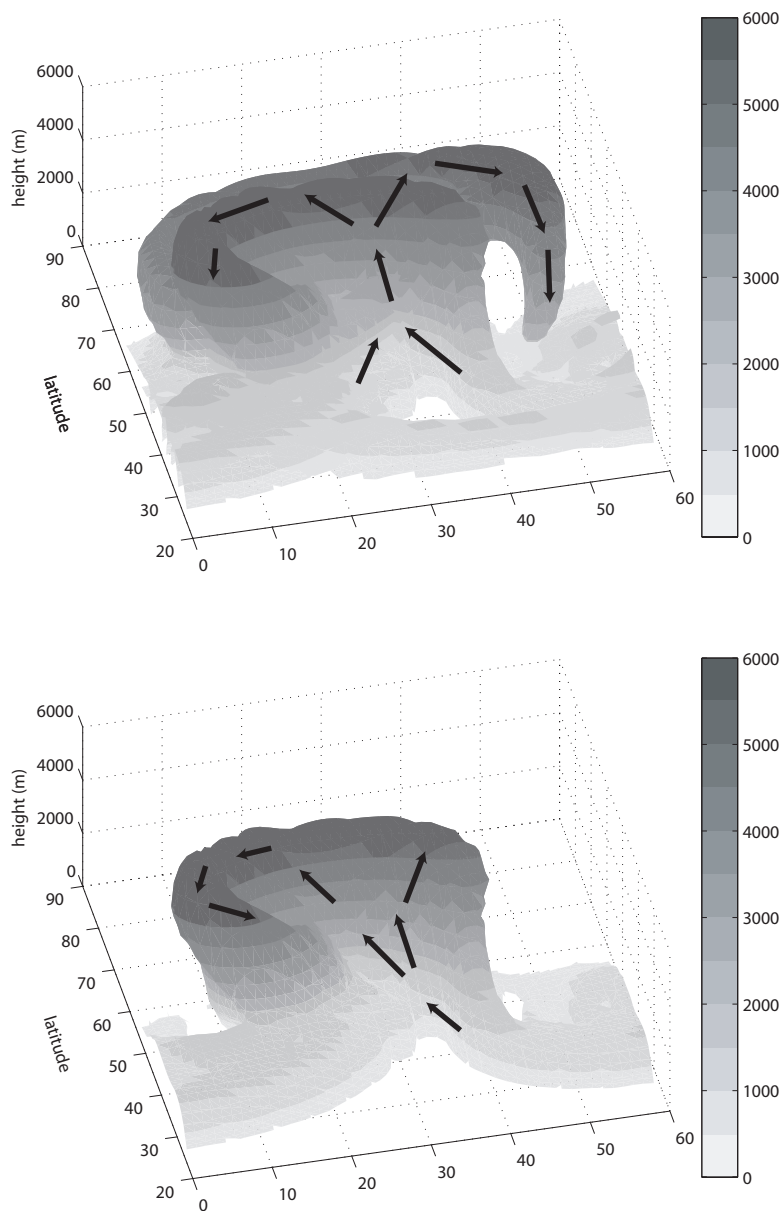


**Figure 5.12:** Surface of the  $0.02 \text{ kg kg}^{-1}$  tracer concentration for the initial condition tracer after 7 days for (a) LC1 and (b) LC2. Grey scale shading denotes the height of the surface. Black arrows schematically show the main airflows.

seen that the tracer distributions within the free troposphere are very similar. However differences exist at low levels. In Polvani and Esler (2007) there is no boundary layer parameterisation scheme so within the “boundary layer” there is an uniform distribution of tracer. In the results presented here there is considerable variability in the tracer distribution within the boundary layer; within the anticyclonic regions there is very little tracer remaining as the turbulence and Ekman motions have transported it towards the cyclonic regions. This comparison shows that the inclusion of a boundary layer parameterisation scheme has a significant effect on the resulting distribution of tracer within the boundary layer but not within the free troposphere.

The transport paths that the tracer follows in the free troposphere in the case of a constant tracer source (not shown) are similar to those found for the initial condition tracer experiment, but some subtle differences exist. Tracer is found higher in the domain; both branches of the tracer in the WCB in LC1 were observed to extend a further  $\sim 2$  km in the vertical compared to the initial condition tracer experiment, as now the full extent of the WCB has been realised. Additionally, the anticyclonic regions are no longer depleted of tracer as the constant tracer source maintains strong near surface tracer concentrations. However, even with the presence of a tracer source, the ridges of high pressure may still be well ventilated if the average flux of tracer out of the boundary layer exceeds the flux of the source into the boundary layer.

## 5.7 Discussion and conclusions

The objectives of this chapter were to develop a conceptual model of boundary-layer ventilation and to identify the processes that act to ventilate pollution out of the boundary layer. This has been achieved by using the IGCM to simulate two contrasting baroclinic life cycles, LC1 and LC2, with a boundary-layer parameterisation scheme acting and a passive tracer included to represent pollutants.

Three distinct physical processes, which cover a large range of spatial and temporal scales, have been found to contribute to the ventilation of the boundary layer during both baroclinic life cycles. These processes are boundary-layer turbulent mixing, horizontal Ekman convergence and divergence within the boundary layer, and advection by the WCB. The vertical mixing of tracer within the boundary layer was shown to be determined by the depth and stability of the boundary layer, both of which have been shown in Chapter 4 to

be driven by synoptic-scale motions. Horizontal variations in the boundary-layer structure lead to highly non-uniform surface tracer concentrations, even during the early stages of the life cycles. The large-scale dynamics, combined with surface friction, were found to induce Ekman convergence and divergence, which causes horizontal advection of the tracer within the boundary layer. Turbulent mixing is essential for boundary-layer ventilation as it mixes tracer to levels penetrated by conveyor belts and where the horizontal Ekman motions are stronger. The Ekman horizontal motions act to enhance the ventilation rate, by supplying tracer into the source region of the WCB. Therefore, turbulent mixing and horizontal advection within the boundary layer potentially can affect how much tracer can be removed from the boundary layer by the WCB.

The results presented in this chapter have confirmed WCBs to be the dominant advective transport mechanism for boundary-layer ventilation and transport in the free troposphere. The cold conveyor belt was identified during the early stages of LC2 but had limited ascent associated with it, and was found to be unimportant in both boundary-layer ventilation and transport within the free troposphere in these dry simulations. Moist processes are likely to produce much stronger ascent and CCBs may contribute to boundary-layer ventilation in moist LC2 type cyclones.

LC1 was found to ventilate 42% of tracer out of the boundary layer in the initial condition case, and LC2 50%, after 15 days of integration. The mass of tracer transported into the free troposphere in LC1 and LC2 is remarkably similar (up until day 12) given the differences in the synoptic evolution of the cyclones. The strength of the ascent in the WCB is one control on the amount of boundary-layer ventilation. The quasi-geostrophic omega equation could be used to determine, to a first order, what governs the magnitude of the large-scale vertical velocity. Written in the ‘VATA’ form (Hoskins, 1997) the total forcing is separated into a Vorticity Advection forcing term and a Thermal Advection forcing term. The thermal advection forcing term represents the rate of thermal advection by the geostrophic wind, and is proportional to the horizontal temperature gradient. In LC1 and LC2 the initial meridional temperature gradient is the same and therefore, assuming that the thermal advection term dominates at low levels (Petterssen and Smebye, 1977), the ascent rate, and ventilation, can be expected to be similar. This suggests that the amount of boundary-layer ventilation can be related to the large-scale baroclinicity, and therefore can be similar for cyclones with different frontal structures.

Both life cycles have a non-negligible tracer flux out of the boundary layer for at

least 4 days, demonstrating that the WCB remains in contact with the boundary layer for this length of time. This is longer than the typical WCB timescale of two days reported by Eckhardt *et al.* (2004). During this period both cyclones travel a considerable distance, up to  $40^\circ$  longitude, allowing for a large swath of longitudes to be ventilated by the WCB ( $40^\circ$  longitude is approximately equal to half the length of the North Atlantic storm track). The footprint of the WCB increases in the meridional but not zonal direction as the cyclone intensifies, allowing a large range of latitudes (between  $35^\circ\text{N}$  and  $65^\circ\text{N}$ ) to be ventilated. The southerly bound compares well with previous studies; Li *et al.* (2005) find WCBs along the Eastern seaboard to originate from north of  $30^\circ\text{N}$ , and in a case study Agustí-Panareda *et al.* (2005) found that tracer was ventilated from the boundary layer between  $40^\circ$  and  $50^\circ\text{N}$ . The ventilation regions found here extend further north than in previous case studies, suggesting that weak boundary-layer ventilation is possible further north than previously expected. In the vertical, both life cycles were found to transport tracer to 6 km, but LC1 was found to transport the tracer in two distinct peaks which are separated by approximately  $25^\circ$  longitude at 4 km. This has important consequences for the chemical composition of the mid-troposphere. In the zonal direction narrow bands of elevated pollutant concentration separated by clean regions may exist along the storm track. Strong low-level horizontal gradients in pollutant concentration also exist in the storm track, due to both transport within the boundary layer and ventilation by the WCB. The altitudes to which the WCBs were found to ascend to may be lower than would be observed if moisture were included in the simulations. With moisture present the ascent would no longer be confined to be along isentropic surfaces and latent heating due to condensation would act to enhance ascent rates. Thus, it is hypothesised that if moisture was included the WCBs may extend a further  $\sim 2$  km in the vertical.

While there may be little difference in the amount of boundary-layer ventilation between the two life cycles, there are notable differences in the locations. The region of maximum ventilation is further north in LC2 than in LC1, despite the low pressure centre tracking considerably further poleward in LC1. The difference in the synoptic evolution is driven by the background state in which the perturbations develop. Therefore, this suggests that the type of background flow (cyclonically or anticyclonally sheared) can alter the boundary-layer locations that are ventilated by the resulting cyclones.

## 5.8 Summary

This chapter has identified how tracers are transported in both the boundary layer and free troposphere. Transport by boundary-layer processes has been identified to be important in controlling the low-level tracer distributions, and potentially the amount of ventilation out of the boundary-layer. The strength of the baroclinicity has also been highlighted as one possible control on the amount of boundary-layer ventilation since both LC1 and LC2 were found to be almost equally efficient at ventilating the boundary layer. It currently remains un-proven which variables control the amount of ventilation; either the boundary layer processes which act to supply the source region of the warm conveyor belt, or the strength of the warm conveyor belts. This will be addressed in Chapter 6.

---

## CHAPTER SIX

# Factors controlling ventilation

---

### 6.1 Introduction

The physical processes acting to ventilate the boundary layer were identified in Chapter 5 to be:

1. vertical turbulent mixing within the boundary layer,
2. horizontal convergence and divergence within the boundary layer, induced by surface friction and large-scale dynamics,
3. large-scale advection by the warm conveyor belt.

In this Chapter the controls on the amount of ventilation are identified. In Chapter 5 it was hypothesised that the ascent associated with the warm conveyor belt is one control on the amount of boundary-layer ventilation, but it was also noted how important the boundary-layer transport processes were in the overall ventilation process. Specifically, it was identified that the horizontal transport by convergence and divergence within the boundary layer may act to enhance the amount of ventilation by increasing the rate at which tracer is supplied to the source region of the warm conveyor belt. Therefore, in this Chapter experiments are designed to test the importance of these two processes, and to identify which one acts as the limiting step in the amount of boundary-layer ventilation. To do this two sets of experiments are conducted: one which alters the amount of surface friction and therefore the strength of the convergence and divergence within the boundary layer, and a second which alters the large-scale dynamics and therefore the strength of

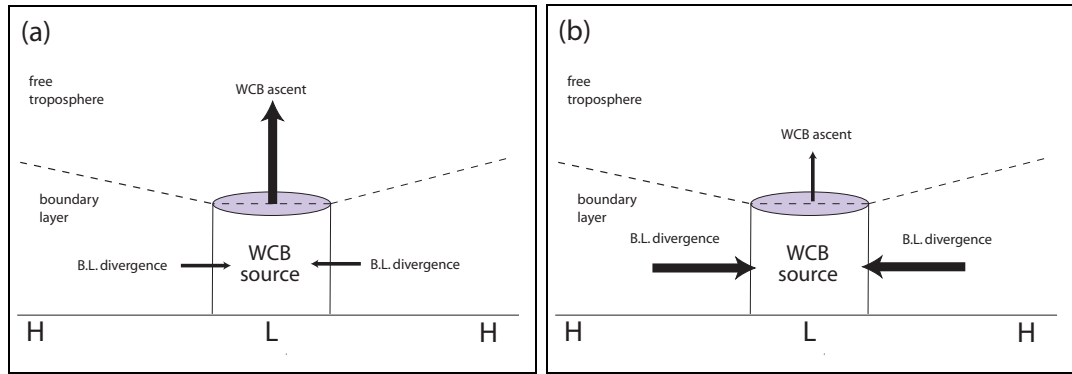


**Figure 6.1:** Schematics showing different ventilation regimes. Size of black arrows indicates the magnitude of the tracer flux. (a) The flux out of the boundary layer by the warm conveyor belt exceeds the flux into the warm conveyor belt source region by the horizontal divergence. (b) The flux out of the boundary layer by the warm conveyor belt is less than the flux into the warm conveyor belt source region by the horizontal divergence. L represents a region of low pressure and H a region of high pressure. Dashed line indicates the boundary-layer depth.

ascent associated with the warm conveyor belt. Two possible ventilation regimes exist. The first (Figure 6.1a) is that the transport by the horizontal divergence and convergence within the boundary layer acts as the limiting factor in the amount of ventilation. In this regime the flux of tracer out of the boundary layer by the warm conveyor belt exceeds the flux into the source regions. This means that the warm conveyor belt source region becomes depleted of tracer and the full ventilation potential of the cyclone will not be fulfilled. The second regime (Figure 6.1b) is the direct opposite; the strength of the warm conveyor belt acts as the constraint on the amount of ventilation. In this regime the flux of tracer into the source region of the boundary layer exceeds the flux out of the boundary layer by the warm conveyor belt, meaning that there will always be tracer available in the source region of the warm conveyor belt for venting. The experiments conducted here aim to identify which regime exists in typical mid-latitude weather systems.

Although the IGCM was used to model LC1 and LC2, and the transport of tracers associated with these two life cycles, it was decided to tackle the questions posed above using the Met Office Unified Model (U.M.) in an idealised configuration. A description of the idealised U.M. was given in section 2.5 and an overview of the control baroclinic life cycle simulated using the U.M. was presented in section 3.3. The dynamical structure of the control life cycle simulated in the U.M. was compared to the IGCM life cycles in section 3.4, and it was shown that the life cycles are dynamically similar. However, some differences were found to exist between the U.M. control cyclone and LC1. The

U.M cyclone was found to develop slower, be more cyclonic and to experience less meridional displacement than LC1. These differences were accounted for by considering the geometrical differences between the two numerical models.

The U.M. has been used to simulate the life cycles analysed in this Chapter for three main reasons. Firstly, as the U.M. includes a complex and thoroughly evaluated convection scheme the dry experiments performed here could provide a foundation for a possible future comparison with a moist life cycle. This would not be possible with the IGCM as the convection scheme in the IGCM is a considerably simplified version of the Betts Miller convective adjustment scheme (Betts, 1986) which cannot act upon tracers, and hence would not permit such a comparison study. Secondly, using an operational model, such as the U.M., to simulate numerous life cycles would allow future case studies to be compared to the idealised experiments without having to account for differences in numerical models. The final motivation for using the U.M. is that it allows the robustness of the results obtained in the IGCM to be investigated and any dependence on the numerical model to be quantified.

The structure of this Chapter is as follows. Firstly, in section 6.2 the boundary-layer structure that develops beneath the U.M. control life cycle is examined and compared to the boundary-layer structures found in the IGCM. In section 6.3 the effect of the source strength on the amount of ventilation is discussed briefly. In section 6.4 the effect of the boundary-layer structure and the boundary-layer transport processes on the overall ventilation characteristics is investigated. The effect of the large-scale dynamics on the amount of ventilation is discussed in section 6.5 and finally a summary of the results obtained in this chapter is given in section 6.6.

## 6.2 Boundary-layer structure in the control U.M. cyclone

Figure 6.2 shows the spatial patterns of three boundary-layer variables after eight and twelve days of the control U.M. cyclone. Very similar boundary layers develop beneath the U.M. cyclone as were observed in LC1 and LC2 in the IGCM. Figures 6.2a and 6.2b show the surface heat flux after eight and twelve days. As was the case in the IGCM simulations (Figures 4.2c and 4.2d) the largest positive values of the heat flux are found in the area of northerly winds on the eastern edge of the anticyclone and the most negative values are found in the warm sector. Additionally, the magnitude of the heat flux increases

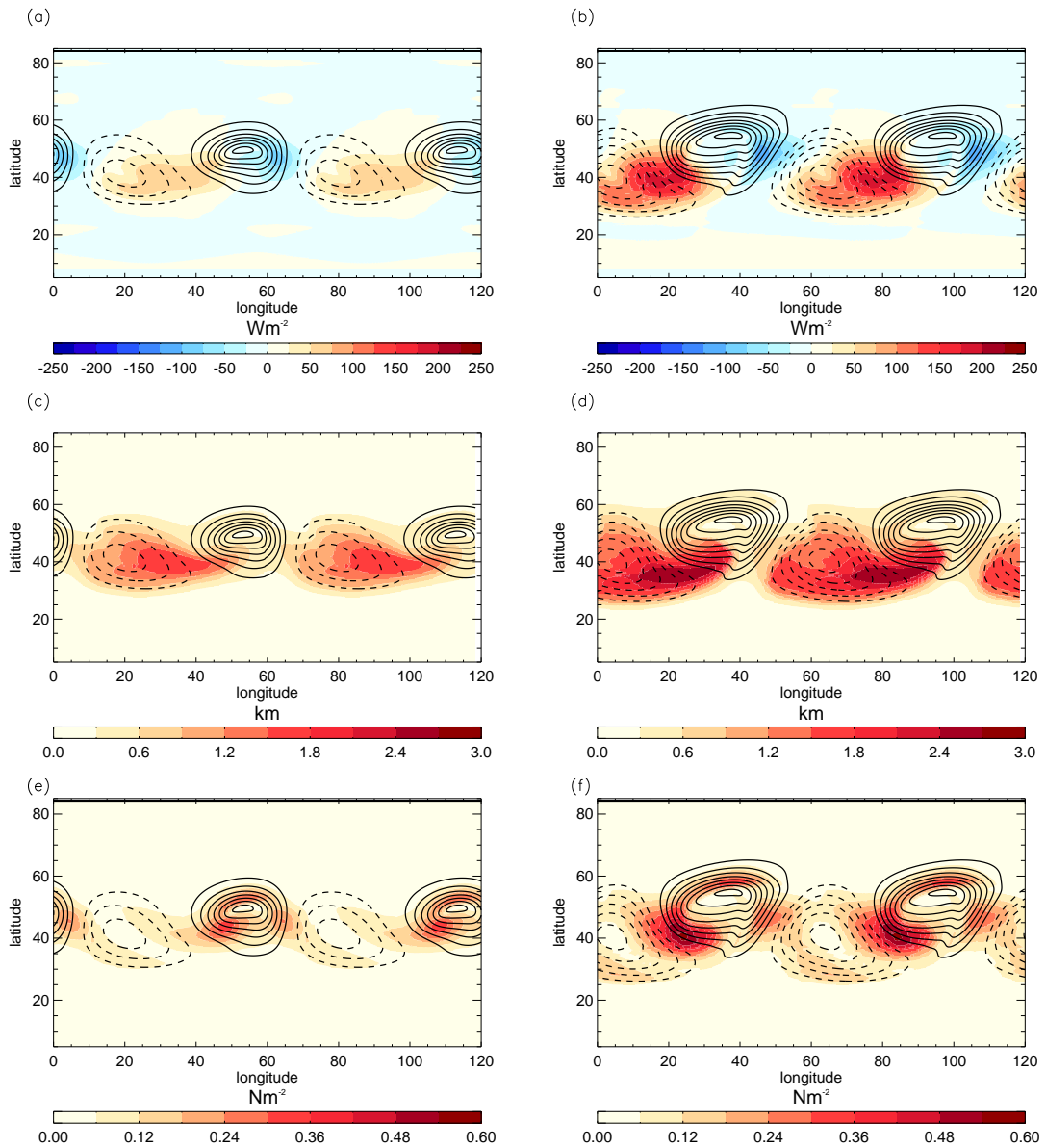


**Figure 6.2:** (a) Surface heat flux after 8 days and (b) 12 days. (c) Boundary-layer depth after 8 days and (d) 12 days. (e) Surface momentum flux after 8 days and (f) 12 days. Contours drawn every 4 mb show surface pressure. Solid lines represent pressures less than 1000 mb and dashed lines pressures greater than 1000 mb. The 1000 mb contour is omitted for clarity. Note that two domains are plotted next to each other here, and in all Figures in this chapter, so that features can be seen clearly, rather than wrapped around the boundary.

with time, again as was the case in the IGCM. The magnitude of the heat fluxes is greater in the U.M. compared to the IGCM; by the mature stage of the U.M. control life cycle the largest heat fluxes are typically  $180 \text{ W m}^{-2}$ , compared to  $85 \text{ W m}^{-2}$  in the IGCM, and the minimum heat fluxes are typically  $-100 \text{ W m}^{-2}$  in the U.M. compared to  $-10 \text{ W m}^{-2}$  in the IGCM. This is because the surface is rougher (higher  $z_{0m}$  values) in the U.M. compared to the IGCM. This results in larger drag coefficients values for both momentum ( $C_d$ ) and heat ( $C_h$ ), and hence larger turbulent fluxes.

Boundary-layer depth has been calculated for the U.M. simulations using the same method as was applied to the life cycle simulated in the IGCM, (described in section 2.8.1). It was decided to use the exact same method to diagnose boundary-layer depth to allow for more accurate comparisons to be made, despite the U.M. providing its own boundary-layer depth diagnostic. The U.M. boundary-layer depth diagnostic is calculated online using a very similar parcel ascent / critical Richardson number method to that used here. However, there is limited interpolation between model levels, especially in the case of stable boundary layers, which means that often the U.M. boundary-layer depth is diagnosed on a model level and the resulting distribution can exhibit a “saw-tooth” type pattern as the diagnostic flips between one model level and the next at alternate grid points. The boundary-layer depth after eight and twelve days, calculated using the method described in section 2.8.1, is shown in Figures 6.2c and 6.2d respectively. The deepest boundary layers are found in regions where the heat fluxes were largest, and shallowest in the warm sector where there were negative heat fluxes, which agrees well with the IGCM results (Figure 4.4a). The maximum diagnosed boundary-layer depth in the U.M. cyclone and LC1 in the IGCM are very similar, at almost 3 km.

Figures 6.2e and 6.2f show the surface momentum flux after eight and twelve days. After eight days the largest values are to the south-west of the low pressure centre. However, local maxima are also evident in the warm sector and also in the region of the bent-back warm front to the north of the low pressure centre. A similar pattern remains at day twelve but the magnitudes have increased; the maximum value in the south-western region of the low pressure is now  $0.56 \text{ N m}^{-2}$  compared to  $0.35 \text{ N m}^{-2}$  four days previously. Again this spatial pattern is in good agreement with that observed in the IGCM cyclones (Figure 4.3) but the maximum value of the surface stress was found to be slightly larger in the IGCM simulation, where a value of  $0.8 \text{ Nm}^{-2}$  was found after 7 days.

In summary, the spatial patterns of the surface fluxes and boundary-layer depth

that develop beneath the control U.M. life cycle are similar to those observed to develop beneath the IGCM cyclones. This adds further confidence in the results presented in Chapter 4.

### 6.3 Ventilation dependence on source strength

Clearly the rate at which tracers are emitted into the domain from the surface will have a large impact on the amount of tracer ventilated out of the boundary layer and also on the resulting tracer concentrations throughout the whole domain. The tracer concentrations are directly proportional to the source strength; for example if the source increased by a factor of ten, then the concentrations in the whole domain would increase by the same factor. This can be shown by considering the tracer equation

$$\frac{DC}{Dt} + \nabla \cdot F = 0, \quad (6.1)$$

where  $C$  is the tracer concentration and  $\nabla \cdot F$  is the divergence of the turbulence fluxes of tracer. The right hand side equals zero as no sources or sinks of tracers exist within the domain, and at the beginning of the simulation the tracer concentration is equal to zero throughout the whole domain. The only source of tracer is at the surface and can therefore be considered as a boundary condition:

$$F = F_s \quad \text{at } z = 0. \quad (6.2)$$

Equation 6.1 can be normalised by the emission strength,  $F_s$ , to give

$$\frac{D\hat{C}}{Dt} + \nabla \cdot \hat{F} = 0 \quad (6.3)$$

where  $\hat{C} = C/F_s$  and  $\hat{F}$  is the normalised emission strength given by  $\hat{F} = F/F_s$ , which at  $z = 0$  equals 1. This then allows the actual concentration,  $C$ , to be written as  $C = F_s \times \hat{C}$ , which demonstrates that the magnitude of the tracer concentration is controlled by the emission strength,  $F_s$ , while the spatial distribution of the tracer is controlled by  $\hat{C}$ . Therefore, doubling the emission strength will double the tracer concentrations throughout the whole domain. This has been verified in the U.M. by performing experiments with different source strengths. The source strength that has been used in all of the experiments presented here is  $1 \times 10^{-4} \text{ kg m}^{-2} \text{ s}^{-1}$ .

## 6.4 Ventilation dependence on boundary layer transport processes

This section describes the experiments that were performed to investigate the importance of the boundary-layer transport processes, turbulent mixing and horizontal Ekman transport, on the overall amount of ventilation.

### 6.4.1 Motivation for the selected experiments

The presence of a boundary layer due to surface friction, will have an effect on the strength of the vertical velocity in the lower part of the troposphere. By adding friction, two competing effects develop. Firstly friction acts to spin down the cyclone, resulting in slower development and weaker systems, and hence weaker vertical velocities. The second effect is due to Ekman pumping. By adding friction, the wind is deflected further away from the geostrophic direction. In cyclonic regions this results in enhanced convergence, and hence by continuity, stronger vertical motion out of the boundary layer. In this thesis the effect of surface drag on the amount of ventilation is investigated by changing the surface drag coefficient,  $C_d$ . In the control experiment, as described in section 3.3, the drag coefficient varies spatially and temporally as the boundary-layer scheme calculates the drag coefficient as a function of stability at each individual grid point. However, in the sensitivity experiments the drag coefficient was held fixed in time and uniform across the domain. The drag coefficient for heat,  $C_h$ , and the eddy diffusivities for momentum,  $K_m$  and heat,  $K_h$  are all still calculated using the full boundary-layer scheme, and therefore vary spatially and with time.

Three of the five drag coefficient values used here were selected to be the same as values used in a previous study by Hines and Mechoso (1993), who investigated the influence of surface drag on frontal structures. This allows the dynamical response of the fronts to the presence of drag in the idealised U.M. to be compared directly to the results of Hines and Mechoso (1993). The values of the drag coefficient used by Hines and Mechoso (1993) were zero (no drag),  $0.56 \times 10^{-3}$  (typical of an ocean surface) and  $2 \times 10^{-3}$  (typical of a land surface), and were constant in time. Here five experiments with different drag coefficients are conducted. Firstly, the Hines and Mechoso (1993) no drag experiment was replicated. However, instead of  $C_d = 0$  the experiment referred to here as no drag has an initial drag coefficient of  $1 \times 10^{-8}$ , and subsequent values are  $1 \times 10^{-8} \times C_{d\text{prev}}$  where  $C_{d\text{prev}}$

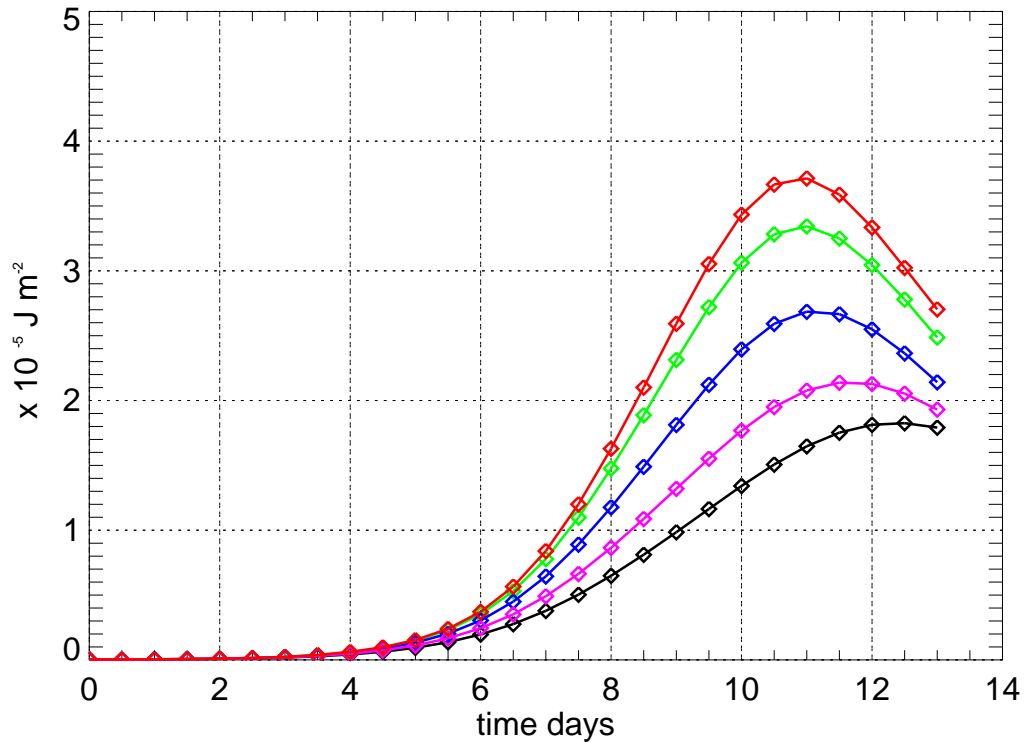


**Figure 6.3:** Domain-averaged eddy kinetic energy. Red:  $C_d = 0$ , green:  $C_d = 0.1 \times 10^{-3}$ , blue:  $C_d = 0.56 \times 10^{-3}$ , purple:  $C_d = 2 \times 10^{-3}$ , and black:  $C_d = 5 \times 10^{-3}$ .

is the drag coefficient value at the previous timestep. This method was used to get drag coefficients as near to zero as possible, without equalling zero as the numerics of the U.M. boundary-layer scheme will not permit  $C_d = 0$ . The ocean and land drag experiments in this thesis have exactly the same drag coefficient values as the corresponding experiments in the Hines and Mechoso (1993) study. Two additional experiments have been conducted here; one which represents a very smooth surface with a drag coefficient of  $0.1 \times 10^{-3}$  and another with a drag coefficient value of  $5 \times 10^{-3}$ , which is referred to as rough land. The smooth ( $C_d = 0.1 \times 10^{-3}$ ) experiment was included to help relate the results of the no drag experiment to the others; without this additional experiment there is a large range of unexplored parameter space. The rough land experiment was included as it is suggested by Stull (1988) that values of  $C_d$  vary between  $1 \times 10^{-3}$  and  $5 \times 10^{-3}$ , and Arya (1999) notes that over land values of  $C_d$  can vary between zero and  $1 \times 10^{-2}$ .

### 6.4.2 Effect of surface drag on life cycle dynamics and boundary-layer structure

The first effect of increased surface drag on the resulting life cycles is to decrease the growth rate and reduce the eddy kinetic energy. This can be seen in Figure 6.3 which shows the eddy kinetic energy for all five drag experiments. There is a day and a half lag in the peak eddy kinetic energy between the experiment with no drag and the rough land drag experiment. Additionally, the peak eddy kinetic energy value that is reached in the rough land drag experiment is 50% less than in the no drag case. The eddy kinetic energy of the control life cycle (Figure 3.10) is similar to that of the ocean drag experiment, in terms of the magnitude and time evolution. The frontal evolution is observed to change with increasing drag, which is shown in terms of potential temperature and vorticity at 1 km in Figure 6.4. 1 km was selected to analyse the frontal structure at, as at this level the fronts are strongest and the frontolytical effects of turbulent mixing are minimised. With no drag there is an exceptionally strong warm front and a strong cold front evident as indicated by the strong temperature gradients and high values of cyclonic vorticity shown in Figures 6.4a and 6.4b respectively. In the ocean and land drag experiments the cold fronts have similar temperature gradients associated with them (Figures 6.4c and 6.4e) but the vorticity is slightly reduced in the case of land drag (Figure 6.4f) compared to ocean drag (Figure 6.4d). In the ocean drag experiment there is an additional strong temperature gradient to the east of the low centre indicating a warm front, and to the west of the low centre is a very strong bent-back warm front indicated by large vorticity values and a strong temperature gradient. In contrast, the land drag case has a significantly weaker bent-back warm front. In the rough land experiment (Figures 6.4g and 6.4h) both fronts are much weaker than in any of the other simulations. These findings, that the warm front is much more sensitive to surface drag than the cold front, agree well with the results of Hines and Mechoso (1993) who came to the same conclusion. The asymmetry in the effect of drag on the warm and cold front is explained by Hines and Mechoso (1993) in terms of how surface drag alters the wind speed and therefore the strength of thermal advection in the frontal regions. In the warm sector, there is an ageostrophic wind component directed towards the low pressure. In the no drag case, the resulting acceleration causes the formation of a low level jet directed towards the warm front, which acts to intensify the front by pushing the potential temperature contours closer together. In the cases with drag, the additional ageostrophic acceleration is balanced by frictional

effects and hence the winds (and therefore the strength of the thermal advection) in the warm sector are much weaker when drag is acting. The cold front is found to be less sensitive to drag as behind the cold front the ageostrophic winds are very weak, and as a result the ageostrophic wind speed in this region does not change as significantly with drag.

The boundary-layer structure is found to vary with the magnitude of surface drag. In the case of smooth drag the cyclone becomes intense and has strong low-level winds. This affects the surface heat fluxes (Figure 6.5a), which are proportional to wind speed. This results in large positive heat fluxes in the region of northerly winds on the eastern edge of the anticyclone which exceed  $250 \text{ W m}^{-2}$ . In the land drag experiment (Figure 6.5b), the surface friction acts to reduce the near surface winds and therefore the heat fluxes on the eastern edge of the anticyclone are smaller, typically  $150 \text{ W m}^{-2}$ . The magnitude of the heat fluxes in the warm sector does not vary significantly with drag. This is due to two competing processes; with less drag there are stronger winds (which act to increase the surface heat flux) but the strong low level winds lead to strong warm advection northwards in the warm sector over much cooler surfaces. This creates very large potential temperature gradients near the surface, which acts to suppress any turbulent motions and therefore decreases the heat flux. When the boundary-layer depth is considered for different values of surface drag (Figures 6.5c and 6.5d) it is evident that decreasing the surface drag increases the depth of the convective boundary layer in the anticyclonic region but decreases the depth of the stable boundary layer in the warm sector. The increase in the anticyclonic region is due to the larger heat fluxes found in this region in the smooth drag experiment compared to the land drag experiment. The decrease in boundary-layer depth in the warm sector is because with little surface friction there is little shear driven turbulence. This is illustrated when the surface momentum fluxes are considered. In the smooth drag experiment there are very small momentum fluxes with local maxima behind the cold front and in the warm sector. A similar pattern is found in the land drag case but the magnitudes are much greater and high fluxes are also observed in the warm front region.

In the no drag experiment the boundary-layer structure that develops is somewhat different to the other experiments. Firstly, the surface momentum fluxes are found to be very small ( $\sim 1 \times 10^{-8} \text{ N m}^{-2}$ ) as they are directly proportional to the drag coefficient. Secondly, very strong, and somewhat un-physical, stratifications develop in the warm sector as a consequence of the very strong warm air advection and the very weak momentum

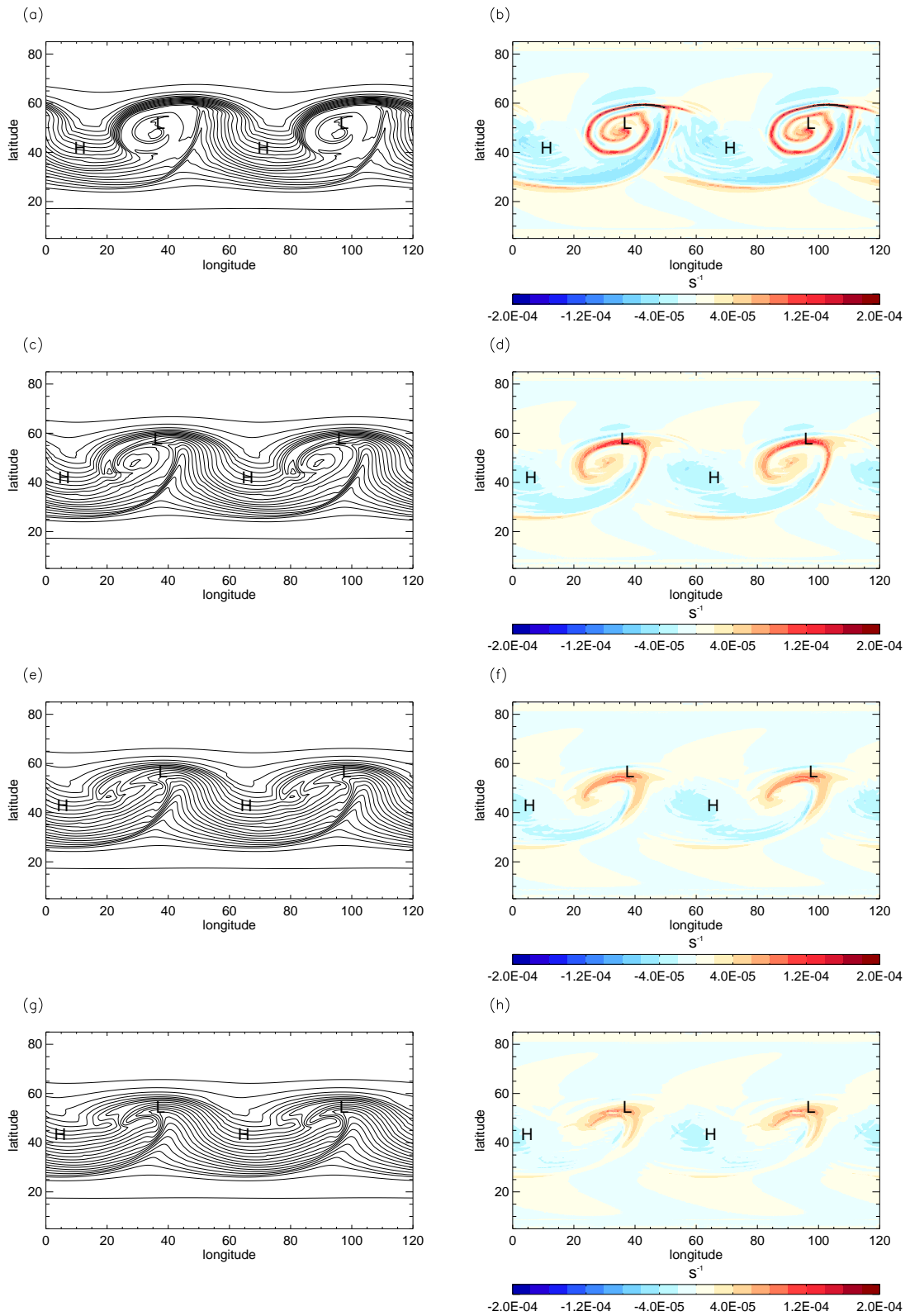


**Figure 6.4:** Potential temperature (contour interval 2 K) at 1 km after 12 days for (a)  $C_d = 0$ , (c)  $C_d = 0.56 \times 10^{-3}$ , (e)  $C_d = 2 \times 10^{-3}$ , (g)  $C_d = 5 \times 10^{-3}$ , and vorticity at 1 km for (b)  $C_d = 0$ , (d)  $C_d = 0.56 \times 10^{-3}$ , (f)  $C_d = 2 \times 10^{-3}$ , (h)  $C_d = 5 \times 10^{-3}$ . *L* marks the location of the minimum pressure and *H* the location of the maximum pressure.

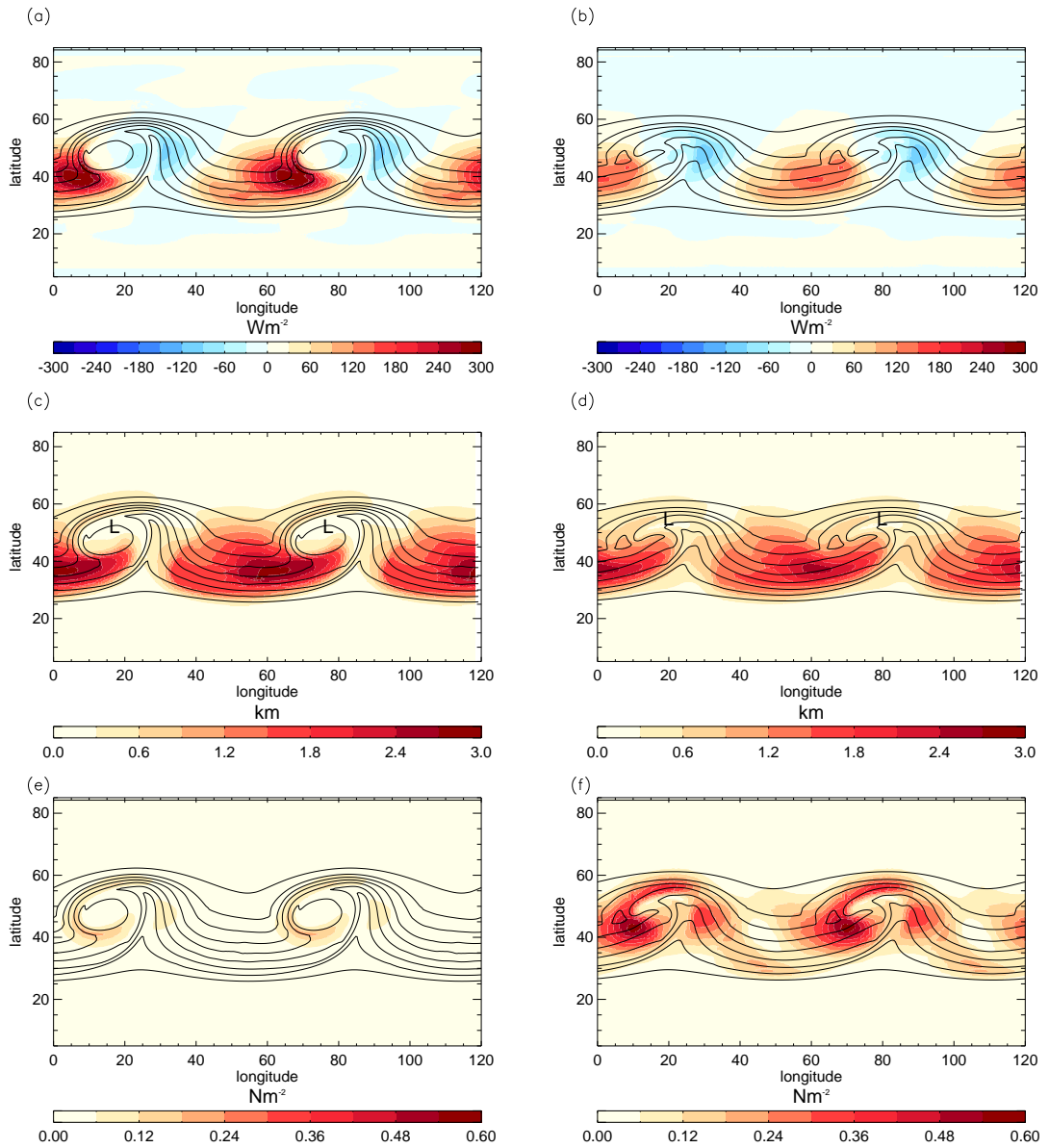


**Figure 6.5:** Boundary-layer characteristics after 10 days in the smooth drag and land drag experiments. Black contours are potential temperature at 1 km. Contour interval is 5 K. Surface heat flux in the (a) smooth drag experiment and (b) in the land drag experiment. Boundary-layer depth in the (c) smooth drag experiment and (d) in the land drag experiment. Surface momentum flux in the (e) smooth drag experiment and (f) in the land drag experiment.

fluxes. Thirdly, when the boundary-layer depth is diagnosed using the parcel ascent / Richardson number based method described in section 2.8.1 care must be taken as the method requires that a representative surface temperature is calculated (equation 2.74). The second term of this equation, which represents a temperature excess at the surface in unstable conditions, is inversely proportional to the friction velocity. As friction velocity is related to the drag coefficient, ( $u_*^2 = C_d U^2$ ), which is very small, the second term in equation 2.74 is un-physically large, which results in unrealistically deep boundary layers being diagnosed. To avoid this, a condition on the magnitude of the temperature excess is included; the maximum allowed value of the temperature excess is 5 K. The resulting boundary-layer depth in the anticyclonic region is very similar to that found in the smooth drag case, but shallower boundary layers are found in the warm sector in the no drag case compared to the smooth drag case.

### 6.4.3 Effect of surface drag on the spatial distribution of mass and tracer fluxes

The transport of both mass and tracer across the boundary-layer top has been studied for the five experiments with differing drag coefficients. The spatial distributions of the mass and tracer fluxes across the boundary-layer top are considered first. However, quantitative comparisons are easier if the total mass and tracer fluxes over the whole domain, or over the duration of each life cycle, are considered. Therefore, the integrated fluxes are discussed in section 6.4.4.

Before the spatial distributions of the mass fluxes are described, a brief review of the structure of the warm conveyor belt is presented to aid the understanding of the processes responsible for transporting mass out of the boundary layer. Figure 6.6 shows the vertical motions in the vicinity of a cold front, which together comprise the warm conveyor belt. Firstly, there is a low-level jet ahead of the cold front which is travelling northwards in the warm sector. As this approaches the surface cold front, it experiences a burst of strong ascent due to line convection on the warm side of the front. This narrow plume of ascent was documented by Keyser and Anthes (1982) and was found to develop due to convergence within the boundary layer. Once air parcels in the warm conveyor belt have ascended through this plume they continue ascending and travel northwards, at a slower rate and in a slantwise manner. The warm conveyor belt then overruns the surface warm front (not shown in Figure 6.6), which forces the warm conveyor belt to rise over the cool

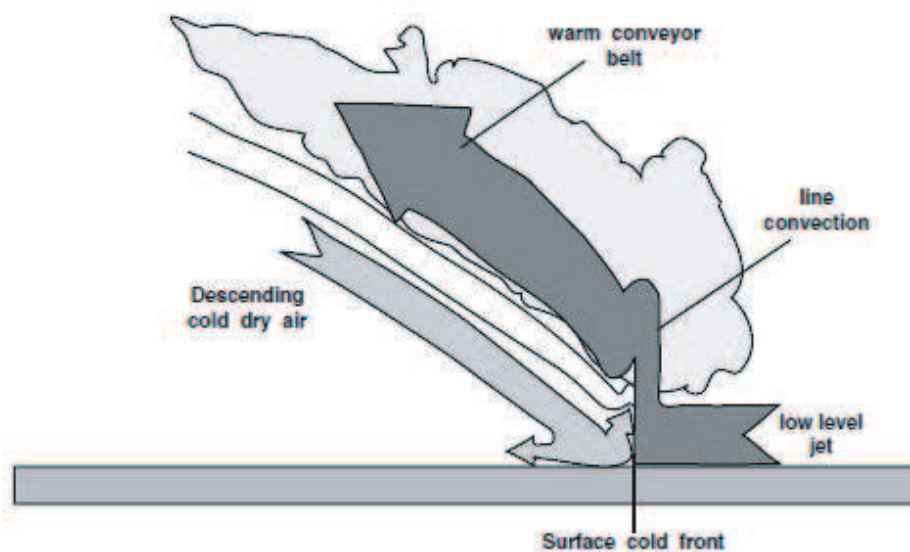


**Figure 6.6:** Schematic of an ana-type cold front (rearward sloping) in which the warm conveyor belt (dark gray shading) undergoes rearwards sloping ascent relative to the approaching cold front. Re-produced from Semple (2003).

air ahead of the front. In addition, the warm front will have localised ascent associated with it (due to the ageostrophic frontal circulation), which may give the warm conveyor belt an extra burst of vertical motion.

Figure 6.7 shows the spatial distribution of the mass flux between the boundary layer and free troposphere for all five life cycles. Positive values represent a transport of mass out of the boundary layer and negative values a transport of mass from the free troposphere into the boundary layer. To ensure a fair comparison, the mass fluxes are compared when each of the cyclones has a similar intensity, diagnosed by both minimum central pressure and eddy kinetic energy. Therefore Figures 6.7a to 6.7e are at different times, ranging from day 8 to day 12.5. Table 6.7 shows the time that each panel is plotted at and also the minimum central pressure at this time. This varies slightly between the life cycles, but all values indicate that a deep low pressure has developed.

In the life cycle with no drag (Figure 6.7a) two regions of positive mass flux are evident. The first is to the north-east of the low centre and is due to ascent associated with warm conveyor belt over-running the warm front. This is where the vast majority of mass is leaving the boundary layer. The second region of positive mass flux is to the

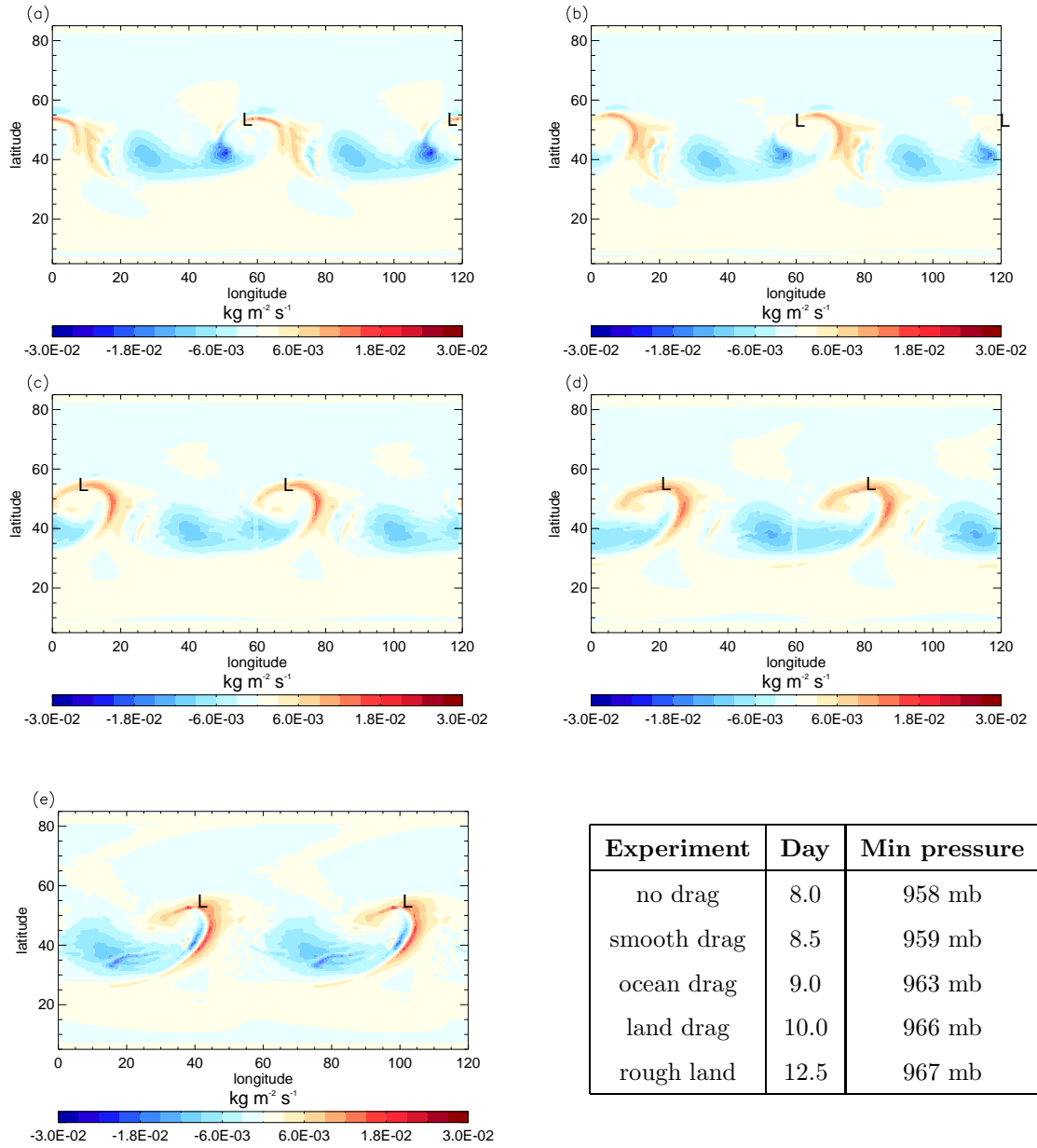


**Figure 6.7:** Mass flux out of the boundary layer at the time given in the table (a)  $C_d = 0$ , (b)  $C_d = 0.1 \times 10^{-3}$ , (c)  $C_d = 0.56 \times 10^{-3}$ , (d)  $C_d = 2 \times 10^{-3}$ , (e)  $C_d = 5 \times 10^{-3}$ . *L* marks the location of the minimum pressure. Minimum pressures are given in the table.

south-east of the low centre, and is much weaker than the flux in the warm frontal region but covers a much greater area. This is due to the warm conveyor belt ascending ahead of the surface cold front. Lower mass flux values are observed in the centre of the warm sector, compared to those on the leading and rearward edges, as the boundary layer is shallower in the centre and therefore the vertical motion is weaker. In the smooth surface drag experiment (Figure 6.7b) the warm conveyor belt acts to ventilate mass out of the boundary layer ahead of the cold front and in the region of the warm front. In comparison with the no drag case, the flux due to the warm conveyor belt over-running the warm front is weaker and much more diffuse. This is directly related to the differences in the strength and structure of the warm fronts; a stronger, more vertically orientated warm front is evident in the case of no drag, which forces the warm conveyor belt to ascend more rapidly over the warm front than in the smooth drag case. Additionally, the flux associated with the warm conveyor belt ahead of the surface cold front is much stronger.

The maximum mass flux out of the boundary layer in the ocean and land drag experiments is shown in Figures 6.7c and 6.7d. It is evident that as the drag increases the maximum mass flux moves southwards and the warm conveyor belt ascent ahead of the cold front becomes the dominant mechanism for mass ventilation. There are many similarities between Figures 6.7c and 6.7d; both the magnitude and the location of the positive mass fluxes are very similar. In the rough land experiment a similar pattern is observed, with the region of maximum mass flux due to the warm conveyor belt at  $40^{\circ}\text{N}$ , and a smaller secondary maximum due to the warm conveyor belts ascent over the bent-back warm front. However, an additional feature in the case of rough land is the increase of the mass flux from the troposphere into the boundary-layer behind the cold front.

The spatial distribution of the tracer flux between the boundary layer and free troposphere is shown in Figure 6.8 for all five experiments at the same times as were shown in Figure 6.7. If there is tracer in the upper regions of the boundary layer, the tracer flux will strongly resemble the mass flux. In the experiments with higher degrees of surface drag it is evident that tracer is only transported from the troposphere back into the boundary layer behind the cold front. This occurs due to the ageostrophic, thermally direct frontal circulation that lifts tracer out of the boundary layer ahead of the cold front and then returns a proportion of the ventilated tracer back into the boundary layer in the descending branch of the circulation behind the front. In all cases the regions where tracer is ventilated out of the boundary layer are very similar to where mass is ventilated out of

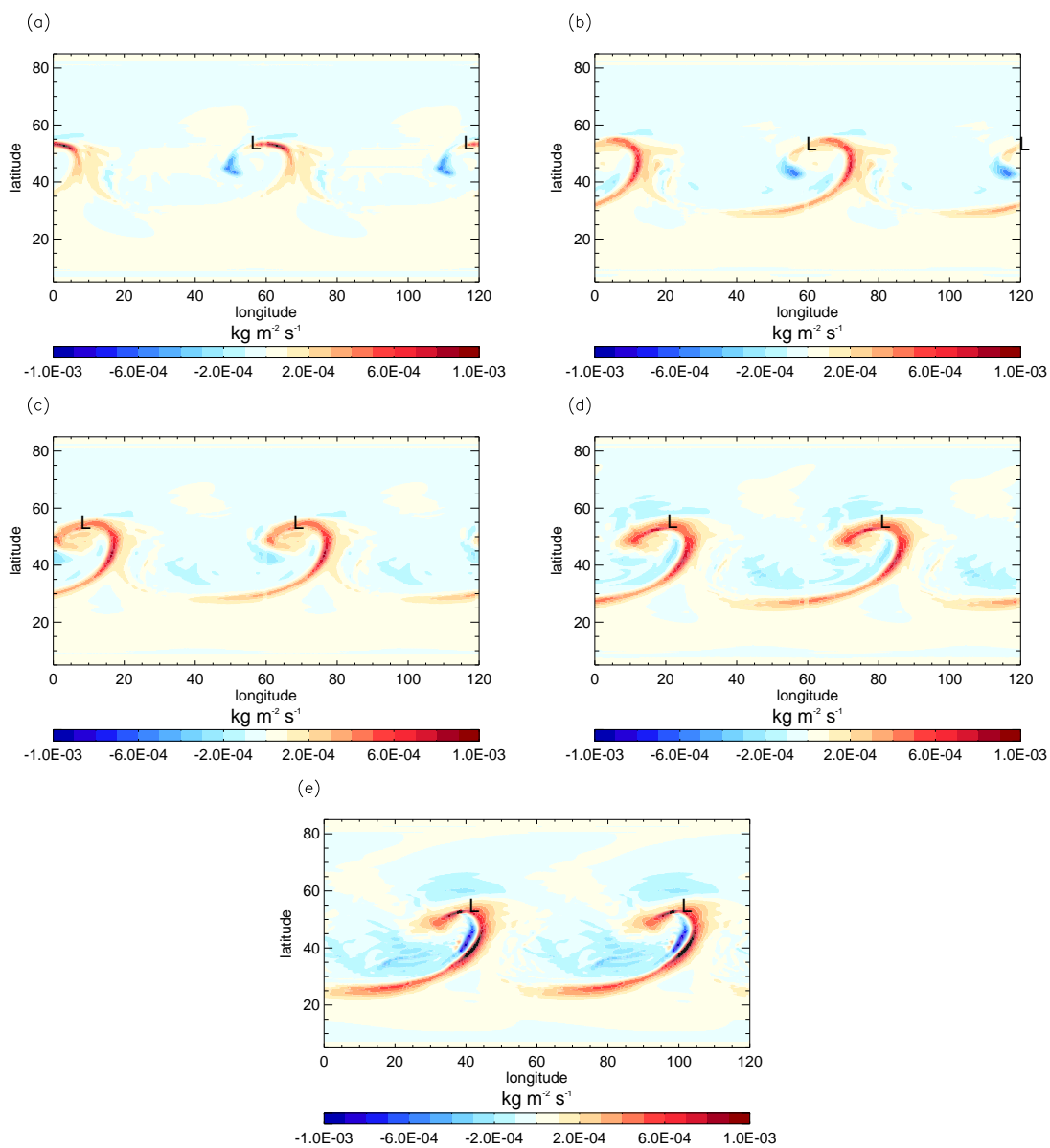


**Figure 6.8:** Tracer flux out of the boundary layer at the same times as plotted in Figure 6.7 for (a)  $C_d = 0$ , (b)  $C_d = 0.1 \times 10^{-3}$ , (c)  $C_d = 0.56 \times 10^{-3}$ , (d)  $C_d = 2 \times 10^{-3}$ , (e)  $C_d = 5 \times 10^{-3}$ .  $L$  marks the location of the minimum pressure.

the boundary layer. Some differences do exist though. Firstly, significant amounts of tracer are fluxed out of the boundary layer to the south of the anticyclone, along the weaker part of the trailing cold front, which is a region where little mass was observed to be ventilated out of the boundary layer. Tracer leaves the boundary layer in this region because high tracer concentrations are found within the boundary layer in this area due to divergence of tracer out of the anticyclone. The second difference is that in all experiments the location of the maximum tracer flux is further south along the cold front than the location of the maximum mass flux. This is because the source of tracer (divergence from the anticyclone) is from the south, and the boundary layer is shallower in the southern-most region of the warm sector than the central area.

#### 6.4.4 Effect of surface drag on total amount of mass and tracer ventilation

Figure 6.9a shows the mass flux out of the boundary layer integrated over the whole domain as a function of time for all five experiments with different drag coefficients. This is calculated by

$$\text{If } w_h > 0 \text{ then } MF = \int_A \rho w_h dA, \quad (6.4)$$

where  $w_h$  is the vertical velocity on the boundary-layer top,  $MF$  is the domain-integrated mass flux and  $A$  is the area of the model domain. The most notable result is that the domain-integrated mass flux (the rate that mass is ventilated out of the boundary layer) is insensitive to the value of the drag coefficient. This is because the vast majority of the ventilation occurs due to the ascent of the warm conveyor belt in the region of the cold front (as was shown in Figure 6.7), and it has been shown that the cold front structure is relatively insensitive to surface drag. It is also surprising that the ventilation rate in all five experiments increases with time in a very similar manner up until day 11, whereas the eddy kinetic energy (Figure 6.3) was observed to increase much more rapidly with time for the experiments with less drag. For example, by day 10 there is a 50% difference in the eddy kinetic energy of the no drag life cycle and the rough land drag life cycle.

The domain-integrated tracer flux,  $TF$ , is calculated by

$$\text{If } w_h > 0 \text{ then } TF = \int_A \rho C_h w_h dA, \quad (6.5)$$

where  $C_h$  is the tracer concentration of the boundary-layer top, and is shown in Figure 6.9b. For all experiments, except the no drag experiment, the rates of tracer ventilation are

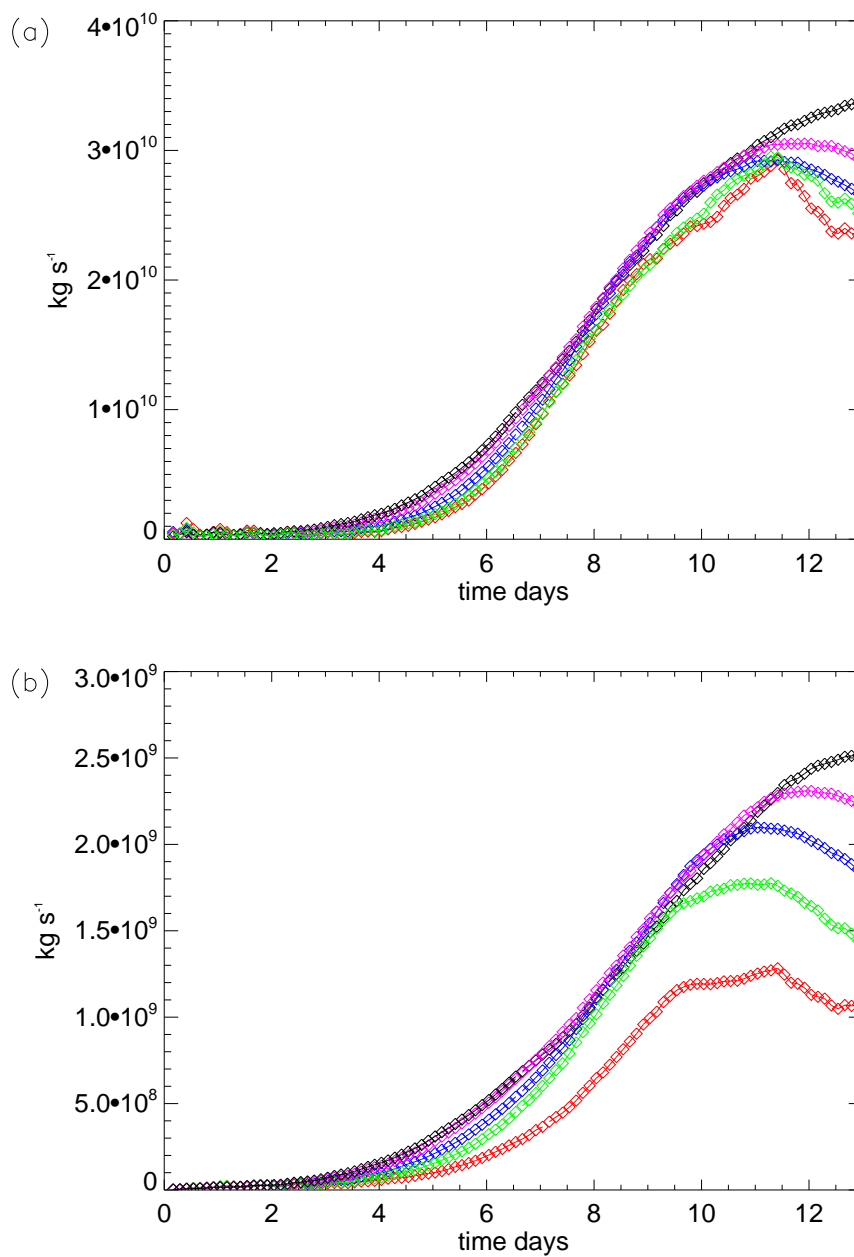


**Figure 6.9:** (a) Domain-integrated mass flux out of the boundary layer and (b) domain-integrated tracer flux out of the boundary layer. Red:  $C_d = 0$ , Green:  $C_d = 0.1 \times 10^{-3}$ , Blue:  $C_d = 0.56 \times 10^{-3}$ , Purple:  $C_d = 2 \times 10^{-3}$ , and Black:  $C_d = 5 \times 10^{-3}$ .

very similar to each other for the first nine days. In the no drag experiment the domain-integrated tracer flux is less than in all other experiments even during the initial stages of the life cycle. Additionally, after day nine the tracer flux in the no drag experiment appears to suddenly switch into a different mode of behaviour. After day 9, the rate of tracer ventilation suddenly stops increasing and almost levels off at a constant value for two days before beginning to decrease. A similar, but less pronounced change also occurs in the smooth drag case, where after nine and a half days the tracer flux levels off and slowly begins decreasing while the mass flux is still increasing. As this change in ventilation behaviour only exists for tracer and not mass, this suggests that tracer is not available in adequate concentrations in the regions of the boundary layer that are ventilated by large-scale ascent. This situation occurs when tracer is not transported into the regions of the boundary layer which are actively ventilated at a rate equal to, or greater than, the rate at which tracer is fluxed out of these regions. This hypothesis will be tested in Section 6.4.5.

Figure 6.10 shows the amount of mass and tracer transported out of the boundary layer over the whole domain and throughout the life cycle (days 0 - 13) for all five experiments with different drag coefficients. The amount of mass transported out of the boundary layer is remarkably constant with surface drag; all experiments ventilate approximately  $1.5 \times 10^{16}$ kg of air out of the boundary layer over 13 days. This amount of mass translates to approximately three times the volume of the boundary layer over the whole domain. When the total amount of tracer ventilated out of the boundary layer is considered, there is a very slight increase in the amount of tracer ventilated between the ocean and rough land drag experiments, but a much larger increase between the no drag and ocean drag experiments. This variation is investigated further in section 6.4.5.

#### 6.4.5 Boundary-layer tracer budgets

It has been shown that the amount of boundary-layer ventilation (ventilation of mass rather than tracer) is largely insensitive to the surface drag as most of the ventilation occurs due to the warm conveyor belt's ascent in the region of the cold front, the structure of which is found to change little with surface drag. However, the decrease in tracer ventilation, but not ventilation of mass, when there is little or no drag needs to be explained. It is hypothesised that this occurs because without drag there is no friction-induced divergence out of the anticyclone or convergence into the cyclonic source region of the warm conveyor

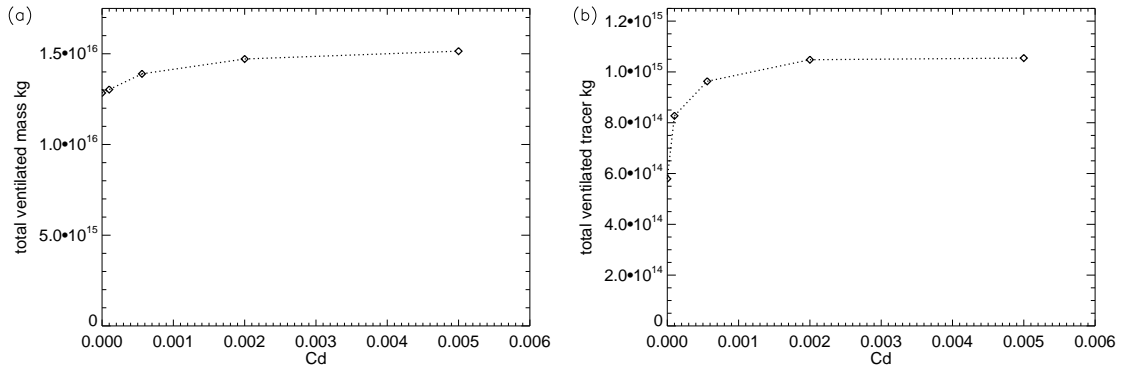


**Figure 6.10:** (a) Total mass of air and (b) total mass of tracer ventilated out of the boundary layer during the whole life cycle.

belt. Therefore, with no friction acting, the tracer will not be transported within the boundary layer to the source regions of the conveyor belt as efficiently as in the experiments which do include surface friction.

This suggests that the horizontal transport within the boundary layer is important, and varies in intensity with differing values of surface drag. To understand how the tracer is transported, and quantify how tracer is lost and gained in different regions of the boundary layer, individual terms in a tracer budget equation are evaluated. The tracer budget equation is closely related to the mass budget equation that was presented in Chapter 4, however, a brief discussion of the tracer budget equation is given here.

The tracer budget equation is derived from the continuity equation, except that the density of air is replaced with the density of tracer,  $\rho_t$ , which is given by the tracer concentration,  $C$ , multiplied by the density of air,  $\rho$ . Additional terms are present in the tracer budget equation compared to the mass budget equation. Firstly, as the tracer is emitted into the domain at the surface there is a source term,  $S$ . Secondly, a turbulent flux term,  $\overline{(w'\rho'_t)_h}$ , is also present which represents the turbulent flux of tracer across the diagnosed boundary-layer top. This is calculated online by the boundary-layer scheme (equation 2.59), and the value used here is the value estimated at the top of the boundary layer. There is no turbulent flux term present in the mass budget equation as the variation in air density across the boundary-layer top is small and therefore the turbulent flux of mass out of the boundary layer equals the turbulent flux of mass into the boundary layer. This is not the case for tracer; above the boundary layer there are much lower tracer concentrations (or even zero tracer) than there are within the boundary layer. The complete form of the resulting tracer budget equation is

$$\frac{\partial \widehat{\rho}_t}{\partial t} = (\rho_t)_h \frac{\partial h}{\partial t} + (u\rho_t)_h \frac{\partial h}{\partial x} + (v\rho_t)_h \frac{\partial h}{\partial y} - \frac{\partial}{\partial x}(\widehat{u\rho}_t) - \frac{\partial}{\partial y}(\widehat{v\rho}_t) - (w\rho_t)_h + S - \overline{(w'\rho'_t)}_h. \quad (6.6)$$

However this can be re-written as

$$\frac{\partial \widehat{\rho}_t}{\partial t} = (\rho_t)_h \frac{\partial h}{\partial t} - \widehat{D}_t + A_t + S - \overline{(w'\rho'_t)}_h, \quad (6.7)$$

where  $\widehat{D}_t$  is the depth integrated divergence of tracer given by

$$\widehat{D}_t = \frac{\partial}{\partial x}(\widehat{u\rho}_t) + \frac{\partial}{\partial y}(\widehat{v\rho}_t), \quad (6.8)$$

and  $A_T$  is large-scale advection of tracer given by

$$A_t = (u\rho_t)_h \frac{\partial h}{\partial x} + (v\rho_t)_h \frac{\partial h}{\partial y} - (\rho_t w)_h = (\rho_t)_h (\mathbf{u} \cdot \mathbf{n})_h. \quad (6.9)$$

The divergence,  $\widehat{D}_t$ , and large-scale advection,  $A_t$ , terms are shown in Figure 6.11 for day 9 and day 11 for both the smooth drag experiment and the land drag experiment. These experiments were chosen for direct comparison as they represent opposite ends of the spectrum. The smooth drag was chosen rather than the no drag case because it produces a more realistic life cycle and boundary-layer structure. The land drag case was selected instead of the rough land case because the life cycle in the rough land case develops at an unrealistically slow rate. After nine days of the smooth drag life cycle (Figures 6.11a and 6.11b) there is strong divergence of tracer on the southern and eastern edges of the anticyclone and significant convergence of tracer into the western edges of the warm conveyor belt source region. At the same time there is a loss of tracer from the boundary layer by large-scale advection in the warm conveyor belt source region, but the rate of increase of tracer due to convergence is greater than the rate of loss by advection. By day eleven the convergence of tracer into the warm conveyor belt footprint has weakened (Figure 6.11c), whereas the loss by large-scale advection (Figure 6.11d) has increased. The warm conveyor belt footprint has changed shape considerably between days nine and eleven, becoming much narrower and extending further south. In the land drag experiment

similar spatial patterns are observed. At both day nine (Figure 6.11e) and eleven (Figure 6.11g) the maximum increase in tracer mass due to convergence occurs on the western most edge of the warm conveyor belt footprint and there is strong divergence of tracer to the south and east of the anticyclone. In contrast to the smooth drag experiment the tracer gain due to convergence increases between days nine and eleven, although the maximum moves southwards, and therefore appears to be more in balance with the loss of tracer due to large-scale advection than was the case for the smooth drag experiment at the same stage. The loss of tracer due to large-scale advection is shown in Figures 6.11f and 6.11h. The greatest decrease in boundary-layer tracer mass occurs on the southern and western-most edges of the conveyor belt footprint, and also moves southwards with time.

To accurately quantify the balance between the convergence term and the large-scale advection term the rate of change of boundary layer tracer mass due to each process can be integrated over the area identified as the conveyor belt footprint. This is the area enclosed within the  $0.65 \text{ cm s}^{-1}$  vertical velocity contour on the boundary-layer top. The same has also been done for the source term and the turbulent flux term, as these two additional processes can alter the amount of tracer available in the footprint region. Figure 6.12 shows the rate of change of tracer mass, integrated over the conveyor belt footprint region, due to these four processes for the smooth drag experiment (Figure 6.12a) and the land drag experiment (Figure 6.12b). In both experiments the large-scale vertical motion and convergence within the boundary layer are the dominant terms. The surface emission and turbulent flux terms are both small. Although the emission strength is uniform in time and space, the rate of change of tracer mass in the conveyor belt footprint area is not constant in time as the area of the footprint changes with time. In the smooth drag experiment the increase of tracer mass due to convergence is greater than the decrease in tracer mass due to the large-scale vertical motion up until day ten and a half. After this point, the tracer convergence is weaker than the removal of tracer due to vertical motion, consistent with Figure 6.11. This indicates that after day 10.5 there is not sufficient tracer in the warm conveyor belt footprint region to realise the full ventilation potential of the life cycle, allowing the mass flux to be greater than the tracer flux. However, the timing of this does not agree with the results shown in Figure 6.9, where after only nine days the tracer flux did not increase at the same rate as the mass flux. This implies that the hypothesis stated previously - that with little frictionally induced convergence tracer is

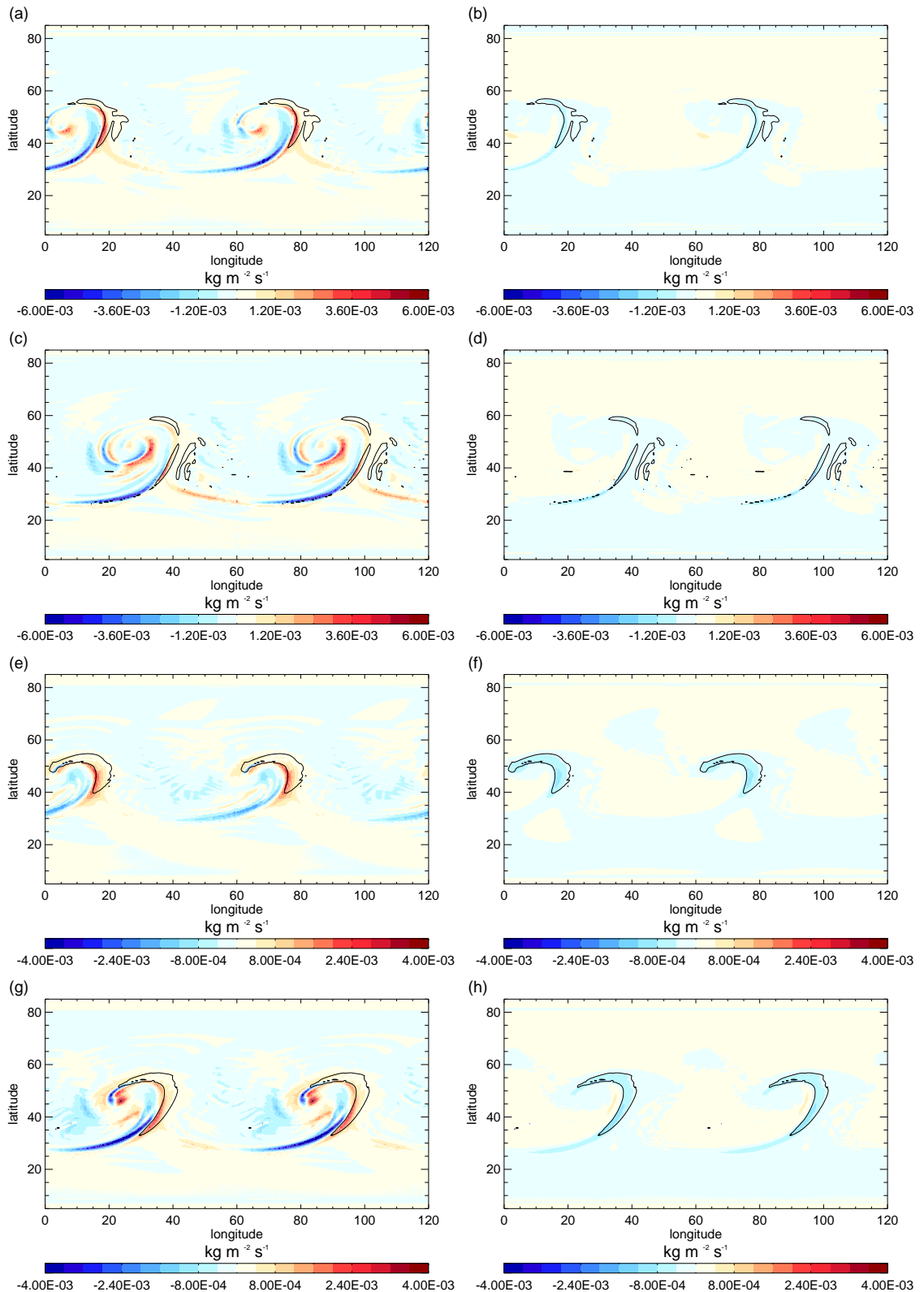


**Figure 6.11:** Rate of change of tracer mass in the boundary layer due to (a) divergence ( $\widehat{D}_t$ ) in the smooth drag case after 9 days, (b) advection ( $A_t$ ) in the smooth drag case after 9 days, (c) divergence in the smooth drag case after 11 days, (d) advection in the smooth drag case after 11 days, (e) divergence in the land drag case after 9 days, (f) advection in the land drag case after 9 days, (g) divergence in the land drag case after 11 days, (h) advection in the land drag case after 11 days. Black contour is on  $0.65 \text{ cm s}^{-1}$  vertical velocity contour on the boundary-layer top. Note different colour scales between panels.

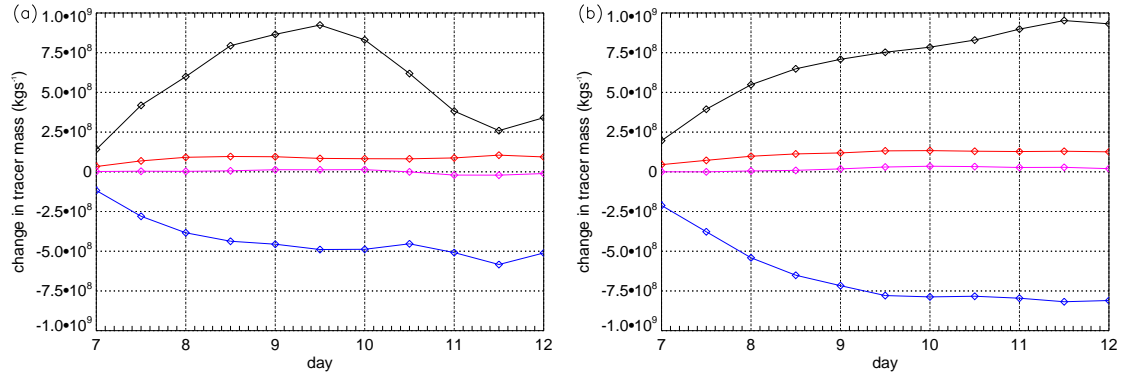


**Figure 6.12:** Rate of change of tracer mass (evaluated over 30 minutes) in the boundary layer within the conveyor belt source region as a function of time due to: horizontal convergence (black), large-scale advection (blue), surface emission of tracer (red) and turbulent exchange between the boundary layer and free troposphere (purple). (a) smooth drag experiments and (b) land drag experiment.

not supplied into the conveyor belt footprint rapidly enough - is partly true. However, this also suggests that another process may be acting to prevent tracer from being ventilated out of the boundary layer between day nine and day ten and a half. The likelihood of this hypothesis is increased when the no drag case is considered; from day 5 onwards the tracer flux is much weaker than the tracer flux in the smooth drag experiment whereas the mass flux in the no drag case is similar to the mass flux in the smooth drag experiment throughout the whole life cycle.

So far the horizontal distribution of tracer in the boundary layer has been considered. However, for tracer to be ventilated, strong tracer concentrations must exist in the mid to upper regions of the boundary layer. Thus, the vertical distribution of tracer is also important and is now considered. The vertical distribution of tracer is determined by the structure of the boundary layer, which is considerably different between the different drag experiments. It was shown in Figure 6.5 that the depth of the boundary layer in the warm sector decreases with decreasing drag.

Figure 6.13 shows the difference in potential temperature,  $\Delta\theta$ , between the top of the boundary layer and the lowest model level ( $\Delta\theta = \theta_h - \theta_1$ ). The difference in potential temperature is a proxy for the thermal stratification of the boundary layer; where large values exist there is a very stably stratified boundary layer. Figure 6.13a shows  $\Delta\theta$  for the smooth drag case after 8 days. Strong stratifications are observed in the northern parts of the warm sector. In contrast, Figure 6.13c shows  $\Delta\theta$  for the land drag experiment, also after 8 days. With the increased drag the stratification in the warm sector is significantly

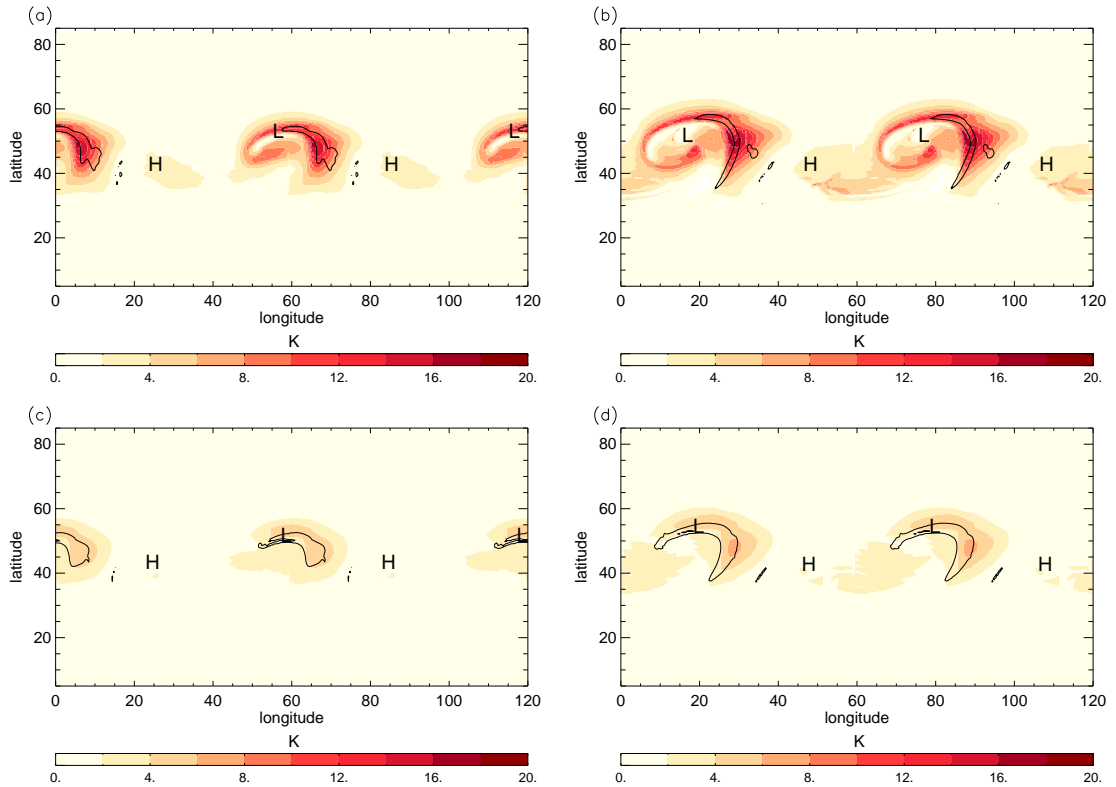


**Figure 6.13:** Difference in potential temperature between the top of the boundary layer and the lowest model level for (a) day 8 of the smooth drag experiment, (b) day 10 of the smooth drag experiment, (c) day 8 of the land drag experiment, (d) day 10 of the land drag experiment. Solid black contour is the  $0.65 \text{ cm s}^{-1}$  vertical velocity contour on the boundary layer top.  $L$  marks the location of the minimum surface pressure and  $H$  the maximum surface pressure.

reduced. In the smooth drag case, the strength of the stratification in the warm sector increases with time and by day 10 (Figure 6.13b) the area of strong stable stratifications has increased, extending southwards to occupy more of the warm sector. Similar behaviour, an increase in stratification with time, is seen in the land drag case. However, even after 10 days the stratification is still much weaker than in the smooth drag experiment.

The stratification of the boundary layer in the warm sector has a large influence on the vertical distribution of the tracer. This is demonstrated in Figure 6.14 where all vertical tracer profiles within the conveyor belt footprint (defined as where the vertical velocity on the boundary-layer top exceeds  $0.65 \text{ cm s}^{-1}$ ) have been plotted for the smooth drag case and the land drag case. After 8 days of both experiments similar surface concentrations are observed (Figures 6.14a and 6.14b). In the land drag case the tracer profiles are more well mixed within the boundary layer than in the smooth drag case. This becomes more evident after 10 days. In the smooth drag case (Figure 6.14c) very high surface concentrations,

especially towards the southern part of the warm sector, are observed and the boundary layer has significant gradients in tracer concentration across its depth. In contrast, after 10 days of the land drag experiment (Figure 6.14d) the boundary layer still appears to be relatively well mixed except at higher latitudes. The effect of the greater stratification in the smooth drag case is even more pronounced after 12 days. Figure 6.14e shows that the boundary-layer depth in the land drag case has increased slightly in the warm sector during the previous two days. The boundary layer remains well mixed with respect to tracer concentrations after 12 days, whereas in the smooth drag case the boundary-layer depth is shallower and tracer concentrations decrease rapidly from the surface to the top of the boundary layer.

This demonstrates that, although tracer is transported into the correct regions of the boundary layer in the horizontal plane for the majority of the life cycle in the smooth drag experiment, the tracer is not mixed to the upper parts of the boundary layer which is where the large-scale vertical motion associated with the warm conveyor belt is strongest. The lack of vertical mixing is due to the minimal amount of surface friction and therefore the lack of shear driven turbulence. Without significant mechanical mixing in the warm sector very strong, and somewhat un-physical, potential temperature gradients were able to develop near the surface which then prevented the tracer mixing to upper levels. Although the no drag and smooth drag experiments are somewhat unrealistic, they were conducted to investigate how important boundary-layer transport processes are in determining the amount of boundary-layer ventilation and the final tracer distribution. The results shown here demonstrate that although the structure of the boundary layer and the boundary-layer transport processes do not control the amount of boundary-layer ventilation they must be included to obtain the correct tracer distributions especially at low levels. Also evident is that the presence of friction almost acts like an ‘on-off’ switch. Without frictional effects the ventilation of tracer is considerably reduced and tracer distributions are strongly altered. However, once a certain threshold in the amount of friction has been reached, for example the value used in the ocean experiment,  $0.56 \times 10^{-3}$ , further increases in friction will no longer increase the amount of tracer ventilated out of the boundary-layer.

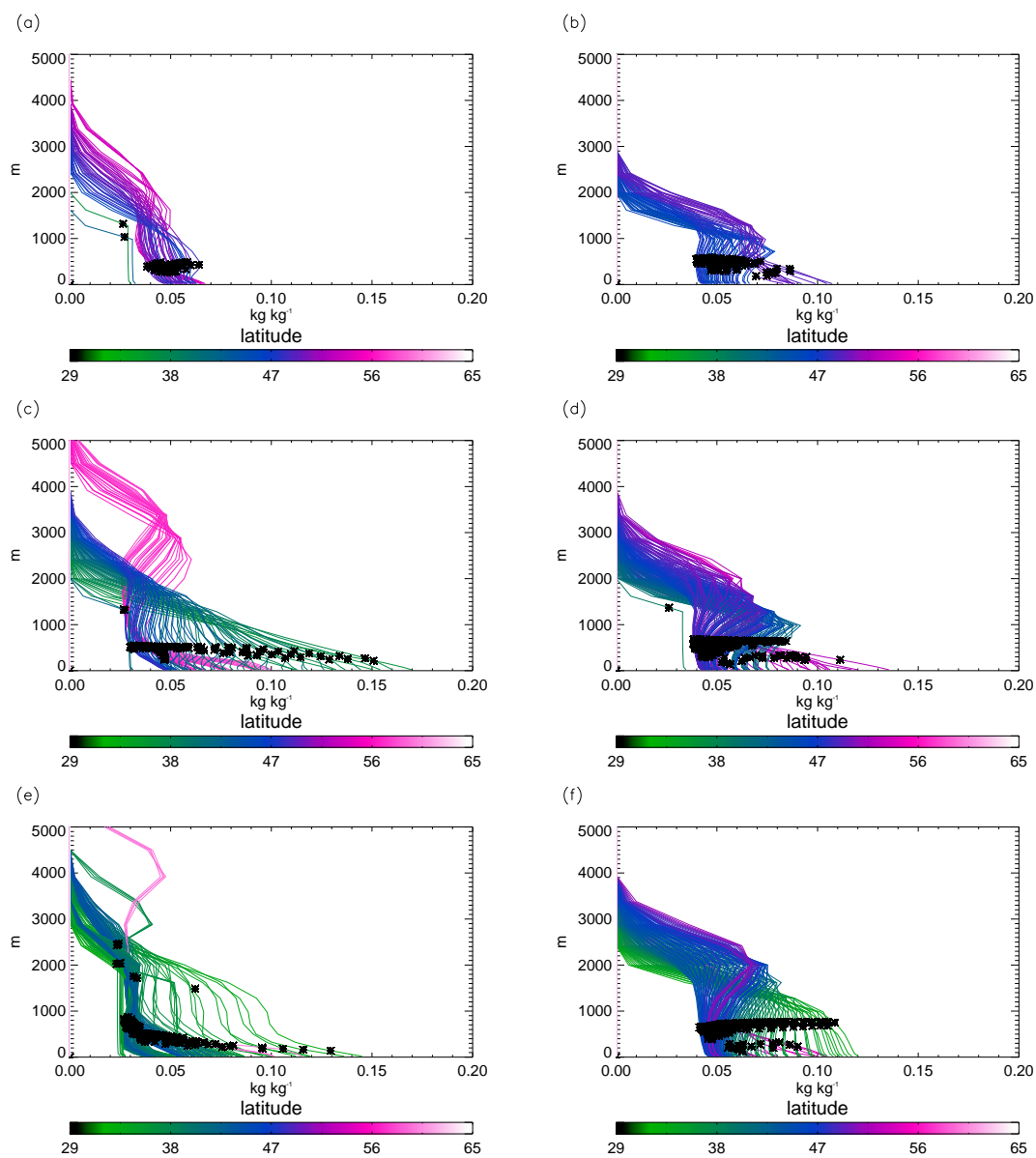


**Figure 6.14:** Vertical profiles of tracer concentration in the conveyor belt footprint areas for (a) Day 8 smooth drag, (b) Day 8 land drag, (c) Day 10 smooth drag, (d) Day 10 land drag, (e) Day 12 smooth drag, (f) Day 12 land drag. The colour of the profiles represents the latitude that the profile is taken at. Asterisks mark the boundary-layer depth.

## 6.5 Dependence of ventilation on large-scale dynamics

The results presented so far in this Chapter have shown how life cycles react to differing degrees of surface drag, and how the ventilation characteristics change as drag is altered. The results have shown that surface drag, and therefore the structure of the boundary layer and transport processes within the boundary layer, do not exert any significant control on the efficiency of a life cycle to ventilate the boundary layer except for very small drag. This implies that the large-scale dynamics is the limiting step in the amount of ventilation, and therefore it is hypothesised that large-scale dynamics control the amount of ventilation. This hypothesis will now be tested.

### 6.5.1 Theory

In Chapter 5 the warm conveyor belt was identified as an important process for transporting mass and tracers out of the boundary layer. To estimate the strength of ascent found in the warm conveyor belt the Quasi-Geostrophic (QG) Omega equation (Hoskins, 1997) can be utilised. A scale analysis can be performed on the QG Omega equation to identify parameters that control the magnitude of ascent. The QG Omega equation can be written in the Vorticity Advection Thermal Advection form (in terms of  $w$  rather than  $\omega$ ),

$$N^2 \nabla_h^2 w + f^2 \frac{\partial^2 w}{\partial z^2} = \frac{g}{\theta_0} \nabla_h^2 (-\mathbf{V}_g \cdot \nabla_h \theta) - f \frac{\partial}{\partial z} (-\mathbf{V}_g \cdot \nabla_h \xi_g), \quad (6.10)$$

assuming that  $\beta = 0$ , as is the case for these U.M. simulations. The terms on the right hand side are the forcing terms: the first term is due to thermal advection and the second term is due to differential vorticity advection. Forcing due to friction and diabatic effects is neglected. For the purpose of estimating the amount of boundary-layer ventilation it is necessary to estimate the vertical velocity near the top of the boundary layer. It is commonly assumed that the thermal advection term dominates at low levels and that vorticity advection is the dominant term at upper levels (Petterssen and Smebye, 1977). Therefore, the differential vorticity advection term can be neglected, and normal scaling arguments can be applied to the remaining terms to obtain

$$w = \frac{-(g/\theta_0) (1/L^2) V_g (\partial\theta/\partial y)}{N^2/L^2 + f^2/H^2}, \quad (6.11)$$

where  $L$  and  $H$  are typical synoptic length and height scales respectively. This scaling assumes that the meridional temperature gradient is much greater than the zonal temperature gradient, which is the case in these U.M. simulations as there is no zonal temperature gradient in the initial conditions. Additionally, by only considering the meridional thermal advection forcing term, the ascent of the warm conveyor belt should be estimated rather than ascent elsewhere in the system. This is because it is northerly advection of warm air that forces the warm conveyor belt to ascend. Equation 6.11 can be simplified firstly by using thermal wind balance to re-write the North-South temperature gradient in terms of the vertical wind shear;

$$\frac{g}{\theta_0} \frac{\partial \theta}{\partial y} = -f \frac{\partial U_g}{\partial z}, \quad (6.12)$$

and secondly by assuming that the horizontal length scale,  $L$ , is equal to the Rossby length scale of deformation,  $L_{Ro}$ ,

$$L_{Ro} = \frac{NH}{f}, \quad (6.13)$$

which is equivalent of assuming a Burger number of unity. By making these substitutions into equation 6.11 an estimate for the strength of ascent in the warm conveyor belt can be obtained;

$$w = w_{wcb} = \frac{+V_g f_0 \frac{\partial U_g}{\partial z}}{2N^2}. \quad (6.14)$$

This suggests that the strength of the warm conveyor belt,  $w_{wcb}$ , and hence the potential for boundary-layer ventilation, is directly proportional to the vertical wind shear,  $\partial U_g / \partial z$  (the strength of the zonal mid-latitude jet), the Coriolis parameter,  $f_0$ , and the magnitude of the north-south geostrophic wind component,  $V_g$ . Additionally the strength of the warm conveyor belt is inversely proportional to the Brunt-Väisälä frequency,  $N^2$ , and hence the stratification of the troposphere.

This scale analysis suggests that a number of different idealised life cycles should be simulated with differing jet strength, static stability parameters and Coriolis parameters to investigate how the strength of the warm conveyor belt affects the amount of boundary-layer ventilation. However, changing the magnitude of these three variables will change significantly more about the life cycle than just the vertical velocity. The Eady Model

(Eady, 1949), a linear analytical model of baroclinic instability, can be used to identify how the growth rate of the cyclones will change. The maximum growth rate,  $\sigma$ , is

$$\sigma = -0.31 \frac{1}{N} \frac{g}{\theta_0} \frac{\partial \theta}{\partial y} = 0.31 \frac{1}{N} f_0 \frac{\partial U_g}{\partial z}, \quad (6.15)$$

assuming an infinitely wide jet. Increasing the strength of the zonal jet, or the Coriolis parameter, will cause the life cycle to develop more rapidly, whereas increasing the stratification will result in slower growth. The Eady Model also predicts the wavenumber,  $k$ , that maximum growth will occur at,  $k = 1.6/L_{Ro}$ . However, in these experiments the perturbation is chosen to force development at wavenumber six. Although this means that the fastest growing mode will not initially be triggered, it does ensure that all the cyclones are the same size. This is vital for this study as a larger cyclone will ventilate more mass and tracer out of the boundary layer than a smaller, but equally intense system.

The QG scaling provides a framework for deciding which idealised experiments to conduct. Additionally, QG theory can be used to develop a diagnostic which provides a scaling for the amount of mass that can be ventilated out of the boundary layer by a mid-latitude cyclone. It should be recalled that the amount of mass ventilated can differ from the amount of tracer ventilated; however the estimate of ventilated mass is useful to apply to tracer problems as it provides an upper bound on the amount of ventilation.

### 6.5.2 Experiments conducted

Numerical experiments have been conducted to investigate the role of vertical shear, tropospheric stability and latitude on the amount of boundary-layer ventilation. The vertical shear is altered by changing the maximum strength of the zonal jet in the initial conditions. This is achieved by changing the value of  $U_0$  in equation 3.1. Five different values of  $U_0$  were used; 35 m s<sup>-1</sup>, 40 m s<sup>-1</sup>, 45 m s<sup>-1</sup>, 50 m s<sup>-1</sup> and 55 m s<sup>-1</sup>. (The height of the jet was kept constant at 13 km in all experiments.) When values less than 35 m s<sup>-1</sup> were used it was found that the resulting baroclinic life cycle took an un-physically long time to develop into a system resembling a real mid-latitude weather system. Jet strengths exceeding 55 m s<sup>-1</sup> resulted in extremely strong frontal features developing and therefore were determined to be unrealistic. Four values of tropospheric stability were investigated. The value in the control run, 0.004 K m<sup>-1</sup>, a slightly more stable value, 0.006 K m<sup>-1</sup>, a very stable value, 0.008 K m<sup>-1</sup>, and also a less stable value, 0.002 K m<sup>-1</sup>. It should

be noted that although the very stable stratification experiment has been included, the life cycle develops very slowly and even after 13 days has barely reached maturity. The lapse rate in the stratosphere was kept constant in all experiments. Life cycles with zonal jets centred on four different latitudes (different values of  $f$ ) were also investigated;  $40^\circ\text{N}$ ,  $45^\circ\text{N}$  (the control latitude),  $50^\circ\text{N}$  and  $55^\circ\text{N}$ .

### 6.5.3 Effect of vertical shear, latitude and stability on life cycle evolution

The Eady model predicts how the large-scale aspects of the life cycle should change, and a simple way to verify that the life cycle experiments performed here do as expected is to consider the evolution of the domain-averaged eddy kinetic energy. Figure 6.15a shows the average eddy kinetic energy as a function of time for the experiments with differing magnitudes of vertical shear. It can be seen that an almost linear increase in the eddy kinetic energy occurs as the vertical shear increases, as predicted by the Eady model. Therefore, as the life cycles become more energetic with increasing shear, and stronger baroclinicity, the hypothesis stated in Chapter 5 that the strength of the baroclinicity exhibits a large control on the amount of boundary-layer ventilation remains plausible. Figure 6.15b shows the domain-averaged eddy kinetic energy for the experiments with differing stabilities. Again, the simulations are in good agreement with the Eady model; the experiments with the strongest stratification develop the slowest and reach the lowest maximums in eddy kinetic energy. The effect of the latitude of the jet, and therefore the Coriolis parameter, on the eddy kinetic energy is shown in Figure 6.15c. As the jet moved northwards and the Coriolis parameter increases, the peak in eddy kinetic energy occurs sooner and is larger, as was expected from the Eady model.

The experiments were designed to force wavenumber six growth to ensure that the cyclone size was kept as a constant. Figure 6.16 shows two life cycles, one with a jet strength of  $40\text{ m s}^{-1}$  and the other  $55\text{ m s}^{-1}$ , both at the time when they reach their maximum in eddy kinetic energy. It is evident that the size of the cyclones is very similar in both experiments, despite the large difference in the intensity of the cyclones.

### 6.5.4 Quasi-Geostrophic mass and tracer fluxes

QG theory has been used to identify the variables that control the strength of the conveyor belt flows. Therefore, before an attempt is made to relate the mass and tracer fluxes to a QG-based diagnostic, the actual mass and tracer fluxes should be compared to those

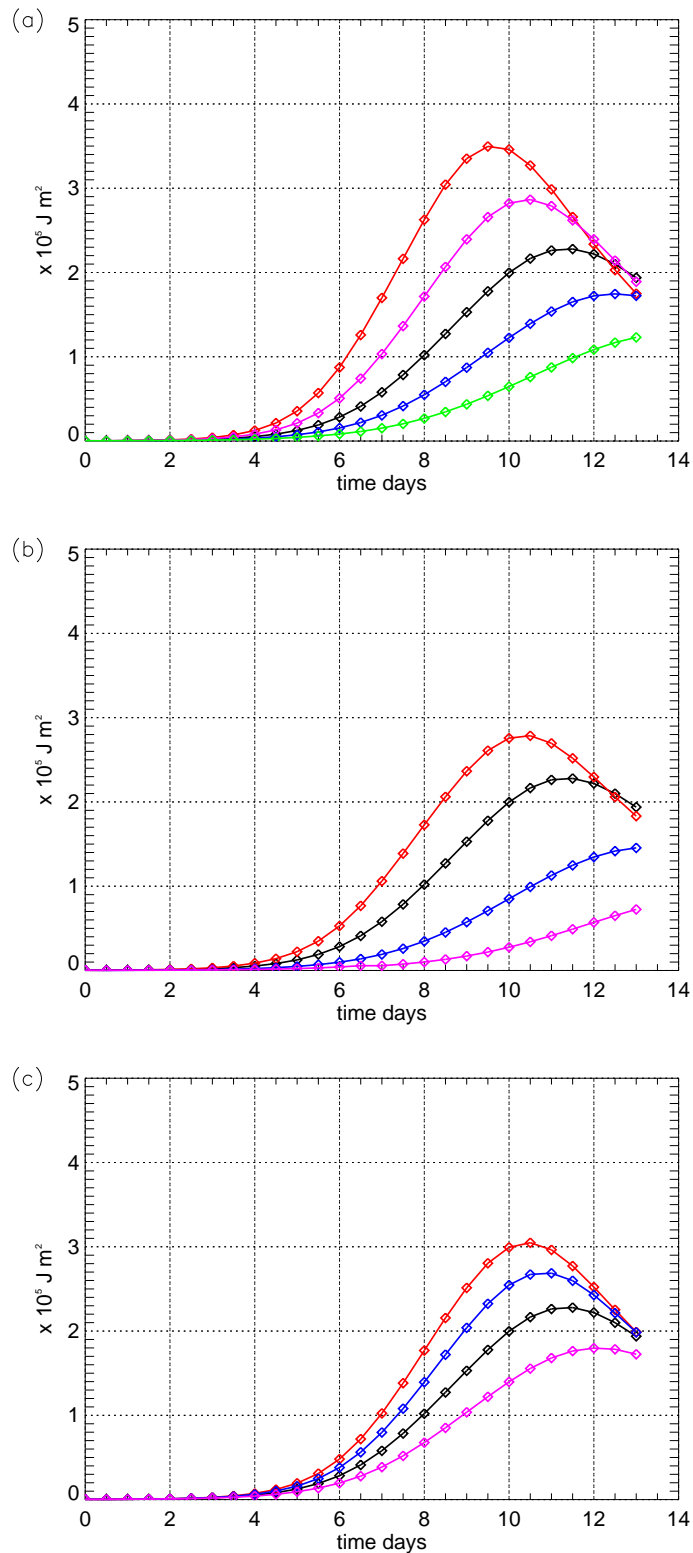


**Figure 6.15:** Domain-averaged eddy kinetic energy for life cycle experiments with (a) different initial jet strengths; green,  $35 \text{ m s}^{-1}$ ; blue,  $40 \text{ m s}^{-1}$ ; black,  $45 \text{ m s}^{-1}$ ; purple,  $50 \text{ m s}^{-1}$ ; and red,  $55 \text{ m s}^{-1}$ . (b) experiments with different initial tropospheric stability; purple,  $d\theta/dz = 0.008 \text{ K m}^{-1}$ ; blue,  $d\theta/dz = 0.006 \text{ K m}^{-1}$ ; black,  $d\theta/dz = 0.004 \text{ K m}^{-1}$ ; and red,  $d\theta/dz = 0.002 \text{ K m}^{-1}$ . (c) experiments with different Coriolis parameters; purple,  $40^\circ \text{N}$ ; black,  $45^\circ \text{N}$ ; blue,  $50^\circ \text{N}$ ; and red,  $55^\circ \text{N}$ . Note that the black line in all three panels is the same and is the control life cycle as described in section 3.3.

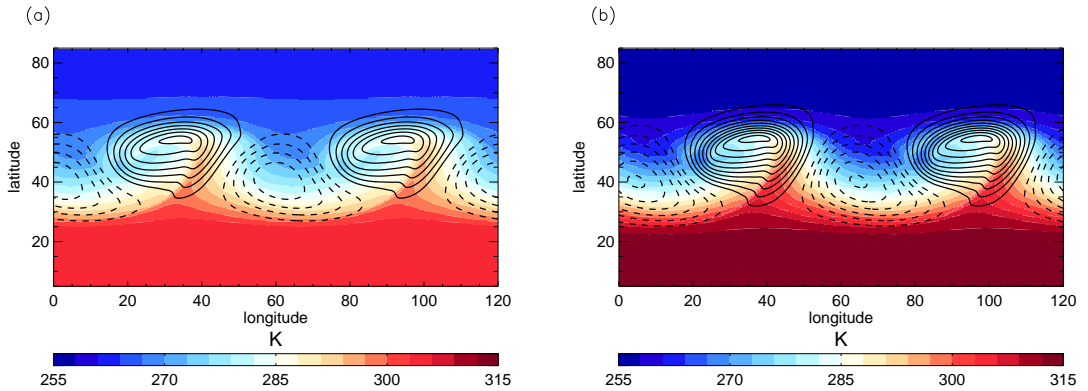


**Figure 6.16:** Surface pressure contours every 4 hPa. Solid contours show values less than 1000 hPa and dashed contours values greater than 1000 hPa. The 1000 hPa contour has been omitted for clarity. Colours show potential temperature at 1 km (a)  $U_0 = 40 \text{ m s}^{-1}$  experiment after 12.5 days of development and (b)  $U_0 = 55 \text{ m s}^{-1}$  experiment after 9.5 days of development

calculated using the QG vertical velocity to ensure that using the QG approximation is appropriate. The QG vertical motion is obtained by inverting equation 6.10 subject to boundary-conditions; the vertical velocity must equal zero at the surface and at the model lid. The vertical velocity on the boundary-layer top is now compared to the QG vertical velocity on the boundary-layer top. Figure 6.17a shows the vertical velocity after eight days of the control life cycle. After eight days there is ascent mainly in the region of the warm front but there is also an area of weaker ascent ahead of the cold front in the warm sector. A very similar pattern is seen in the QG vertical motion (Figure 6.17c) and the magnitude of QG ascent is remarkably similar. By day twelve (Figure 6.17b) the total ascent associated with the cold front is much stronger than that associated with the warm front, and is found in a narrow, well defined band between  $30^\circ\text{N}$  and  $50^\circ\text{N}$ . The QG vertical motion after twelve days is shown in Figure 6.17d. Differences are now evident between this and the actual vertical velocity; in the cold frontal region (and especially along the southern most part of the frontal zone) the QG vertical motion is significantly weaker.

However, although during the later stages of the life cycle differences are evident, when the domain-integrated total mass flux is compared to the QG domain-integrated mass flux surprisingly good agreement is found. The QG domain-integrated mass flux is calculated by interpolating the QG vertical velocity,  $w_{\text{QG}}$ , onto the boundary-layer top to

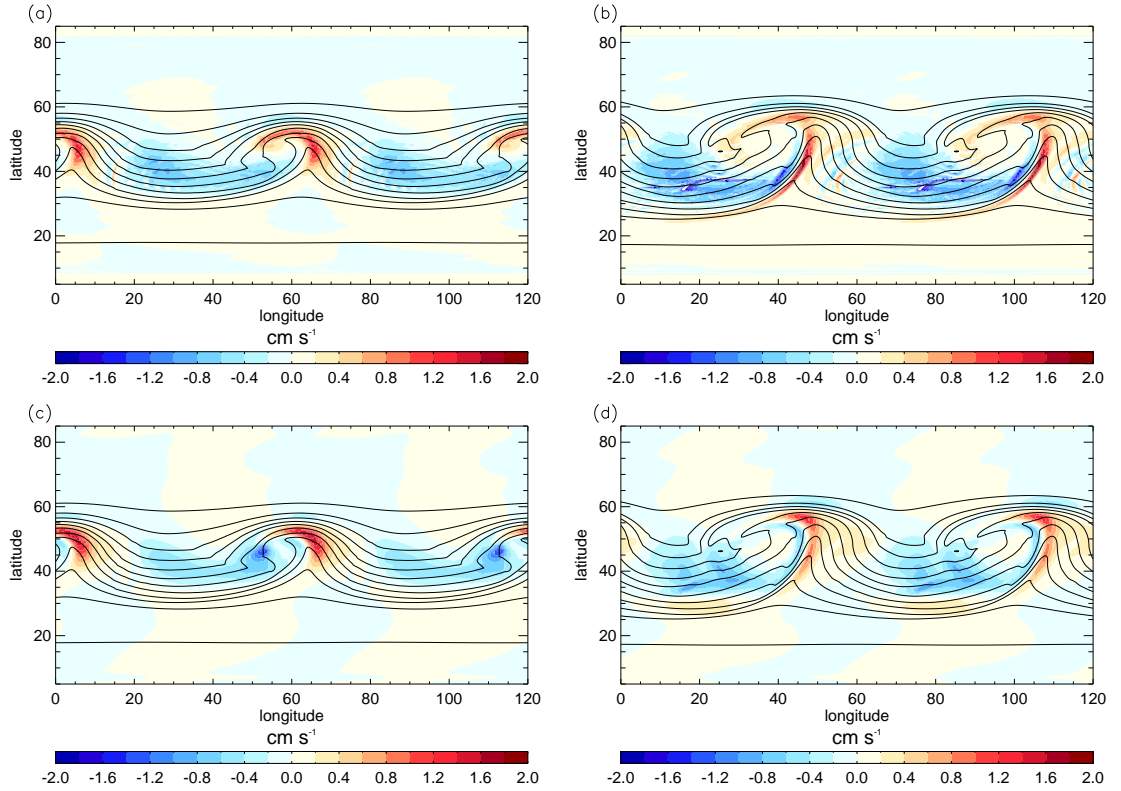


**Figure 6.17:** Actual vertical velocity (coloured contours) on the boundary layer top after (a) 8 days and (b) 12 days of the control life cycle. Quasi-Geostrophic vertical velocity on the boundary layer top after (c) 8 days and (d) 12 days. Black contours show potential temperature (contour interval of 4 K) at 1 km.

obtain  $(w_{QG})_h$  and then by using

$$\text{If } (w_{QG})_h > 0 \text{ then } MF = \int_A \rho_h (w_{QG})_h dA. \quad (6.16)$$

Figures 6.18a-e shows both the actual and QG flux of mass out of the boundary-layer for all experiments with different jet strengths. For all experiments good agreement is found up until day eight, after which the QG mass flux is weaker than the actual mass flux. The peak in the QG mass flux tends to occur a day before the actual mass flux. The QG mass flux is less than the actual mass flux as QG theory neglects terms in the equations of motions which are small compared to the Rossby number. The neglected terms include advection of momentum by both the vertical wind component and the ageostrophic part of the wind, and advection of ageostrophic momentum by the geostrophic part of the wind. Without the inclusion of these terms fronts are not captured correctly; the ageostrophic circulation does not alter the frontal structure, whereas when all terms are included the ageostrophic circulation acts to tilt the frontal surface and increases the temperature gradient associated

with the front, significantly strengthening the front. Figure 6.18f shows that using the QG mass flux as a proxy for the total mass flux is a reasonable approximation to make; between 75% and 90% of the mass flux is captured by the QG mass flux. Interestingly, the QG mass flux becomes a better approximation with stronger systems.

When the actual tracer fluxes are compared with the QG tracer flux (Figure 6.19a) good agreement is found during the early stages of the cyclone. During the later part of the cyclone a weaker correlation is found than that observed in the case of mass. The QG approximation is poorer for tracer than for mass as the spatial distribution is much more critical for tracer. The peak QG vertical velocity is found to be located mainly in the warm frontal region and the warm sector throughout the life cycles, whereas the peak in actual vertical velocity moves southwards along the cold front over time to regions which have not experienced the same degree of ventilation as the warm sector has done, and hence have more tracer available for venting.

### 6.5.5 Quantifying ventilation using QG theory

It has been shown in section 6.5.4 that using the Quasi-Geostrophic vertical velocity in place of the actual vertical velocity when estimating the amount of ventilation out of the boundary-layer is a reasonable approximation to make. This approximation is especially valid during the growth stages of cyclogenesis. This indicates that a strong correlation should exist between a QG-based diagnostic for the strength of the warm conveyor belt and the actual amount of boundary-layer ventilation. This can be tested by plotting the amount of ventilation against  $f_0 \frac{\partial U_g}{\partial z} / 2N^2$ , which is proportional to the strength of the QG vertical motion (equation 6.14), and therefore the intensity of the warm conveyor belt. The values of all parameters ( $f_0$ ,  $\partial U_g / \partial z$  and  $N$ ) in this diagnostic are calculated for all experiments from the initial conditions.  $f_0$  is calculated based on the latitude that the zonal jet is initially centred upon.  $\partial U_g / \partial z$  is calculated using  $U_0 / z_t$  where  $U_0$  is the maximum jet strength in the initial conditions and  $z_t$  is the height of the jet.  $N$  is calculated from the specified tropospheric potential temperature profile. Figure 6.20a shows the maximum domain-integrated rate of ventilation of mass that occurs during the whole life cycle for the 11 different experiments plotted against the proxy for warm conveyor belt strength. A very strong correlation can be seen. This implies that the large-scale dynamics exert a strong control on the rate of ventilation of mass. Figure 6.20b is the same except for tracer, and again a high degree of correlation is seen between

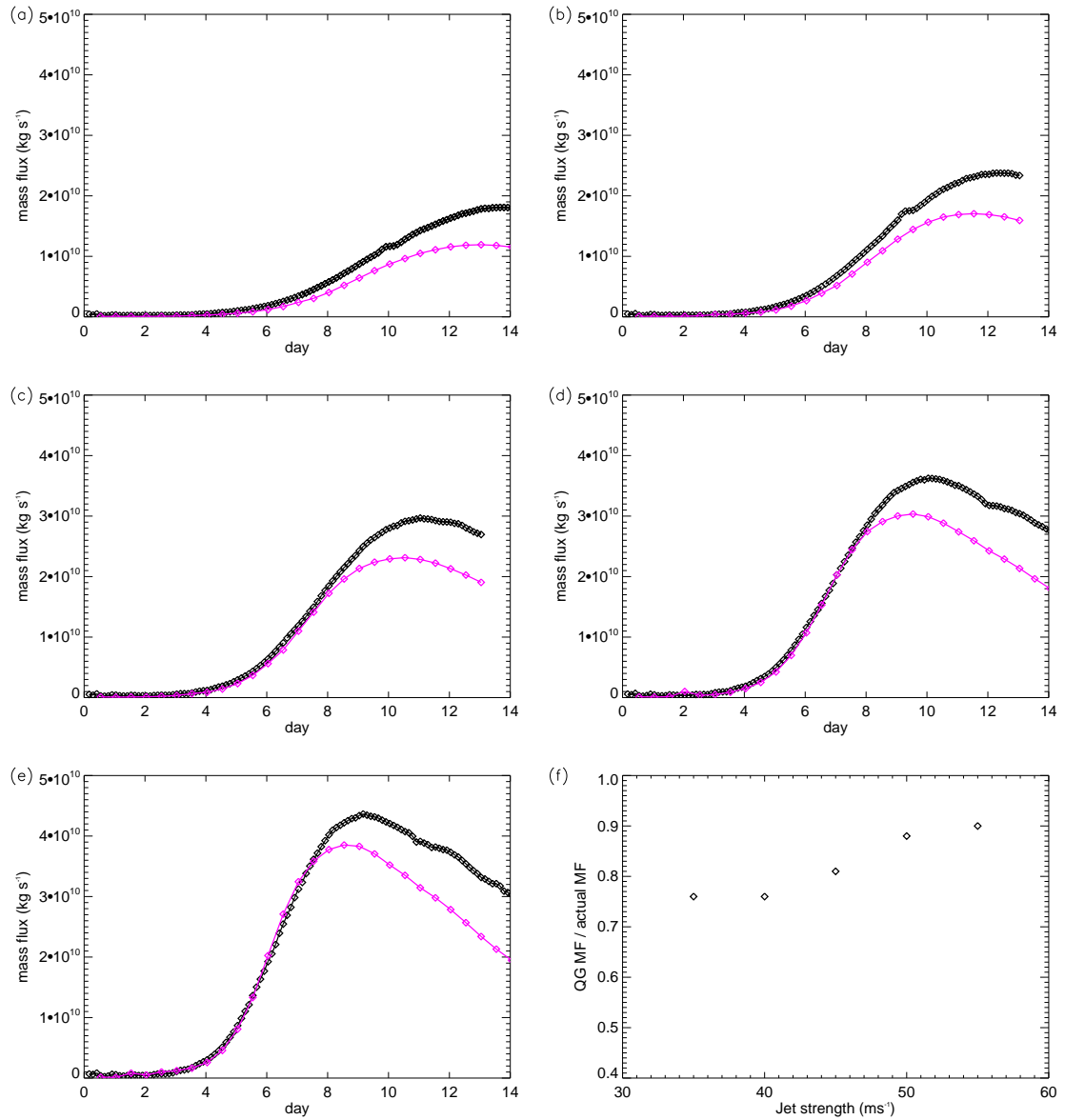


**Figure 6.18:** Domain-integrated mass flux out of the boundary layer (black lines) and the Quasi-Geostrophic domain integrated mass flux (purple line) as a function of time for different jet strength experiments. (a) 35 m s<sup>-1</sup>, (b) 40 m s<sup>-1</sup>, (c) 45 m s<sup>-1</sup>, (d) 50 m s<sup>-1</sup>, (e) 50 m s<sup>-1</sup>. (f) The ratio of the Quasi-Geostrophic time and domain-integrated mass flux to the actual time and domain-integrated mass flux versus jet strength.

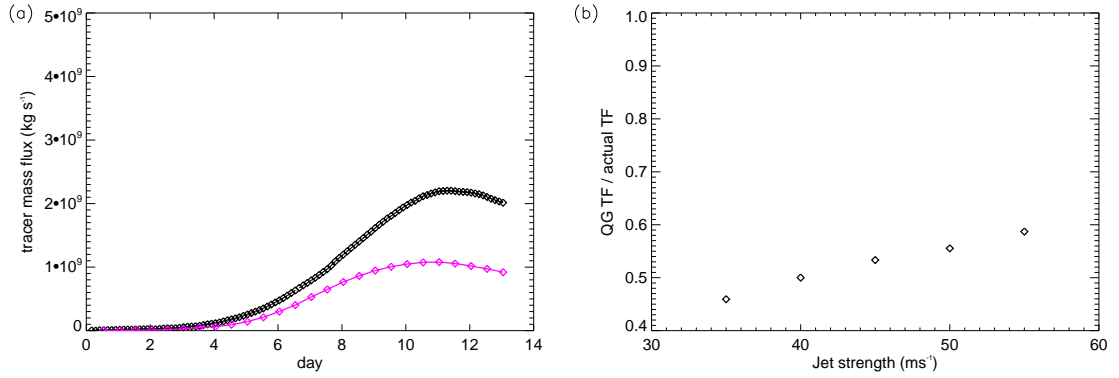


**Figure 6.19:** (a) Domain-integrated tracer flux out of the boundary layer (black lines) and the Quasi-Geostrophic domain-integrated tracer flux (purple line) as a function of time for the control experiment ( $U_{\text{jet}}=45 \text{ m s}^{-1}$ ). (b) Ratio of the Quasi-Geostrophic time and domain-integrated tracer flux to the actual time and domain-integrated tracer flux for different jet strengths.

the QG-based diagnostic and the rate of tracer transport out of the boundary layer. It should be noted that the source strength controls the absolute rate of ventilation, however changing the source strength would not change the gradient of Figure 6.20b due to the reasons discussed in section 6.3.

Figures 6.20c and 6.20d show the total amount of mass and tracer ventilated over the whole domain and over the whole evolution of the life cycle (days 0 to 13). A strong linear correlation is found to exist between the QG-based diagnostic and the total amount of ventilation. To quantify the relationships shown in Figure 6.20 the R-squared values, y-intercept values and the gradients of the best fit lines that could be fitted to the data are shown in Table 6.1. The gradients for all four regressions are strongly positive, which demonstrates that as the system's strength increases, the amount of ventilation does as well. In all cases the best fit line does not go through the origin; all of the y-intercept values are far from zero. In Figures 6.20a, 6.20c and 6.20d the y-intercept is negative, which indicates that ventilation will be zero when  $f_0 \frac{\partial U_g}{\partial z} / 2N^2$  is small but positive. This suggests that QG theory does not apply in this region of the parameter space, which is plausible as baroclinic systems would not be expected to develop with such weak forcing.

## 6.6 Summary

The aim of this Chapter was to investigate the relative importance of the three transport processes identified in Chapter 5, and to identify which process controls the amount of

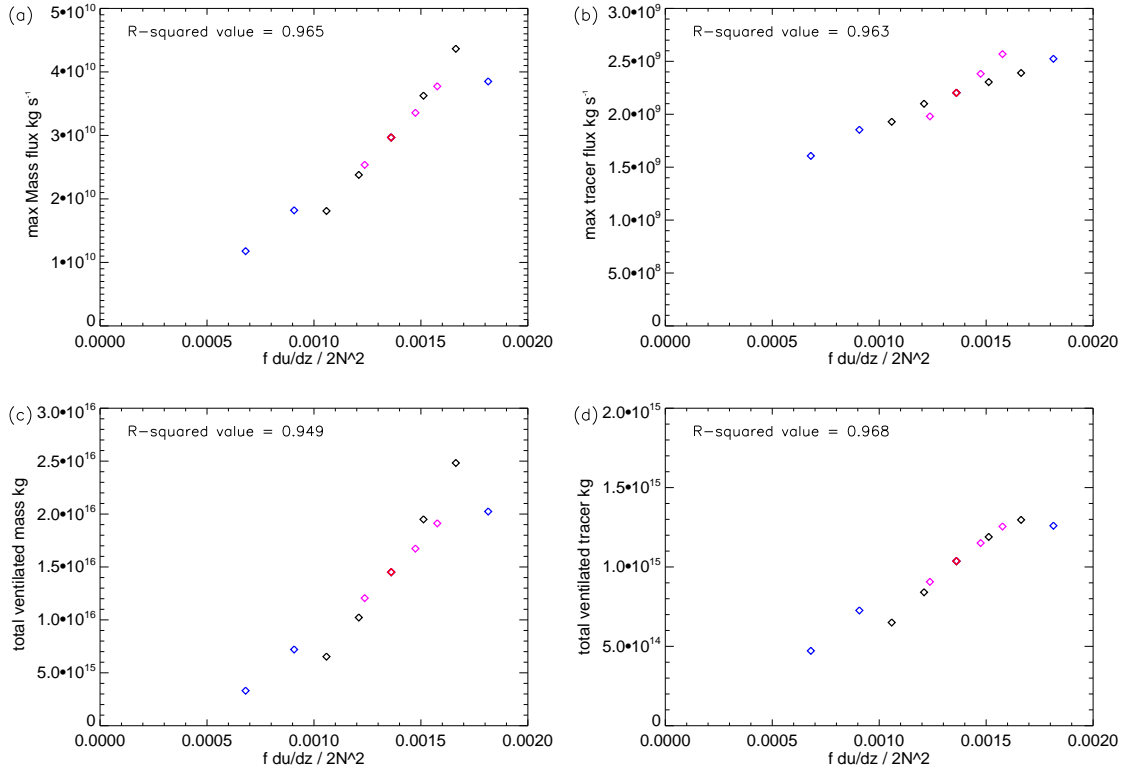


**Figure 6.20:** (a) Maximum domain integrated instantaneous mass flux against the QG diagnostic (dimensionless) for all experiments with different values of jet strength (black points), latitude (purple points) and stability (blue points). The red point is the control simulation. (b) Same as (a) but for tracer instead of mass. (c) Total ventilated mass plotted against QG diagnostics, colours are the same as in (a). (d) Same as (c) but for ventilated tracer not mass.

ventilation. This was achieved by simulating a number of idealised baroclinic life cycles in the idealised version of the Met Office Unified Model. Two sets of experiments were conducted, one to quantify the importance of the boundary-layer transport processes, and one to quantify the importance of the large-scale dynamics.

The results have shown that the amount of boundary-layer ventilation is controlled by the large-scale dynamics, and therefore the strength of the warm conveyor belt acts as the rate limiting step in determining the amount of ventilation. This can be concluded due to the strong correlation that was found between a QG-based diagnostic,  $f \frac{\partial u_g}{\partial z} / 2N^2$ , and both the maximum rate of ventilation and the total amount of ventilation out of the boundary layer. This correlation was found to be linear. In direct contrast, the surface drag, and hence the horizontal convergence and divergence within the boundary layer, was found to have little impact on the amount of mass ventilated out of the boundary-layer (the amount of tracer ventilated was found to be insensitive to surface drag once realistic

**Table 6.1:** Properties of the linear relationships shown in Figure 6.20

Panel in Fig. 6.20	Variable	R <sup>2</sup> value	y-intercept	gradient
(a)	maximum mass flux	0.965	$-9.13 \times 10^9 \text{ kg s}^{-1}$	$2.87 \times 10^{13} \text{ kg s}^{-1}$
(b)	maximum tracer flux	0.963	$1.04 \times 10^9 \text{ kg s}^{-1}$	$8.55 \times 10^{11} \text{ kg s}^{-1}$
(c)	total mass flux	0.949	$-1.08 \times 10^{16} \text{ kg}$	$1.88 \times 10^{19} \text{ kg}$
(d)	total tracer flux	0.968	$-7.01 \times 10^{13} \text{ kg}$	$8.00 \times 10^{17} \text{ kg}$

values of drag were used, but more sensitive when very small ( $C_d \leq 0.1 \times 10^{-3}$ ), and un-realistic, surface drag values were used). This does not mean that the boundary-layer transport processes are un-important, but shows that the horizontal transport within the boundary layer is not a limiting step on the efficiency of cyclones to ventilate the boundary layer.

In the experiments with very little drag, strong stratifications within the warm sector developed, which trapped the tracer near the surface, preventing mixing to the upper parts of the boundary-layer, and therefore reducing the amount of ventilation. Additionally, during the later stages of the life cycles with weak surface drag, the importance of the horizontal transport of tracer within the boundary-layer was realised. With little drag the horizontal convergence of tracer into the warm conveyor belt source region was weaker than the removal of tracer due to the warm conveyor belt's ascent, and therefore in this un-physical parameter space the rate limiting step is the horizontal divergence and convergence within the boundary layer.

---

## CHAPTER SEVEN

# Conclusions and Discussion

---

The overall aim of this thesis was to develop a thorough understanding of how dry mid-latitude weather systems transport pollutants out of the boundary layer and into the free troposphere. The approach taken in this thesis to address this aim differs somewhat to the case study approach used in the vast majority of previous studies. An idealised modelling approach was used, as it allowed for more controlled experiments to be performed, and for the complex problem to be reduced to only its crucial ingredients; transport by boundary-layer turbulent mixing, transport by frictionally-induced horizontal motions within the boundary layer and transport of tracer by large-scale advection. Decreasing the amount of complexity, such as removing transport by moist processes, meant that these processes could be understood clearly.

A review of the literature in Chapter 1 highlighted that transport of pollutants once in the free troposphere has been investigated frequently by numerous authors and consequently is reasonably well understood. In contrast, transport of pollutants on synoptic scales within the boundary layer had not received any significant attention in previous studies. On smaller scales, pollution transport within the boundary layer has been studied in detail, for example, the distribution of pollutants in urban areas and the evolution of pollution plumes from smoke-stacks. These studies have shown the structure of the boundary layer to be fundamental in determining the resulting pollution distribution. This provided the motivation for the first section of the thesis, which is presented in Chapter 4; how do synoptic-scale weather systems affect the structure of the boundary layer? Although many conceptual models of boundary-layer structure exist, for example the diurnal cycle, no conceptual model previously existed for boundary layers driven by

synoptic-scale forcing, and therefore this was one aim of this thesis. Chapter 4 also quantified how air is exchanged between the boundary layer and free troposphere, indicating the potential regions where the boundary layer could be ventilated and also the magnitude of the ventilation. The interaction between the large-scale dynamics and the boundary-layer structure was investigated by simulating two contrasting life cycles, LC1 and LC2, in the Reading Intermediate Global Circulation Model (IGCM).

The second aim of this thesis was to identify the physical processes that lead to the transport of pollutants within the boundary layer and free troposphere. This was achieved by adding a passive tracer to the simulations of LC1 and LC2 in the IGCM. The tracer was re-distributed throughout the domain by the model-resolved winds and the turbulence diagnosed by the boundary-layer parameterisation scheme. Initialising the tracer at the lowest model level of the IGCM and including a realistic boundary-layer scheme allowed for the transport of tracer within the boundary layer to be investigated in detail. The transport above the boundary-layer was also analysed by examining tracer concentration in the troposphere. The results of this were discussed in Chapter 5.

The final aims of this thesis were to quantify the efficiency of mid-latitude cyclones in ventilating the boundary-layer and to identify which atmospheric parameters determine the amount of ventilation. This was investigated in Chapter 6 by simulating sixteen life cycles in the idealised version of the Met Office Unified Model. Two sets of experiments were designed and conducted. The first set aimed to quantify the importance of the boundary-layer transport processes, which was achieved by simulating five life cycles with different surface drag coefficients, and therefore different boundary-layer structures. The second set of experiments was designed to test the importance of the large-scale dynamics and hence the transport of pollutants out of the boundary-layer by the warm conveyor belt. Eleven experiments were conducted with differing values of large-scale variables; jet strength, jet latitude and tropospheric stability. These parameters were identified as having a potentially large effect on the strength of ascent out of the boundary layer by scaling the Quasi-Geostrophic omega equation.

## 7.1 Main Conclusions

The structure of the boundary layer has been shown to be strongly coupled to the large-scale dynamics. Low-level thermal advection is the driving force of the boundary-layer

structure on synoptic scales in these idealised life cycles. In the warm sector of both LC1 and LC2 warm air is advected northwards over cooler surface temperatures resulting in negative heat fluxes and stable stratifications. In contrast, on the eastern edge of the anticyclone there are strong northerly winds advecting cold air over warmer surfaces, inducing large positive heat fluxes and deep convective boundary layers. The mass budget analysis showed that mass is transported into the boundary layer by entrainment behind the cold front, and by large-scale subsidence in the central regions of the anticyclone. Air was found to be transported from the boundary-layer to the free troposphere by large-scale ascent in the warm sector of the cyclone. The mass budgets demonstrated that regions of the boundary layer can lose or gain mass due to horizontal advection of mass within the boundary layer by large-scale induced, and frictionally-enhanced, divergence and convergence. Mass was shown to be diverged out of the anticyclonic region and converged into the warm sector region. These results indicate that air can be cycled between the boundary layer and free troposphere on synoptic time and spatial scales, which has important consequences. Firstly, this shows that the boundary layer modifies the properties of tropospheric air, as it is likely that the majority of tropospheric air in the mid-latitudes has recently been transported through the boundary layer. Secondly, this demonstrates that the passage of a mid-latitude cyclone can completely remove, and replace, all of the air originally contained within the boundary layer. In the warm sector, the boundary layer loses mass at an approximate rate of  $0.03 \text{ kg m}^{-2} \text{ s}^{-1}$ . Over a day this corresponds to a transfer of approximately 2500 kg of air, per unit area, from the boundary layer to the troposphere. The boundary layer in the warm sector has a typical depth of 1000 m, and hence the boundary-layer integrated mass per unit area is 1000 kg. Therefore, during one day a cyclone can easily completely remove the original boundary-layer air mass. The rate that mass is transported out of the boundary layer by the cyclones in this idealised study agrees reasonably well with results from Cotton *et al.* (1995), who made global estimates of the rate of boundary-layer ventilation associated with many different types of cloud systems. Cotton *et al.* (1995) estimated that each mid-latitude cyclone ventilated  $1 \times 10^{16} \text{ kg}$  of mass out of the boundary layer, and by assuming that each cyclone lasted five days and covered an area of  $1.4 \times 10^6 \text{ km}^2$ , calculated that, on average, a mid-latitude cyclone will vent the boundary layer at a rate of  $0.016 \text{ kg m}^{-2} \text{ s}^{-1}$ .

The evidence for transport within the boundary layer by divergence and convergence has important consequences for air quality and pollution transport studies. It suggests

that long range transport of atmospheric pollutants can occur within the boundary layer as well as in the free troposphere. Finally, it has been emphasised that there are strong interactions between boundary layer and synoptic-scale processes, which suggests that to fully understand boundary-layer, or synoptic-scale features, it may be necessary to consider processes at a range of scales.

Chapter 5 investigated the physical processes that transport pollutants within the boundary layer and free troposphere. The first conclusion drawn from Chapter 5 is that pollutants are transported by three physical processes. They are:

1. vertical turbulent mixing within the boundary layer,
2. horizontal transport within the boundary layer due to Ekman induced motions (convergence and divergence),
3. transport across the boundary-layer top and through the free troposphere due to large-scale advection, associated with the warm conveyor belt.

A second important conclusion from Chapter 5 is that all three of these processes are highly interlinked, indicating that transport on all spatial and temporal scales needs to be considered together rather than as independent processes.

Since two out of the three transport processes occur in the boundary layer, this stresses the importance of the boundary-layer structure; the boundary-layer transport processes determine the distribution of pollutants at low levels where they have the greatest impact on day to day life. Additionally, as turbulent mixing and horizontal advection affect the amount of tracer located in the conveyor belt source region this suggests that it is necessary to consider boundary-layer processes in ventilation studies, even on synoptic scales. Previous studies which examined transport by conveyor belts have not considered the tracer distribution within the boundary layer, but have identified turbulent mixing to increase the amount of boundary-layer ventilation. Agustí-Panareda *et al.* (2005) found that when only advection acted on a passive tracer significantly less tracer was removed from the boundary layer than when turbulent mixing and advection were allowed to act together.

Chapter 5 also confirmed the warm conveyor belt to be the dominant pollution transport process once pollutants are in the free troposphere. No boundary-layer ventilation or pollution transport by the cold conveyor belt was identified, which is thought to be due to

the lack of moisture in these experiments. However, even if moisture was included, transport by the cold conveyor belt is expected to be less than the warm conveyor belt. Firstly, because in conceptual models of cyclones the cold conveyor belt is weaker, and secondly, because in previous case studies the cold conveyor belt has not been found to ventilate the boundary layer. The warm conveyor belt was found to actively ventilate the boundary layer for up to four days and to have a meridional extent ranging from 35°N to 60°N. The amount of ventilation between LC1 and LC2 was remarkably similar up until day 12 and, by day 15, LC1 had ventilated 42% of the tracer out of the boundary layer and LC2 50%. This suggests that the strength of the baroclinicity, which is the same in the initial conditions of LC1 and LC2, exerts a control on the efficiency of mid-latitude cyclones to ventilate the boundary layer. In simulations of LC1 and LC2 without a boundary-layer scheme acting, Polvani and Esler (2007) also found that the amount of boundary-layer ventilation by LC1 and LC2 is very similar. However, the percentage of tracer found to be ventilated out of the boundary layer by Polvani and Esler (2007) is much lower than found here. Polvani and Esler (2007) find that LC1 (LC2) ventilates 17% (14%) and 31% (31%) of tracer initialised beneath 0.5 km and 2.5 km respectively, whereas in this thesis, where a boundary-layer scheme is included, values between 40% and 50% are found. This comparison suggests that the inclusion of a boundary-layer parameterisation scheme, and hence the turbulent mixing and Ekman divergence processes, increases the amount of boundary-layer ventilation. However, it should be noted that the inclusion of a boundary-layer parameterisation scheme does not change the similarity in the amount of ventilation between LC1 and LC2.

It would be inappropriate to directly compare the percentages obtained in this idealised study with those found in previous case studies due to differences in the domain size (the domain used here extends from the pole to equator) and in the method of tracer initialisation. Additionally, the quantitative values of boundary-layer ventilation reported here may differ from those found in the real atmosphere due to the assumptions made in this idealised framework; for example moist processes were excluded in these experiments. Including moist processes, and therefore latent heat release, would decrease the static stability and lead to stronger ascent, as well as increasing the growth rate of the baroclinic life cycle. Combined, these two consequences of moisture are likely to lead to more rapid transport of tracer, and transport of tracer to higher levels. However, the inclusion of moisture would also result in the tracer being transported by convection. This transport

would be on much faster timescales than transport by conveyor belts, and if included here would likely increase the amount of boundary-layer ventilation. It has been shown that, when comparing the efficiency of mid-latitude cyclones to ventilate the boundary layer, the percentage of tracer transported to the free troposphere is an inappropriate diagnostic, and a much more meaningful diagnostic is the mass or tracer flux out of the boundary layer. By considering a flux, the rate of ventilation is quantified, rather than just the total amount, and a mass or tracer flux is much less sensitive to the domain size than a percentage value is.

Although the amount of ventilation is found to be remarkably similar between LC1 and LC2, the regions of the boundary layer that are ventilated differ between the two life cycles; the region of maximum ventilation is further north in LC2 than in LC1. This is a consequence of the differing degrees of meridional displacement that the two life cycles experience, which occurs due to the background state that the initial perturbation develops in. Therefore, if there is a preference for either type of background state (cyclonically or anticyclonically sheared) to dominate within a storm track then there will also be a preference in the boundary-layer locations to be ventilated by the resulting cyclones. The background state of the storm tracks has previously been documented to be related to climatic states such as the North Atlantic Oscillation (NAO) and the El Niño Southern Oscillation (ENSO). The positive phase of the NAO is found to be related with anticyclonically breaking synoptic scale waves, and the negative phase cyclonic breaking (Rivière and Orlanski, 2007). Additionally, Eckhardt *et al.* (2004) found that when the NAO is in a positive phase warm conveyor belt transport is faster and directed further north. Shapiro *et al.* (2001) found that during the 1997 - 99 ENSO cycle the upper level jet was displaced in the meridional direction which altered the barotropic wind shear over the Central and Eastern Pacific storm track, and hence influenced the evolution of extra-tropical cyclones.

The relative importance of the three transport processes was investigated in Chapter 6 by conducting two sets of experiments. Life cycles were simulated in the U.M. with either different large-scale dynamics or different surface drag coefficients to determine whether the large-scale advection, or the horizontal convergence and divergence within the boundary layer, is the limiting step in determining the amount of boundary-layer ventilation.

A diagnostic based on Quasi-Geostrophic theory has been developed to estimate the baroclinicity, and therefore the strength of ascent, in a mid-latitude cyclone. Strong

correlations were found to exist between this diagnostic and both the total amount of ventilation and the maximum rate of ventilation. This strong correlation between the large-scale dynamics and the amount of ventilation shows that advection by the warm conveyor belt is the transport process which acts as the limiting step, and therefore determines the amount of boundary-layer ventilation. This has significant consequences; it indicates that using Lagrangian trajectory models to study pollution transport will capture the majority of the transport in non-convective conditions. This is an approach taken previously by numerous authors, but with little proof for neglecting boundary-layer processes (most trajectory models such as FLEXPART (Stohl *et al.*, 2005) do include an estimate of turbulent transport but the turbulence is estimated using the Langevin equation, and therefore is statistically based). The results presented here provide justification for this approach.

It was shown that the ventilation of mass was insensitive to the surface drag coefficient. This shows that transport by the frictionally-enhanced divergence and convergence within the boundary layer is not a constraining, or limiting, factor in the ventilation process. The amount of tracer ventilated was found to be sensitive to the drag coefficient, but only when very smooth surfaces ( $C_d \leq 0.1 \times 10^{-3}$ ) were considered. In the experiments with little drag the amount of tracer ventilated into the free troposphere decreased considerably compared to the experiments with higher drag coefficients. Additionally, the tracer flux decreased at stages of the life cycle when the mass flux was still increasing, implying that the life cycles were not fully achieving their potential for ventilation. Without surface friction, very strong stable stratifications developed in the warm sector, which prevented the tracer from mixing in the vertical to the upper parts of the boundary-layer, which is where the warm conveyor belt removes tracer from. In the experiments with little surface drag, the absence of friction was found to reduce the horizontal convergence of tracer into the source regions of the warm conveyor belt during the later stages of the life cycle. This meant that the warm conveyor belt began to run out of tracer to ventilate, and that the full tracer ventilation potential of the life cycle was not realised. This shows that in the case of un-physically smooth surfaces the limiting transport process is horizontal convergence and divergence within the boundary layer.

These results show that from a theoretical viewpoint, two possible ventilation regimes exist; one over rough (realistic) surfaces in which the large-scale dynamics limit the amount of ventilation, and the second over very smooth (un-realistic) surfaces where

boundary-layer transport processes limit the amount of ventilation. However, the second regime does not occur within realistic parameter space, and therefore would not be observed in any ventilation case studies.

These results have considerable consequences for climatology studies. The large-scale dynamical variables that are required to estimate the QG diagnostic are commonly available in re-analysis datasets, such as ERA-40. Therefore, climatologies of boundary-layer ventilation could be derived by estimating the QG diagnostic for each cyclone in different storm tracks, and therefore obtaining an estimate of the potential amount of ventilation. Additionally, as the amount of ventilation was found to be independent of the magnitude of surface drag, it would not be necessary to treat cyclones over land differently to those over the ocean in a climatology study. This would simplify the task of calculating a climatology considerably.

## 7.2 Future work

The results found from the idealised modelling experiments presented in this thesis have enhanced the understanding of how pollutants are ventilated out of the boundary layer by mid-latitude weather systems. However, to understand the complex problem of boundary-layer ventilation, considerable simplifications to reality were made in this thesis and many potentially important processes were omitted from the experiments. Primarily, these include moist processes, the diurnal cycle, temporal variations in the surface temperatures and spatial variations in surface type (roughness). Additionally, the tracer that was used in all experiments was a highly simplified approximation to a pollutant; no sinks, such as chemical destruction or dry deposition, were included.

If this work was to be continued, further degrees of complexity should be added, one by one, to the idealised simulation. The absence of a diurnal cycle means that the boundary-layer structure in these experiments is only influenced by synoptic-scale forcing. If a diurnal cycle was included the relative importance of the diurnal cycle forcing of the boundary layer to the synoptic forcing could be quantified. The inclusion of a diurnal cycle would also introduce a new process for transporting pollutants from the boundary layer to the free troposphere. During the daytime, pollutants are mixed throughout the boundary layer. At sunset the boundary layer collapses, leaving pollutants in the residual layer above the boundary layer where there is little turbulence. When this occurs the

pollutants form a low-level layer which is decoupled from the surface and therefore the pollutants have effectively been transported into the free troposphere. The significance of this processes in the overall amount of ventilation could be quantified if a diurnal cycle was included.

Moisture could also be added to the simulations, which would introduce pollution transport by convection. Embedded convection within the frontal zones and the warm conveyor belt, along with shallow convection in the cold air behind the cold front, would enhance the amount of ventilated tracer, but without performing the experiments it is difficult to estimate by how much. Therefore, if a moist idealised life cycle was simulated, an attempt at quantifying the relative importance of transport by convection and transport by advection could be made. Additionally, if a range of moist life cycles were performed, an investigation into which types of life cycles are more likely to be dominated by convective, rather than advective, transport could be performed. However, as well as introducing a new transport process, including moisture would increase the growth rate and intensity of the life cycles, which may also alter the efficiency of the life cycles to ventilate the boundary layer.

Complexity could also be added to the simulations by introducing sinks of tracer, mainly dry deposition, wet deposition (rain out) and chemical destruction. The simplest way to introduce chemical destruction would be to examine the transport of multiple tracers with different (constant) decay rates, and investigate how the chemical sink affects the tracer distribution. A slightly more complex, and more realistic, method would be to introduce tracers which have decay rates that are dependent on temperature. This would allow the idealised experiments to be closer to reality in terms of chemical behaviour.

A second approach which could be taken to extend the work presented in this thesis towards more realistic situations would be to apply the results of Chapter 6 to re-analysis data such as the ERA-40 dataset. The potential for ventilation for each cyclone within the dataset could be estimated using the Quasi-Geostrophic diagnostic developed in Chapter 6. This would provide the opportunity to develop a climatology of boundary-layer ventilation by mid-latitude weather systems. The regions of the boundary-layer on a global scale that are most likely to be ventilated could be located and compared with the latitude bands identified in Chapter 5. A time series of boundary-layer ventilation over the 40 years that ERA-40 is available for could also be calculated, allowing for any changes in boundary-layer ventilation to be quantified.

---

# References

---

- Adamson, D. S. (2001). Boundary layer frictional processes in mid-latitude cyclones. *University of Reading, Ph.D. thesis.*
- Adamson, D. S., Belcher, S. E., Hoskins, B. J., and Plant, R. S. (2006). Boundary-layer friction in midlatitude cyclones. *Q. J. R. Meteorol. Soc.*, **132**, 101–124.
- Agustí-Panareda, A., Gray, S., and Methven, J. (2005). Numerical modeling study of boundary layer ventilation by a cold front over Europe. *J. Geophys. Res.*, **110**, D18304.
- Arya, S. P. (1999). *Air pollution meteorology and dispersion*. Oxford University Press.
- Arya, S. P. (2001). *Introduction to Micrometeorology*. Academic Press.
- Bader, M. J., Forbes, G. S., Grant, J. R., Lilley, R. B. E., and Waters, A. J. (1995). *Images in weather forecasting*. Cambridge University Press.
- Balasubramanian, G. and Garner, S. T. (1997). The role of momentum fluxes in shaping the life cycle of a baroclinic wave. *J. Atmos. Sci.*, **54**, 510–533.
- Beare, R. J. (2007). Boundary layer mechanisms in extratropical cyclones. *Q. J. R. Meteorol. Soc.*, **133**, 503–515.
- Beljaars, A. C. M. and Holtslag, A. A. M. (1991). Flux parameterization over land surfaces for atmospheric models. *J. Appl. Meteor.*, **30**, 327–341.
- Bethan, S., Vaughan, G., Gerbig, C., Volz-Thomas, A., Richer, H., and Tiddeman, D. A. (1998). Chemical air mass differences near fronts. *J. Geophys. Res.*, **D11**, 13413–13434.
- Betts, A. K. (1986). A new convective adjustment scheme. I: Observational and theoretical basis. *Q. J. R. Meteorol. Soc.*, **112**, 677–691.

- Bey, I., Jacob, D. J., Logan, J. A., and Yantosca, R. M. (2001). Asian chemical outflow to the Pacific in Spring: Origins, pathways, and budgets. *J. Geophys. Res.*, **106**, 23097–23113.
- Blackadar, A. K. (1962). The vertical distribution of wind and turbulent exchange in a neutral atmosphere. *J. Geophys. Res.*, **97**, 3095 – 3102.
- Bond, N. A. and Fleagle, R. G. (1988). Prefrontal and postfrontal boundary layer processes over the ocean. *Mon. Wea. Rev.*, **116**, 1257–1273.
- Branscome, L. E., Gutowski Jr, W. J., and Stewart, D. A. (1989). Effect of surface fluxes on the non-linear development of baroclinic waves. *J. Atmos. Sci.*, **46**, 460–475.
- Bretherton, F. P. (1966). Critical layer instability in baroclinic flows. *Q. J. R. Meteorol. Soc.*, **92**, 325–334.
- Browning, K. A. (1985). Conceptual models of precipitating systems. *Meteor. Mag.*, **114**, 293–319.
- Browning, K. A. and Roberts, N. M. (1994). Structure of a frontal cyclone. *Q. J. R. Meteorol. Soc.*, **120**, 1535 – 1557.
- Businger, J. A. and Charnock, H. (1983). Boundary layer structure in relation to larger-scale flow: Some remarks on the JASIN observations. *Phil. Trans. R. Soc. Lond. A*, **308**, 445–449.
- Card, P. and Barcilon, A. (1982). The Charney stability problem with a lower Ekman layer. *J. Atmos. Sci.*, **39**, 2128–2137.
- Carlson, T. N. (1980). Airflow through mid-latitude cyclones and the comma cloud pattern. *Mon. Wea. Rev.*, **108**, 1498–1509.
- Carson, D. J. (1973). The development of a dry inversion-capped convectively unstable boundary layer. *Q. J. R. Meteorol. Soc.*, **99**, 450–467.
- Charney, J. G. (1947). The dynamics of long waves in a baroclinic westerly current. *J. Atmos. Sci.*, **4**, 136–162.
- Charnock, H. (1955). Wind stress on a water surface. *Q. J. R. Meteorol. Soc.*, **81**, 639–640.
- Chelton, D. B., Mestas-Nunez, A. M., and Freilich, M. H. (1990). Global wind stress and Sverdrup circulation from the Seasat scatterometer. *J. Phys. Oceanogr.*, **20**, 1175 – 1205.

- Chou, S. H., Nelkin, J., Ardizzone, J., Atlas, R. M., and Shie, C. L. (2003). Surface turbulent heat and momentum fluxes over global oceans based on Goddard Satellite Retrievals, version 2 (GSSTF2). *J. Climate*, **16**, 3256 – 3273.
- Cooper, O. R., Moody, J., Parrish, D., Trainer, M., Ryerson, T., Holloway, J., Hubler, G., Fehsenfeld, F. C., Oltmans, S., and Evans, M. J. (2001). Trace gas signature of the airstreams within north atlantic cyclones: Case studies from the north atlantic regional experiment (NARE'97) aircraft intensive. *J. Geophys. Res.*, **106**, 5437–5456.
- Cooper, O. R., Moody, J., Parrish, D., Trainer, M., Ryerson, T., Holloway, J., Ryerson, T., Hubler, G., Fehsenfeld, F. C., and Evans, M. J. (2002). Tracer gas composition of mid-latitude cyclones over the western north atlantic ocean: A conceptual model. *J. Geophys. Res.*, **107**, 4056.
- Cooper, O. R., Forster, C., Parrish, D., Trainer, M., Dunlea, E., Ryerson, T., Hubler, G., Fehsenfeld, F., Nicks, D., Holloway, J., de Gouw, J., Warneke, C., Roberts, J. M., Flocke, F., and Moody, J. (2004). A case study of transpacific warm conveyor belt transport: Influences of merging airstream on trace gas import to North America. *J. Geophys. Res.*, **109**, D23S08.
- Cotton, W. R., Alexander, G. D., Hertenstein, R., Walko, R. L., McAnelly, R. L., and Nicholls, M. (1995). Cloud venting - a review and some new global estimates. *Earth Science Reviews*, **39**, 169 – 206.
- Dacre, H. F. and Gray, S. L. (2006). Life cycle simulations of shallow frontal waves and the impact of deformation strain. *Q. J. R. Meteorol. Soc.*, **132**, 2171–2190.
- Dacre, H. F., Gray, S. L., and Belcher, S. E. (2007). A case study of boundary layer ventilation by convection and coastal processes. *J. Geophys. Res.*, **112**, D17106.
- Danielsen, E. F. (1993). In situ evidence of rapid, vertical, irreversible transport of lower tropospheric air into the lower tropical stratosphere by convective cloud turrets and by larger-scale upwelling in tropical cyclones. *J. Geophys. Res.*, **98**, 8665–8681.
- Davies, T., Cullen, M. J. P., Malcolm, A. J., Mawson, M. H., Staniforth, A., White, A. A., and Wood, N. (2005). A new dynamical core for the Met Office's global and regional modelling of the atmosphere. *Q. J. R. Meteorol. Soc.*, **131**, 1759–1782.

- Dickerson, R. R., Huffman, G. J., Luke, W. T., Nunnermacker, L. J., Pickering, K. E., Leslie, A. C. D., Lindsey, C. G., Slinn, W. G. N., Kelly, T. J., Daum, P. H., Delany, A. C., Greenberg, J. P., Zimmerman, P. R., Boatman, J. F., Ray, J. D., and Stedman, D. H. (1987). Thunderstorms: An important mechanism in the transport of air pollutants. *Science*, **235**, 460–465.
- Donnell, E., Fish, D. J., Dicks, E. M., and Thorpe, A. J. (2001). Mechanisms for pollutant transport between the boundary layer and the free troposphere. *J. Geophys. Res.*, **106**, 7847–7856.
- Eady, E. T. (1949). Long waves and cyclonic waves. *Tellus*, **1**, 33–52.
- Eckhardt, S., Stohl, A., Beirle, S., Spichtinger, N., James, P., Forster, C., Junker, C., Wagner, T., Platt, U., and Jennings, S. G. (2003). The North Atlantic Oscillation controls air pollution transport to the Arctic. *Atmos. Chem. Phys.*, **3**, 1769–1778.
- Eckhardt, S., Stohl, A., Wernli, H., James, P., Forster, C., and Spichtinger, N. (2004). A 15-year climatology of warm conveyor belts. *J. Climate*, **17**, 218–237.
- ECMWF Research Department (1991). ECMWF forecast model: Physical parameterizations. Research manual 3 (3rd ed.). Technical report, ECMWF, Reading, UK.
- Ekman, V. W. (1905). On the influence of the Earth's rotation on ocean currents. *Arkiv. Math. Astron. Fys.*, **2**, 1–53.
- Ertel, H. (1942). Ein neuer hydrodynamischer Wirbelsatz. *Met Z*, **59**, 277–281.
- Esler, J. G., Haynes, P. H., Law, K. S., Barjat, H., Dewey, K., Kent, J., Schmitgen, S., and Brough, N. (2003). Transport and mixing between airmasses in cold frontal regions during Dynamics and Chemistry of Frontal Zones (DCFZ). *J. Geophys. Res.*, **108**, 4142.
- Farrell, B. (1985). Transient growth of damped baroclinic waves. *J. Atmos. Sci.*, **42**, 2718–2727.
- Fischer, H., de Reus, M., Traub, M., Williams, J., Lelieveld, J., de Gouw, J., Warneke, C., Schlager, H., Minikin, A., Scheele, R., *et al.* (2003). Deep convective injection of boundary layer air into the lowermost stratosphere at midlatitudes. *Atmos. Chem. Phys.*, **3**, 739–745.

- Fleagle, R. G. and Nuss, W. A. (1985). The distribution of surface heat fluxes and boundary layer divergence in mid-latitude ocean storms. *J. Atmos. Sci.*, **42**, 784–799.
- Fuelberg, H. E., Kiley, C. M., Hannan, J. R., Westberg, D. J., Avery, M. A., and Newell, R. E. (2003). Meteorological conditions and transport pathways during the Transport and Chemical Evolution over the Pacific (TRACE-P) experiment. *J. Geophys. Res.*, **108**, 8782.
- Gimson, N. R. (1997). Pollution transport by convective clouds in a mesoscale model. *Q. J. R. Meteorol. Soc.*, **123**, 1805 – 1828.
- Hannan, J. R., Fuelberg, H. E., Crawford, J. H., Sachse, J. L., and Blake, D. R. (2003). Role of wave cyclones in transporting boundary layer air to the free troposphere during the Spring 2001 NASA/TRACE-P experiment. *J. Geophys. Res.*, **108**, 8785.
- Harrold, T. W. (1973). Mechanisms influencing the distribution of precipitation within baroclinic disturbances. *Q. J. R. Meteorol. Soc.*, **99**, 232–251.
- Henne, S., Furger, M., Nyeki, S., Steinbacher, M., Neining, B., de Wekker, S. F. J., Dommen, J., Spichtinger, N., Stohl, A., and Prevot, A. S. H. (2004). Quantification of topographic venting of boundary layer air to the free troposphere. *Atmos. Chem. Phys.*, **4**, 497–509.
- Hess, P. G. (2005). A comparison of two paradigms: The relative global roles of moist convective versus non-convective transport. *J. Geophys. Res.*, **110**, D20302.
- Hess, P. G. and Vukicevic, T. (2003). Intercontinental transport, chemical transformations and baroclinic systems. *J. Geophys. Res.*, **108**, 4354.
- Hines, K. M. and Mechoso, C. R. (1993). Influence of surface drag on the evolution of fronts. *Mon. Wea. Rev.*, **121**, 1152–1175.
- Hollingsworth, A., Simmons, A. J., and Hoskins, B. J. (1976). The effect of spherical geometry on momentum transport in simple baroclinic flows. *Q. J. R. Meteorol. Soc.*, **102**, 901–911.
- Holt, T. and Raman, S. (1990). Marine boundary layer structure and circulation in the region of offshore development of a cyclone during GALE. *Mon. Wea. Rev.*, **118**, 392–410.

- Holton, J. R. (1992). *An introduction to dynamical meteorology*. Academic Press.
- Holtstlag, A. A. M. and Boville, B. A. (1993). Local versus nonlocal boundary layer diffusion in a global climate model. *J. Climate*, **6**, 1825–1842.
- Hoskins, B. J. (1997). A potential vorticity view of synoptic development. *Meteorol. Appl.*, **4**, 325 – 334.
- Hoskins, B. J. and Simmons, A. J. (1975). A multi-layer spectral model and the semi-implicit method. *Q. J. R. Meteorol. Soc.*, **101**, 627–655.
- Hoskins, B. J., McIntyre, M. E., and Robertson, A. W. (1985). On the use and significance of isentropic potential vorticity maps. *Q. J. R. Meteorol. Soc.*, **111**, 877–946.
- Huntrieser, H., Heland, J., Schlager, H., Forster, C., Stohl, A., Arnold, F., Scheel, H. E., Campana, M., Gilge, S., Eixmann, R., and Cooper, O. (2005). Intercontinental air pollution transport from North America to Europe: Experimental evidence from airborne measurements and surface observations. *J. Geophys. Res.*, **110**, D01305.
- James, I. N. (1995). *Introduction to circulating atmospheres*. Cambridge University Press.
- Keyser, D. and Anthes, R. A. (1982). The influence of planetary boundary layer physics on frontal structure in the Hoskins - Bretherton horizontal shear model. *J. Atmos. Sci.*, **39**, 1783–1802.
- Kiley, C. M. and Fuelberg, H. E. (2006). An examination of summertime cyclone transport processes during Intercontinental Chemical Transport Experiment (INTEX-A). *J. Geophys. Res.*, **111**, D24S0.
- Kowol-Santen, J., Beekman, M., Schmitgen, S., and Dewey, K. (2001). Tracer analysis of transport from the boundary layer to the free troposphere. *Geophys. Res. Lett.*, **28**, 2907–2910.
- Leon, J. F., Chazette, P., Dulac, F., Pelon, J., Flamant, C., Bonazzola, M., Foret, G., Alfaro, S. C., Cachier, H., Cautenet, S., Hamonou, E., Gaudichet, A., Gomes, L., Rajot, J. L., Lavenu, F., Inamdar, S. R. and Sarode, P. R., and Kadadevarmath, J. S. (2001). Large-scale advection of continental aerosols during INDOEX. *J. Geophys. Res.*, **106**, 28.

- Li, Q., Jacob, D. J., Bey, I., Palmer, P. I., Duncan, B. N., Field, B. D., Martin, R. V., Fiore, A. M., Yantosca, R. M., Parrish, D., Simmonds, P. G., and Oltmans, S. J. (2002). Transatlantic transport of pollution and its effects on surface ozone in Europe and North America. *J. Geophys. Res.*, **107**, 4166.
- Li, Q., Jacob, D. J., Park, R., Wang, Y., Heald, C. L., Hudman, R., and Yantosca, R. M. (2005). North American pollution outflow and the trapping of convectively lifted pollution by upper-level anticyclone. *J. Geophys. Res.*, **110**, D10301.
- Lock, A. P., Brown, A. R., Bush, M. R., Martin, G. M., and Smith, R. N. B. (2000). A new boundary layer mixing scheme. Part 1: Scheme description and single-column model tests. *Mon. Wea. Rev.*, **128**, 3187–3199.
- Louis, J. F. (1979). A parametric model of vertical eddy fluxes in the atmosphere. *Boundary-Layer. Meteorol.*, **17**, 187–202.
- Lowry, W. P. (1967). The climate of cities. *Sci. Am.*, **217**, 15–23.
- Mari, C., Evans, M. J., Palmer, P. I., Jacob, D. J., and Sachse, G. W. (2004). Export of Asian pollution during two cold front episodes of the TRACE-P experiment. *J. Geophys. Res.*, **109**, D15S17.
- Monin, A. S. and Obukhov, A. M. (1954). Basic turbulent mixing laws in the atmospheric surface layer. *Tr. Geofiz. Inst. Akad. Nauk. SSSR.*, **24**, 163 – 187.
- Nakamura, N. (1993). Momentum flux, flow symmetry and the non-linear barotropic governor. *J. Atmos. Sci.*, **50**, 2159–2179.
- Neiman, P. J., Shapiro, M. A., Donall, E. G., and Kreitzberg, C. W. (1990). Diabatic modification of an extratropical marine cyclone warm sector by cold underlying water. *Mon. Wea. Rev.*, **118**, 1576–1590.
- Oke, T. R. and East, C. (1971). The urban boundary layer in Montreal. *Boundary Layer Meteorol.*, **1**, 411–437.
- Parker, D. J. (1999). Passage of a tracer through frontal zones: A model for the formation of forward sloping cold front. *Q. J. R. Meteorol. Soc.*, **125**, 1785 – 1800.
- Persson, P. O. G., Hare, J. E., Fairall, C. W., and Otto, W. D. (2005). Air-sea interaction processes in warm and cold sectors of extratropical cyclonic storms observed during FASTEX. *Q. J. R. Meteorol. Soc.*, **131**, 877–912.

- Petterssen, S. and Smebye, S. J. (1977). On the development of extratropical cyclones. *Q. J. R. Meteorol. Soc.*, **97**, 457 – 482.
- Plant, R. S. and Belcher, S. E. (2007). Numerical simulations of baroclinic waves with a parameterized boundary layer. *J. Atmos. Sci.*, **64**, 4383 – 4399.
- Pollard, R. T., Guymer, T. H., and Taylor, P. K. (1983). Summary of the JASIN 1978 field experiment. *Phil. Trans. R. Soc. Lond. A*, **308**, 221–230.
- Polvani, L. M. and Esler, J. G. (2007). Transport and mixing of chemical airmasses in idealized baroclinic lifecycles. *J. Geophys. Res.*, **112**, D23102.
- Purvis, R. M., Lewis, A. C., Carney, R. A., McQuaid, J. B., Arnold, S. R., Methven, J., Barjat, H., Dewey, K., Kent, J., Monks, P. S., Carpenter, L. J., Brough, N., Penkett, S. A., and Reeves, C. E. (2003). Rapid uplift of nonmethane hydrocarbons in a cold front over central Europe. *J. Geophys. Res.*, **108**, 4224.
- Rigby, M. and Toumi, R. (2008). London air pollution climatology: Indirect evidence for urban boundary layer height and wind speed enhancement. *Atmos. Environ.*, **42**, 4932–4947.
- Rivière, G. and Orlanski, I. (2007). Characteristics of the Atlantic storm track eddy activity and its relation with the North Atlantic Oscillation. *J. Atmos. Sci.*, **64**, 241 – 266.
- Roelofs, G.-J. and Lelieveld, J. (1995). Distribution and budget of O<sub>3</sub> in the troposphere calculated with a chemistry general circulation model. *J. Geophys. Res.*, **100**, 20,983–20,998.
- Rossby, C. G. (1940). Planetary flow patterns in the atmosphere. *Q. J. R. Meteorol. Soc.*, **66**, 68–87.
- Rotunno, R., Skamarock, W. C., and Snyder, C. (1994). An analysis of frontogenesis in numerical simulations of baroclinic waves. *J. Atmos. Sci.*, **51**, 3373–3398.
- Rotunno, R., Skamarock, W. C., and Snyder, C. (1998). Effects of surface drag on fronts within numerically simulated baroclinic waves. *J. Atmos. Sci.*, **55**, 2119–2129.
- Schultz, D. M. (2001). Reexamining the cold conveyor belt. *Mon. Wea. Rev.*, **129**, 2205–2225.

- Semple, A. T. (2003). A review and unification of conceptual models of cyclogenesis. *Meteorol. Appl.*, **10**, 39–59.
- Shapiro, M. A. and Keyser, D. A. (1990). Fronts, jet streams and the tropopause. In C. W. Newton and E. O. Holopainen, editors, *Extratropical cyclones: The Erik Palmén Memorial volume*. American Meteorological Society.
- Shapiro, M. A., Wernli, H., Bond, N. A., and Langland, R. (2001). The influence of the 1997-9 El Niño Southern Oscillation on extratropical baroclinic lifecycles over the Eastern North Pacific. *Q. J. R. Meteorol. Soc.*, **127**, 331–342.
- Simmons, A. J. and Hoskins, B. J. (1978). The lifecycles of some nonlinear baroclinic waves. *J. Atmos. Sci.*, **35**, 414–432.
- Snyder, C., Skamarock, W. C., and Rotunno, R. (1991). A comparison of primitive-equation and semigeostrophic simulations of baroclinic waves. *J. Atmos. Sci.*, **48**, 2179–2194.
- Stohl, A. (2001). A 1-year Lagrangian "climatology" of airstreams in the northern hemisphere troposphere and lowermost stratosphere. *J. Geophys. Res.*, **106**, 7263 – 7279.
- Stohl, A., Eckhardt, S., Forster, C., James, P., Spichtinger, N., and Seibert, P. (2002). A replacement for simple back trajectory calculations in the interpretation of atmospheric trace substance measurements. *Atmos. Environ.*, **36**, 4635–4648.
- Stohl, A., Forster, C., Eckhardt, S., Spichtinger, N., Huntrieser, H., Heland, J., Schlager, H., Wilhelm, S., Arnold, F., and Cooper, O. (2003a). A backward modeling study of intercontinental pollution transport using aircraft measurements. *J. Geophys. Res.*, **108**, 4370.
- Stohl, A., Huntrieser, H., Richter, A., Beirle, S., Cooper, O., Eckhardt, S., Forster, C., James, P., Spichtinger, N., Wenig, M., Wagner, T., Burrows, J., and Platt, U. (2003b). Rapid intercontinental air pollution transport associated with a meteorological bomb. *Atmos. Chem. Phys.*, **3**, 2101–2141.
- Stohl, A., Forster, C., Frank, A., Seibert, P., and Wotawa, G. (2005). Technical note: The Lagrangian particle dispersion model FLEXPART version 6.2. *Atmos. Chem. Phys.*, **5**, 4739–4799.

- Stone, E. M., Randel, W. J., and Stanford, J. L. (1999). Transport of passive tracers in baroclinic wave life cycles. *J. Atmos. Sci*, **56**, 1364–1381.
- Stull, R. B. (1988). *An Introduction to Boundary Layer Meteorology*. Kluwer Academic Publishers, first edition.
- Thompson, A. M., Pickering, K. E., Dickerson, R. R., Ellis Jr., W. G., Jacob, D. J., Scala, J. R., Tao, W. K., McNamara, D. P., and Simpson, J. (1994). Convective transport over the central United States and its role in regional CO and ozone budgets. *J. Geophys. Res.*, **99**, 18703 – 18711.
- Thorncroft, C. D. and Hoskins, B. J. (1990). Frontal cyclogenesis. *J. Atmos. Sci*, **47**, 2317–2336.
- Thorncroft, C. D., Hoskins, B. J., and McIntyre, M. E. (1993). Two paradigms of baroclinic-wave life-cycle behaviour. *Q. J. R. Meteorol. Soc.*, **119**, 17–55.
- Thuburn, J. (1993). Use of a flux-limited scheme for vertical advection in a GCM. *Q. J. R. Meteorol. Soc.*, **119**, 469 – 487.
- Trickl, T., Cooper, O. R., Eisele, H., James, P., Mücke, R., and Stohl, A. (2003). Inter-continental transport and its influence on the ozone concentrations over central Europe: Three case studies. *J. Geophys. Res.*, **108**, 8530.
- Troen, I. B. and Mahrt, L. (1986). A simple model of the atmospheric boundary layer; sensitivity to surface evaporation. *Boundary-Layer Meteorol.*, **37**, 129–148.
- Valdes, P. J. and Hoskins, B. J. (1988). Baroclinical instability of the zonally averaged flow with boundary layer damping. *J. Atmos. Sci*, **45**, 1584–1593.
- Wernli, H. (1997). A Lagrangian-based analysis of extratropical cyclones. ii: A detailed case-study. *Q. J. R. Meteorol. Soc.*, **123**, 1677–1706.
- Wernli, H. and Davies, H. C. (1997). A Lagrangian-based analysis of extratropical cyclones. i: The method and some applications. *Q. J. R. Meteorol. Soc.*, **123**, 476 – 489.
- Wernli, H., Fehlmann, R., and Lüthi, D. (1998). The effect of barotropic shear on upper-level induced cyclogenesis: semigeostrophic and primitive equation numerical simulations. *J. Atmos. Sci*, **55**, 2080–2094.

- 
- Williams, G. P. and Robinson, J. B. (1974). Generalized Eady waves with Ekman pumping. *J. Atmos. Sci.*, **31**, 1768–1776.
- Woodruff, S. D., Diaz, H. F., Elms, J. D., and Worley, S. J. (1998). COADS Release 2 data and metadata enhancements for improvements of marine surface flux fields. *Phys. Chem. Earth.*, **23**, 517 – 527.